

## ABSTRACT

Title of dissertation: ANALYTICAL AND COMPUTATIONAL  
INVESTIGATIONS INTO WAVE  
PROPAGATION THROUGH  
SOFT TISSUE

Marcelo Valdez, 2013

Dissertation directed by: Professor Balakumar Balachandran  
Department of Mechanical Engineering

The influence of nonlinearities on the propagation of stress waves through soft tissues is currently an open research area. Understanding this influence could yield insights into the damage mechanisms of soft tissues in response to rapid and strong external excitations. In the context of this dissertation, soft tissues are idealized as nonlinear viscoelastic materials, and the focus is on the mechanical aspects of the tissue behavior. Two nonlinear material models are explored. One of them, a nonlinear extension of the standard solid viscoelastic model, is employed first to describe brain tissue behavior, and second, to study the interaction of blast pressure waves with viscoelastic systems. The second material model, obtained through a maximum dissipation, thermodynamically consistent construction, is employed for the studies of longitudinal wave propagation.

In order to focus on the effects of the material nonlinearity, a geometrically fundamental model for longitudinal stress waves is employed. Theoretical studies

including dispersion and asymptotic analyses are carried out in order to further the current understanding of wave propagation characteristics, such as the dependence of the wave speed and attenuation on the frequency, the effect of material dissipation, and the nonlinear steepening of wave fronts. Computational studies are carried out to examine various aspects of the nonlinear wave propagation. A unique nonlinear phenomenon related to the steepening of wave fronts is observed: the tissue absorbs energy in a localized fashion at the location of the moving steep wave front. This situation could be potentially detrimental to the tissue. Finally, the interplay between geometry (non-uniform cross-section) and material nonlinearity is studied. It is observed that a contracting cross-section promotes the development of much steeper stress wave fronts. The spatial location at which the steep wave front develops appears to be related to the elapsed time and the amplitude of the external load. Understanding this relationship could help establish a link between the location of the tissue damage and the external loading. This dissertation work can serve as a basis for better understanding the mechanical causes underlying mild traumatic brain injury, for example, as a consequence of head impact or explosive blast waves.

ANALYTICAL AND COMPUTATIONAL INVESTIGATIONS  
INTO WAVE PROPAGATION THROUGH  
SOFT TISSUE

by

Marcelo F. Valdez

Dissertation submitted to the Faculty of the Graduate School of the  
University of Maryland, College Park in partial fulfillment  
of the requirements for the degree of  
Doctor of Philosophy  
2013

Advisory Committee:

Professor Balakumar Balachandran, Chair and Advisor

Professor Amr Baz

Professor Abhijit Dasgupta

Research Associate Professor Henry Haslach, Jr.

Professor Sung Lee, Dean's Representative

Associate Professor Teng Li

© Copyright by  
Marcelo F. Valdez  
2013

## Dedication

*A la memoria de laucha, mi amigo del alma.*

## Acknowledgments

First, I would like express my deep gratitude to my advisor, Professor B. Balachandran for giving me the great opportunity to pursue my PhD as a part his research group at the University of Maryland at College Park, for his unconditional support, guidance and advise throughout my graduate studies, and for his help and understanding regarding my future post-graduation endeavors.

I would also like to thank the members of my dissertation committee: Professor Amr Baz, Professor Abhijit Dasgupta, Professor Henry Haslach, Professor Sung Lee and Professor Teng Li for their time and insightful feedback during my proposal and dissertation defenses. I have had the wonderful chance of taking classes with most of them, and to hold one-on-one discussions about research related topics.

My appreciation goes to my past and present lab mates: Tim Fitzgerald, Nick Vlajic, Edmon Perkins, Ishita Chakraborty, Chien-Min Liao, Chris Chabalko, Vince Nguyen, Rubyka Jaai and Hesham Ismail for all these years together on the pursue of our goals, and for their inputs during our uncountable group meetings.

A special place in this acknowledgement belongs to my friends Marcos Vanella, Patri Forcinito, Nikos Beratlis, Antonio Cardone and Tim Fitzgerald for the fun times together and for always being present during the good and the not so good times of my life in the United States. I specially thank Christine Ikeda for her unconditional company and love, and for her helping with my dissertation writing and defense. I do not want to forget my lifelong friends from Argentina specially: Daniel Padilla, Hernán Gudiño, Silvio Bruna, Ezequiel Pistone, Guillermo Doallo,

and Daniel Benito. Although I only get to see them once a year, it always feels like I have never left. I want to thank also my intramural soccer teammates with whom I have played exciting tournaments, and won some of them, at the University of Maryland, specially to Mike Siemann for organizing and keeping the team together throughout the past four years.

My immense gratitude to Professor Sergio Preidikman, for helping me make my first steps in these long lasting research career, and for introducing me to Professor Balachandran. For his company during his stays at my apartment and for sharing his musical interests with me.

Le agradezco profundamente a mi familia, que a pesar de la distancia siempre me ha apoyado, especialmente a mi papá Roberto, my mamá Nancy, mis hermanos Francisco y Martín y a mi abuela Sara.

Finally, the support received for this work through the Center for Energetic Concepts Development (CECD) at the University of Maryland is gratefully acknowledged.

# Table of Contents

List of Tables	viii
List of Figures	ix
1 Introduction	1
1.1 Soft Tissue Mechanics . . . . .	1
1.2 Brain Tissue: Anatomy . . . . .	4
1.3 Brain Tissue: Experimental Characterization and Constitutive Mod- eling . . . . .	6
1.4 Studies on Brain Injury by Direct and Indirect Head Impact . . . . .	19
1.4.1 Analytical Studies . . . . .	19
1.4.2 Finite Element Studies . . . . .	25
1.5 Blast Induced Brain Injury . . . . .	29
1.6 Axonal Injury . . . . .	31
1.7 Objectives . . . . .	34
1.8 Dissertation Organization . . . . .	35
2 Nonlinear Viscoelastic Modeling and Fluid–Structure Interaction Studies	37
2.1 Nonlinear Standard Solid Viscoelastic Model . . . . .	37
2.2 Nonlinear Standard Solid Viscoelastic Model Curve–Fitting to Brain Tissue Experimental Data . . . . .	40
2.2.1 Standard Solid Viscoelastic Model with One Maxwell Mode .	41
2.2.2 Standard Solid Viscoelastic Model with Two Maxwell Modes .	42
2.3 Interactions of Pressure Waves with Nonlinear Viscoelastic Systems .	45
2.3.1 System Description and Governing Equations . . . . .	48
2.3.2 Scaling of Variables and Non–dimensional Governing Equations	50
2.3.3 Exponential Wave Profile . . . . .	52
2.4 Maximum Dissipation Nonlinear Viscoelastic Constitutive Equation for Uniaxial Stress State . . . . .	57
2.4.1 Maximum Dissipation Viscoelastic Model Curve–Fitting to Brain Tissue Experimental Data . . . . .	61
3 Longitudinal Wave Propagation through Viscoelastic Material with Constant Cross–Section	66
3.1 Governing Equations . . . . .	66
3.2 Rod with Uniform Cross–Section . . . . .	68
3.3 Linear Viscoelastic Material Case . . . . .	68
3.3.1 Scaling of Variables . . . . .	70
3.4 Linear Viscoelastic Rod with Weak Dissipation: Asymptotic Analysis	71
3.4.1 Semi–Infinite Linear Viscoelastic Rod with Prescribed Dis- placement . . . . .	76
3.4.1.1 Stress–Wave Solution for Linear Viscoelastic Rod Initially at Rest . . . . .	79

3.4.2	Semi-Infinite Linear Viscoelastic Rod with Prescribed Stress . . . . .	79
3.4.2.1	Stress-Wave Solution for Linear Viscoelastic Rod Initially at Rest . . . . .	82
3.5	Dispersion Relation for Semi-Infinite Linear Viscoelastic Rod . . . . .	82
3.5.1	Phase speed . . . . .	85
3.5.2	Attenuation . . . . .	85
3.5.2.1	Frequency Bounds for Wave Propagation in Axon Tracts . . . . .	86
3.5.2.2	Brain Tissue “Bulk” Attenuation . . . . .	89
3.6	Longitudinal Standing Waves in Linear Viscoelastic Rods . . . . .	91
3.6.1	Fixed-Fixed Boundary Conditions . . . . .	92
3.6.2	Fixed-Free Boundary Conditions . . . . .	93
3.6.3	Linear Kelvin-Voigt Viscoelastic Supports at Both Ends . . . . .	93
3.6.4	Free-Vibrations Characteristics . . . . .	96
3.7	Nonlinear Viscoelastic Material Case . . . . .	99
3.7.1	Scaling of Variables . . . . .	99
3.8	Nonlinear Viscoelastic Rod: Asymptotic Analysis . . . . .	100
3.8.1	Stress-Wave Solution for Nonlinear Viscoelastic Rod Initially at Rest . . . . .	104
3.8.2	Representative Results for a Particular Displacement Input . . . . .	105
3.9	Frequency Response of a Nonlinear Viscoelastic Rod . . . . .	108
3.9.1	Case 1: $B_k = \mathcal{O}(\eta_k^2) = \mathcal{O}(\alpha\dot{\eta}_k) = \mathcal{O}(\epsilon^2)$ . . . . .	110
3.9.2	Case 2: $B_k = \mathcal{O}(\eta_k^3) = \mathcal{O}(\alpha\dot{\eta}_k) = \mathcal{O}(\epsilon^3)$ . . . . .	114
3.9.2.1	Primary Resonance of the First Mode . . . . .	120
3.10	Numerical Simulations of Longitudinal Wave Propagation through Nonlinear Viscoelastic Rod with Uniform Cross-Section . . . . .	121
3.10.1	Nonlinear Viscoelastic Material Models . . . . .	125
3.10.2	Compression Waves . . . . .	127
3.10.3	Tension Waves . . . . .	128
3.10.4	Wave Speed . . . . .	130
3.10.5	Concluding Remarks on Material Nonlinearity Effects on Lon- gitudinal Wave Propagation . . . . .	134
4	Longitudinal Wave Propagation through Non-Uniform Structures . . . . .	139
4.1	Introduction . . . . .	139
4.2	Non-Uniform Rod Model . . . . .	140
4.2.1	Scaling of Variables . . . . .	140
4.3	Linear Viscoelastic Material Case . . . . .	141
4.3.1	Dispersion Relation for a Semi-Infinite, Non-Uniform Linear Viscoelastic Rod . . . . .	142
4.4	Semi-Infinite Linear Viscoelastic Rod with Weakly (Slowly) Varying Cross-Section . . . . .	145
4.4.1	Semi-Infinite Linear Viscoelastic Rod with Varying Cross- Section and with Prescribed Stress . . . . .	149

4.5	Numerical Simulations for Longitudinal Wave Propagation through Nonlinear Viscoelastic Rod with Non-Uniform Cross-Section	150
4.5.1	Exponential Cross-Section Variation . . . . .	152
4.5.1.1	Results for a Rod with Exponentially Decreasing Cross-Section . . . . .	153
4.5.1.2	Results for a Rod with Exponentially Increasing Cross-Section . . . . .	156
4.5.2	Localized Cross-Section Variation: Bulge-Shaped Geometry .	160
4.5.2.1	Numerical Simulation Results . . . . .	163
4.6	Final Remarks on Geometry Effects on Longitudinal Wave Propagation	163
5	Summary and Concluding Remarks	168
5.1	Summary of Contributions . . . . .	169
5.2	Recommendations for Future Work . . . . .	172
A	Maximum Dissipation Nonlinear Viscoelastic Material Model	173
A.1	Mathematical Construction of the Constitutive Equation . . . . .	173
A.2	Simple tension of incompressible, isotropic hyperelastic material . . .	176
B	Particular Solutions for the Wave Equation in Semi-Infinite Domain	178
B.1	Homogeneous Dirichlet (Displacement) Boundary Condition . . . . .	178
B.2	Homogeneous Initial Conditions and Dirichlet Boundary Condition .	179
B.3	Homogeneous Neumann (Force) Boundary Condition . . . . .	180
B.4	Homogeneous Initial Conditions and Neumann Boundary Condition .	182
C	Galerkin Projection Procedure and Particular Resonance Case Study	184
C.1	Galerkin Projection . . . . .	184
C.2	Primary Resonance of the First Mode . . . . .	186
D	Numerical Scheme for the Study of Wave Propagation through Nonlinear Viscoelastic Material	191
D.1	Finite Difference Scheme . . . . .	191
	Bibliography	200

## List of Tables

1.1	Experimental characterization of brain tissue mechanical behavior . . .	20
1.2	Experimental studies on axonal injury . . . . .	32
2.1	Curve-fitted material constants for the nonlinear viscoelastic model with one Maxwell mode . . . . .	42
2.2	Curve-fitted material constants for the nonlinear viscoelastic model with two Maxwell modes . . . . .	45
2.3	Curve-fitted material parameters for different maximum dissipation nonlinear viscoelastic material models . . . . .	63
3.1	Values of $\mathcal{T}$ and $P_0^*$ for constant energy value $E_P = 0.01$ . . . . .	126
4.1	Values of $\mathcal{X}_B$ and $\mathcal{A}_{\min}^*/\mathcal{A}_0^*$ defining bulges with mass ratio $R = 0.25$ . . . . .	162
C.1	Values of $p_{mi}$ ( $i = 1, 2, \dots, 7$ ; $m=1,2$ ) from Eq. (3.165) corresponding to $k = 1$ and $M = 2$ . . . . .	187

## List of Figures

1.1	Different types of soft, biological tissues. . . . .	3
1.2	Neuron physiology. . . . .	6
2.1	Nonlinear standard solid viscoelastic model. . . . .	38
2.2	Experimental data for unconfined compression of swine brain tissue (Miller and Chinzei, 1997). . . . .	43
2.3	Comparison between the predictions of the one–Maxwell mode nonlinear viscoelastic model with curve–fitted parameters and the experimental data for $\dot{\lambda}_\infty = 0.64 \text{ sec}^{-1}$ . . . . .	43
2.4	Comparison between the predictions of the one–Maxwell mode nonlinear viscoelastic model with curve–fitted parameters and the experimental data for $\dot{\lambda}_\infty = 0.64 \text{ sec}^{-1}$ . . . . .	44
2.5	Comparison between the predictions of the one–Maxwell mode nonlinear viscoelastic model with curve–fitted parameters and the experimental data for $\dot{\lambda}_\infty = 0.64 \text{ sec}^{-1}$ . . . . .	44
2.6	Comparison between the predictions of the two–Maxwell mode nonlinear viscoelastic model with curve–fitted parameters and the experimental data for $\dot{\lambda}_\infty = 0.64 \text{ sec}^{-1}$ . . . . .	46
2.7	Comparison between the predictions of the two–Maxwell mode nonlinear viscoelastic model with curve–fitted parameters and the experimental data for $\dot{\lambda}_\infty = 0.64 \text{ sec}^{-1}$ . . . . .	46
2.8	Comparison between the predictions of the two–Maxwell mode nonlinear viscoelastic model with curve–fitted parameters and the experimental data for $\dot{\lambda}_\infty = 0.64 \text{ sec}^{-1}$ . . . . .	47
2.9	Schematic of the interaction of an incoming pressure wave in air with a mass supported by a nonlinear viscoelastic material. . . . .	49
2.10	Exponential pressure profile at the location $\zeta = 0$ for different values of $\beta_0$ . . . . .	53
2.11	Ratio of impulse transmitted to available impulse ( $I_m/I_p$ ) as a function of $\beta_0$ for $p_0 = 0.01$ and for different values of the damping parameter $\alpha_1$ . . . . .	56
2.12	Ratio of impulse transmitted to available impulse ( $I_m/I_p$ ) as a function of $\beta_0$ for $p_0 = 0.1$ and for different values of the damping parameter $\alpha_1$ . . . . .	57
2.13	Ratio of impulse transmitted to available impulse ( $I_m/I_p$ ) as a function of $\beta_0$ for $p_0 = 1$ and for different values of the damping parameter $\alpha_1$ . . . . .	58
2.14	Non–dimensional force transmitted to the base ( $F_s/(p_s\mathcal{A})$ ) as a function of $\beta_0$ for $p_0 = 0.01$ and for different values of the damping parameter $\alpha_1$ . . . . .	59
2.15	Non–dimensional force transmitted to the base ( $F_s/(p_s\mathcal{A})$ ) as a function of $\beta_0$ for $p_0 = 0.1$ and for different values of the damping parameter $\alpha_1$ . . . . .	60

2.16	Non-dimensional force transmitted to the base ( $F_s/(p_s\mathcal{A})$ ) as a function of $\beta_0$ for $p_0 = 1$ and for different values of the damping parameter $\alpha_1$ . . . . .	61
2.17	Comparison between the predictions of the maximum dissipation nonlinear viscoelastic models with curve-fitted parameters and the experimental data for $\dot{\lambda} = -0.64 \text{ sec}^{-1}$ . . . . .	64
2.18	Comparison between the predictions of the maximum dissipation nonlinear viscoelastic models with curve-fitted parameters and the experimental data for $\dot{\lambda} = -0.64 \times 10^{-2} \text{ sec}^{-1}$ . . . . .	65
2.19	Comparison between the predictions of the maximum dissipation nonlinear viscoelastic models with curve-fitted parameters and the experimental data for $\dot{\lambda} = -0.64 \times 10^{-5} \text{ sec}^{-1}$ . . . . .	65
3.1	Rod model for uniaxial stress state. . . . .	67
3.2	Non-dimensional phase speed $\tilde{c}$ and attenuation $\tilde{\beta}$ as a function of non-dimensional frequency $\tilde{\omega}$ . . . . .	86
3.3	Frequency lower bound for wave propagation in an axon tract of length $L = 10 \text{ mm}$ with fixed-fixed ends. . . . .	89
3.4	Comparison between experimental measurements of attenuation in bovine brain tissue and model with curve-fitted parameters. . . . .	91
3.5	Rod with linear Kelvin-Voigt supports at both ends. . . . .	94
3.6	First wave number root $\bar{k}_1$ of Eq. (3.97) as a function of the non-dimensional stiffnesses $k_1^*$ and $k_2^*$ . . . . .	96
3.7	$\text{Im}[r_{1n,2n}]/\bar{k}$ as a function of the non-dimensional wave number $\bar{k}\alpha$ . . . . .	98
3.8	Shape of the displacement pulse (3.135) introduced at $\xi = 0$ . . . . .	106
3.9	Comparison between asymptotic solutions for the compression stress wave corresponding to the linear and nonlinear viscoelastic rods. . . . .	107
3.10	Comparison between asymptotic solutions for the tension stress wave corresponding to the linear and nonlinear viscoelastic rods. . . . .	107
3.11	Effect of nonlinear material properties $C_1$ on the frequency response for $\vartheta = 0.01$ and $Q_1 = 0.3$ . . . . .	122
3.12	Effect of the amplitude of excitation $Q_1$ on the frequency response for $\vartheta = 0.01$ and $C_1 = -10$ . . . . .	122
3.13	Effect of damping $\vartheta$ the frequency response for $C_1 = -10$ and $Q_1 = 0.3$ . . . . .	123
3.14	Input stresses with energy $E_P = 0.01$ as a function of time for different values of $\mathcal{T}$ . . . . .	125
3.15	Snapshots of compression wave profiles obtained with the two nonlinear viscoelastic models and the linear viscoelastic model. . . . .	129
3.16	Normalized compression peak amplitude as a function of its location along the rod. . . . .	130
3.17	Snapshots of tension wave profiles obtained with the two nonlinear viscoelastic models and the linear viscoelastic model. . . . .	131
3.18	Normalized tension peak amplitude as a function of its location along the rod . . . . .	132
3.19	Compression and tension wave speeds as a function of distance traveled. . . . .	134

3.20	Snapshot of the energy absorption density $w(\xi, \tau = \tau_i)$ at $\tau_i = 0.61625$ for a compressive wave pulse propagating through nonlinear and linear viscoelastic materials. . . . .	136
3.21	Snapshots of the energy absorption density $w(\xi, \tau_i)$ at different instants of time $\tau_i$ , corresponding to the compressive input load with $\mathcal{T} = 0.03125$ and the indicated material models. . . . .	137
4.1	Phase speed and attenuation of harmonic waves for a rod with exponential cross-sectional area. . . . .	146
4.2	Two geometries of a rod with exponentially varying cross-section. . . . .	153
4.3	Snapshots of the tension and compression wave profiles propagating through the nonlinear viscoelastic rod with exponentially decreasing cross-section. . . . .	154
4.4	Snapshots of the tension and compression wave profiles propagating through the linear viscoelastic rod with exponentially decreasing cross-section. . . . .	154
4.5	Stress peak as a function of its location along the rod corresponding to an exponentially decreasing cross-section. . . . .	156
4.6	Effect of the exponentially decreasing cross-section on the steepening of tension and compression wave fronts. . . . .	157
4.7	Snapshots of the tension and compression wave profiles propagating through the nonlinear viscoelastic rod with exponentially increasing cross-section. . . . .	158
4.8	Snapshots of the tension and compression wave profiles propagating through the linear viscoelastic rod with exponentially increasing cross-section. . . . .	158
4.9	Stress peak as a function of its location along the rod corresponding to an exponentially increasing cross-section. . . . .	159
4.10	Effect of the exponentially increasing cross-sectional area on the steepening of tension and compression wave fronts. . . . .	160
4.11	Different bulge geometries for constant mass ratio $R = 0.25$ . . . . .	162
4.12	Snapshots of the compression and tension wave profiles propagating through the nonlinear viscoelastic rod with a bulge characterized by $\mathcal{X}_B = 0.125000$ at the center. . . . .	164
4.13	Snapshots of the compression and tension wave profiles propagating through the nonlinear viscoelastic rod with a bulge characterized by $\mathcal{X}_B = 0.062500$ at the center. . . . .	165
4.14	Snapshots of the compression and tension wave profiles propagating through the nonlinear viscoelastic rod with a bulge characterized by $\mathcal{X}_B = 0.031250$ at the center. . . . .	166
4.15	Snapshots of the compression and tension wave profiles propagating through the nonlinear viscoelastic rod with a bulge characterized by $\mathcal{X}_B = 0.0156125$ at the center. . . . .	167

# Chapter 1

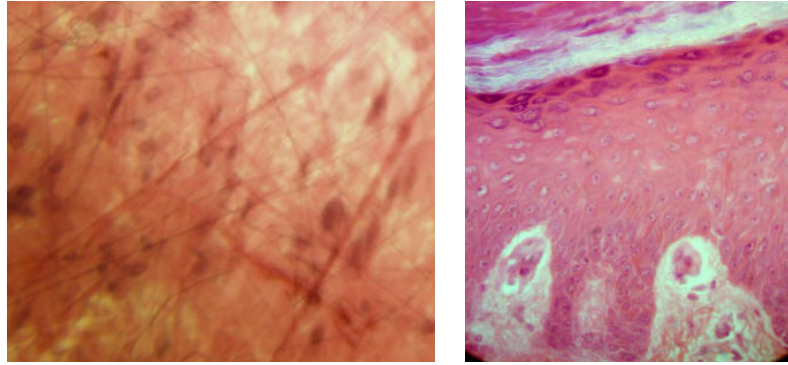
## Introduction

In this chapter, an introduction to soft tissue mechanics and brain tissue cellular anatomy is presented. In addition, literature reviews relevant to the topics of brain tissue experimental characterization and material modeling, head impact and blast-related injury studies, and experimental investigations on axon mechanics and injury are presented. Finally, the objectives and organization of this dissertation are presented.

### 1.1 Soft Tissue Mechanics

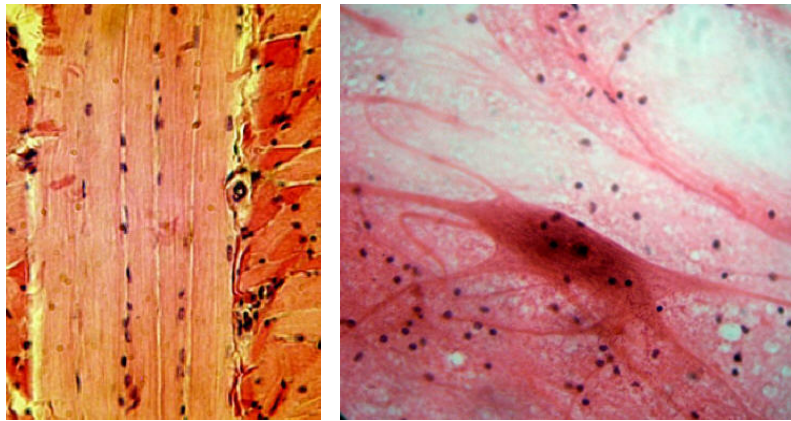
Biomaterials are usually classified as hard tissues (bone, wood) and soft tissues (skin, muscles, organs). Hard tissues exhibit small deformations and a linear elasticity theory is often more than sufficient for the analysis of their behavior to externally applied loads. Conversely, soft tissues usually undergo large (finite) strains and their behavior is regarded as nonlinear viscoelastic in nature. A review on the modeling of soft tissues can be found in the work of Humphrey (2003). A tissue constitutes a collection of cells bonded together through an extracellular matrix consisting of protein fibers such as collagen, elastin, actin, and so on. In Fig. 1.1, different types of tissue are shown. A common classification of animal tissue is given next (Cowin and Doty, 2007).

- **Connective tissue:** This type of tissue is composed of a large number of fibers (polymers of elastin or collagen proteins) embedded in the extracellular substance, forming a network that holds the relatively small and few cells in position. The network of fibers may have a regular (woven fabric) or irregular arrangement; and they can be either densely or loosely packed. Examples of this tissue include cartilage, tendons, and ligaments.
- **Epithelium tissue, or epithelium:** These tissues line surfaces and cavities of the body and internal organs. The epithelial cells have different functions that include secretion, absorption, protection, transcellular transport, and sensation. An example of this kind of tissue is the external layer of the skin or the epithelial layer. Epithelial tissue consists of densely packed cells with little extracellular substance between them forming tight junctions.
- **Muscle tissue:** This tissue can be subdivided in three main categories: striated, smooth, and cardiac muscles. Striated muscles are responsible for voluntary motions of the different parts of the body, as they are attached to the bone. Smooth muscles form internal organs and vessels perform involuntary motions, such as the peristalsis motion of the digestive tract. Cardiac muscles, also involuntary, are responsible for the diastolic and systolic motions of heart.
- **Nerve tissue:** This tissue is composed of networks of nerve cells or neurons, supported by neuroglia. The nerve tissue constitutes the major component of the nervous system; that is, the central nervous system consisting of the brain and the spinal cord, and the peripheral nervous system composed of



(a)

(b)



(c)

(d)

Figure 1.1: Different types soft, biological tissues. (a): Areolar connective tissue; (b): Epithelial tissue from skin; (c): Striated muscle tissue (d): Nerve tissue. Images reproduced with permission<sup>1</sup>.

the cranial and spinal nerves and their associated ganglia. Its function is to transport information in the form of electric and chemical pulses between different parts of the body.

---

<sup>1</sup>source: [http://www2.yvcc.edu/histologyzoomer/HistologyTutorials/histology\\_tutorials.htm](http://www2.yvcc.edu/histologyzoomer/HistologyTutorials/histology_tutorials.htm).

## 1.2 Brain Tissue: Anatomy

Amongst the soft tissues described in §1.1, brain tissue is of particular interest in this work. Although the studies presented in this dissertation apply to soft tissues in general, conclusions regarding mechanical implications of wave propagation to brain tissue damage will be drawn when possible. The following description of brain tissue anatomy was adapted from the book of Snell (2009).

At the macroscopic level, the brain is mainly composed of a core of white matter surrounded by gray matter. Gray matter consists of neurons embedded in neuroglia and it is characterized by a gray color. White matter consists of nerve fibers embedded in neuroglia and its characteristic white color is due to lipids present in the myelin sheaths of many nerve fibers.

The principal nerve cells of the central nervous systems are the neurons. These excitable cells receive external stimuli and transmit nerve impulses. Although their size and shape are not uniform, they have similar anatomical features: a cell body with one or more processes called neurites or nerve fibers. The cell bodies have diameters that range from  $5\ \mu\text{m}$  to  $135\ \mu\text{m}$ .

Dendrites are short neurites, which receive information and conduct it towards the cell body. Their diameter usually tapers as they extend away from the cell body, and usually present a large amount of ramifications or branches.

On the other hand, the axon is the single, long tubular neurite that conducts electrical impulses from the cell body to other neighboring neurons. It begins from a rather conical extension of the cell body called axon hillock and ends at the cone of

growth, from where there is a profuse branching. Axons usually do not have branches close to the cell body and can be as short as 0.1 mm, as observed in several neurons in the brain; or as long as 3 m, extending from the toe to the brain. The diameter of the axons determines the speed of the electrical impulses transmitted. Those of larger diameter conduct impulses faster than those with smaller diameter.

The neurons on the brain are supported by the neuroglia including varieties of non-excitabile cells. These cells are usually smaller than neurons and outnumber them by a 5:1 to 10:1 ratio. There are four types of neuroglial cells: (*i*) astrocytes, (*ii*) oligodendrocytes, (*iii*) microglia, and (*iv*) ependyma.

Astrocytes have small cell bodies and branching extensions in all directions. Two different types of astrocytes can be found: fibrous astrocytes, mostly located in the white matter; and protoplasmic astrocytes distributed mainly in the gray matter. Fibrous and protoplasmic astrocytes, with their branching processes form a supporting framework for nerve cells and nerve fibers, respectively.

Oligodendrocytes are in charge of the production of the myelin sheath that cover nerve fibers. They have a small cell body and a few specialized processes. They are usually located along myelinated nerve fibers and surrounding nerve cell bodies.

Microglial cells are the smallest neuroglia and can be found scattered throughout the brain tissue. Microglial cells are usually inactive but become active during inflammatory and degenerative lesions in the brain by moving to the place of the injury.

An schematic representation of the neuron physiology is presented in Fig. 1.2

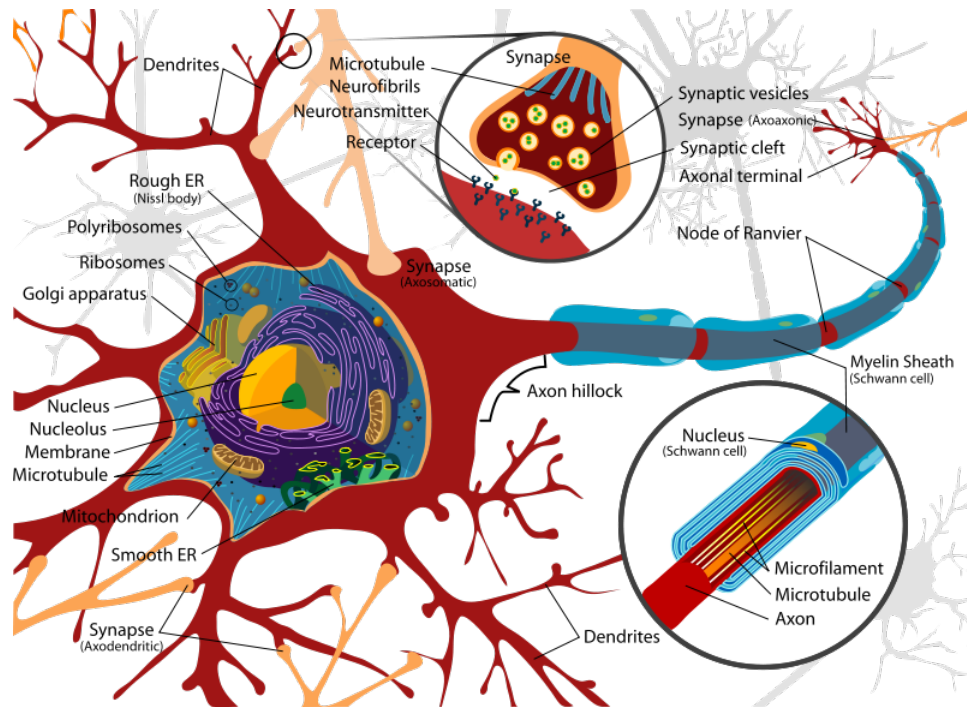


Figure 1.2: Neuron physiology<sup>2</sup>.

### 1.3 Brain Tissue: Experimental Characterization and Constitutive Modeling

The correct estimation of the mechanical properties of brain tissue is of primary importance to subsequent studies related to brain injury. Early reports of experimental determination of the mechanical behavior of brain tissue date back to Fallenstein, Hulce, and Melvin (1969) and Estes and McElhaney (1970). Fallenstein *et al.* attempted to measure the dynamic shear modulus of post-mortem brain tissue by using a sinusoidal shear input. Estes and McElhaney performed experiments with human brain tissue in compression at constant stretch rates ranging from 0.08 to 40  $\text{sec}^{-1}$  and up to a compressive natural strain of 1. These early experimental results

<sup>2</sup>source: [http://en.wikipedia.org/wiki/File:Complete\\_neuron\\_cell\\_diagram\\_en.svg](http://en.wikipedia.org/wiki/File:Complete_neuron_cell_diagram_en.svg)

were used extensively by other researchers in the field, to validate their constitutive models. During the last forty years, numerous experiments with animal brain tissue have been reported; however, there is still no general agreement on the mechanical properties of the brain tissue, nor on a material model that best describe its behavior. Hrapko, van Dommelen, Peters, and Wismans (2008b) recount different experiments with brain tissue conducted by different research groups, in order to assess the impact of the testing conditions (temperature, protocols and methods, and so on) on the reported material properties. The following observations regarding shear deformations were pointed out by these researchers: brain tissue appears to be stiffer at room temperature than it is at body temperature; anisotropy of the tissue produce different stiffness in different planes (coronal, sagittal and transverse) for the same sample; and finally, pre-compression has been found to stiffen the samples. The fact that the great majority of experimental studies do not carefully control and/or report their testing conditions (temperature, humidity, pressure, pre-conditioning, and so on) provide an explanation to why there is not general consensus regarding the mechanical behavior brain tissue. In Table 1.1 some of the experimental studies on brain tissue carried out throughout the years, with additional details regarding their experimental set-ups and protocols are presented. This list is far from being exhaustive.

Mendis, Stalnaker, and Advani (1995) developed a modified incompressible Mooney–Rivlin hyperelastic model. Dissipative effects were incorporated by defining relaxation functions for the coefficients of the Mooney–Rivlin strain energy function.

These relaxation functions were defined in terms of Prony series as follows:

$$C_{ij} = \left( C_{ij}^{\infty} + \sum_{k=1}^M (C_{ij}^k - C_{ij}^{\infty}) e^{-\frac{t}{\tau_k}} \right) h(t). \quad (1.1)$$

Here,  $C_{ij}^{\infty}$  is the steady-state value of the coefficient determined from quasi-static tests,  $\tau_k$  are relaxation times, and  $h(t)$  is the Heaviside step function. The strain energy density function with two time varying coefficients has been defined in terms of the convolution integral

$$\Psi(I_1, I_2, t) := \int_0^t \left[ C_{10}(t - \xi) \frac{d}{d\xi} I_1(\xi) + C_{01}(t - \xi) \frac{d}{d\xi} I_2(\xi) \right] d\xi, \quad (1.2)$$

where  $I_1$  and  $I_2$  are the first and second invariants of the strain tensor, respectively.

The stress is computed as

$$\sigma(\lambda_1, t) = \lambda_1 \frac{\partial \Psi}{\partial \lambda_1}, \quad (1.3)$$

where  $\lambda_1$  is the uniaxial stretch. The model parameters were estimated by curve-fitting the experimental data of Estes and McElhaney (1970) on constant strain rate compression experiments. Mendis *et al.* found two terms in the Prony series, one with a fast decay time and another with a slow decay time, sufficient to represent the experimental data.

Arbogast and Margulies (1998) performed oscillatory shear tests on adult porcine brainstem along three mutually orthogonal directions; their results show that the brainstem exhibits significant transversely isotropic behavior. Particularly, these researchers found that both components of the complex modulus obtained by shearing the tissue across the axonal fibers were higher than those obtained in the other two shear directions.

Experiments with swine brain tissue in uniaxial unconfined compression and uniaxial tension at various (and small) constant strain rates have been conducted by Miller and Chinzei (1997, 2002), respectively. It was stated by Miller and Chinzei that brain tissue behaves differently in compression and tension. However, this different behavior could also be attributed to the differences between the experimental set-ups used for the compression (slip allowed between tissue and parallel platens) and tension experiments (tissue glued to the parallel platens). These researchers also presented a nonlinear viscoelastic model that constitutes a generalization of an Ogden type hyperelastic material with time dependent coefficients, and obtained a reasonable agreement with the experimental data. The form of the strain energy function proposed by these researchers is given by

$$\Psi(I_1, I_2, t) := \int_0^t \left[ \sum_{i+j=1}^N C_{ij}(t-\tau) \frac{d}{dt} \left( (I_1 - 3)^i (I_2 - 3)^j \right) \right] d\tau. \quad (1.4)$$

The time varying coefficients  $C_{ij}(t)$  were expressed in terms of Prony series, similar to the work of Mendis *et al.* (1995). Miller and Chinzei found that four terms  $N = 2$  were necessary to obtain good agreement with the experiments. In addition, two terms in the Prony series for the  $C_{ij}(t)$  were employed. However, these researchers hand-picked the decay times  $\tau_k$  to be equal to the elapsed time of their experiments at medium and fast strain rates. This choice of the decay times, although providing relatively good agreement with the experimental results, lacks physical meaning in the sense that a constitutive model must be independent of the experimental technique used to determine it.

Darvish and Crandall (2001) performed simple shear tests at frequencies rang-

ing from 0.5 to 200 Hz, with amplitudes of up to 20% shear strain. Two constitutive models were presented as well: a quasilinear viscoelastic model (QLV) with a single hereditary integral, and a nonlinear model with multiple hereditary integrals (Green-Rivlin model). In the QLV model, the Cauchy shear stress is given by

$$\sigma_{12} = \sigma_{21} = 2\mu_0 \int_0^t G(t - \tau) [1 + 12\gamma e_{12}^2(\tau)] \dot{e}_{12} d\tau, \quad (1.5)$$

where  $e_{12} = e_{21}$  is the Eulerian shear strain,  $\mu_0$  and  $\gamma$  are the linear elasticity shear modulus and the nonlinearity coefficient, respectively, and  $G(t)$  is the reduced relaxation function. In the multiple hereditary integrals model (MHI), the shear strain is given by

$$\begin{aligned} \Sigma_{12} = \Sigma_{21} = & 2\mu_0 \int_0^t G_1(t - \tau_1) \dot{E}_{12}(\tau_1) d\tau \\ & + 4 \int_0^t \int_0^t G_2(t - \tau_1, t - \tau_2) \dot{E}_{12}(\tau_1) \dot{E}_{12}(\tau_2) d\tau_1 d\tau_2 \\ & + \int_0^t \int_0^t \int_0^t G_3(t - \tau_1, t - \tau_2, t - \tau_3) \dot{E}_{12}(\tau_1) \dot{E}_{12}(\tau_2) \dot{E}_{12}(\tau_3) d\tau_1 d\tau_2 d\tau_3, \end{aligned} \quad (1.6)$$

where  $\Sigma_{12}$  is the shear component of the pulled back Cauchy stress tensor to the frame that is rotated with the rotation component of the deformation gradient at time  $t$ .

Bilston, Liu, and Phan-Thien (2001) performed experiments with bovine brain tissue under large shear strain and developed a constitutive model whose predictions acceptably represent the experimental results. The experimental results show that the relaxation of the tissue is slower for higher strains. Their proposed constitutive model consisted of a combination of an hyperelastic model (Mooney–Rivlin type) with a nonlinear viscoelastic model. The Cauchy stress tensor has been expressed

as

$$\boldsymbol{\sigma} = -p\mathbf{I} + \boldsymbol{\sigma}_E + \boldsymbol{\sigma}_V, \quad (1.7)$$

where  $p$  is the hydrostatic pressure,  $\boldsymbol{\sigma}_E$  is the elastic component of the stress, and  $\boldsymbol{\sigma}_V$  is the viscous contribution. The elastic stress was expressed as a Mooney–Rivlin model, modified with a damping function  $f(I_1, I_2)$  of the invariants of the strain tensor as follows:

$$\boldsymbol{\sigma}_E = f(I_1, I_2) \frac{G_E}{1+a} (\mathbf{b} - a\mathbf{b}^{-1}). \quad (1.8)$$

Here,  $G_E$  is a long-term elastic modulus,  $a$  is a constant and  $\mathbf{b}$  is the left Cauchy–Green tensor or Finger deformation tensor. The viscous stress  $\boldsymbol{\sigma}_V$  was modeled as an upper convected multi-mode Maxwell model

$$\boldsymbol{\sigma}_V = f(I_1, I_2) \sum_{j=1}^N \boldsymbol{\sigma}^j, \quad (1.9)$$

where each mode  $j$  was defined as

$$\boldsymbol{\sigma}^j + \kappa_j(I_1, I_2) \left[ \frac{d\boldsymbol{\sigma}^j}{dt} - \nabla \mathbf{v}^T \boldsymbol{\sigma}^j - \boldsymbol{\sigma}^j \nabla \mathbf{v} \right] = 2\eta_j \mathbf{d}, \quad (1.10)$$

with  $\nabla \mathbf{v}$  the velocity gradient,  $\mathbf{d}$  the strain rate tensor, and  $\kappa_j$  the strain dependent relaxation parameters.

Ehlers and Markert (2001) developed a linear viscoelastic, biphasic model for soft tissue based on the theory of porous media, and they presented a numerical treatment to allow its usage in finite element models. The viscoelastic constitutive model for the organic matrix was based on the one-dimensional rheological structure of the generalized Maxwell model. The total (Cauchy) stress was expressed as the

sum of an equilibrium (elastic) part and a non-equilibrium (viscous) part as follows:

$$\boldsymbol{\sigma}_E := \boldsymbol{\sigma}_{EQ} + \boldsymbol{\sigma}_{NEQ}. \quad (1.11)$$

Here,  $\boldsymbol{\sigma}_{NEQ} = \sum_{n=1}^N \boldsymbol{\sigma}_n$  is the sum of the stresses on the individual Maxwell modes.

The individual stress tensors are given by

$$\boldsymbol{\sigma}_{EQ} = \mathbb{C}_0 \boldsymbol{\varepsilon}_E; \quad \boldsymbol{\sigma}_n = \mathbb{C}_n \boldsymbol{\varepsilon}_n = \mathbb{C}_n [\boldsymbol{\varepsilon}_E - \boldsymbol{\gamma}_i], \quad (1.12)$$

where  $\boldsymbol{\gamma}_i$  are internal variables associated with the deformation of the damping elements in the Maxwell modes. The fourth-order elasticity tensors are given by

$$\mathbb{C}_0 = 2\mu_0 \mathbb{I} + \lambda_0 (\mathbf{I} \otimes \mathbf{I}); \quad \mathbb{C}_n = 2\mu_n \mathbb{I} + \lambda_n (\mathbf{I} \otimes \mathbf{I}), \quad (1.13)$$

where  $\lambda_i$  and  $\mu_i$  ( $i = 0, 1, \dots, N$ ) are the Lamé constants. The inelastic (viscous) tensors were expressed using viscosity parameters  $\eta_n$  and  $\zeta_n$  as follows:

$$\boldsymbol{\sigma}_n = \mathbb{D}_n \dot{\boldsymbol{\gamma}}_n; \quad \mathbb{D}_n = 2\eta_n \mathbb{I} + \zeta_n (\mathbf{I} \otimes \mathbf{I}). \quad (1.14)$$

Prange and Margulies (2002) measured the mechanical properties of adult porcine brain tissue gray and white matter under large shear and compression strains. Anisotropy was found to be prominent in the corpus callosum and insignificant in the gray matter. In addition, the inhomogeneous nature of the brain tissue was demonstrated by the different regional properties found.

Velardi, Fraternali, and Angelillo (2006) performed experimental analysis and mechanical modeling of the behavior of porcine brain tissue. A transversely isotropic augmented Ogden-type hyperelastic model was adopted and mathematically studied under uniaxial loading conditions. Focus was placed on the short-term response

under impact and acceleration loading; hence, viscous effects were neglected and not included in the constitutive model. The transversely isotropic hyperelastic constitutive model employed by the researchers was described by the following strain energy function

$$\Psi = \frac{2\mu}{\alpha^2} (\lambda_1^2 + \lambda_2^2 + \lambda_3^2 - 3) + \frac{2k\mu}{\alpha^2} \left( I_4^{\alpha/2} + 2I_4^{-\alpha/4} - 3 \right), \quad (1.15)$$

with  $\lambda_1\lambda_2\lambda_3 = 1$ .  $\lambda_1$ ,  $\lambda_2$  and  $\lambda_3$  are the principal stretches and  $I_4$  is equal to the square of the material stretch in the fiber direction. When  $k$  is set to zero, the isotropic constitutive model is recovered.

Franceschini, Bigoni, Regitnig, and Holzapfel (2006) performed *in vitro* experiments on human brain tissue that revealed that the tissue exhibits hysteresis, Mullin's effect and residual strain under quasi-static uniaxial cyclic loading, and softening due to local failure during quasi-static uniaxial loading. In addition, they found that the consolidation theory involving interstitial fluid migration acceptably reproduce brain tissue deformation during eodometric (free-drainage) experiments. The researchers argued that the response of the tissue can be described in terms of a pseudo-energy function (for uniaxial stress) given by

$$\Psi(\lambda, \eta) = \eta \check{\Psi}(\lambda) + \phi(\eta), \quad (1.16)$$

where  $\check{\Psi}(\lambda)$  is the strain energy function corresponding to an Ogden incompressible model and  $\eta$  was defined by the ad-hoc formula

$$\eta = 1 - \frac{1}{r} \text{Erf} \left[ \frac{1}{m} \left( \check{\Psi}(\lambda_m) - \check{\Psi}(\lambda) \right) \right], \quad (1.17)$$

in which  $r$  and  $m$  are material parameters and  $\lambda_m$  represent the stretch at which

the unloading is initiated.

Hrapko, van Dommelen, Peters, and Wismans (2006, 2008a) reported experiments in compression (quasi-static) and shear (oscillatory, constant rate and relaxation) with porcine brain tissue. These researchers observed that the samples stiffen with increasing frequency and that the relaxation shear modulus decreases with increasing strain. In addition, a nonlinear differential viscoelastic model was introduced and curve-fitted to experimental data on shear experiments. Their constitutive model has similarities to that of Ehlers and Markert (2001) in that it is based on the generalized Maxwell model. The Cauchy stress tensor is given by

$$\boldsymbol{\sigma} = -p\mathbf{I} + \boldsymbol{\sigma}_e^d + \sum_{i=1}^N \boldsymbol{\sigma}_{ve_i}^d, \quad (1.18)$$

where the superscript  $d$  refers to the deviatoric part. In each viscoelastic mode of the model, the deviatoric part of the stress tensor is assumed to be given by an hyperelatic law. In particular, Mooney–Rivlin model was used with the strain energy function,

$$\Psi_{ve} = \frac{1}{2}G_{ve} [aI_{e_1} + (1 - a)I_{e_2} - 3], \quad (1.19)$$

with  $I_{e_i}$  the invariants of the Finger deformation tensor  $\mathbf{b}_e$ . The inelastic flow in a Maxwell mode is driven by the deviatoric elastic stress and it is given by the following flow rule:

$$\mathbf{D}_v = \frac{1}{2\eta(\tau)} \boldsymbol{\sigma}_{ve}^d. \quad (1.20)$$

Here, the viscosity parameter  $\eta$  depends on  $\tau := \sqrt{0.5\boldsymbol{\sigma}^d : \boldsymbol{\sigma}^d}$ , the equivalent stress measure, in the following form

$$\eta = \eta_\infty + \frac{\eta_0 - \eta_\infty}{1 + (\tau/\tau_0)^{n-1}}. \quad (1.21)$$

The elastic behavior of each mode, was modeled with a Mooney–Rivlin law. This material model required up to nineteen material parameters in order to reproduce the experimental data. Other nonlinear viscoelastic material models for brain tissue have been proposed by Brands, Peters, and Bovendeerd (2004) and El Sayed, Mota, Fraternali, and Ortiz (2008b), to mention just a few.

Elkin, Azeloglu, Costa, and Morrison III (2007) employed atomic force microscopy (AFM) to determine local mechanical properties of anatomical regions within the hippocampus of living rat brain tissue. An apparent, point–wise depth–dependent elastic modulus was determined, demonstrating the nonlinearity of the brain tissue and the heterogeneity of the hippocampus.

Pervin and Chen (2009, 2011) presented a modified version of the Hopkinson pressure bar technique for the characterization of high strain–rate mechanical behavior of brain tissue under compression. The reported results show high sensitivity of the gray and whiter matter responses to strain rates over a wide range:  $0.01 \text{ sec}^{-1}$  to  $3000 \text{ sec}^{-1}$ . White matter specimens with different orientations were employed to characterize anisotropy properties. However, the anisotropy was found to be insignificant across all strain rates. In addition, the effects of species, gender, and breeding were assessed.

Shafieian, Darvish, and Stone (2009) showed, through impact experiments on rats (closed–head experiment), that the viscoelastic properties of the brain tissue significantly change after traumatic axonal injury. The viscoelastic behavior of the rat brain tissue was modeled with a quasi–linear viscoelastic model. In addition, a finite element model was developed to replicate the indentation tests. Interregional

differences on the mechanical properties of porcine white and gray matter were investigated by van Dommelen, van der Sande, Hrapko, and Peters (2010) through indentation tests at different indentation speeds. These researchers observed that white matter is stiffer than gray matter.

Feng, Abney, Okamoto, Pless, Genin, and Bayly (2010) presented *in vivo* measurements of brain–skull relative displacement fields obtained through tagged magnetic resonance imaging and digital image analysis. In this study, mild frontal impacts, constrained to the sagittal plane, were produced on human volunteers, and the displacement of the brain was measured. Their results show that although the head undergoes translational motion, the brain rotates inside the skull. For the events characterized by linear decelerations near 1.5 g and angular accelerations of 120–140 rad/sec<sup>2</sup>, 2–3 mm relative skull–brain displacement was observed. These results may provide clues regarding the boundary conditions linking the brain to the skull, a topic which is usually disregarded or overlooked in the development of finite element of models for brain injury studies.

Chatelin, Constantinesco, and Willinger (2010) present a review on experimental characterization of brain tissue, and they elaborated on a comparison between findings, difficulties and advantages of both *in vivo* and *in vitro* experimental protocols. It was pointed out by these researchers that disparity in the experimental results, due mainly to the different protocols employed, is an evident characteristic of the last fifty years of experimental testing of soft tissues.

Rashid, Destrade, and Gilchrist (2012a) developed and calibrated a novel experimental device for tensile tests at high strain rates up to 90 s<sup>-1</sup>. Appropriate

size of the specimens was determined in order to ensure almost uniform deformation field. In addition, a linear model was used to estimate a Young's modulus of 11.2 kPa for porcine brain tissue. Rashid *et al.* (2012b) and Rashid *et al.* (2012c) conducted *in vitro* unconfined compression and tensile tests at several strain rates up to  $90 \text{ s}^{-1}$  and strain level of 0.3. These researchers observed a stiffening response of the brain tissue with increasing strain rates. In addition, they found that one-term Fung, Gent, and Ogden hyperelastic material models provide an excellent representation of the experimental data. However, it should be noted that these researchers obtained a different set of material parameters at each value of the strain rate considered. In addition, a single hereditary integral approach was used to introduce time dependence into the one-term Ogden hyperelastic model through a relaxation function defined in terms of Prony series. Rashid *et al.* (2013) presented an experimental setup to perform simple shear tests on porcine brain tissue at strain rates up to  $120 \text{ s}^{-1}$ . Good agreement was found between the experimental data and the predictions of their viscoelastic models. These material models were constructed by modifying the Ogden and Mooney–Rivlin hyperelastic models through the introduction of a relaxation function in terms of Prony series, and through the single hereditary integral approach.

Feng, Clayton, Chang, Okamoto, and Bayly (2013) used magnetic resonance elastography to measure linear viscoelastic properties of ferret brain tissue *in vivo* by applying a harmonic excitation to the skull at different frequencies. Linear viscoelastic parameters (storage and loss moduli) governing dynamic shear deformation were estimated in gray and white matter. They observed that the estimated com-

plex modulus of gray and white matter were similar in the range of frequencies examined. A review on the fast growing elasticity imaging (elastography) of tissues was prepared by Gao, Parker, Lerner, and Levinson (1996). With these techniques, it is possible to obtain complete maps of the material properties along the tissue. However, the predicted material properties usually rely on a linear (visco)elastic assumption.

As it can be observed, the determination of brain tissue mechanical properties remains an active area of research and it will continue to be so long as new and more sophisticated experimental techniques, such as *in vivo* methods, continue to be developed. As previously stated by Hrapko *et al.* (2008a), it is persistent throughout the experimental studies the fact that laboratory ambient conditions are hardly documented and/or controlled, or they are different across the various research groups. In addition, repeatability of results is very difficult to achieve, even within the same research groups, due to the marked sample-dependent (animal type, size of the sample, region of the brain, and so on) nature of the experiments. This fact explains the high variability and distribution in the reported mechanical properties of brain tissue.

Regarding the constitutive modeling of brain tissue, some comments are in order. Many of the models presented are developed in an ad-hoc fashion to provide good agreement with the experimental data. However, it is noted that a constitutive model cannot depend on the experimental technique or protocol used. From this point of view, although those models may represent the experimental data, they do not provide any further insights as to the physical interpretation of the phenomenon.

Other material models were developed by adapting/modifying other models which were known to work well for different types of materials. This does not guarantee that the constitutive model is a good model. It is observed that few efforts have been devoted towards building constitutive models of brain tissue from fundamental principles. In addition, it should be noted that brain tissue (and soft tissue in general) is not an engineering material. This fact should be considered also in the construction of material models. It seems inevitable the fact that in order to predict tissue damage, the constitutive modeling of soft tissues needs to include information regarding their microstructural features.

## 1.4 Studies on Brain Injury by Direct and Indirect Head Impact

The study of mild traumatic brain injury caused by direct head impacts and by accelerations/decelerations (indirect impact) of the head dates back to 60 years ago. These studies fall into two main groups: analytical studies being rather limited and sparse; and finite element studies, widely popular and abundant. Some of the studies are summarized next.

### 1.4.1 Analytical Studies

Several simplified models have been developed to isolate and understand the physics behind head impacts. Usually in these models, a small number of variables and parameters are included, and simplified geometries are considered, so that analytical solutions, or relatively simple and fast numerical solutions can be obtained.

Table 1.1: Experimental characterization of brain tissue mechanical behavior

Reference	Experiment Type	Brain Tissue	Details
Fallenstein <i>et al.</i> (1969)	Sinusoidal shear stress under resonant conditions	<ul style="list-style-type: none"> <li>• Human</li> <li>• Monkey</li> </ul>	<ul style="list-style-type: none"> <li>• <i>in vitro</i> rectangular specimens: <math>2 \times 3 \times 0.4-0.7</math> cm</li> <li>• <i>in vivo</i> tests on monkeys</li> </ul>
Miller and Chinzei (1997, 2002)	Constant rate uniaxial: <ul style="list-style-type: none"> <li>• Compression</li> <li>• Tension</li> </ul>	Swine	<ul style="list-style-type: none"> <li>• Cylindrical samples (diam.: 30 mm, height: 13 mm)</li> <li>• Strain rates: <math>0.64 \times 10^{-5}</math>, <math>0.64 \times 10^{-2}</math> and <math>0.64 s^{-1}</math></li> </ul>
Arbogast and Margulies (1998)	Oscillatory shear stress	Porcine Brainstem	<ul style="list-style-type: none"> <li>• Frequency range: 20-200 Hz</li> <li>• Strains: 2.5%, 5.0% and 7.5% along three mutually orthogonal directions</li> </ul>
Prange and Margulies (2002)	Stress relaxation: <ul style="list-style-type: none"> <li>• Simple shear</li> <li>• Unconfined compression</li> </ul>	Porcine	<ul style="list-style-type: none"> <li>• Rectangular tissue samples: <math>10 \times 5 \times 1</math> mm</li> <li>• White matter under shear</li> <li>• Gray matter under shear</li> </ul>
Darvish and Crandall (2001)	Oscillatory simple shear	Bovine	<ul style="list-style-type: none"> <li>• Disc samples (diam.: 15-20 mm, height: 4.8 mm)</li> <li>• Frequency range: 0.5 to 200 Hz</li> <li>• Amplitudes of up to 20% strain</li> </ul>

Table 1.1: (continued)

Reference	Experiment Type	Brain Tissue	Details
Bilston <i>et al.</i> (2001)	<ul style="list-style-type: none"> <li>• Constant shear strain rate</li> <li>• Shear relaxation</li> <li>• Oscillatory shear stress</li> </ul>	Bovine white matter	<ul style="list-style-type: none"> <li>• Cylindrical samples (diam.: 20 mm, thickness: 2 mm)</li> <li>• Shear strain rate range: 0.05 to 1 <math>s^{-1}</math></li> <li>• Strain range: 0.001 to 0.15 (shear relaxation)</li> <li>• 0.1% strain amplitude over 0.01-20 Hz frequency range (oscillatory shear)</li> </ul>
Velardi <i>et al.</i> (2006)	Constant strain rate in tension	Porcine	<ul style="list-style-type: none"> <li>• Prismatic samples (length: 4-6 cm, width: 1 cm, thickness: 0.2-0.5 cm.</li> <li>• Pure gray and white matter samples from different brain regions, and different axonal orientation</li> <li>• Fixed strain rate <math>\sim 0.01 s^{-1}</math></li> </ul>
Franceschini <i>et al.</i> (2006)	Quasi-static, uniaxial: <ul style="list-style-type: none"> <li>• Tension/compression cyclic loading</li> <li>• Controlled drainage</li> </ul>	Human	<ul style="list-style-type: none"> <li>• Cylindrical and prismatic samples (diam.:5-11 mm, height: 9-15 mm) for cyclic loading</li> <li>• Quasi-static uniaxial strain rate of 5 mm/min</li> <li>• Cylindrical samples (diam.: 30mm, height: 5-8 mm) for free-drainage tests</li> <li>• Free-drainage under dead load</li> </ul>
Hrapko <i>et al.</i> (2006)	<ul style="list-style-type: none"> <li>• Oscillatory shear</li> <li>• Shear stress relaxation</li> <li>• Constant shear rate</li> </ul>	Porcine	<ul style="list-style-type: none"> <li>• White matter cylindrical samples (diam.: 7-10 mm, height: 1-3mm)</li> <li>• Shear strain amplitude: 1%</li> <li>• Frequency range: 0.04 to 16 Hz (oscillatory shear)</li> <li>• Shear strains up to 20% (shear stress relaxation)</li> <li>• Shear strain rates: 0.01 to 1 <math>s^{-1}</math> (constant rate tests)</li> </ul>

Table 1.1: (continued)

Reference	Experiment Type	Brain Tissue	Details
Elkin <i>et al.</i> (2007)	Atomic Force Microscopy (AFM)	Rat	<ul style="list-style-type: none"> <li>• Determined local mechanical properties of anatomical subregions within rat hippocampus</li> </ul>
Hrapko <i>et al.</i> (2008a)	<ul style="list-style-type: none"> <li>• Compression stress relaxation</li> <li>• Dynamic shear test</li> <li>• Shear stress relaxation</li> </ul>	Porcine	<ul style="list-style-type: none"> <li>• Cylindrical samples (diam.: 8-12mm, height: 2mm)</li> <li>• Strain amplitude: 1%</li> <li>• Frequency range: 1-10 Hz (dynamic test)</li> <li>• 10% shear strain (relaxation test)</li> </ul>
Pervin and Chen (2009, 2011)	Dynamic compression	Bovine	<ul style="list-style-type: none"> <li>• Modified split-Hopkinson pressure bar set-up</li> <li>• Strain rates range: 0.01 to 3000 <math>s^{-1}</math></li> <li>• White and gray matter annular samples (diam.: 10 mm, 4.7 mm, thick.: 1.7 mm)</li> </ul>
Shafieian <i>et al.</i> (2009)	Impact test	Rat	<ul style="list-style-type: none"> <li>• <i>In vivo</i>, close head impact</li> <li>• 500 g weight dropped from 2 m height</li> <li>• Indentation test after injury: 1-2 mm penetration depth, 60 ms ramp time</li> </ul>
van Dommelen <i>et al.</i> (2010)	Constant speed indentation	Porcine	<ul style="list-style-type: none"> <li>• Slices of (1-2 mm thick, up to 30 mm length) from four brain sections</li> <li>• Indentation speeds: 0.1, 0.34 and 1 mm/s</li> <li>• Indentation depth of 0.4 mm</li> </ul>
Feng <i>et al.</i> (2010)	Magnetic Resonance dynamic experiments	Human	<ul style="list-style-type: none"> <li>• <i>In vivo</i>, close-head experiments</li> <li>• Head dropped from 2 cm onto elastic rubber stop</li> <li>• Linear deceleration of 1.5 g and angular accelerations of 120-140 <math>rad.s^{-1}</math></li> </ul>

Table 1.1: (continued)

Reference	Experiment Type	Brain Tissue	Details
Rashid <i>et al.</i> (2012c,b)	<ul style="list-style-type: none"> <li>• Dynamic tensile</li> <li>• Unconfined compression</li> </ul>	Porcine	<ul style="list-style-type: none"> <li>• Cylindrical samples (diam. :15 mm; height: 5 mm) of mixed white and gray matter</li> <li>• Strain rates: 30, 60 and 90 <math>s^{-1}</math></li> <li>• Up to 30% strain</li> <li>• Relaxation tests at 10%, 20%, 30%, 40%, and 50% strain with 10 ms average rise time.</li> </ul>
Feng <i>et al.</i> (2013)	Magnetic Resonance Elastography with harmonic excitation	Ferret	<ul style="list-style-type: none"> <li>• Frequencies: 400, 600, and 800 Hz</li> </ul>

Such models prove helpful in uncovering particular aspects of the phenomenon in isolation. Several analytical and computational models developed to study head trauma regard the skull–brain system as a water–filled spherical or ellipsoidal shell. This simplification of the mechanical behavior of the brain is based on the experimental finding that brain tissue has similar dynamic bulk modulus to water, because of its almost 80% water composition. A brief description of some of these works is presented next.

Engin and Liu (1970) studied the free vibrations of a fluid–filled spherical shell model of the human head in order to determine intracranial pressure distribution and high stress locations on the skull. Similarly, Akkas (1975) investigated the response of a fluid–filled, three–layer sandwich spherical shell to an arbitrary, time dependent impact. Talhouni and DiMaggio (1975) presented an slightly improved skull–brain model consisting of an elastic prolate spheroidal shell enclosing an acoustic medium; and the response of the model to an impulsively applied uniform pressure was studied. The latter researchers found a significant difference in the tensile stress on the shell and on the compressive stresses on the fluid when compared to the perfectly spherical model; however, the predicted maximum negative pressure (important with regards to cavitation) was almost the same for both models.

Young (2003) developed a fluid–filled spherical shell head model to study impacts with elastic bodies. Young noted that impacts with light objects are more likely to produce large dynamic pressure transients than impacts with heavier objects.

### 1.4.2 Finite Element Studies

With the fast increasing computational power, analytical models have given way to more sophisticated and high fidelity finite element models. However, these highly complex models may be criticized due to the several factors disregarded. Examples of not well understood aspects include the following: (*i*) mechanical behavior of the brain tissue (constitutive modeling), (*ii*) boundary conditions between skull and brain, (*iii*) influence of cerebrospinal fluid (CSF), (*iv*) brain gray and white matter interface, and (*v*) link between mechanical response and brain damage. In addition, the results produced by these finite element models are sometimes difficult to interpret and analyze.

Finite element analysis has been widely used to generate complex and anatomically detailed models in the study of brain concussion due to impacts. For a rather complete review of the finite element models developed up to 1996, the reader is referred to the work of Voo, Kumaresan, Pintar, Yoganandan, and Sances (1996). The material constitutive properties adopted for the different head components vary from one study to another. A general trend observed is the use of a linear elastic material model for the skull and interior membranes. On the other hand, the brain tissue has been modeled in a variety of different ways. These include water-like fluid models, linear and nonlinear elastic material models, and linear and nonlinear viscoelastic material models. The cerebrospinal fluid surrounding the brain is usually modeled as a thin layer with bulk properties of water. Due to this modeling assumption, the fluid-structure interactions between the skull-brain system and

the CSF are not addressed. The cerebrospinal fluid in the ventricles of the brain is usually not considered in the models.

Anatomically detailed models that include components such as the scalp, three layered skull, CSF, interior membranes, and brain tissue have been presented by several research groups. Valdez and Balachandran (2011) presented a review with details and contributions of some of these studies. Next, a brief overview of related finite element modeling efforts is provided. Due to the high volume of literature available, the following list is intended to be representative and not exhaustive by any means.

Ruan, Khalil, and King (1994) presented a three-dimensional finite element model of the skull and brain. They observed that rear impacts generate higher pressure peaks inside the brain than frontal impacts.

Claessens, Sauren, and Wismans (1997) developed a three-dimensional finite element model of the human head from Computed Tomography (CT) and Magnetic Resonance Imaging (MRI) data. These researchers parametrically studied the influence of the geometrical details of the different components and the conditions at the interfaces. It was observed that variation of the Young's modulus of the brain tissue highly affected the response. In addition, they found that the relative motion at the skull-brain interface had large implication for the pressures in the frontal and occipital regions of the brain. The presented model was later adapted by Brands (2002) to introduce their own nonlinear viscoelastic constitutive model for the brain tissue. In this last study, the researchers advised that intracranial pressure gradient history is a poor measure to validate a head model. This conclusion is based on the

observation that the pressure gradient is completely determined by the equilibrium of momentum, and therefore, it is independent of the choice of the brain material model.

Willinger, Kang, and Diaw (1999) used a three-dimensional human head finite element model to replicate the results of two human cadaver impact tests. They found good agreement between the model predictions and the experimental data for the fast impact (6 ms elapsed time); however, the model did not provide a good estimation of the slower impact test (15 ms elapsed time). The researchers attributed this discrepancy to the nonlinear dynamic behavior of the intracranial stress and to inaccurate modeling of the neck joint. In addition, they observed that the predicted responses of the model with a linear elastic and with a linear viscoelastic brain were fundamentally the same.

Huang, Lee, Lee, Chiu, Pan, and Chen (2000) validated its anatomically based finite element model against experimental data. The indirect impact simulations carried out showed high gradient of intracranial pressure and concentrations of shear stress within the brain. However, the negative contre-coup pressure observed, was not enough to produce cavitation.

Wittek and Omori (2003) investigated the effects of the brain-skull boundary conditions on the mechanical response of a simplified three-dimensional finite element model of a thin sagittal slice of the human head. Their results suggest that the modeling of the CSF-filled subarachnoidal space as a fluid-like medium is necessary in order to accurately represent brain-skull boundary conditions.

Zhang, Teo, and Ng (2005) developed a three-dimensional model that includes

the neck up to the seventh cervical bone. It was observed that intervertebral discs represent the major weakness in neck injury. Suh, Kim, and Oh (2005) constructed a three-dimensional model from MRI images and investigated the brain deformation under frontal head impact, as well as the intracranial pressure and relative displacement between the skull and the brain. In addition, the head injury criterion was used to determine the occurrence of brain injury.

Zong, Lee, and Lu (2006) employed a three-dimensional finite element model to study energy transmission paths during head impacts. Three energy paths were observed, two of them in the skull and one through the brain. The spinal cord was observed to be highly vulnerable during head impacts.

Pinnoji and Mahajan (2007) developed a complete finite element model to compare the response of the human head under frontal impacts with and without a helmet. The helmet was shown to reduce the coup pressure but no influence was detected in the contre-coup pressure. It was observed that helmet padding with lower densities helped reduce the contact forces and coup pressures for low speed impacts.

El Sayed, Mota, Fraternali, and Ortiz (2008a) developed a biomechanical model for traumatic brain injury and soft tissue damage. Frontal and oblique impacts with external objects were examined and prediction of extension, intensity and reversibility of tissue damage was performed. The authors claim that their model is able to reproduce permanent brain tissue damage.

Takhounts, Ridella, Hasija, Tannous, Campbell, Malone, Danelson, Stitzel, Rowson, and Duma (2008) presented a three-dimensional finite element model

whose topology was obtained from CT images. Their results suggested that an angular acceleration criteria better predicts brain injury than the linear acceleration criterion.

Chen and Ostoja-Starzewski (2010) presented a three-dimensional finite element model of the human head accounting for geometric characteristics of the various components within the human head. The model was generated through a magnetic resonance imaging voxel-based mesh generation method. These researchers observed that an impact gives rise to not only a fast pressure wave but also a slow and spherically convergent shear stress wave.

## 1.5 Blast Induced Brain Injury

Blast-related brain injury, in contrast to head impacts, is caused by the interaction of blast explosive pressure waves with the human brain through the skull. Research on blast related brain injury has seen a recent spurt due to the wars in Iraq, Afghanistan, and Pakistan. It is commonly agreed that the effects of blast waves over obstacles (human or not) are four-fold: (*i*) primary effects, arising from the direct influence of the blast overpressure on the object, (*ii*) secondary effects, constituting the damage produced to the object by the impact of other objects accelerated by the blast, (*iii*) tertiary effects, produced when the body itself is accelerated by the blast producing a posterior collision against walls, ground, and so on, and finally, (*iv*) quaternary effects, which include burning, blindness, hearing impairment and inhalation of toxic gases produced by the explosion. However, only

primary effects can be regarded as the unique and distinctive characteristic of blast wave interactions (Stuhmiller, 2008).

Moss, King, and Blackman (2009) carried out numerical simulations of the interaction of blast waves generated by explosions and a water-filled human head model. Skull deformation was proposed as a new mechanism for brain injury resulting from exposure to blast waves. Moore, Jérusalem, Nyein, Noels, Jaffee, and Radovitzky (2009) developed a numerical model to study the interactions between a detonation shock wave and the human head. They concluded that propagation of the blast shock wave through the skull into the brain is possible. Taylor and Ford (2009) numerically studied the role of stress wave interactions in the genesis of traumatic brain injury. They concluded that traumatic brain injury from blast exposure can occur before the onset of linear or rotational accelerations. Nyein, Jason, Yu, Pita, Joannopoulos, Moore, and Radovitzky (2010) conducted coupled fluid-solid simulations including a biofidelic model of the human head and a model of the Advance Combat Helmet. The use of a face mask was proposed as a strategy for mitigation of blast waves. Grujicic, Bell, Pandurangan, and He (2010) investigated the blast wave mitigation ability of polyurea when used as a helmet suspension-pad material. A computational model was used to reproduce the fluid-structure interactions between the blast wave and the human head with and without helmet.

Alley, Schimizza, and Son (2011) carried out an experimental study of blast related traumatic brain injuries. The results found suggest that shock waves traveling inside the head may be amplified at the interfaces between the skull and the brain.

## 1.6 Axonal Injury

The studies of head impact as those discussed previously in §1.4 are helpful in providing qualitative and quantitative estimations on stress levels and stress/strain distributions, as well as location of stress extrema within the brain when the human head suffers an impact. These predictions, however are highly dependent on how the brain tissue and its interaction with the skull are modeled. In addition, this information alone may not be enough to predict the tissue damage at the microscopic level. It has been clinically reported that axonal damage constitutes one of the most important signatures of traumatic brain injury. This fact indicates that mechanical models intending to predict brain injury should account for the internal structure of the brain tissue. Wang and Ma (2010) presented a review of experimental models of traumatic axonal injury. Some of the experimental efforts attempting to understand the mechanics of axonal growth and damage are summarized in Table 1.2.

Table 1.2: Experimental studies on axonal injury

Reference	Experiment Details	Observations and Findings
Dennerll <i>et al.</i> (1988, 1989)	Axial stress relaxation experiments on axons. Two methods: <ul style="list-style-type: none"> <li>• Axons pulled transversely with both ends fixed</li> <li>• Axons pulled axially from the growth cone</li> </ul>	<ul style="list-style-type: none"> <li>• Assessed mechanical properties of neurites</li> <li>• Positive axonal rest tensions of the order of 30-40 <math>\mu</math>dynes</li> <li>• Stress relaxation curves are presented.</li> <li>• Upon suppression of the external force, a slack in the axon was present (growth), followed by a tension recovery (retraction).</li> <li>• Neurite length found to be regulated by axial tension.</li> </ul>
Lamoureux <i>et al.</i> (1989)	Quasi-static axial pulling of neurites of chick sensory neurons using glass needles of known compliance	<ul style="list-style-type: none"> <li>• Direct measurements of neurite force as a function of growth-cone advance.</li> <li>• Neurite force and growth-cone advance linearly related and accompanied by apparent neurite growth.</li> <li>• Pulling growth cone provides an important stimulus for growth.</li> </ul>
Zheng <i>et al.</i> (1991)	Static axial stretching of neurites of chick sensory neuron.	<ul style="list-style-type: none"> <li>• Increasing tensions as step of constant force lasting 30-60 min.</li> <li>• Neurite elongation rate increases almost linearly with tension magnitude above a tension threshold.</li> </ul>
Smith <i>et al.</i> (1999)	Dynamic stretch of human neuron cell cultures	<ul style="list-style-type: none"> <li>• Axons demonstrated high tolerance to dynamic stretch injury with no axotomy (breakage) at strains up to 65%.</li> <li>• Axons developed undulating shape immediately after injury.</li> <li>• Original, straight shape gradually recovered, but swellings developed.</li> </ul>
Bernal <i>et al.</i> (2007)	Quasi-static, relaxation test using micro-needle technique	<ul style="list-style-type: none"> <li>• Elastic response, viscoelastic relaxation and active contraction observed.</li> <li>• Under certain conditions, axons show transition from viscoelastic elongation to active contraction due to molecular motors.</li> <li>• A model including the effects of molecular motors is presented.</li> </ul>

Table 1.2: (continued)

Reference	Experiment Details	Observations and Findings
Tang-Schomer <i>et al.</i> (2010)	Dynamic stretch of rat neuron cell cultures	<ul style="list-style-type: none"> <li>• After stretch, undulations are formed along the axon as it gradually relaxes back to the original shape.</li> <li>• Results suggest immediate breakage and buckling of microtubules in axon undulations, and progressive loss of microtubules.</li> <li>• Loss of microtubules may impede normal transport along the axon, leading to localized swellings.</li> </ul>
Chetta <i>et al.</i> (2010)	Quasi-static stretching of axons of cultured rat sensory neurons	<ul style="list-style-type: none"> <li>• Axonal cytoskeleton acts as a dynamic structure that responds to stretch rapidly and locally.</li> <li>• Axial strain was found to vary along the length of the axon.</li> <li>• Presented a sliding filament model of cytoskeletal remodeling</li> </ul>

## 1.7 Objectives

As observed from the literature review presented in the previous sections, the study of brain injury has been inevitably geared toward highly computationally expensive finite element simulations, with models that accurately represent anatomical features of the human head. However, it is observed that little advance has been made regarding the understanding mechanisms of brain injury, and in general soft tissue damage. Classical brain injury mechanisms proposed half a century ago, such as the shear strain theory (Holbourn, 1945) and the cavitation theory (Gross, 1958) are not sufficient to explain the mechanical damage of brain tissue under rapid transient loads as they disregard stress wave propagation in the brain. In addition, from a modeling perspective, the use of linear (visco)elastic material models for brain tissue is attractive, but on the other hand, completely disregard nonlinear effects that could indeed be an important factor in the development of tissue internal damage.

The present dissertation is concerned with the physics of wave propagation through soft tissue, such as brain tissue. Particularly, the goal of this effort is to establish the fundamental basis upon which more complex models and analysis can be built. Through simplified models, it provides clues about what types of phenomenon to look for in more holistic finite element models.

The overall objective of this doctoral dissertation is to provide a better understanding of the wave propagation phenomenon through soft tissue, particularly focusing on the effect of the nonlinearities of the material behavior. Specific goals include the following:

- To model soft tissue mechanical behavior, particularly, that of brain tissue
- To study the propagation of stress waves through soft tissue
- To better understand the effect of material nonlinearity on the propagation of stress waves
- To provide insights into damage mechanisms associated with the nonlinear material behavior of soft tissues

## 1.8 Dissertation Organization

In Chapter 1, an introduction to soft tissue mechanics and brain tissue cellular anatomy is presented. Following that, an extensive literature review of brain tissue experimental characterization and material modeling, head impact and blast-related injury studies, and axonal injury experimental investigations are presented.

In Chapter 2, a nonlinear standard solid viscoelastic model is presented and curve-fitted to experimental data on brain tissue unconfined compression. The same model is used in a study of the interaction of blast pressure waves and a structure supported by a nonlinear viscoelastic material. Finally, another soft tissue constitutive model for uniaxial stress state based on a maximum dissipation construction is introduced. This last model will be used throughout the rest of the dissertation for the different studies presented. This constitutive model was also curve-fitted to experimental data on brain tissue unconfined compression.

Chapter 3 constitutes the bulk of this dissertation. In this chapter, propaga-

tion of mechanical longitudinal waves through a structure with uniform cross-section is studied. First, the system with the linearized viscoelastic material model is analyzed by means of asymptotic analysis, dispersion analysis and modal analysis. The results from the dispersion analysis are used to determine lower frequency bounds for wave propagation through axons, and also, to produce an estimation of brain tissue damping characteristics. The last part of this chapter is devoted to the system with nonlinear viscoelastic material model. First, asymptotic wave propagation and frequency response solutions for weak dissipation are presented. Finally, the results from numerical simulations are presented and analyzed, emphasizing the differences between the nonlinear and the linearized system.

Chapter 4 is structured similarly to Chapter 3, but in this case, the geometric effect of a varying cross-section is studied. Simple asymptotic solutions for the linearized model are obtained first. Next, dispersion relation analysis on the linearized system is performed. Finally, the results from numerical simulations of the nonlinear system are presented.

In Chapter 5, concluding remarks, as well as suggestions for possible future paths of research that can build upon the present work are presented.

Several appendices are included to present additional mathematical derivations, models, and details that complement the material in the core of this dissertation.

## Chapter 2

### Nonlinear Viscoelastic Modeling and Fluid–Structure Interaction

#### Studies

In this chapter, an early attempt to model brain tissue material behavior through a phenomenological viscoelastic material model is presented. The material model is curve-fitted to brain tissue experimental data next. Following that, the study of the interaction between an incoming pressure wave and a mass supported by a nonlinear viscoelastic material is presented. Finally, the model of nonlinear viscoelasticity that will be used in Chapters 3 and 4 for the wave propagation studies is presented, and material parameter estimation is carried out through curve-fitting of brain tissue experimental data.

#### 2.1 Nonlinear Standard Solid Viscoelastic Model

As a first model of nonlinear viscoelasticity, a generalization of the standard solid viscoelastic model, as shown in Figure 2.1, is proposed. Similar models based on the standard solid viscoelastic model have been used extensively in the literature since they are simple to implement computationally and they provide an intuitive representation in terms of springs and dampers (Holzapfel, 2000). The one-dimensional model developed here consists of a nonlinear spring in parallel with a number of nonlinear Maxwell modes composed, in turn, of a nonlinear spring in

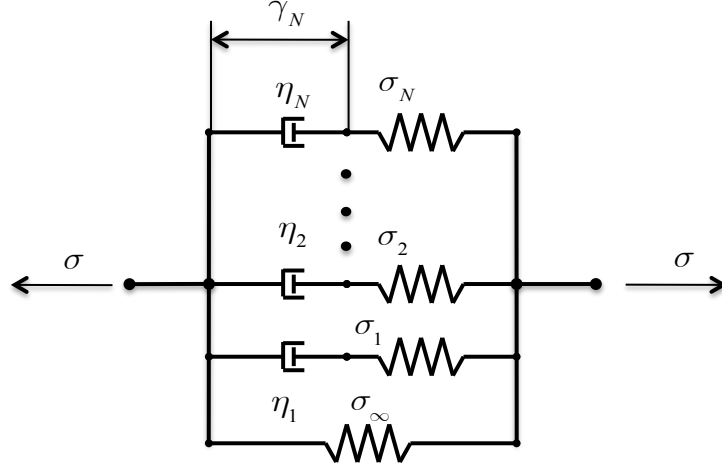


Figure 2.1: Nonlinear standard solid viscoelastic model.

series with a linear dashpot. The novelty of this model is that mechanical response of the nonlinear springs is modeled through a hyperelastic constitutive law.

The variables  $\sigma_i$  ( $i = 1, 2, \dots, N$ ) are the stresses in the corresponding  $i$ -th Maxwell mode, and  $\sigma_\infty$  and  $\lambda_\infty$  are the stress and stretch in the nonlinear spring in parallel, respectively. The variables  $\lambda_i$  and  $\gamma_i$  ( $i = 1, 2, \dots, N$ ) are internal variables corresponding to the stretches of the springs and of the dashpots in the  $i$ -th Maxwell mode, respectively. These internal variables are related to the energy dissipation mechanism. However, these internal variables may lack physical meaning and are a simple artifact of the model. Next, the governing equations relating the total stress with the total stretch are derived.

The total Cauchy stress  $\sigma$  applied to the viscoelastic element is given by

$$\sigma = \sigma_\infty + \sum_{i=1}^N \sigma_i. \quad (2.1)$$

To describe the nonlinear elastic part of the model, incompressible hyperelastic constitutive models with strain energy function  $\Psi_*$  ( $* = \infty$  or  $* = i$ ) are considered.

As a consequence the individual Cauchy stresses are written as follows (Holzapfel, 2000)

$$\sigma_\infty = \lambda_\infty \frac{d\Psi_\infty}{d\lambda_\infty} \quad (2.2a)$$

$$\sigma_i = \lambda_i \frac{d\Psi_i}{d\lambda_i}. \quad (2.2b)$$

Also, for each Maxwell mode the stretch in the spring  $\lambda_i$  and the stress  $\sigma_i$  are given by the following expressions

$$\lambda_i = \lambda_\infty - \gamma_i \quad (2.3a)$$

$$\sigma_i = \dot{\gamma}_i \eta_i. \quad (2.3b)$$

Taking the time derivative of Eq. (2.3a), and eliminating  $\gamma_i$  from Eq. (2.3b) the following result is obtained:

$$\dot{\lambda}_i = \dot{\lambda}_\infty - \frac{\sigma_i}{\eta_i}. \quad (2.4)$$

Collecting Eqs. (2.2) with (2.4), the governing equations for this viscoelastic model are expressed as

$$\sigma = \sigma_\infty + \sum_{i=1}^N \sigma_i \quad (2.5a)$$

$$\dot{\lambda}_i = \dot{\lambda}_\infty - \frac{\sigma_i}{\eta_i} \quad i = 1, 2, \dots, N \quad (2.5b)$$

$$\sigma_i = h_i(\lambda_i) \quad (2.5c)$$

$$\sigma_\infty = h_\infty(\lambda_\infty), \quad (2.5d)$$

where the functions  $h_\infty$  and  $h_i$  ( $i = 1, 2, \dots, N$ ) are defined as follows

$$h_*(\lambda) := \lambda_* \frac{d\Psi_*}{d\lambda}(\lambda) \quad * = i \text{ or } * = \infty. \quad (2.6)$$

A drawback of the model presented, as mentioned before, is that the introduced internal variables  $\lambda_i$  (or  $\gamma_i$ ) lack physical interpretation, and cannot be associated to any state variable measured in an experiment. In latter sections, a different nonlinear viscoelastic material model without internal variables will be introduced.

## 2.2 Nonlinear Standard Solid Viscoelastic Model Curve-Fitting to Brain Tissue Experimental Data

In this section, the viscoelastic model developed in §2.1 is curve-fitted to experimental data in order obtain the material parameters corresponding to brain tissue. In this case, data from constant speed, unconfined compression experiments on swine brain tissue (Miller and Chinzei, 1997) is used. Three experimental data sets are available. These data sets correspond to experiments at constant strain rates of  $0.64 \text{ sec}^{-1}$ ,  $0.0064 \text{ sec}^{-1}$ , and  $6.4 \times 10^{-6} \text{ sec}^{-1}$  and are presented in Fig. 2.2.

For the purpose of this section, the mechanical response of the nonlinear springs in the viscoelastic model, determined by the hyperelastic strain energy functions  $\Psi_*$  ( $* = \infty$  or  $* = i$ ), is modeled as an incompressible, uniaxial Mooney–Rivlin hyperelastic material. This particular hyperelastic strain energy function, with certain modifications, has been used in other studies to model brain tissue (e.g. Mendis *et al.*, 1995). For this particular hyperelastic material, the strain energy function for uniaxial stress state is given by (refer to §A),

$$\Psi_*(\lambda) = c_{1*}(\lambda^2 + \lambda^{-1} - 3) + c_{2*}(\lambda^{-2} + \lambda - 3). \quad (2.7)$$

Therefore, it can be shown by Eq. (2.6) that

$$h_*(\lambda) = 2 \left( \lambda^2 - \frac{1}{\lambda} \right) \left( c_{1*} + \frac{1}{\lambda} c_{2*} \right). \quad (2.8)$$

The curve-fit of the model to the experimental data is performed with Matlab by using the *lsqcurvefit* function. Several approaches to curve-fit the model to the experimental data were attempted. The approach that produced better results consisted in curve-fitting the model parameters simultaneously to all three data sets. In addition, a model with one and two Maxwell modes were studied and their results are presented in the following sections. The goodness of the fit (GOF) is determined through the Normalized Mean Square Error (NMSE) defined as

$$\text{GOF} = 1 - \left( \frac{\|P_{\text{model}} - P_{\text{ref}}\|_2}{\|P_{\text{ref}} - \text{mean}(P_{\text{ref}})\|_2} \right)^2, \quad (2.9)$$

where  $P_{\text{model}}$  is the Lagrangian stress predicted by the model,  $P_{\text{ref}}$  the experimental value of the Lagrangian stress and  $\|\cdot\|_2$  represents the 2-norm. A value of GOF close to 1 implies an excellent fit.

### 2.2.1 Standard Solid Viscoelastic Model with One Maxwell Mode

As a first attempt, only one Maxwell mode is used in the viscoelastic model. As a consequence, five material parameters, two for each Mooney–Rivlin nonlinear spring and one for the linear dashpot are required. The values of the material constants obtained are shown in Table 2.1. The comparison between the predictions of the curved-fitted viscoelastic model and the experimental data for the three different strain rates are shown in Figs. 2.3, 2.4, and 2.5 corresponding to strain

Table 2.1: Curve-fitted material constants for the nonlinear viscoelastic model with one Maxwell mode

Curve-Fitted Constants				
$c_{1\infty}$ [Pa]	$c_{2\infty}$ [Pa]	$c_{11}$ [Pa]	$c_{21}$ [Pa]	$\eta_1$ [Pa.sec/m]
$3.804 \times 10^{-14}$	$1.282 \times 10^2$	$3.828 \times 10^{-14}$	$4.656 \times 10^2$	$6.333 \times 10^4$

rates  $\dot{\lambda}_\infty$  of  $0.64 \text{ sec}^{-1}$ ,  $0.0064 \text{ sec}^{-1}$ , and  $6.4 \times 10^{-6} \text{ sec}^{-1}$ , respectively. Based on the GOF values for the different cases, it is concluded that the model acceptably represents the experiments corresponding to the higher and lower strain rates, but provides a poor prediction of the experimental data at the moderate strain rate.

## 2.2.2 Standard Solid Viscoelastic Model with Two Maxwell Modes

Based on the previous observation, an additional Maxwell mode was introduced in pursue of an improvement in the predictions of the nonlinear viscoelastic model. For this particular case, eight material constants are required: two for each of the three nonlinear Mooney–Rivlin springs, and one for each of the two linear dashpots. The obtained curve-fitted material parameters are presented in Table 2.2. For this particular model, the curve-fitting procedure was observed to have convergence problems and required a large number of function evaluations. The comparison between the predictions of the viscoelastic model and the experimental data is presented in Figs. 2.6, 2.7, and 2.8 corresponding to strain rates  $\dot{\lambda}_\infty$  of  $0.64 \text{ sec}^{-1}$ ,  $0.0064 \text{ sec}^{-1}$ , and  $6.4 \times 10^{-6} \text{ sec}^{-1}$ , respectively. It is observed that

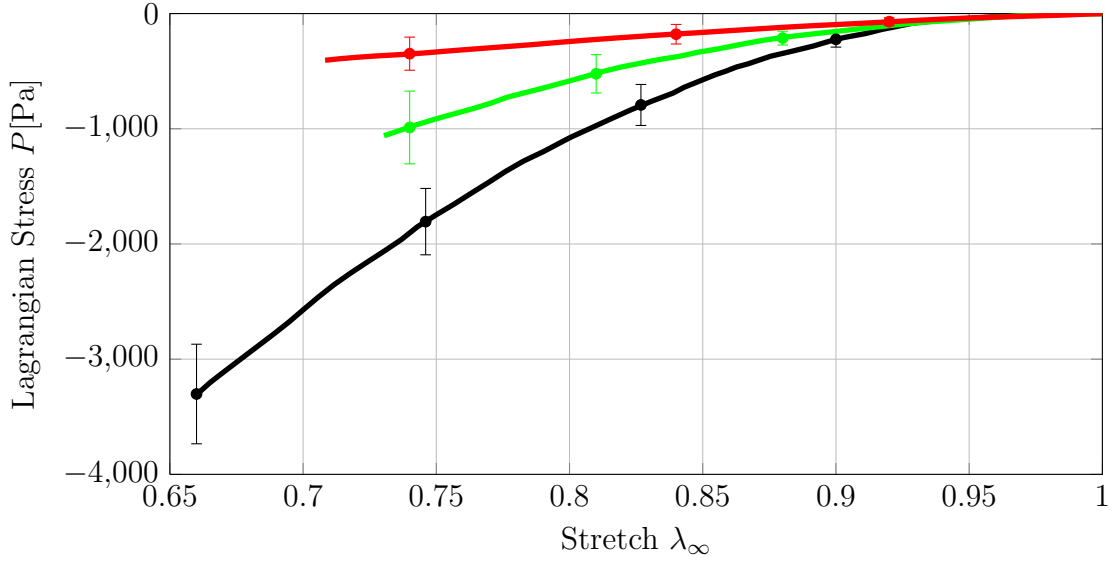


Figure 2.2: Experimental data for unconfined compression of swine brain tissue (Miller and Chinzei, 1997). Error bars indicate the standard deviation of the experimental results. ( — ):  $\dot{\lambda}_\infty = 6.4 \times 10^{-6} \text{ sec}^{-1}$ ; ( — ):  $\dot{\lambda}_\infty = 0.0064 \text{ sec}^{-1}$ ; ( — ):  $\dot{\lambda}_\infty = 0.64 \text{ sec}^{-1}$ .

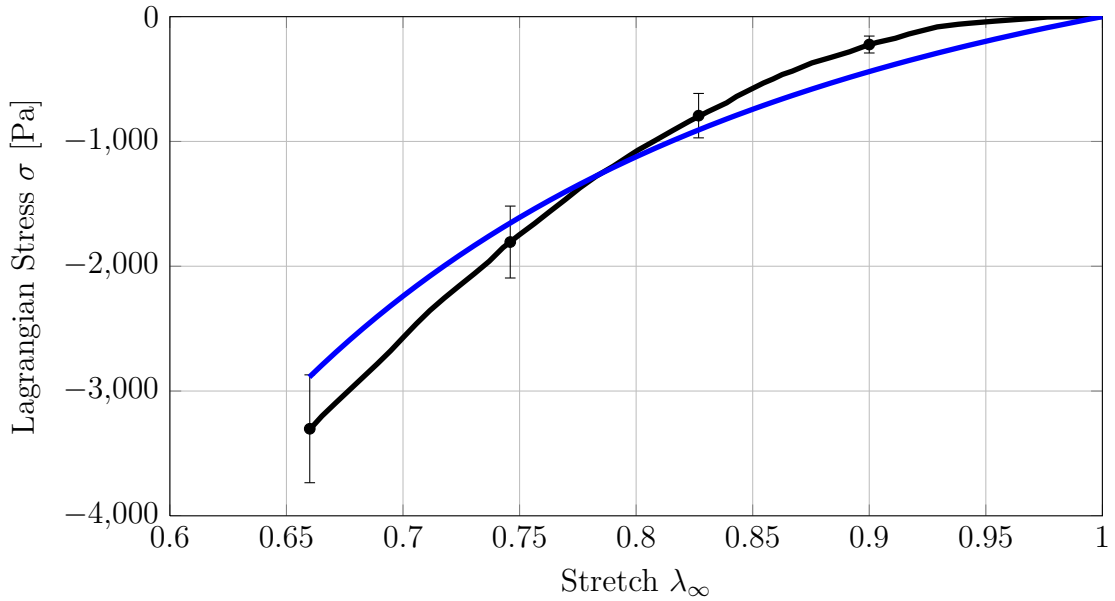


Figure 2.3: Comparison between the predictions of the one-Maxwell mode nonlinear viscoelastic model with parameters from Table 2.1 and the experimental data for  $\dot{\lambda}_\infty = 0.64 \text{ sec}^{-1}$ . ( — ): Model prediction (GOF= 0.94); ( — ): Experimental data (Miller and Chinzei, 1997).

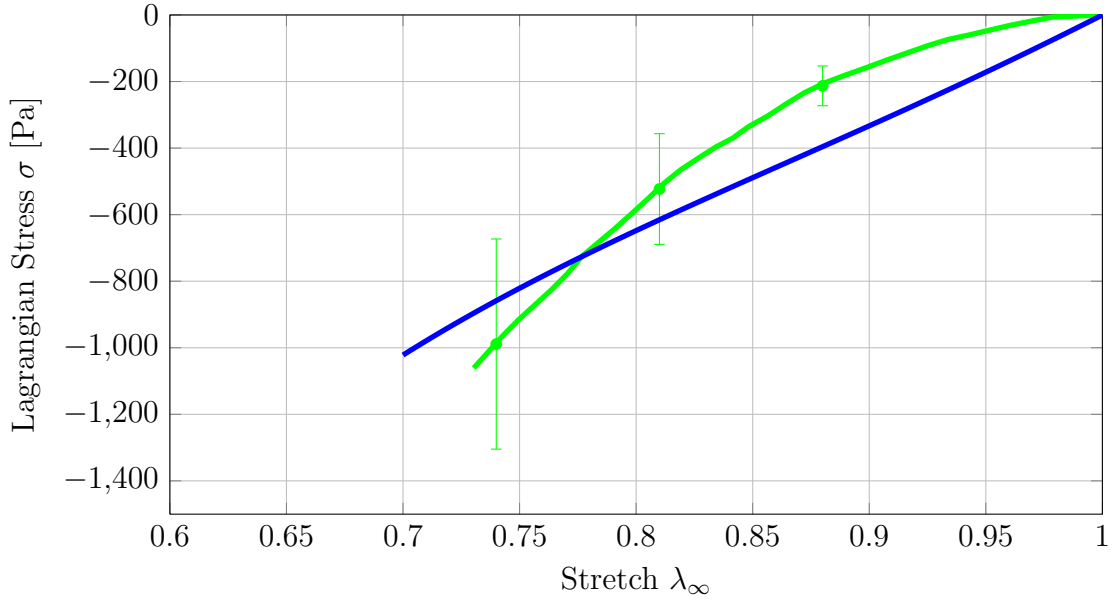


Figure 2.4: Comparison between the predictions of the one–Maxwell mode nonlinear viscoelastic model with parameters from Table 2.1 and the experimental data for  $\dot{\lambda}_\infty = 0.0064 \text{ sec}^{-1}$ . ( — ): Model prediction (GOF= 0.83); ( — ): Experimental data (Miller and Chinzei, 1997).

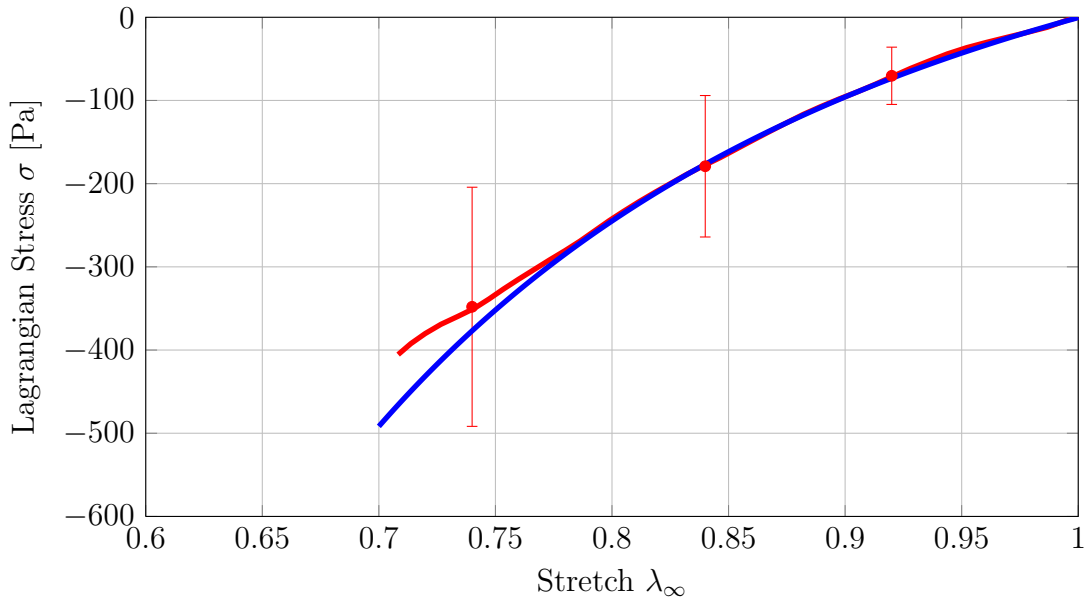


Figure 2.5: Comparison between the predictions of the one–Maxwell mode nonlinear viscoelastic model with parameters from Table 2.1 and the experimental data for  $\dot{\lambda}_\infty = 6.4 \times 10^{-6} \text{ sec}^{-1}$ . ( — ): Model prediction (GOF= 0.98); ( — ): Experimental data (Miller and Chinzei, 1997).

Table 2.2: Curve-fitted material constants for the nonlinear viscoelastic model with two Maxwell modes

Curve-Fitted Constants			
	$c_{1A}$ [Pa]	$c_{2A}$ [Pa]	$\eta_A$ [Pa.sec/m]
Parallel Spring $A = \infty$	$3.820 \times 10^{-14}$	$1.093 \times 10^2$	–
Maxwell mode $A = 1$	$2.990 \times 10^{-14}$	$3.234 \times 10^2$	$7.422 \times 10^3$
Maxwell mode $A = 2$	$3.219 \times 10^{-14}$	$1.838 \times 10^2$	$3.025 \times 10^6$

the model predictions show some improvement, particularly in the case of moderate strain rate, when compared to the model with one Maxwell mode. However, the increased number of material parameters needed may not be worth the improvement.

### 2.3 Interactions of Pressure Waves with Nonlinear Viscoelastic Systems

In this section, a model for fluid-structure interaction between acoustic pressure waves traveling in air (fluid) and a point mass supported by a nonlinear viscoelastic element (structure) is developed. This model could be employed to provide insights into the interaction between blast pressure waves and protective equipment, or between blast pressure waves and the skull-brain system. The model is shown in Fig. 2.9. The viscoelastic support is modeled using the nonlinear viscoelastic model introduced in §2.1. The model presented is similar to that analyzed by Kam-

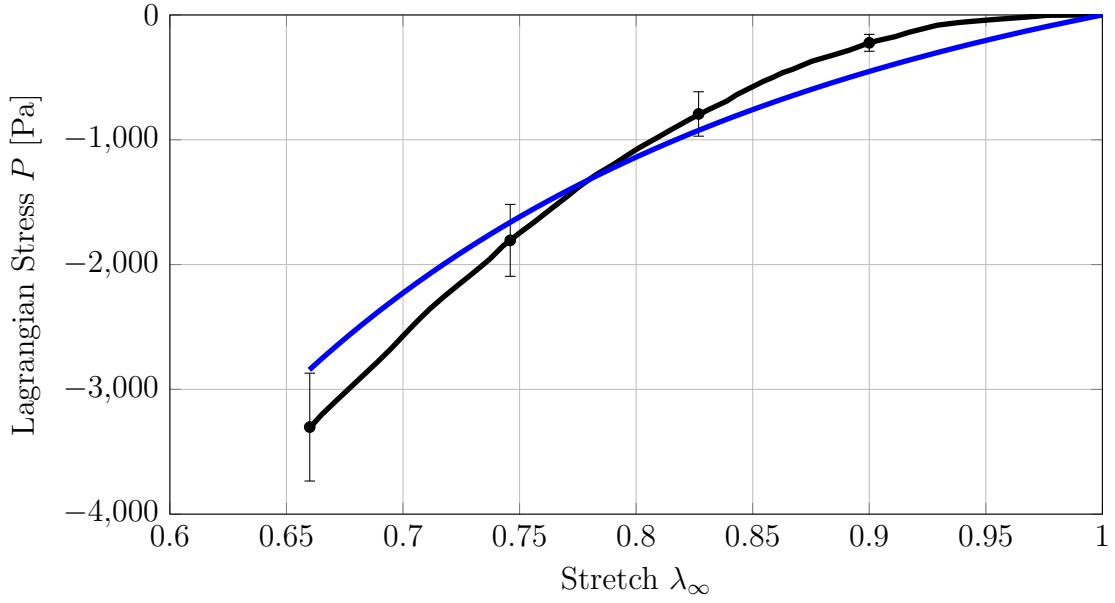


Figure 2.6: Comparison between the predictions of the two–Maxwell mode nonlinear viscoelastic model with parameters from Table 2.2 and the experimental data for  $\dot{\lambda}_\infty = 0.64 \text{ sec}^{-1}$ . ( — ): Model prediction (GOF= 0.93); ( — ): Experimental data (Miller and Chinzei, 1997).

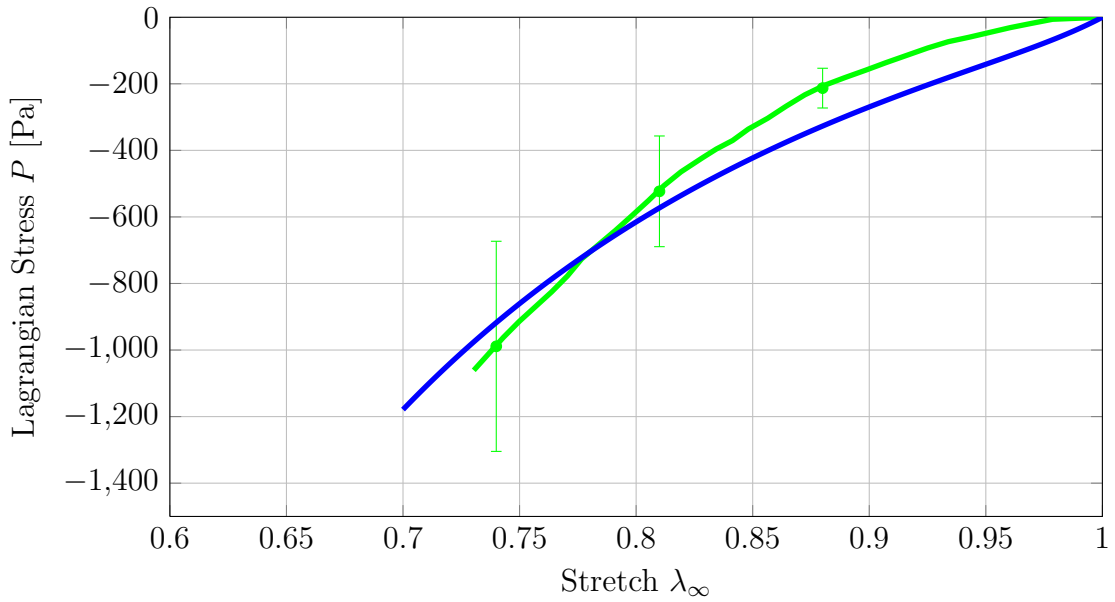


Figure 2.7: Comparison between the predictions of the two–Maxwell mode nonlinear viscoelastic model with parameters from Table 2.2 and the experimental data for  $\dot{\lambda}_\infty = 0.0064 \text{ sec}^{-1}$ . ( — ): Model prediction (GOF= 0.93); ( — ): Experimental data (Miller and Chinzei, 1997).

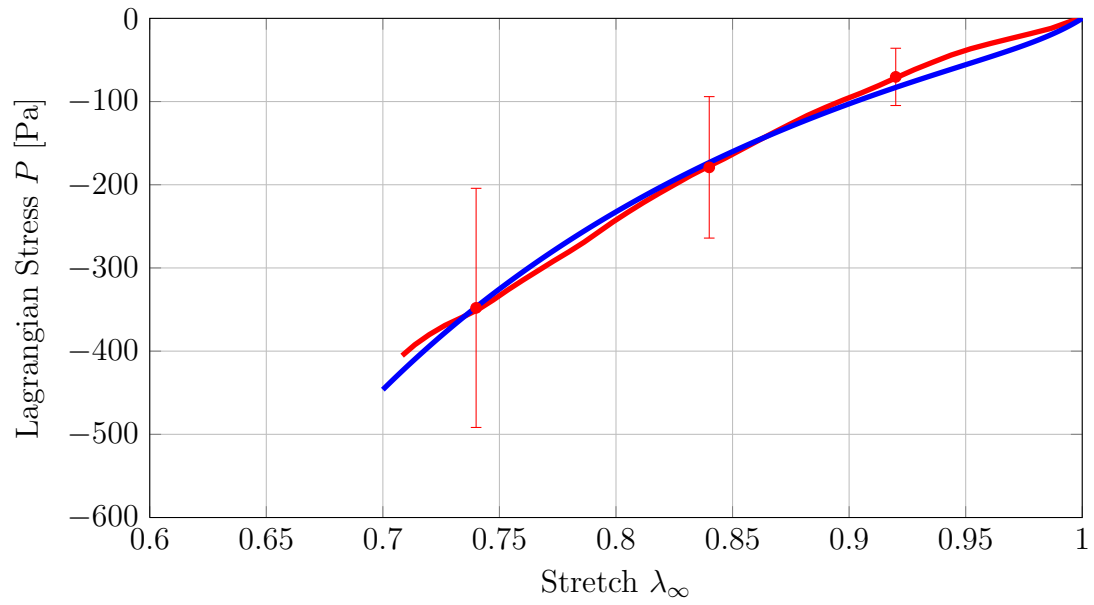


Figure 2.8: Comparison between the predictions of the two–Maxwell mode nonlinear viscoelastic model with parameters from Table 2.2 and the experimental data for  $\dot{\lambda}_\infty = 6.4 \times 10^{-6} \text{ sec}^{-1}$ . ( — ): Model prediction (GOF= 0.99); ( — ): Experimental data (Miller and Chinzei, 1997).

bouchev (2007) to study the interaction of exponential waves with monolithic plates on a viscoelastic support. However, in the present case, the viscoelastic support is nonlinear, as opposed to the linear Kelvin–Voigt viscoelastic model used by Kam-bouchev. Following, a description of the model variables and governing equations is presented.

### 2.3.1 System Description and Governing Equations

The position of the mass is given by  $\xi$ . The origin of the coordinate  $x$  coincides with the rest position of the mass. The mass is acted on from the left by the pressure  $p$  in the air, and from the right by the total stress on the viscoelastic support  $\sigma$ . The pressure in the air is assumed to follow the linear wave equation of acoustics (Eq. (2.10c)). The equations of the viscoelastic support are given by Eqs. (2.5). The equations governing the interaction of the acoustic fluid medium and the viscoelastic system are summarized as follows

$$m\ddot{\xi} = [\sigma + p(x = \xi, t)] \mathcal{A} \quad (2.10a)$$

$$\dot{\xi} = u(x = \xi, t) = \frac{1}{\rho_0 c} (f(\xi - ct) - g(\xi + ct)) \quad (2.10b)$$

$$p(x, t) = f(x - ct) + g(x + ct) \quad (2.10c)$$

$$\sigma = h_\infty(\lambda_\infty) + \sum_{i=1}^N h_i(\lambda_i) \quad (2.10d)$$

$$\dot{\lambda}_i = \dot{\lambda}_\infty - \frac{h_i(\lambda_i)}{\eta_i} \quad i = 1, 2, \dots, N \quad (2.10e)$$

$$\lambda_\infty = 1 - \frac{\xi}{L_0}, \quad (2.10f)$$

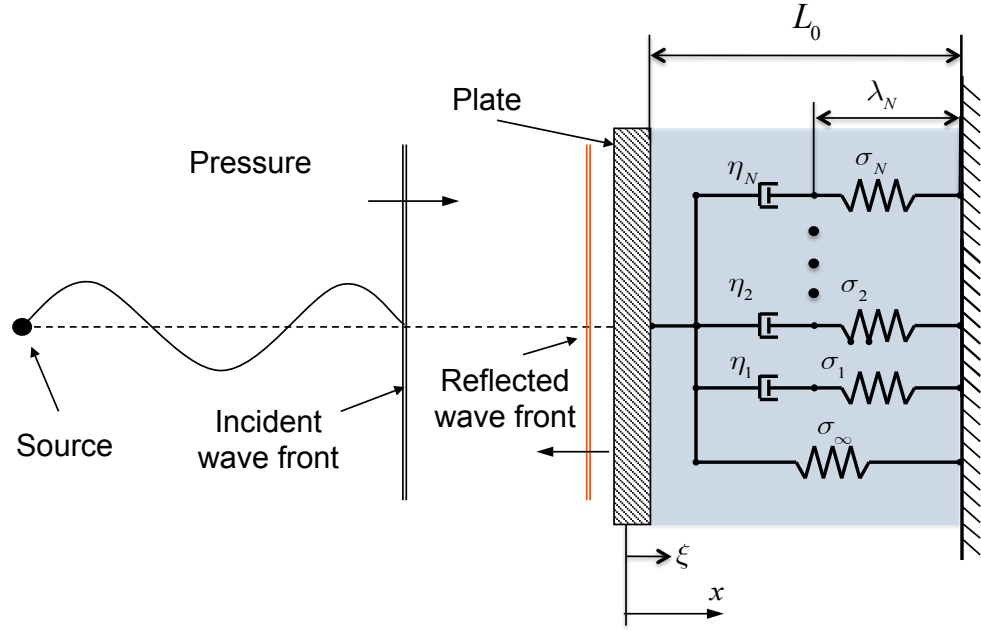


Figure 2.9: Schematic of the interaction of an incoming pressure wave in air (fluid) with a mass supported by a nonlinear viscoelastic material (structure).

where  $m$  is the mass of the structure,  $\mathcal{A}$  is its cross-sectional area,  $f(\cdot)$  and  $g(\cdot)$  are arbitrary functions solving the linear wave equation which are determined from the boundary conditions; and the functions  $h_\infty(\cdot)$  and  $h_i(\cdot)$  ( $i = 1, 2, \dots, N$ ) were defined in Eq. (2.6). In the context of the present problem,  $f(x - ct)$  is the incoming (known) pressure wave traveling to the right, whereas  $g(x + ct)$  is the pressure wave reflected off the plate (unknown) and traveling to the left.

Combining Eqs. (2.10e) and (2.10f), and eliminating  $g(\xi + ct)$  from Eqs. (2.10a),

(2.10b) and (2.10c), the following reduced system of equations is obtained:

$$m\ddot{\xi} + \mathcal{A}\rho_0 c \dot{\xi} = [\sigma + 2f(\xi - ct)] \mathcal{A} \quad (2.11a)$$

$$\sigma = h_\infty(\lambda_\infty) + \sum_{i=1}^N h_i(\lambda_i) \quad (2.11b)$$

$$\dot{\lambda}_i = - \left[ \frac{\dot{\xi}}{L_0} + \frac{h_i(\lambda_i)}{\eta_i} \right] \quad i = 1, 2, \dots, N \quad (2.11c)$$

$$\lambda_\infty = 1 - \frac{\xi}{L_0}. \quad (2.11d)$$

The reflected pressure wave  $g(x + ct)$  is computed from the solution of the previous system.

### 2.3.2 Scaling of Variables and Non-dimensional Governing Equations

A non-dimensionalization of the governing equations is pursued next in order to reduce the number of parameters involved and to aid the studies pursued later on. In order to accomplish this, the following yet undetermined characteristic variables: length  $L_C$ , time  $T_C$  and pressure  $P_C$ , are chosen. Then, the following non-dimensional variables are defined

$$\begin{aligned} \zeta &:= \frac{\xi}{L_C} & \tau &:= \frac{t}{T_C} & \sigma^* &:= \frac{\sigma}{P_C} \\ f^*(\zeta, \tau) &:= \frac{1}{P_C} f(\zeta L_C - c\tau T_C) & h_\infty^*(\lambda_\infty) &:= \frac{h_\infty(\lambda_\infty)}{P_C} & h_i^*(\lambda_i) &:= \frac{h_i(\lambda_i)}{P_C}. \end{aligned} \quad (2.12)$$

Introduction of the variables (2.12) into Eq. (2.11a) yields

$$\frac{d^2\zeta}{d\tau^2} + \rho_0 \mathcal{A} c \frac{T_C}{m} \frac{d\zeta}{d\tau} = \left[ \sigma^* \frac{T_C^2 P_C}{m L_C} + 2f^*(\zeta, \tau) \frac{T_C^2 P_C}{m L_C} \right] \mathcal{A}.$$

In looking at the previous equation, a convenient choice of the characteristic variables is

$$\rho_0 c \frac{T_C}{m} \mathcal{A} = 1 \Rightarrow T_C := \frac{m}{\rho_0 c \mathcal{A}} \quad (2.13)$$

$$\frac{T_C^2 P_C}{m L_C} \mathcal{A} = 1 \Rightarrow \frac{L_C}{P_C} := \frac{m}{\rho_0^2 c^2 \mathcal{A}}. \quad (2.14)$$

Introducing the non-dimensional variables (2.12) and the characteristic variables (2.13) and (2.14) into Eq. (2.11c) yields

$$\frac{d\lambda_i}{d\tau} = - \left[ \frac{1}{l_0} \frac{d\zeta}{d\tau} + \frac{h_i^*(\lambda_i)}{\alpha_i} \right] \quad i = 1, 2, \dots, N,$$

where the following non-dimensional parameters are defined

$$l_0 := \frac{L_0}{L_C} = \frac{L_0 \rho_0^2 c^2 \mathcal{A}}{m P_C} \quad \alpha_i := \frac{\eta_i}{P_C T_C} = \frac{\eta_i}{\rho_0 c}. \quad (2.15)$$

Collecting the results, the non-dimensional governing equations of the interaction between pressure waves in air and the nonlinear viscoelastic system are given by

$$\frac{d^2 \zeta}{d\tau^2} + \frac{d\zeta}{d\tau} = \sigma^* + 2f^*(\zeta, \tau) \quad (2.16a)$$

$$\sigma^* = h_\infty^*(\lambda_\infty) + \sum_{i=1}^N h_i^*(\lambda_i) \quad (2.16b)$$

$$\frac{d\lambda_i}{d\tau} = - \left[ \frac{1}{l_0} \frac{d\zeta}{d\tau} + \frac{h_i^*(\lambda_i)}{\alpha_i} \right] \quad i = 1, 2, \dots, N \quad (2.16c)$$

$$\lambda_\infty = 1 - \frac{\zeta}{l_0}. \quad (2.16d)$$

These equations are the starting point for the analysis presented next. The characteristic pressure  $P_C$  will be chosen based on the amplitude of the incoming wave  $f(\xi - \tau)$ .

### 2.3.3 Exponential Wave Profile

Due to its resemblance to an explosive blast pressure signature, an exponential incident pressure wave is considered. The incident pressure wave is given by the following expression

$$f(\xi - ct) = \begin{cases} p_s e^{\frac{(\xi - ct)}{ct_s}} & \xi - ct \leq 0 \\ 0 & \xi - ct > 0, \end{cases} \quad (2.17)$$

where  $t_s$  is the characteristic time of the exponential wave,  $p_s$  is the peak overpressure and  $c$  is the speed of sound in air. Choosing  $P_C = p_s$ , and introducing the non-dimensional variables (2.12), the non-dimensional version of this wave profile  $f^*(\zeta, \tau)$  is

$$f^*(\zeta, \tau) = \begin{cases} e^{\frac{1}{\beta_0}(\zeta p_0 - \tau)} & \zeta p_0 - \tau \leq 0 \\ 0 & \zeta p_0 - \tau > 0, \end{cases} \quad (2.18)$$

where the following non-dimensional parameters were introduced:

$$\beta_0 := \frac{ct_s}{cT_C} = \frac{\rho_0 c \mathcal{A} t_s}{m} \quad (2.19)$$

$$p_0 := \frac{L_C}{cT_C} = \frac{mp_s}{\rho_0^2 c^2 \mathcal{A}} \frac{\rho_0 c \mathcal{A}}{mc} = \frac{p_s}{\rho_0 c^2}. \quad (2.20)$$

The parameter  $\beta_0$  indicates the ratio of the fluid mass (with volume  $c\mathcal{A}t_s$ ) to the structure mass. The function  $f^*(\zeta, \tau)$ , for different values of  $\beta_0$  is plotted in Fig. 2.10.

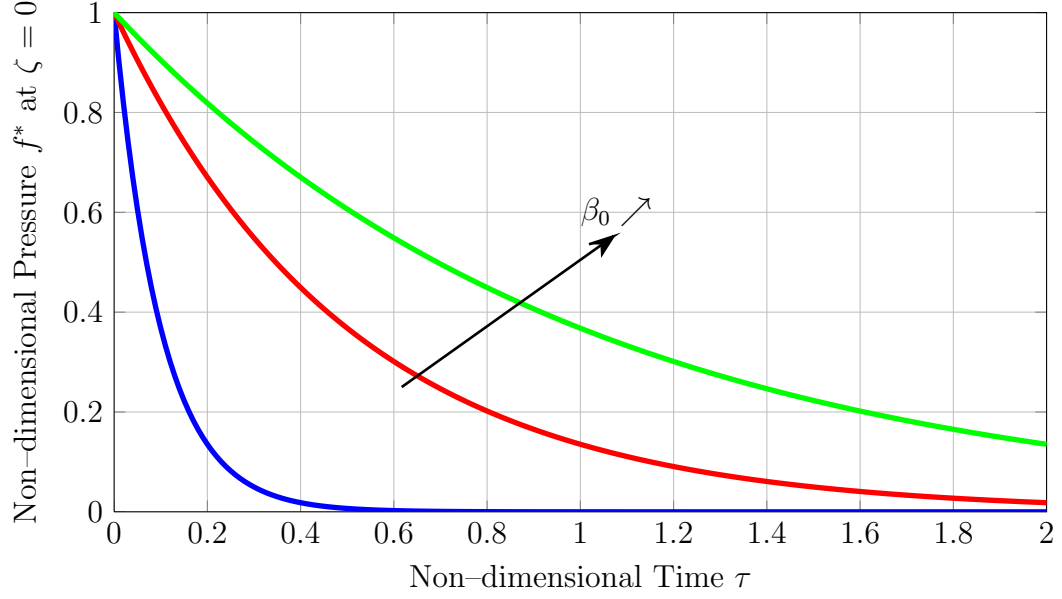


Figure 2.10: Exponential pressure profile at the location  $\zeta = 0$  for different values of  $\beta_0$ .

The governing equations for this particular problem are summarized as follows

$$\left\{ \begin{array}{l} \frac{d^2\zeta}{d\tau^2} + \frac{d\zeta}{d\tau} = \sigma + 2e^{\frac{1}{\beta_0}(\zeta p_0 - \tau)} \\ \sigma^* = h_\infty^*(\lambda_\infty) + \sum_{i=1}^N h_i^*(\lambda_i) \\ \frac{d\lambda_i}{d\tau} = - \left[ \frac{1}{l_0} \frac{d\zeta}{d\tau} + \frac{h_i^*(\lambda_i)}{\alpha_i} \right] \quad i = 1, 2, \dots, N \\ \lambda_\infty = 1 - \frac{\zeta}{l_0}. \end{array} \right. \quad (2.21)$$

The parameters determining the interaction between the incoming pressure wave and the nonlinear viscoelastic structure are:  $\beta_0$ ,  $p_0$ ,  $l_0$ ,  $\alpha_i$ , ( $i = 1, 2, \dots, N$ ). In addition, the following non-dimensional parameters are defined to characterize the viscoelastic structure

$$\kappa_\infty := \frac{1}{P_C} \left. \frac{dh_\infty}{d\lambda} \right|_{\lambda=1} \quad \kappa_i := \frac{1}{P_C} \left. \frac{dh_i}{d\lambda} \right|_{\lambda=1} \quad (i = 1, 2, \dots, N). \quad (2.22)$$

In the present study, the interest is focused on understanding how the point-mass

acquires impulse (change of linear momentum) as a consequence of its interaction with the pressure wave. Therefore, the maximum impulse  $I_m$  of the mass is computed. A measure of the available impulse in the incoming pressure wave is given by  $I_p = p_s t_s \mathcal{A}$ . The ratio of impulse transmitted to impulse available is given by

$$\frac{I_m}{I_p} = \frac{\max(m\dot{\xi})}{p_s \mathcal{A} t_s} = \frac{m L_C}{T_C p_s \mathcal{A} t_s} \max\left(\frac{d\zeta}{d\tau}\right) = \frac{1}{\beta_0} \max\left(\frac{d\zeta}{d\tau}\right). \quad (2.23)$$

In addition, the (non-dimensional) maximum force transmitted to the fixed support  $F_S/(p_s \mathcal{A})$  is analyzed.

The limitations, or range of validity, of the presented model need to be pointed out here in order to avoid misleading conclusions. First, the model only accounts for one reflected wave off the plate; therefore, oscillations of the mass cannot be studied since they will introduce multiple wave reflections. As a consequence, the numerical simulations are run until the moment in which the mass first stops ( $d\zeta/d\tau = 0$ ). Secondly, a situation in which the incoming pressure wave imparts a motion to the mass with a speed higher than the speed of sound  $c$  could potentially be predicted by the model. Under these circumstances, air compressibility effects will have significance at the mass-air interface. This situation violates the acoustic assumption of the model, and therefore it needs to be avoided.

It is observed that the parameters  $\beta_0$ ,  $p_0$  and  $l_0$  are related through

$$\beta_0 = p_0 l_0 \frac{c t_s}{L_0}.$$

Therefore, the effects of  $p_0$  and  $l_0$  are interchangeable. A study of the influence of the different parameters,  $\beta_0$ ,  $p_0$ ,  $\alpha_i$  and  $\kappa_1/\kappa_0$  on the impulse transmitted to the

mass, and on the force exerted on the support is carried out next. For simplicity, only one Maxwell mode ( $N = 1$ ) is used in the following simulations.

It is noted that the parameters pertaining to the structure need to be carefully chosen in order to be able to observe their influence on the system behavior. For example, if the value of  $\alpha_1$  is large enough, the viscoelastic support becomes an elastic support with two nonlinear springs in parallel. On the other hand, if the ratio  $\kappa_1/\kappa_0$  becomes large enough, then the structure behaves like a nonlinear Kelvin–Voigt model with a nonlinear spring in parallel with a linear dashpot. Finally, if either  $\kappa_1/\kappa_0$  or  $\alpha_1$  become small enough, the structure behaves as a single nonlinear spring  $\kappa_\infty$ .

In Figs. 2.11 through 2.13, the impulse transmitted by pressure wave to the mass as a function of the parameter  $\beta_0$  are presented for values  $p_0 = 0.01, 0.1, 1$ . Upon observation of the results corresponding to the impulse transmitted, the following remarks are in order. For small and large values of  $\beta_0$ , the impulse transmitted to the mass is almost indifferent to the damping parameter  $\alpha_1$ , to the intensity of the pressure wave  $p_0$ , and to the value  $\kappa_1/\kappa_0$ . For small  $\beta_0$ , the mass of the structure becomes large compared to the reference air mass and therefore, the structure behaves as a rigid wall, reflecting almost all the incoming pressure wave and acquiring a non-dimensional impulse approaching a value of 2. For large  $\beta_0$ , the mass of the structure becomes much smaller than the reference air mass, and as a consequence, almost no impulse is transmitted to the mass by the incoming pressure wave.

It is observed that for  $\alpha_1 = 1$ , all the curves of impulse transmitted for different values of  $\kappa_1/\kappa_0$  are practically on superposed. It is also noted that increasing the

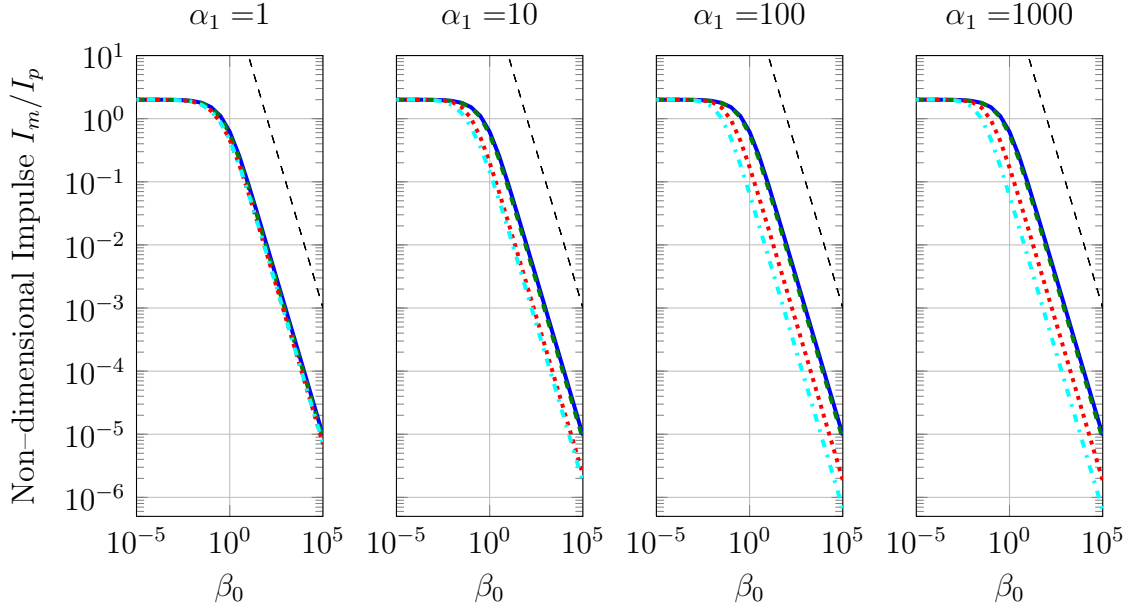


Figure 2.11: Ratio of impulse transmitted to impulse available ( $I_m/I_p$ ) as a function of  $\beta_0$  for  $p_0 = 0.01$  and for different values of the damping parameter  $\alpha_1$ . (—):  $\kappa_1/\kappa_0 = 0.01$ ; (---):  $\kappa_1/\kappa_0 = 1$ ; (···):  $\kappa_1/\kappa_0 = 100$ ; (- · - ·):  $\kappa_1/\kappa_0 = 1000$ . (---): applicability limit of the model.

damping  $\alpha_1$  has little effect for the cases studied here. The influence of the damping seems to be more noticeable in the range  $\alpha_1 \in [10, 100]$ .

For a given value of the damping  $\alpha_1$  and of the non-dimensional pressure  $p_0$ , it is observed that increasing the value of  $\kappa_1/\kappa_0$  decreases the impulse transmitted to the mass. The effect of  $\kappa_1/\kappa_0$  is more prominent for the range of damping  $\alpha_1 \in [10, 100]$ .

Finally, it is observed that the impulse transmitted to the mass, for intermediate to large values of  $\beta_0$  increases as the value of  $p_0$  increases.

In Figs. 2.14 through 2.16, the force exerted on the fixed support as a function of the parameter  $\beta_0$  are presented for values  $p_0 = 0.01, 0.1, 1$ . The same comments made for the impulse apply for the maximum force transmitted to the base. In

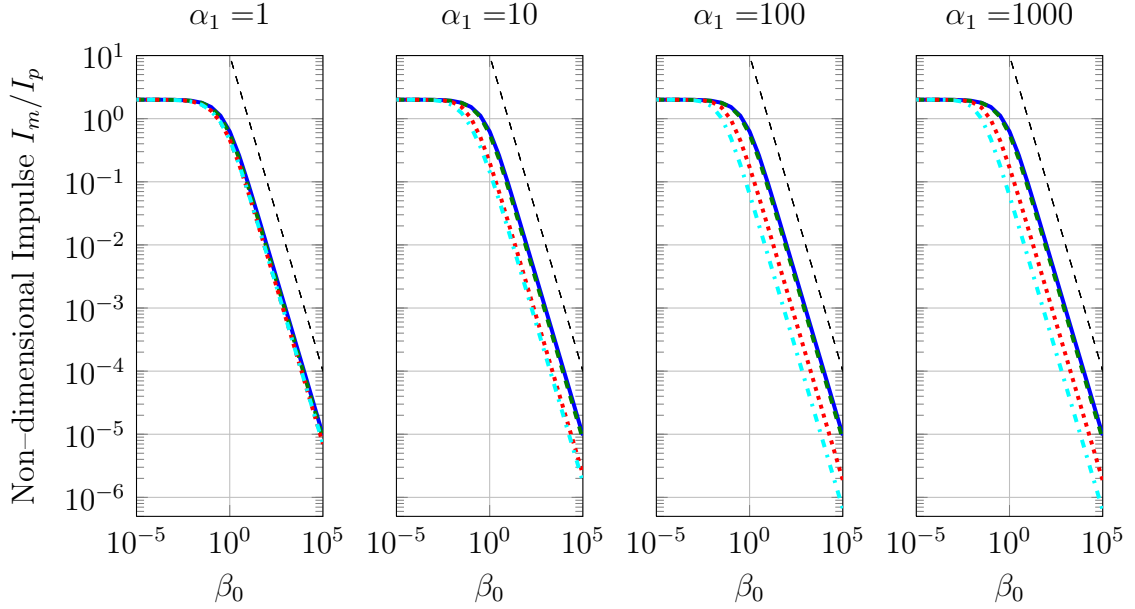


Figure 2.12: Ratio of impulse transmitted to impulse available ( $I_m/I_p$ ) as a function of  $\beta_0$  for  $p_0 = 0.1$  and for different values of the damping parameter  $\alpha_1$ . ( — ):  $\kappa_1/\kappa_0 = 0.01$ ; ( - - ):  $\kappa_1/\kappa_0 = 1$ ; ( ··· ):  $\kappa_1/\kappa_0 = 100$ ; ( - · - · ):  $\kappa_1/\kappa_0 = 1000$ . ( - - ): applicability limit of the model.

particular, it is observed that the non-dimensional force  $F_s/(p_s\mathcal{A})$  varies little with  $p_0$ , as Figs. 2.14 through 2.16 look similar. Upon closer examination, it was observed that the influence of  $p_0$  on  $F_s/(p_s\mathcal{A})$  is only important for intermediate values of  $\beta_0$  and for  $\kappa_1/\kappa_0 < 1$ . Again, it is observed that the influence the parameters  $\alpha_1$  and  $\kappa_1/\kappa_0$  on  $F_s/(p_s\mathcal{A})$  is more noticeable in range of damping  $\alpha_1 \in [10, 100]$ .

## 2.4 Maximum Dissipation Nonlinear Viscoelastic Constitutive Equation for Uniaxial Stress State

The phenomenological model introduced in §2.1 was shown to provide a good representation of brain tissue behavior under uniaxial compression, provided a suit-

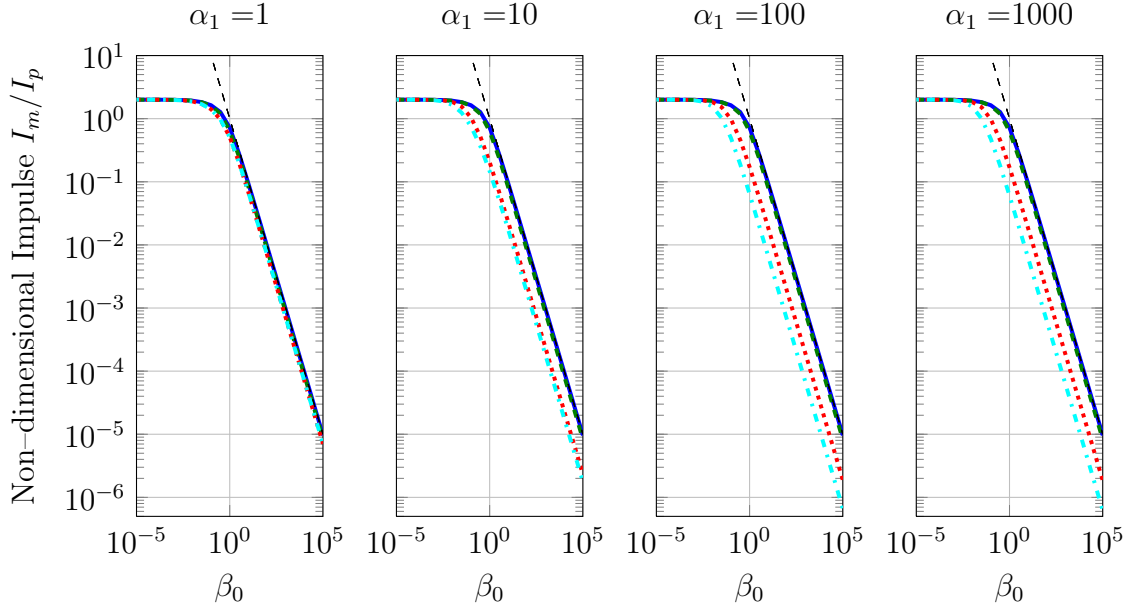


Figure 2.13: Ratio of impulse transmitted to impulse available ( $I_m/I_p$ ) as a function of  $\beta_0$  for  $p_0 = 1$  and for different values of the damping parameter  $\alpha_1$ . ( — ):  $\kappa_1/\kappa_0 = 0.01$ ; ( - - ):  $\kappa_1/\kappa_0 = 1$ ; ( ··· ):  $\kappa_1/\kappa_0 = 100$ ; ( - · - ):  $\kappa_1/\kappa_0 = 1000$ . ( - - ): applicability limit of the model.

able number of material parameters is used. However, some of these material parameters lack physical interpretation, and therefore, cannot be tracked or obtained experimentally. In addition, a large number of material parameters makes parametric studies a rather cumbersome task.

Due to the limitations mentioned before, and to ease the analytic and computational studies that follow in this dissertation another model of nonlinear viscoelasticity is explored. This model will be adopted throughout the rest of this dissertation.

The present material model is obtained through a mathematical construction given by Haslach (2011), which is briefly reviewed in Appendix B. As described there, the material model is determined by the choices of the *control*  $y_i$  and *state*

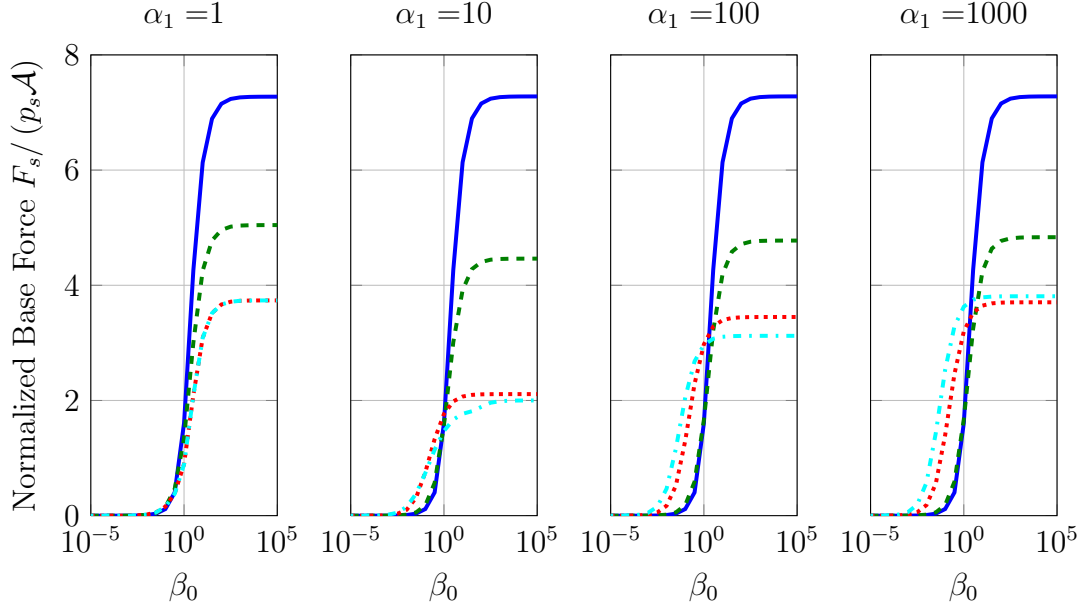


Figure 2.14: Non-dimensional force transmitted to the base ( $F_s / (p_s \mathcal{A})$ ) as a function of  $\beta_0$  for  $p_0 = 0.01$  and for different values of the damping parameter  $\alpha_1$ . (—):  $\kappa_1/\kappa_0 = 0.01$ ; (---):  $\kappa_1/\kappa_0 = 1$ ; (···):  $\kappa_1/\kappa_0 = 100$ ; (- · - ·):  $\kappa_1/\kappa_0 = 1000$ .

variables  $x_i$ , and of the *energy function*  $\Psi$  that relates control and state variables at *equilibrium* through  $\partial\Psi/\partial x_i = -y_i$ . The potential of this construction to obtain material models for soft biological tissues was demonstrated by Haslach (2005).

In the case of uniaxial stress state, the following choice of the control and state variables is made. The negative value of the only nonzero component of the first Piola–Kirchhoff stress tensor is taken to be the control variable,  $y_1 \mapsto -P(t)$ ; and the uniaxial stretch in the rod  $\lambda$  is chosen as the state variable,  $x_1 \mapsto \lambda$ . In addition, using the results from Eq. (A.12), a hyperelastic strain energy function  $\Psi(\lambda)$  is chosen. By using Eq. (A.6), the resulting nonlinear viscoelastic constitutive

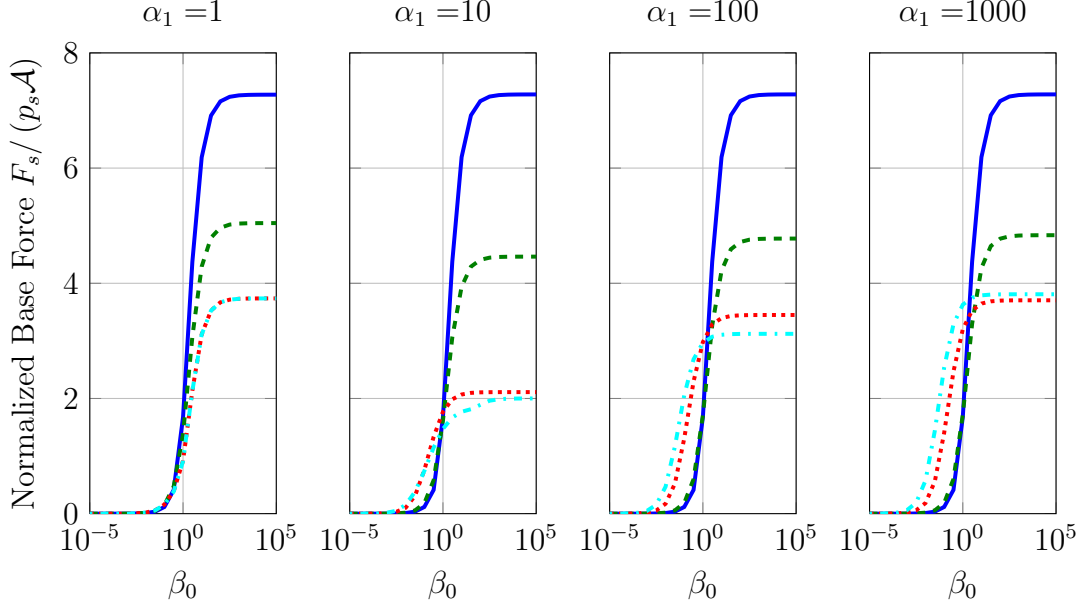


Figure 2.15: Non-dimensional force transmitted to the base ( $F_s / (p_s \mathcal{A})$ ) as a function of  $\beta_0$  for  $p_0 = 0.1$  and for different values of the damping parameter  $\alpha_1$ . ( — ):  $\kappa_1/\kappa_0 = 0.01$ ; ( - - ):  $\kappa_1/\kappa_0 = 1$ ; ( ··· ):  $\kappa_1/\kappa_0 = 100$ ; ( - · - ):  $\kappa_1/\kappa_0 = 1000$ .

model for uniaxial stress state is given by

$$\frac{d^2\Psi}{d\lambda^2} \dot{\lambda} = -\kappa \left[ \frac{d^2\Psi}{d\lambda^2} \right]^{-1} \left( \frac{d\Psi}{d\lambda} - P(t) \right), \quad (2.24)$$

where  $\kappa$  is the relaxation modulus. The term in parenthesis on the right-hand-side of Eq. (2.24) is the affinity, which expresses the difference between the current value of the control stress  $P$ , and the current equilibrium value of the stress for the current state  $\lambda$ . Provided  $\kappa > 0$ , Eq. (2.24) can be rewritten as

$$P = \frac{d\Psi}{d\lambda} + \frac{1}{\kappa} \left[ \frac{d^2\Psi}{d\lambda^2} \right]^2 \dot{\lambda}. \quad (2.25)$$

Equations (2.24), or (2.25), represent a family of nonlinear viscoelastic models. Particular models can be obtained by choosing different forms of the strain energy function  $\Psi(\lambda)$ .

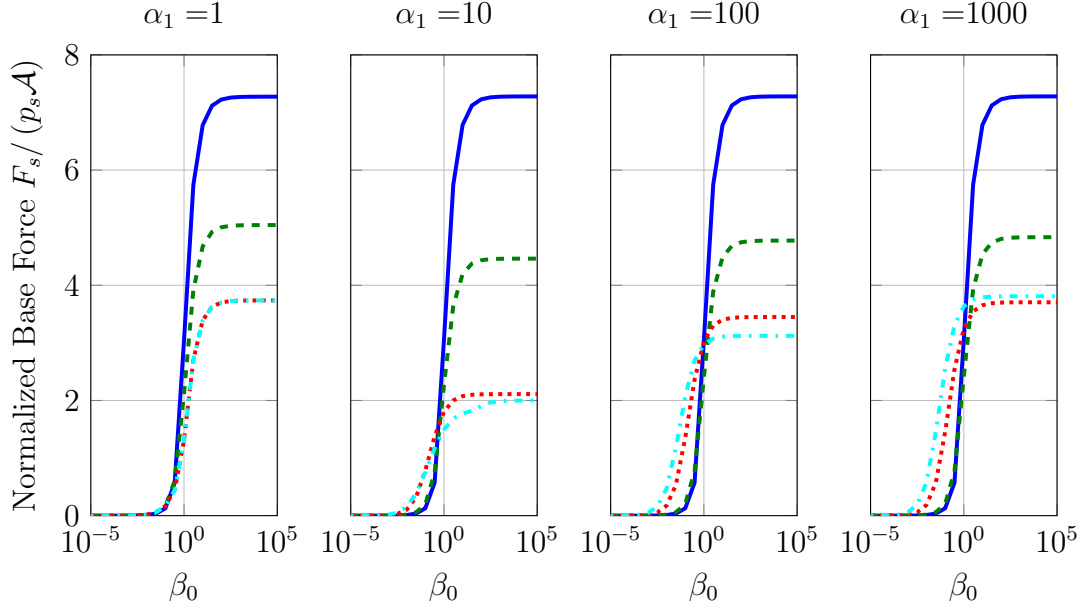


Figure 2.16: Non-dimensional force transmitted to the base ( $F_s / (p_s \mathcal{A})$ ) as a function of  $\beta_0$  for  $p_0 = 1$  and for different values of the damping parameter  $\alpha_1$ . ( — ):  $\kappa_1 / \kappa_0 = 0.01$ ; ( - - ):  $\kappa_1 / \kappa_0 = 1$ ; ( ··· ):  $\kappa_1 / \kappa_0 = 100$ ; ( - · - ):  $\kappa_1 / \kappa_0 = 1000$ .

## 2.4.1 Maximum Dissipation Viscoelastic Model Curve-Fitting to Brain

### Tissue Experimental Data

In this section, the nonlinear viscoelastic constitutive model for uniaxial stress state introduced in §2.4 is curve-fitted to experimental data on constant strain rate, unconfined compression experiments with swine brain tissue. The experimental data used in this case is the same as the previously employed in §2.2. Here, it is important to note the following: in the experiments by Miller and Chinzei (1997), the variable that is controlled is the stretch whereas the stress is the measured state variable. These roles of the state and control variables are reversed in the construction leading to Eq. (2.24). As a consequence, the constitutive equation

(2.24) is in principle not adequate to represent this type (constant strain rate) of experiment. The constitutive model is suited for describing experiments with constant stress (creep). Baring in mind the mentioned incompatibility, the following curve-fitting is pursued anyways in order to generate an idea of the values of the material parameters for brain tissue.

In order to perform the curve-fitting, the following relations are derived through algebraic manipulation of Eq. (2.25) for *constant stretch rate* with values  $\dot{\lambda}_i$  and  $\dot{\lambda}_j$ .

$$\frac{P(\lambda, \dot{\lambda}_i) \dot{\lambda}_j - P(\lambda, \dot{\lambda}_j) \dot{\lambda}_i}{\dot{\lambda}_j - \dot{\lambda}_i} = \frac{d\Psi}{d\lambda}(\lambda) \quad (2.26a)$$

$$\frac{P(\lambda, \dot{\lambda}_j) - P(\lambda, \dot{\lambda}_i)}{\dot{\lambda}_j - \dot{\lambda}_i} = \frac{1}{\kappa} \left[ \frac{d^2\Psi}{d\lambda^2}(\lambda) \right]^2, \quad (2.26b)$$

with  $\dot{\lambda}_j > \dot{\lambda}_i$ . The curve-fitting process is done as follows: A first fitting of Eq. (2.26a) is done to determine the constants that define  $d\Psi/d\lambda$ , and hence, the hyperelastic strain energy function  $\Psi$ . Finally, Eq. (2.26b) is fitted to determine the relaxation constant  $\kappa$ . Only the experimental data corresponding to the medium and high strain rates are used for the curve-fitting process. The curve-fitting was performed with Matlab through the *lsqcurvefit* function.

Two different viscoelastic models are compared in this study. They correspond to two different choices of the strain energy functions  $\Psi$ . A four-parameter (two-term) incompressible Ogden model,  $\Psi_{\text{Og}}$ , and an incompressible Mooney-Rivlin

Table 2.3: Curve-fitted material parameters for different maximum dissipation non-linear viscoelastic material models

	Constants	4-Param. Ogden	Mooney-Rivlin
1	$\mu_1$ [kPa]	605.1	0.0510
2	$\mu_2$ [kPa]	-0.0086	0.6234
3	$\alpha_1$ [-]	0.0020	2.000
4	$\alpha_2$ [-]	-9.305	-2.000
5	$\kappa$ [Pa.sec <sup>-1</sup> ]	79.02	37.14

model,  $\Psi_{\text{MR}}$  are considered. These functions are given by

$$\Psi_{\text{Og}}(\lambda) = \frac{\mu_1}{\alpha_1} \left( \lambda^{\alpha_1} + 2\lambda^{-\frac{1}{2}\alpha_1} - 3 \right) + \frac{\mu_2}{\alpha_2} \left( \lambda^{\alpha_2} + 2\lambda^{-\frac{1}{2}\alpha_2} - 3 \right) \quad (2.27)$$

$$\Psi_{\text{MR}}(\lambda) = \frac{\mu_1}{2} (\lambda^2 + 2\lambda^{-1} - 3) - \frac{\mu_2}{2} (\lambda^{-2} + 2\lambda - 3). \quad (2.28)$$

Functions (2.27) and (2.28) are introduced into Eq. (2.25) to obtain the different viscoelastic models. The obtained curve-fitted material constants corresponding to each of the models are summarized in Table 2.3.

The comparisons between the experimental data and the predictions from the different viscoelastic models are shown in Figures 2.17, 2.18, and 2.19 for the constant strain rates of  $\dot{\lambda}_1 = -0.64 \text{ sec}^{-1}$ ,  $\dot{\lambda}_2 = -0.64 \times 10^{-2} \text{ sec}^{-1}$ , and  $\dot{\lambda}_3 = -0.64 \times 10^{-5} \text{ sec}^{-1}$ , respectively.

The following observations are in order. For the high strain rate cases, the nonlinear viscoelastic material model with Mooney-Rivlin long term strain energy seems to describe the mechanical behavior of swine brain tissue better than the

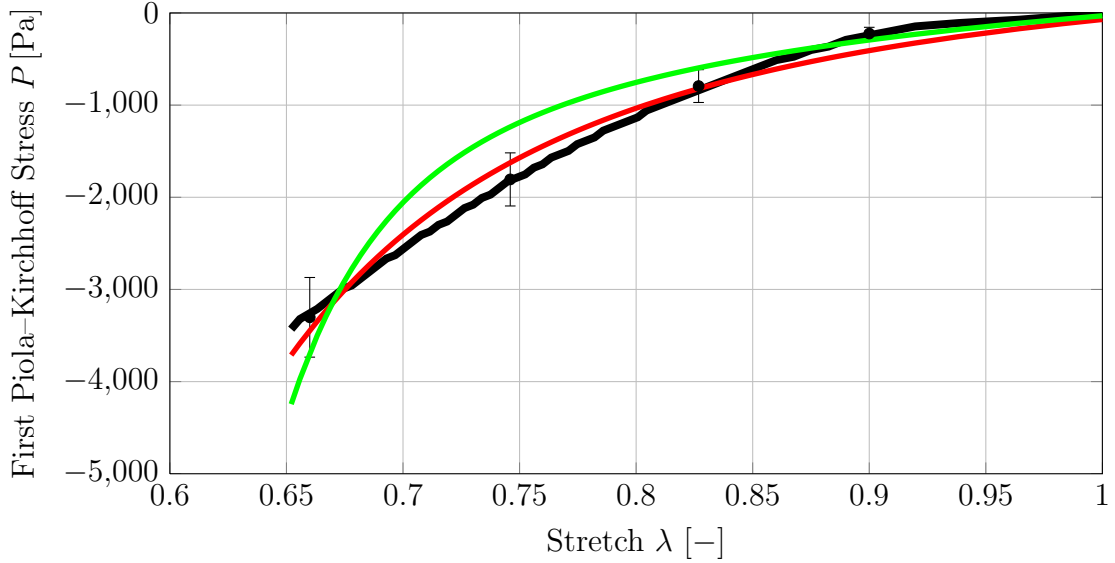


Figure 2.17: Comparison between the predictions of the maximum dissipation nonlinear viscoelastic models with curve-fitted parameters from Table 2.3 and the experimental data for  $\dot{\lambda} = -0.64 \text{ sec}^{-1}$ . ( — ): Experimental data; ( — ): four-parameter Ogden (GOF=0.84); ( — ): Mooney-Rivlin (GOF=0.98).

model with Ogden long term strain energy function. For the lower strain rate case, all the material models provide poor prediction of the tissue mechanical behavior by largely overestimating the compressive stress.

The differences between the model predictions and the experimental data may be due to several factors, amongst which, the incompatibility of the model construction with the experimental set-up is the strongest one. In addition, it is noted that although nonlinear with respect to the stretch  $\lambda$ , the constitutive model given by Eq. 2.24 is affine with respect to the strain rate  $\dot{\lambda}$ . Therefore, materials with nonlinear dependence on the stretch rate cannot be described by this material model.

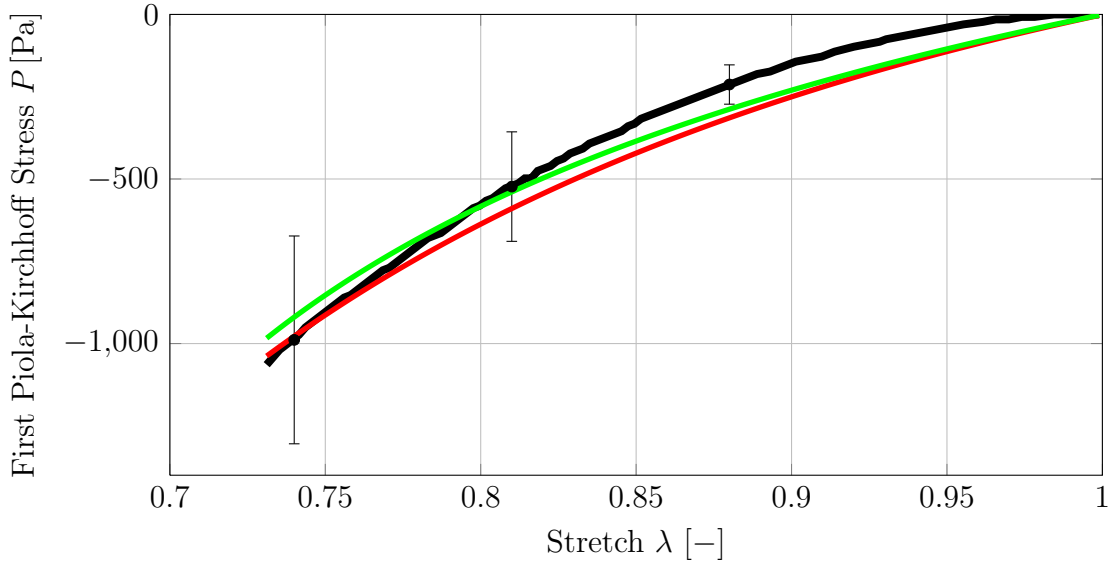


Figure 2.18: Comparison between the predictions of the maximum dissipation nonlinear viscoelastic models with curve-fitted parameters from Table 2.3 and the experimental data for  $\dot{\lambda} = -0.64 \times 10^{-2} \text{ sec}^{-1}$ . ( — ): Experimental data; ( — ): four-parameter Ogden (GOF=0.97); ( — ): Mooney-Rivlin (GOF=0.95).

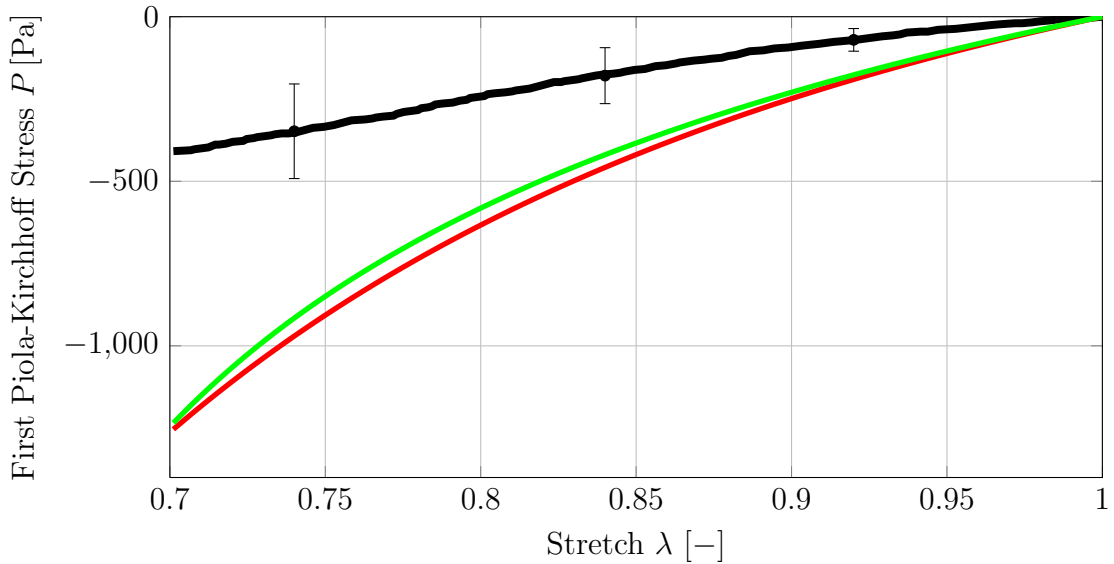


Figure 2.19: Comparison between the predictions of the maximum dissipation nonlinear viscoelastic models with curve-fitted parameters from Table 2.3 and the experimental data for  $\dot{\lambda} = -0.64 \times 10^{-5} \text{ sec}^{-1}$ . ( — ): Experimental data; ( — ): four-parameter Ogden; ( — ): Mooney-Rivlin.

## Chapter 3

### Longitudinal Wave Propagation through Viscoelastic Material with Constant Cross-Section

A primary aim of this investigation is to gain fundamental understanding of the influence of the nonlinear mechanical behavior of soft tissues on the propagation of the stress waves generated by transient loadings. The soft tissue is modeled as a nonlinear viscoelastic material, whose mechanical behavior is described by Eq. (2.25). In order to simplify the analysis, a one-dimensional rod is considered, and propagation of longitudinal waves is studied.

#### 3.1 Governing Equations

A general rod structure, as the one shown in Figure 3.1, is considered. The variable  $X$  indicates the position of material points along the rod in the reference configuration. After a time  $t$ , the body deforms, and a material point  $Q$  originally located at  $X_Q$  moves to a new location described by the mapping  $x_Q = \chi(X_Q, t)$ . The cross-sectional area of the rod in the reference configuration, which may be a function of  $X$ , is denoted by  $\mathcal{A}(X)$ , and the uniform material density in the reference configuration is denoted  $\rho_0$ . If the lateral surface of the rod is traction-free, and if the rod is assumed to be very thin, then the first Piola-Kirchhoff stress tensor can be assumed to have only one nonzero component, which is denoted by  $P$ ,

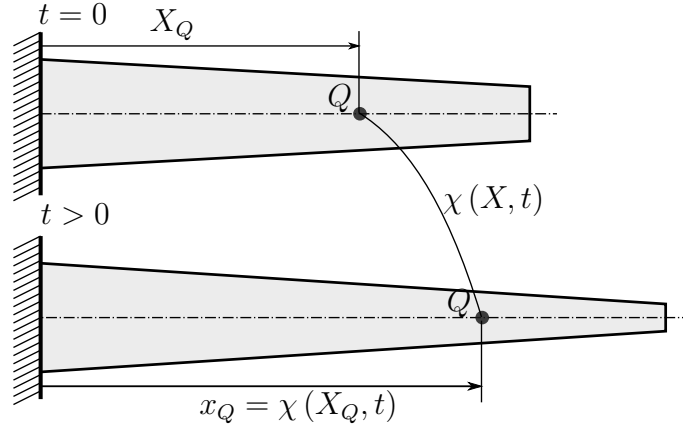


Figure 3.1: Rod model for uniaxial stress state.

corresponding to the stress normal to the cross-section of the rod. Ignoring second order terms, the linear momentum balance for a differential rod element leads to

$$\frac{\partial}{\partial X} (P\mathcal{A}) = \rho_0 \mathcal{A} \frac{\partial^2 \chi}{\partial t^2}.$$

Considering the nonlinear viscoelastic material model introduced in §2.4 and introducing the displacement field  $u(X, t) := \chi(X, t) - X$ , the governing equations for the present model, in terms of quantities defined in the reference configuration, can be written as follows:

$$\left\{ \begin{array}{l} \frac{\partial}{\partial X} (P\mathcal{A}) = \rho_0 \mathcal{A} \frac{\partial^2 u}{\partial t^2} \\ \frac{\partial^2 u}{\partial X \partial t} = -\kappa g(\lambda)^{-2} [f(\lambda) - P] \\ \lambda = \frac{\partial u}{\partial X} + 1, \end{array} \right. \quad (3.1)$$

where

$$\begin{aligned} f(\lambda) &:= \frac{d\Psi}{d\lambda} \\ g(\lambda) &:= \frac{d^2\Psi}{d\lambda^2} = \frac{df}{d\lambda}, \end{aligned} \quad (3.2)$$

and  $\kappa$  is the relaxation modulus. In addition, a set of boundary conditions and initial conditions need to be supplied for the problem. In the present chapter, a rod with uniform cross-section  $\mathcal{A}(X) = \mathcal{A}_0$  is studied, whereas in Chapter 4, different rod shapes are considered through different choices of  $\mathcal{A}(X)$ .

### 3.2 Rod with Uniform Cross-Section

In the particular case in which the cross-section is constant along the rod, that is to say  $\mathcal{A}(X) = \mathcal{A}_0$ , Eq. (3.1) leads to

$$\frac{\partial P}{\partial X} = \rho_0 \frac{\partial^2 u}{\partial t^2} \quad (3.3a)$$

$$P = \frac{1}{\kappa} g(\lambda)^2 \frac{\partial u}{\partial t \partial X} + f(\lambda) \quad (3.3b)$$

$$\lambda = \frac{\partial u}{\partial X} + 1. \quad (3.3c)$$

Equations (3.3) together with Eq. (3.2) are the focus of attention of this chapter. The analyses that follow build up in complexity, starting with the analysis of the system with the linearized viscoelastic material model, and finalizing with the study of the fully nonlinear system by the means of numerical simulations.

### 3.3 Linear Viscoelastic Material Case

In order to simplify the analysis and to obtain insights into the characteristics of stress waves propagating in systems described by Eqs. (3.2) and (3.3), the system with linearized material behavior is analyzed first. Linear analysis results helpful for understanding the propagation of small amplitude waves, and sometimes can be

used to explain certain nonlinear behavior.

For small deformations; that is to say  $\lambda \approx 1$ , the following Taylor's expansions are constructed:

$$\Psi(\lambda) = \sum_{n \geq 0}^{N-3} \frac{\mu_n}{(n+2)!} (\lambda-1)^{n+2} + \mathcal{O}\left((\lambda-1)^N\right), \quad (3.4)$$

$$f(\lambda) := \frac{d\Psi}{d\lambda} = \sum_{n \geq 0}^{N-2} \frac{\mu_n}{(n+1)!} (\lambda-1)^{n+1} + \mathcal{O}\left((\lambda-1)^N\right), \quad (3.5)$$

$$g(\lambda) := \frac{d^2\Psi}{d\lambda^2} = \sum_{n \geq 0}^{N-1} \frac{\mu_n}{n!} (\lambda-1)^n + \mathcal{O}\left((\lambda-1)^N\right), \quad (3.6)$$

where  $N \geq 3$  and the coefficients  $\mu_n$  are defined as follows

$$\mu_n := \left. \frac{d^{n+2}\Psi}{d\lambda^{n+2}} \right|_{\lambda=1}. \quad (3.7)$$

It can be shown that the Taylor expansion of the nonlinear viscoelastic constitutive equation (3.3b) is given by

$$\begin{aligned} P = & \mu_0 (\lambda - 1) + \frac{\mu_0^2}{\kappa} \dot{\lambda} \\ & + \frac{1}{2} \mu_1 (\lambda - 1) \left( (\lambda - 1) + 4 \frac{\mu_0}{\kappa} \dot{\lambda} \right) + \mathcal{O}\left((\lambda - 1)^3, \dot{\lambda}^i (\lambda - 1)^{3-i}\right). \end{aligned} \quad (3.8)$$

with  $2 \leq i \leq 3$ . Keeping only the linear terms in the stretch  $\lambda$  and the stretch rate  $\dot{\lambda}$ , the resulting linearized viscoelastic constitutive equation becomes

$$P = \mu_0 (\lambda - 1) + \frac{\mu_0^2}{\kappa} \dot{\lambda}. \quad (3.9)$$

The same linear constitutive equation (3.9) is arrived at if a quadratic strain energy function  $\Psi = \frac{1}{2} \mu_0 (\lambda - 1)^2$  is selected in Eq. (2.25). Equation (3.9) is nothing but the equation for a Kelvin–Voigt material, which is usually visualized, or interpreted, as a spring in parallel with a dashpot.

If the stress (the control)  $P(X, t)$  at a material point  $X$  is known as a function of time, then it can be shown that Eq. (3.9) is equivalent to the following integral from

$$\lambda(X, t) = \frac{\kappa}{\mu_0^2} \int_0^t e^{-\frac{\kappa}{\mu_0}(t-\tau)} P(X, \tau) d\tau + (\lambda(X, 0) - 1) e^{-\frac{\kappa}{\mu_0}t} + 1. \quad (3.10)$$

From Eq. (3.10) it is observed that the constant  $\mathcal{T}_d := \mu_0/\kappa$  represents a “relaxation” time. It represents a time-lapse during which dissipative effects are significant.

Combining Eqs. (3.3a), (3.3c) and (3.9), the following partial differential equation (PDE) is obtained:

$$c_0^2 \mathcal{T}_d \frac{\partial^3 u}{\partial X^2 \partial t} + c_0^2 \frac{\partial^2 u}{\partial X^2} = \frac{\partial^2 u}{\partial t^2}, \quad (3.11)$$

where  $c_0 = \sqrt{\mu_0/\rho_0}$  is the phase speed of purely elastic waves. Equation (3.11) can be classified as a parabolic–hyperbolic PDE.

### 3.3.1 Scaling of Variables

In this section a scaling of the variables appearing in Eq. (3.11) is sought. In order to perform the scaling, yet unspecified characteristic length  $L_C$  and time  $T_C$  variables are selected; and the following non–dimensional variables are defined,

$$\xi := \frac{X}{L_C} \quad \tau := \frac{t}{T_C} \quad v(\xi, \tau) := \frac{u(\xi L_C, \tau T_C)}{L_C}.$$

Introducing the new variables into Eq. (3.11), and choosing  $L_C/T_C = c_0^2$  yields the following equation:

$$c_0 \frac{\mathcal{T}_d}{L_C} \frac{\partial^3 v}{\partial \xi^2 \partial \tau} + \frac{\partial^2 v}{\partial \xi^2} = \frac{\partial^2 v}{\partial \tau^2}.$$

If a physical length  $L$  is considered to be the characteristic length of the problem, then this choice yields the following non-dimensional governing PDE:

$$\alpha \frac{\partial^3 v}{\partial \xi^2 \partial \tau} + \frac{\partial^2 v}{\partial \xi^2} = \frac{\partial^2 v}{\partial \tau^2}, \quad (3.12)$$

where

$$\alpha := \frac{\mathcal{T}_d c_0}{L} = \frac{\mu_0 / \kappa}{L / c_0}. \quad (3.13)$$

The parameter  $\alpha$  is interpreted as the ratio between the characteristic dissipation time  $\mathcal{T}_d$ , and the characteristic propagation time  $T_w = L/c_0$ . Another interpretation of  $\alpha$  is the ratio between the physical length  $L$  and the length  $c_0 \mathcal{T}_d$  travelled by the wave during a unit of relaxation time  $\mathcal{T}_d$ . Equation (3.12), is sometimes referred to as the strongly damped wave equation; it has been studied by Neves (2000), for example.

The non-dimensional constitutive equation is explored next. A characteristic stress  $P_C = \mu_0$  is chosen, and the non-dimensional stress  $P^* := P/P_C$  is defined. From Eq. (3.9) with  $\lambda = \partial v / \partial \xi - 1$ , it can be shown that

$$P^* = \frac{\partial v}{\partial \xi} + \alpha \frac{\partial^2 v}{\partial \xi \partial \tau}. \quad (3.14)$$

### 3.4 Linear Viscoelastic Rod with Weak Dissipation: Asymptotic Analysis

In order to gain insights into the longitudinal wave propagation phenomenon on viscoelastic materials, asymptotic solutions of Eq. (3.12), for rods of infinite length ( $0 \leq \xi < +\infty$ ), are pursued first.

To that purpose, a small parameter  $\epsilon \ll 1$  is introduced, and the damping parameter is rescaled as  $\alpha = \epsilon\vartheta$ , where  $\vartheta = \mathcal{O}(1)$ . Initial displacement and velocity conditions, and different types of boundary conditions at  $\xi = 0$  are considered. Asymptotic solutions of the following problem are sought

$$\epsilon\vartheta \frac{\partial^3 v}{\partial \xi^2 \partial \tau} + \frac{\partial^2 v}{\partial \xi^2} = \frac{\partial^2 v}{\partial \tau^2} \quad \text{for } 0 < \xi < +\infty, \tau > 0; \quad (3.15)$$

with initial conditions

$$v(\xi, \tau)|_{\tau=0} = \phi(\xi) \quad \frac{\partial v}{\partial \tau}(\xi, \tau)|_{\tau=0} = \psi(\xi), \quad (3.16)$$

where  $\phi(\xi)$ ,  $\psi(\xi)$  are known functions with  $\phi(0) = \psi(0) = 0$ . The particular boundary condition at  $\xi = 0$  is specified in the following sections. In §3.4.1, a displacement boundary condition at  $\xi = 0$  is imposed. In §3.4.2, a force boundary condition at  $\xi = 0$  is utilized. Since the rod is infinite, an additional regularity condition,  $|v(\xi, \tau)| < \infty$  is required.

In order to perform the asymptotic analysis, the method of multiple scales is employed (Nayfeh and Mook, 2008). In the context of this method, the fast spatial scale  $X_0 := \xi$  and the fast time scale  $T_0 := \tau$  are defined. Additionally, a slow time scale  $T_1 := \epsilon\tau$  is introduced to capture the slowly varying dissipation process. The new variable  $T_1$  is considered independent from  $T_0$ . When deemed convenient, the following fast scales are introduced as replacement of  $X_0$  and  $T_0$

$$s_1 := \xi - \tau = X_0 - T_0 \quad s_2 := \xi + \tau = X_0 + T_0. \quad (3.17)$$

In addition, the notation  $(\sim)$  to indicate functions of the variables  $s_1$  and  $s_2$ , is

employed according to the following rule:

$$\check{\mathbf{g}}(s_1, s_2, \cdot) = \mathbf{g}(\check{X}_0(s_1, s_2), \check{T}_0(s_1, s_2), \cdot), \quad (3.18)$$

where

$$\check{X}_0(s_1, s_2) = \frac{s_1 + s_2}{2} \quad \check{T}_0(s_1, s_2) = \frac{s_1 - s_2}{2}. \quad (3.19)$$

In terms of the new independent variables, the time and spatial derivatives become

$$\frac{\partial}{\partial \tau} = \frac{\partial}{\partial T_0} + \epsilon \frac{\partial}{\partial T_1} = -\frac{\partial}{\partial s_1} + \frac{\partial}{\partial s_2} + \epsilon \frac{\partial}{\partial T_1}, \quad (3.20a)$$

$$\frac{\partial^2}{\partial \tau^2} = \frac{\partial^2}{\partial T_0^2} + 2\epsilon \frac{\partial^2}{\partial T_0 \partial T_1} + \epsilon^2 \frac{\partial^2}{\partial T_1^2}, \quad (3.20b)$$

$$\frac{\partial^2}{\partial \tau^2} = \frac{\partial^2}{\partial s_1^2} - 2\frac{\partial^2}{\partial s_1 \partial s_2} + \frac{\partial^2}{\partial s_2^2} + \epsilon^2 \frac{\partial^2}{\partial T_1^2} + 2\epsilon \frac{\partial}{\partial T_1} \left( -\frac{\partial}{\partial s_1} + \frac{\partial}{\partial s_2} \right), \quad (3.20c)$$

and

$$\frac{\partial}{\partial \xi} = \frac{\partial}{\partial X_0} = \frac{\partial}{\partial s_1} + \frac{\partial}{\partial s_2}, \quad (3.21a)$$

$$\frac{\partial^2}{\partial \xi^2} = \frac{\partial^2}{\partial X_0^2} = \frac{\partial^2}{\partial s_1^2} + \frac{\partial^2}{\partial s_2^2} + 2\frac{\partial^2}{\partial s_1 \partial s_2}. \quad (3.21b)$$

An asymptotic solution of the following form is pursued

$$v(\xi, \tau; \epsilon) = v_0(X_0, T_0, T_1) + \epsilon v_1(X_0, T_0, T_1) + \mathcal{O}(\epsilon^2) \Big|_{\substack{X_0=\xi \\ T_0=\tau \\ T_1=\epsilon\tau}}; \quad (3.22)$$

or equivalently,

$$v(\xi, \tau; \epsilon) = \check{v}_0(s_1, s_2, T_1) + \epsilon \check{v}_1(s_1, s_2, T_1) + \mathcal{O}(\epsilon^2) \Big|_{\substack{s_1=\xi+\tau \\ s_2=\xi-\tau \\ T_1=\epsilon\tau}}. \quad (3.23)$$

Introducing Eqs. (3.20) through (3.22) into Eq. (3.15), and equating coefficients of

like powers of  $\epsilon$  yields

$$\mathcal{O}(\epsilon^0) : \quad \frac{\partial^2 v_0}{\partial X_0^2} - \frac{\partial^2 v_0}{\partial T_0^2} = 0, \quad (3.24)$$

$$\mathcal{O}(\epsilon^1) : \quad \frac{\partial^2 v_1}{\partial X_0^2} - \frac{\partial^2 v_1}{\partial T_0^2} = 2\frac{\partial^2 v_0}{\partial T_0 \partial T_1} - \vartheta \frac{\partial^3 v_0}{\partial T_0 \partial X_0^2}. \quad (3.25)$$

Similarly, the initial conditions become

$$\mathcal{O}(\epsilon^0) : \quad v_0(X_0, 0, 0) = \phi(X_0), \quad \frac{\partial v_0}{\partial T_0}(X_0, 0, 0) = \psi(X_0), \quad (3.26)$$

$$\mathcal{O}(\epsilon^1) : \quad v_1(X_0, 0, 0) = 0, \quad \frac{\partial v_0}{\partial T_1}(X_0, 0, 0) + \frac{\partial v_1}{\partial T_0}(X_0, 0, 0) = 0. \quad (3.27)$$

Introducing the variables  $s_1$  and  $s_2$  according to (3.17), using the definition (3.18)

and the expressions (3.20) and (3.21), Eq. (3.24) can be expressed as

$$\frac{\partial^2 \check{v}_0}{\partial s_1 \partial s_2} = 0. \quad (3.28)$$

The general solution  $\check{v}_0(s_1, s_2, T_1)$  is given by d'Alembert's formula in the following form

$$\check{v}_0(s_1, s_2, T_1) = \check{F}_0(s_1, T_1) + \check{G}_0(s_2, T_1), \quad (3.29)$$

where  $\check{F}_0(s_1, T_1)$  and  $\check{G}_0(s_2, T_1)$  are arbitrary functions to be obtained from the initial conditions and from the boundary condition.

Similarly, employing the variables  $s_1$  and  $s_2$ , and using the result (3.29), Eq. (3.25) can be rewritten as

$$4 \frac{\partial^2 \check{v}_1}{\partial s_1 \partial s_2} = 2 \frac{\partial}{\partial T_1} \left( -\frac{\partial \check{F}_0}{\partial s_1} + \frac{\partial \check{G}_0}{\partial s_2} \right) - \vartheta \left( -\frac{\partial^3 \check{F}_0}{\partial s_1^3} + \frac{\partial^3 \check{G}_0}{\partial s_2^3} \right). \quad (3.30)$$

Integrating Eq. (3.30) with respect to  $s_1$  and  $s_2$  results in

$$\begin{aligned} 2\check{v}_1(s_1, s_2, T_1) &= \left( -\frac{\partial \check{F}_0}{\partial T_1} + \frac{1}{2} \vartheta \frac{\partial^2 \check{F}_0}{\partial s_1^2} \right) s_2 + \left( \frac{\partial \check{G}_0}{\partial T_1} - \frac{1}{2} \vartheta \frac{\partial^2 \check{G}_0}{\partial s_2^2} \right) s_1 \\ &+ \check{F}_1(s_1, T_1) + \check{G}_1(s_2, T_1). \end{aligned} \quad (3.31)$$

It is observed that  $\check{v}_1$  grows unbounded as  $s_1 \rightarrow \infty$  and  $s_2 \rightarrow \infty$  unless the secular

terms in the right-hand-side (RHS) of Eq. (3.31) are eliminated by requiring that

$$\frac{\partial \check{F}_0}{\partial T_1} - \frac{1}{2} \vartheta \frac{\partial^2 \check{F}_0}{\partial s_1^2} = 0 \quad \text{for } -\infty < s_1 < +\infty, \quad (3.32)$$

$$\frac{\partial \check{G}_0}{\partial T_1} - \frac{1}{2} \vartheta \frac{\partial^2 \check{G}_0}{\partial s_2^2} = 0 \quad \text{for } 0 \leq s_2 < +\infty. \quad (3.33)$$

From Eq. (3.32), it is observed that  $\check{F}_0(s_1, T_1)$  solves the heat equation for  $T_1 > 0$  and  $s_1 \in \mathbb{R}$ , subjected to initial condition  $\check{F}_0(s_1, T_1 = 0)$ . Since the domain in  $s_1$  is the real line, no boundary conditions are needed to determine  $\check{F}_0$ . The solution for  $\check{F}_0$  is given by (Evans, 2010)

$$\check{F}_0(s_1, T_1) = \int_{-\infty}^{+\infty} \Phi(s_1 - y, T_1) \check{F}_0(y, T_1 = 0) dy, \quad (3.34)$$

where  $\Phi(x, t)$  is the *heat kernel* in  $\mathbb{R}$  for diffusivity equal to  $\vartheta/2$

$$\Phi(x, t) = \frac{1}{\sqrt{2\pi\vartheta t}} e^{-\frac{x^2}{2\vartheta t}}. \quad (3.35)$$

On the other hand, from Eq. (3.33)  $\check{G}_0(s_2, T_1)$  solves the heat equation for  $T_1 > 0$  and  $s_2 > 0$ , subjected to initial condition  $\check{G}_0(s_2, T_1 = 0)$ . Since the domain of  $s_2$  is the non-negative real line, a boundary condition at  $s_2 = 0$  needs to be specified. The type of boundary condition for  $\check{G}_0$  depends on the type of boundary condition specified at  $\xi = 0$ . In consequence, the explicit solution formula for  $\check{G}_0$  is deferred to the following sections when specific boundary conditions are considered.

It is observed that in order to obtain  $\check{F}_0(s_1, T_1)$  and  $\check{G}_0(s_2, T_1)$ , the expressions of  $\check{F}_0(s_1, T_1 = 0)$  and  $\check{G}_0(s_2, T_1 = 0)$  are required. These expressions will be produced by evaluating the boundary and initial conditions in Eq. (3.29).

### 3.4.1 Semi-Infinite Linear Viscoelastic Rod with Prescribed Displacement

In this section, an asymptotic solution is pursued for Eqs. (3.15) with initial conditions (3.16) and with a displacement boundary condition at  $\xi = 0$  defined as

$$v(\xi = 0, \tau) = \mu(\tau), \quad (3.36)$$

where  $\mu(\tau)$  is a given function, with  $\mu(0) = 0$  and  $\mu'(0) = 0$ . Introducing Eq. (3.22) into (3.36), and collecting terms of equal powers of  $\epsilon$  yields the following result

$$\mathcal{O}(\epsilon^0) : \quad v_0(X_0 = 0, T_0, T_1) = \mu(T_0), \quad (3.37)$$

$$\mathcal{O}(\epsilon^1) : \quad v_i(X_0 = 0, T_0, T_1) = 0 \quad \forall i > 0. \quad (3.38)$$

Applying Eq. (3.37) to expression (3.29) yields

$$\check{v}_0(s_1 = -T_0, s_2 = T_0, T_1) = \check{F}_0(-T_0, T_1) + \check{G}_0(T_0, T_1) = \mu(T_0). \quad (3.39)$$

From the previous expression, the boundary condition for  $\check{G}_0$  at  $s_2 = 0$  is generated in the following form:

$$\check{G}_0(s_2 = 0, T_1) = \mu(0) - \check{F}_0(s_1 = 0, T_1) = -\check{F}_0(s_1 = 0, T_1). \quad (3.40)$$

However, since  $s_2 \geq 0$ ,  $s_2 = 0$  implies that  $X_0 = -T_0 = 0$ , which in turns implies  $T_1 = 0$ . Therefore, Eq. (3.40) implies that

$$\check{G}_0(s_2 = 0, T_1) = \check{G}_0(s_2 = 0, T_1 = 0) = -\check{F}_0(s_1 = 0, T_1 = 0). \quad (3.41)$$

It can be shown (Evans, 2010) that the solution for  $\check{G}_0(s_2, T_1)$  subjected to initial conditions  $\check{G}_0(s_2, T_1 = 0)$  and boundary condition (3.41) is given by

$$\begin{aligned} \check{G}_0(s_2, T_1) &= \int_0^{+\infty} [\Phi(s_2 - y, T_1) - \Phi(s_2 + y, T_1)] \check{G}_0(y, T_1 = 0) dy \\ &+ \int_0^{T_1} \frac{s_2}{T_1 - y} \Phi(s_2, T_1 - y) \check{G}_0(s_2 = 0, y) dy. \end{aligned} \quad (3.42)$$

In what follows, the explicit expressions for  $\check{F}_0(s_1, T_1 = 0)$  and  $\check{G}_0(s_2, T_1 = 0)$  are obtained. To do so, the explicit solution of Eq. (3.24) with initial condition (3.26) and with boundary condition (3.37) is obtained next. A solution of the following form is assumed

$$v_0(X_0, T_0, T_1) = w(X_0, T_0, T_1) + m(X_0, T_0, T_1), \quad (3.43)$$

where  $w(X_0, T_0, T_1)$  satisfies Eq. (3.24) with initial conditions (3.26) and homogeneous boundary condition at  $X_0 = 0$ ; and  $m(X_0, T_0, T_1)$  satisfies Eq. (3.24) with boundary condition (3.37) at  $X_0 = 0$  and zero initial conditions. Using the results (B.4) and (B.8) from Appendix B, it can be shown that

$$\check{F}_0(s_1, T_1 = 0) = W_1(s_1) u(s_1) + W_3(s_1) u(-s_1) + \mu(-s_1) u(-s_1), \quad (3.44)$$

$$\check{G}_0(s_2, T_1 = 0) = W_2(s_2), \quad (3.45)$$

where  $W_1$ ,  $W_2$  and  $W_3$  were defined in Eq. (B.5). Substituting Eq. (3.44) into Eq. (3.34) yields

$$\begin{aligned} \check{F}_0(s_1, T_1) &= \int_0^{+\infty} \Phi(s_1 - y, T_1) W_1(y) dy \\ &+ \int_{-\infty}^0 \Phi(s_1 - y, T_1) [W_3(y) + \mu(-y)] dy. \end{aligned} \quad (3.46)$$

Substituting Eq. (B.5) into Eq. (3.46), and operating on the integrals results in

$$\begin{aligned} \check{F}_0(s_1, T_1) = & \frac{1}{2} \int_0^{+\infty} [\Phi(s_1 - y, T_1) - \Phi(s_1 + y, T_1)] \phi(y) dy \\ & - \frac{1}{2} \int_0^{+\infty} \left\{ [\Phi(s_1 - y, T_1) + \Phi(s_1 + y, T_1)] \int_0^y \psi(s) ds \right\} dy \\ & + \int_0^{+\infty} \Phi(s_1 + y, T_1) \mu(y) dy. \end{aligned} \quad (3.47)$$

From Eq. (3.44), using the definitions of  $W_1$ ,  $W_2$  and  $W_3$  from Eq. (B.5), and recalling that  $\phi(0) = 0$  and  $\mu(0) = 0$ , the following result is obtained

$$\check{G}_0(s_2 = 0, T_1) = -\check{F}_0(s_1 = 0, T_1 = 0) = 0. \quad (3.48)$$

Introducing Eqs. (3.45), (B.5) and (3.48) into Eq. (3.42), and operating on the integrals yields the following result:

$$\begin{aligned} \check{G}_0(s_2, T_1) = & \frac{1}{2} \int_0^{+\infty} [\Phi(s_2 - y, T_1) - \Phi(s_2 + y, T_1)] \phi(y) dy \\ & + \frac{1}{2} \int_0^{+\infty} \left\{ [\Phi(s_2 - y, T_1) - \Phi(s_2 + y, T_1)] \int_0^y \psi(s) ds \right\} dy. \end{aligned} \quad (3.49)$$

Finally, the solution for  $\check{v}_0(s_1, s_2, T_1)$  is obtained by substituting Eqs. (3.47) and (3.49) into Eq. (3.29).

It is observed from Eqs. (3.47) and (3.49) that the main features of the solution is a propagating pulse composed of  $\phi(y)$  and  $\int_0^y \psi(s) ds$  that splits into two parts, one traveling to the right, and the other to the left. The second part of the wave pulse will reflect off the boundary at  $X_0 = \xi = 0$ . Each pulse suffers viscous diffusion controlled by the heat kernel  $\Phi$  as they travel. Therefore, the amplitude of the wave pulse progressively decreases as it travels.

### 3.4.1.1 Stress–Wave Solution for Linear Viscoelastic Rod Initially at Rest

The results in Eqs. (3.47) and (3.49) can be simplified if the initial conditions are set to zero,  $\phi = \psi = 0$ . In this way, only waves generated at the boundary  $\xi = 0$  are considered. In order to study the stress waves, the zero–th order stress solution is computed as follows:

$$\check{P}^*(s_1, T_1) \sim \frac{\partial \check{v}_0}{\partial s_1} + \frac{\partial \check{v}_0}{\partial s_2} = \frac{\partial \check{F}_0}{\partial s_1} + \frac{\partial \check{G}_0}{\partial s_2}. \quad (3.50)$$

Thus, the following result is obtained upon using Eqs. (3.47) and (3.49) with  $\phi = \psi = 0$ ,

$$\check{P}^*(s_1, s_2, T_1) \sim - \int_0^{+\infty} \frac{s_1 + y}{\vartheta T_1} \Phi(s_1 + y, T_1) \mu(y) dy. \quad (3.51)$$

Expression (3.51) will be analyzed in §3.8.2 when the case of a nonlinear viscoelastic rod is treated.

### 3.4.2 Semi–Infinite Linear Viscoelastic Rod with Prescribed Stress

In this section, an asymptotic solution of Eq. (3.15) with initial conditions (3.16) and with a force boundary condition at  $\xi = 0$  is pursued. The boundary condition is given by

$$P^*(\xi = 0, \tau) = \frac{\partial v}{\partial \xi} + \alpha \frac{\partial^2 v}{\partial \tau \partial \xi} \Big|_{\xi=0} = \varrho(\tau), \quad (3.52)$$

where  $\varrho(\tau)$  is a given function with  $\varrho(0) = 0$  and  $\varrho'(0) = 0$ . For this particular case, it is also required that  $\phi'(0) = \psi'(0) = 0$ . Introducing Eq. (3.22) into (3.52)

and collecting terms of equal powers of  $\epsilon$  yields the following:

$$\mathcal{O}(\epsilon^0) : \quad \left. \frac{\partial v_0}{\partial X_0} \right|_{X_0=0} = \varrho(T_0) \quad (3.53)$$

$$\mathcal{O}(\epsilon^1) : \quad \left. \frac{\partial v_1}{\partial X_0} + \vartheta \frac{\partial^2 v_0}{\partial X_0 \partial T_0} \right|_{X_0=0} = 0. \quad (3.54)$$

Upon applying the boundary condition (3.53) at  $X_0 = 0$  to Eq. (3.29) the following result is obtained:

$$\left. \frac{\partial \check{v}_0}{\partial s_1} + \frac{\partial \check{v}_0}{\partial s_2} \right|_{\substack{s_1=-T_0 \\ s_2=T_0}} = \frac{\partial \check{F}_0}{\partial s_1}(-T_0, T_1) + \frac{\partial \check{G}_0}{\partial s_2}(T_0, T_1) = \varrho(T_0). \quad (3.55)$$

From the previous expression, the boundary condition for  $\check{G}_0$  at  $s_2 = 0$  is generated in the form

$$\frac{\partial \check{G}_0}{\partial s_2}(s_2 = 0, T_1) = \varrho(0) - \frac{\partial \check{F}_0}{\partial s_1}(s_1 = 0, T_1) = -\frac{\partial \check{F}_0}{\partial s_1}(s_1 = 0, T_1). \quad (3.56)$$

Using the same reasoning preceding Eq. (3.41), it is concluded that

$$\frac{\partial \check{G}_0}{\partial s_2}(s_2 = 0, T_1) = \frac{\partial \check{G}_0}{\partial s_2}(s_2 = 0, T_1 = 0) = -\frac{\partial \check{F}_0}{\partial s_1}(s_1 = 0, T_1 = 0) \quad (3.57)$$

It can be shown (Evans, 2010) that the solution for  $\check{G}_0(s_2, T_1)$  subjected to initial condition  $\check{G}_0(s_2, T_1 = 0)$  and boundary condition (3.57) is given by

$$\begin{aligned} \check{G}_0(s_2, T_1) = & \check{G}_0(s_2 = 0, T_1) + \int_0^{+\infty} [\Phi(s_2 - y, T_1) + \Phi(s_2 + y, T_1)] \check{G}_0(y, T_1 = 0) dy \\ & + \int_0^{s_2} \left[ \int_0^{T_1} \frac{s}{T_1 - y} \Phi(s, T_1 - y) \frac{\partial}{\partial s} \check{G}_0(s_2 = 0, y) dy \right] ds, \end{aligned} \quad (3.58)$$

where again, from Eq. (3.41),  $\check{G}_0(s_2 = 0, T_1) = \check{G}_0(s_2 = 0, T_1 = 0)$ .

Similar to the procedure presented in §3.4.1, the explicit expressions of  $\check{F}_0(s_1, T_1 = 0)$  and  $\check{G}_0(s_2, T_1 = 0)$  are needed. In consequence, a solution of Eq. (3.24) in the form

of Eq. (3.43) is sought

$$v_0(X_0, T_0, T_1) = w(X_0, T_0, T_1) + m(X_0, T_0, T_1), \quad (3.59)$$

where  $w(X_0, T_0, T_1)$  satisfies Eq. (3.24) with initial conditions (3.26) and homogeneous Neumann boundary condition  $\partial v_0/\partial X_0 = 0$  at  $X_0 = 0$ , and  $m(X_0, T_0, T_1)$  satisfies Eq. (3.24) with Neumann boundary condition (3.53) at  $X_0 = 0$  and zero initial conditions. Using the results (B.13) and (B.16) from Appendix B, it can be shown that

$$\check{F}_0(s_1, 0) = W_1(s_1)u(s_1) + W_2(-s_1)u(-s_1) - u(-s_1) \int_0^{-s_1} \varrho(s) ds, \quad (3.60)$$

$$\check{G}_0(s_2, 0) = W_2(s_2), \quad (3.61)$$

where  $W_1$  and  $W_2$  are defined in Eq. (B.5). Introducing Eq. (3.60) into Eq. (3.34) results in

$$\begin{aligned} \check{F}_0(s_1, T_1) &= \int_0^{+\infty} \Phi(s_1 - y, T_1) W_1(y) dy \\ &+ \int_{-\infty}^0 \Phi(s_1 - y, T_1) \left[ W_2(-y) - \int_0^{-y} \varrho(s) ds \right] dy. \end{aligned} \quad (3.62)$$

Using expressions (B.5), and after some manipulations, the following final result is obtained:

$$\begin{aligned} \check{F}_0(s_1, T_1) &= \frac{1}{2} \int_0^{+\infty} [\Phi(s_1 - y, T_1) + \Phi(s_1 + y, T_1)] \phi(y) dy \\ &+ \frac{1}{2} \int_0^{+\infty} \left\{ [\Phi(s_1 + y, T_1) - \Phi(s_1 - y, T_1)] \int_0^y \psi(s) ds \right\} dy \\ &- \int_0^{+\infty} \left\{ \Phi(s_1 + y, T_1) \int_0^y \varrho(s) ds \right\} dy. \end{aligned} \quad (3.63)$$

From Eqs. (3.60), (3.61), and (3.57), using the definitions (B.5), and recalling that  $\varrho(0) = \phi(0) = \psi(0) = 0$  and  $\phi'(0) = 0$ , it is observed that

$$\check{G}_0(s_2 = 0, T_1) = \check{G}_0(s_2 = 0, T_1 = 0) = 0, \quad (3.64)$$

and

$$\frac{\partial \check{G}_0}{\partial s_2}(s_2 = 0, T_1) = -\frac{\partial \check{F}_0}{\partial s_1}(s_1 = 0, T_1 = 0) = 0. \quad (3.65)$$

Introducing Eqs. (3.61), (B.5), (3.64) and (3.65) into Eq. (3.58), and operating on the integrals yields the following result:

$$\begin{aligned} \check{G}_0(s_2, T_1) = & \frac{1}{2} \int_0^{+\infty} [\Phi(s_2 - y, T_1) + \Phi(s_2 + y, T_1)] \phi(y) dy \\ & + \frac{1}{2} \int_0^{+\infty} \left\{ [\Phi(s_2 - y, T_1) + \Phi(s_2 + y, T_1)] \left( \int_0^y \psi(s) ds \right) \right\} dy. \end{aligned} \quad (3.66)$$

Finally, the zero-th order solution  $\check{v}_0(s_1, s_2, T_1)$  is obtained by substituting Eqs. (3.63) and (3.66) into Eq. (3.29).

### 3.4.2.1 Stress-Wave Solution for Linear Viscoelastic Rod Initially at Rest

Here, the case in which the rod is initially at rest, that is to say,  $\phi = \psi = 0$ , is considered. Substitution of Eqs. (3.63) and (3.66) into Eq. (3.50) yields the zero-th order asymptotic approximation of the stress as follows

$$\check{P}^*(s_1, s_2, T_1) \sim \int_0^{+\infty} \frac{s_1 + y}{\vartheta T_1} \Phi(s_1 + y, T_1) \left( \int_0^y \varrho(s) ds \right) dy. \quad (3.67)$$

It is observed that Eq. (3.67) is equivalent to Eq. (3.51) if  $\mu(y)$  is identified with  $-\int_0^y \varrho(s) ds$ .

## 3.5 Dispersion Relation for Semi-Infinite Linear Viscoelastic Rod

The purpose of the following study is to determine how harmonic waves with a particular frequency  $\tilde{\omega}$  are affected by the viscoelastic material properties of the

structure. In particular, the dispersion relation, which dictates how the wave number  $\tilde{k}$  depends on the frequency  $\tilde{\omega}$  is of interest. From the dispersion relation, it is possible to obtain the characteristics of harmonic waves: phase speed and attenuation, as a function of  $\tilde{\omega}$ .

In this section, a semi-infinite rod subjected to a harmonic load applied to the left end,  $P^*(\xi = 0, \tau) = P_0 e^{-i\tilde{\omega}\tau}$  is studied. In order to obtain the dispersion relation, a solution in the following form is assumed,

$$v(\xi, \tau) = V(\xi) e^{-i\tilde{\omega}\tau}. \quad (3.68)$$

On substituting Eq. (3.68) into Eq. (3.12), the result is

$$V'' + \frac{\tilde{\omega}}{1 - i\alpha\tilde{\omega}} V = 0, \quad (3.69)$$

where the primes indicate differentiation with respect to  $\xi$ . The solution of Eq. (3.69) is given by  $V(\xi) = Ae^{-i\tilde{k}\xi} + Be^{i\tilde{k}\xi}$  where  $\tilde{k} \in \mathbb{C}$  is the (complex) wave number, whose dependence on the frequency  $\tilde{\omega}$  is given by the following dispersion relation

$$D(\tilde{k}, \tilde{\omega}) = \frac{\tilde{\omega}^2}{1 - i\alpha\tilde{\omega}} - \tilde{k}^2 = 0. \quad (3.70)$$

The displacement solution is then given by

$$v(\xi, \tau) = Ae^{-i(\tilde{k}\xi + \tilde{\omega}\tau)} + Be^{i(\tilde{k}\xi - \tilde{\omega}\tau)}. \quad (3.71)$$

It is observed that the first term corresponds to a wave traveling to the left, whereas the second term constitutes a wave traveling to the right. Since the rod is semi-infinite ( $\xi \geq 0$ ) and excited at the left end, only right-traveling waves make physical sense in this case. This is due to the fact that there is no source or boundary

at  $\xi = +\infty$  for waves to be generated or reflected to the left. This “boundary condition” at infinity is usually referred to as “radiation condition” (Graff, 1975). This boundary condition implies that  $A = 0$ . The remaining boundary condition at  $\xi = 0$  implies that

$$P^*(\xi = 0, \tau) = \frac{\partial v}{\partial \xi} + \alpha \frac{\partial^2 v}{\partial \xi \partial \tau} \Big|_{\xi=0} = P_0 e^{-i\tilde{\omega}\tau} \Rightarrow B = \frac{P_0}{i\tilde{k}(1 - i\alpha\tilde{\omega})}. \quad (3.72)$$

Now, from Eqs. (3.14) and (3.72) it can be shown that the stress is given by

$$P^*(\xi, \tau) = P_0 e^{i(\tilde{k}\xi - \tilde{\omega}\tau)}. \quad (3.73)$$

From the dispersion relation (3.70), it is observed that the system is dispersive since the wave number depends nonlinearly on the frequency. The wave number is given by

$$\tilde{k} = \sqrt{\frac{\tilde{\omega}^2}{1 + \alpha^2 \tilde{\omega}^2}} \sqrt{1 + i\alpha\tilde{\omega}} = A(\tilde{\omega}) e^{i\frac{\phi(\tilde{\omega})}{2}}, \quad (3.74)$$

where

$$A(\tilde{\omega}) := \frac{\tilde{\omega}}{(1 + \alpha^2 \tilde{\omega}^2)^{\frac{1}{4}}}, \quad \tan \phi(\tilde{\omega}) := \alpha\tilde{\omega} \quad (3.75)$$

were introduced.

The real and imaginary parts of  $\tilde{k}$  are then given by,

$$\tilde{k}_{\text{Re}} = A(\tilde{\omega}) \cos\left(\frac{\phi(\tilde{\omega})}{2}\right), \quad \tilde{k}_{\text{Im}} = A(\tilde{\omega}) \sin\left(\frac{\phi(\tilde{\omega})}{2}\right).$$

Using trigonometric identities, it can be shown that

$$\tilde{k}_{\text{Re}} = \tilde{\omega} \left[ \frac{\sqrt{1 + \alpha^2 \tilde{\omega}^2} + 1}{2(1 + \alpha^2 \tilde{\omega}^2)} \right]^{1/2}, \quad (3.76)$$

$$\tilde{k}_{\text{Im}} = \tilde{\omega} \left[ \frac{\sqrt{1 + \alpha^2 \tilde{\omega}^2} - 1}{2(1 + \alpha^2 \tilde{\omega}^2)} \right]^{1/2}. \quad (3.77)$$

The stress  $P^*(\xi, \tau)$  is therefore given by

$$P^*(\xi, \tau) = P_0 e^{-\tilde{k}_{\text{Im}}\xi} e^{i(\tilde{k}_{\text{Re}}\xi - \tilde{\omega}\tau)}, \quad (3.78)$$

or

$$P^*(\xi, \tau) = P_0 e^{-\tilde{\beta}\xi} e^{i\tilde{k}_{\text{Re}}(\xi - \tilde{c}\tau)}. \quad (3.79)$$

The quantities  $\tilde{c}$  and  $\tilde{\beta}$  are the wave phase speed and attenuation, respectively, and they are functions of the frequency  $\tilde{\omega}$  defined in the following sections.

### 3.5.1 Phase speed

From Eqs. (3.79) and (3.76), the effective non-dimensional phase speed is obtained as,

$$\tilde{c}(\tilde{\omega}) := \frac{\tilde{\omega}}{\tilde{k}_{\text{Re}}} = \sqrt{2} \frac{(1 + \alpha^2 \tilde{\omega}^2)^{\frac{1}{2}}}{(\sqrt{1 + \alpha^2 \tilde{\omega}^2} + 1)^{\frac{1}{2}}}. \quad (3.80)$$

For  $\alpha \neq 0$ , the variable  $\check{\omega} := \alpha\omega$  can be defined. In terms of  $\check{\omega}$  the non-dimensional wave speed results

$$\tilde{c}(\check{\omega}) = \sqrt{2} \frac{(1 + \check{\omega}^2)^{\frac{1}{2}}}{(\sqrt{1 + \check{\omega}^2} + 1)^{\frac{1}{2}}}. \quad (3.81)$$

In Figure 3.2, the non-dimensional wave speed is shown as a function of the non-dimensional frequency  $\check{\omega}$ . It is observed that higher frequencies propagate faster. This fact is a consequence of the dissipative nature of the material.

### 3.5.2 Attenuation

In Eq. (3.79), it is observed that the amplitude of a traveling stress wave is attenuated as it propagates (increasing  $\xi$ ). From Eqs. (3.77) and (3.79) it follows

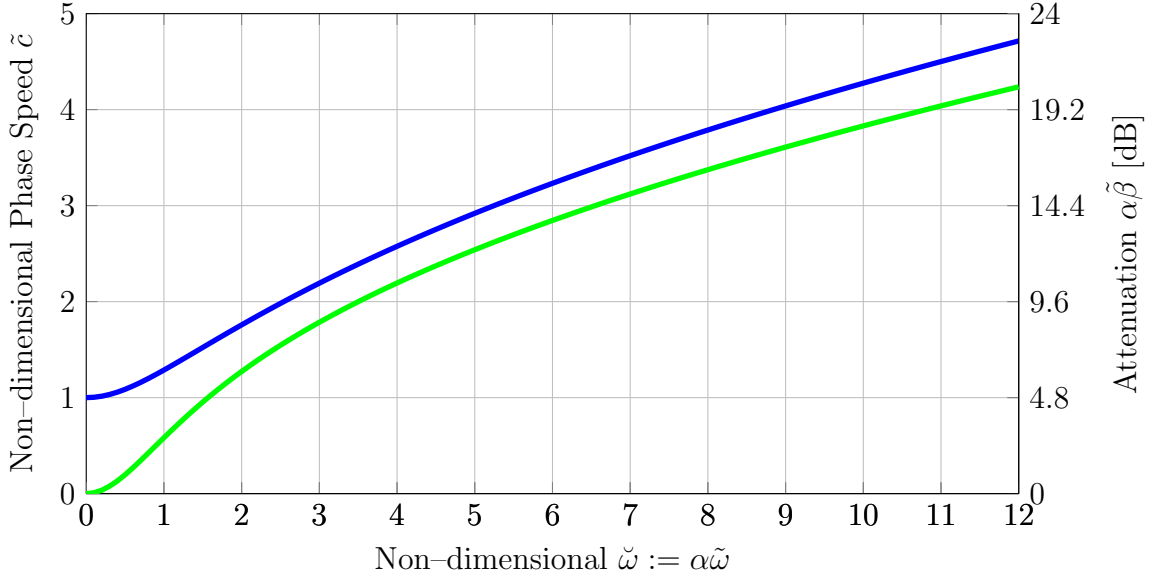


Figure 3.2: Non-dimensional phase speed  $\check{c}$  and attenuation  $\check{\beta}$  as a function of non-dimensional frequency  $\check{\omega}$ . ( — ): Non-dimensional phase speed  $\check{c}$ ; ( — ): Attenuation  $\check{\beta}$ .

that

$$\check{\beta}(\check{\omega}) := \check{k}_{\text{Im}} = \frac{\check{\omega} (\sqrt{1 + \alpha^2 \check{\omega}^2} - 1)^{\frac{1}{2}}}{\sqrt{2} (1 + \alpha^2 \check{\omega}^2)^{\frac{1}{2}}}. \quad (3.82)$$

Introducing the variable  $\check{\omega} := \alpha\omega$  yields

$$\alpha\check{\beta}(\check{\omega}) = \frac{\check{\omega} (\sqrt{1 + \check{\omega}^2} - 1)^{\frac{1}{2}}}{\sqrt{2} (1 + \check{\omega}^2)^{\frac{1}{2}}}. \quad (3.83)$$

In Figure 3.2, the attenuation is shown as a function of the non-dimensional frequency  $\check{\omega}$ . It is observed that higher frequencies are more attenuated than lower frequencies.

### 3.5.2.1 Frequency Bounds for Wave Propagation in Axon Tracts

Axons in the white matter of the brain may be as short 1 mm or less (on the order of the micrometers), whereas other axons, such as those extending from the

cerebral cortex to the sacrum can extend distances of the order of meters (Nolte, 2002). An axon tract is a collection or bundle of aligned axons.

The length of a structure (e.g. an axon tract) and its boundary conditions determine the largest wavelength that the structure can accommodate. Knowledge of this largest wavelength can be used to determine the lowest frequency for which wave propagation is important on the structure. For waves with frequencies below this lowest frequency, dynamic effects (wave propagation) become negligible, as the response of the structure can be considered static.

As it will be shown in §3.6, the largest wavelength for a linear viscoelastic rod of length  $L$  with free–free (or fixed–fixed) ends is  $\lambda_{\max} = 2L$ . For fixed–free ends, the largest wavelength is  $\lambda_{\max} = 4L$ . For a given maximum wavelength  $\lambda_{\max}$ , the corresponding minimum frequency  $\tilde{\omega}_{\min}$  can be obtained from the dispersion relation (3.70) by using the definition of the wavelength as follows:

$$\frac{\alpha}{L} \operatorname{Re} \left[ \tilde{k} \right] = \alpha \frac{2\pi}{\lambda_{\max}}, \quad (3.84)$$

where the relation between the dimensional and non–dimensional wave numbers,  $k = \tilde{k}/L$ , was used. Upon introducing Eq. (3.76) and using the definition of  $\alpha$  and  $\check{\omega} := \alpha\tilde{\omega}$ , the following expression is obtained

$$\check{\omega}_{\min} \left[ \frac{\sqrt{1 + \check{\omega}_{\min}^2} + 1}{2(1 + \check{\omega}_{\min}^2)} \right]^{1/2} = \frac{2\pi\mathcal{T}_d c_0}{\lambda_{\max}}. \quad (3.85)$$

Since the material properties of axons are not well known,  $\mathcal{T}_d$  is left as an extra parameter. The same is true regarding the boundary conditions of axon tracts (and therefore  $\lambda_{\max}$ ). Solving for  $\check{\omega}_{\min}$  from Eq. (3.85) provides a (non–dimensional) lower

frequency bound as a function of  $\mathcal{T}_d$  and  $\lambda_{\max}$ . The dimensional frequency bound is obtained as  $\omega_{\min} = \check{\omega}_{\min}/\mathcal{T}_d$ .

This frequency bound can be used to determine whether or not certain frequency components of explosive blasts pressure waves can produce wave propagation along axon tracts in the brain. The results of this analysis are summarized in Fig. 3.3. For a representative case, an axon tract length of  $L = 10$  mm with fixed-fixed ends is considered. Also, it is assumed that the speed of propagation in axons is  $c_0 = 1557$  m/sec. This value corresponds to the phase speed in brain tissue found by Etoh, Mitaku, Yamamoto, and Okano (1994). In order for this simplified theory to apply, the cross-section of the axon tracts considered needs to be small enough so that shear effects due to changes in the cross-sectional area can be neglected.

In order to determine the blast frequency components analyses such as harmonic wavelet analysis (Newland, 1993) can be carried out. If the frequency (or frequency component) of an incoming wave is above the lower frequency bound of this particular axon tract, then, indeed such wave will be able to travel along the axon tract. For example, a blast frequency component with  $f = 100$  Hz will not produce longitudinal waves along axon tracts with  $L = 10$  mm and shorter, for any value of  $\mathcal{T}_d$ . In contrast, a frequency component with  $f = 1$  MHz will produce propagation of longitudinal stress waves along axon tracts  $L = 10$  mm provided the  $\mathcal{T}_d$  of the axons is small enough. The frequency lower is decreased if the length of the structure increases, or if the end conditions are such that  $\lambda_{\max}$  increases. Knowledge of harmful blast frequency components could potentially allow a better design of protective equipment, especially, designed to target those particular frequency

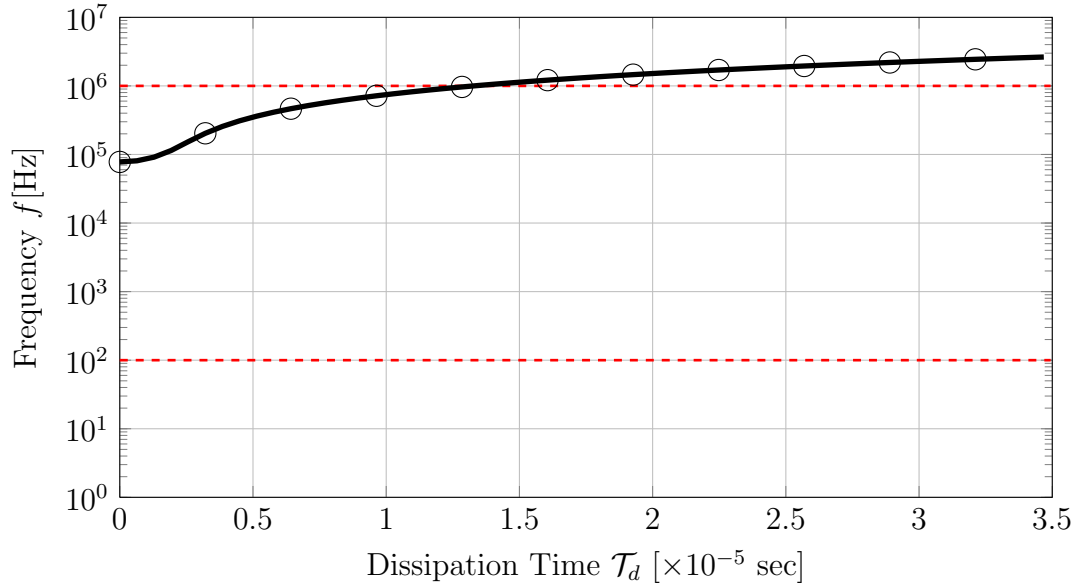


Figure 3.3: Frequency bounds for wave propagation in an axon tract of length  $L = 10$  mm with fixed–fixed ends ( $\lambda_{\max} = 2L$ ). ( - - ): Representative range of blast frequency components; (  $\ominus$  ): Frequency lower bound.

components.

### 3.5.2.2 Brain Tissue “Bulk” Attenuation

The expression of the wave attenuation as a function of frequency, given by Eq. (3.82), can be employed to generate a rough estimate of the relaxation time  $\mathcal{T}_d$ . Studies on the attenuation properties of brain tissue have been reported by Kremkau, Barnes, and McGraw (1981), Etoh *et al.* (1994), and Culjat, Goldenberg, Tewari, and Singh (2010), among others. Kremkau, Barnes, and McGraw (1981) found the propagation speed of ultrasonic waves in human brain tissue to be 1561.6 m/sec at 1MHz and 1565.8 m/sec at 5 MHz.

In this section, Eq. (3.82) is curve–fitted to the experimental data of Etoh

*et al.* (1994) on the attenuation of bovine brain tissue. The parameter  $\mathcal{T}_d = \mu_0/\kappa$  is computed through least squares regression.

Although unrealistic, in this analysis the brain is assumed to be a homogeneous body. Therefore, the present study only provides a bulk estimation for  $\mathcal{T}_d$ , without any consideration regarding the internal structure of the brain tissue. The value of  $c_0 = 1557$  m/sec was used, following the study of Etoh *et al.* (1994).

In Fig. 3.4, a comparison between the experimental measurements of Etoh *et al.* and the theoretical expression (3.82) with curve-fitted parameter  $\mathcal{T}_d$  is shown. The curve-fit has been performed in Matlab with the *lsqcurvefit* function, and the obtained value of the relaxation time is  $\mathcal{T}_d = 2.32 \times 10^{-7}$  msec. It is observed in Fig. 3.4 that the linear model provides a good representation for high frequencies, but under-estimates the attenuation coefficient for lower frequencies. The discrepancies between the model predictions and the experimental measurements can be attributed to the evident geometric simplicity of the model and to the material model employed.

For the obtained value of  $\mathcal{T}_d$  and the range of frequencies considered by Etoh *et al.* (700 kHz – 5 MHz), it is observed that  $\check{\omega} = \alpha\tilde{\omega} = \mathcal{T}_d\omega \ll 1$ ; therefore, the speed of propagation of waves in the brain can be roughly approximated as  $\tilde{c} \approx 1 \Rightarrow c \approx c_0$ . This result implies that brain tissue is weakly dispersive for the range of frequencies considered. In applications related to blast-induced traumatic brain injury, for rapid transient loadings lasting  $\sim 0.001$  msec ( $f=1$  MHz), this linear theory predicts that the viscoelastic properties of the brain tissue will not significantly affect the speed of propagation of stress waves. This conclusion, of

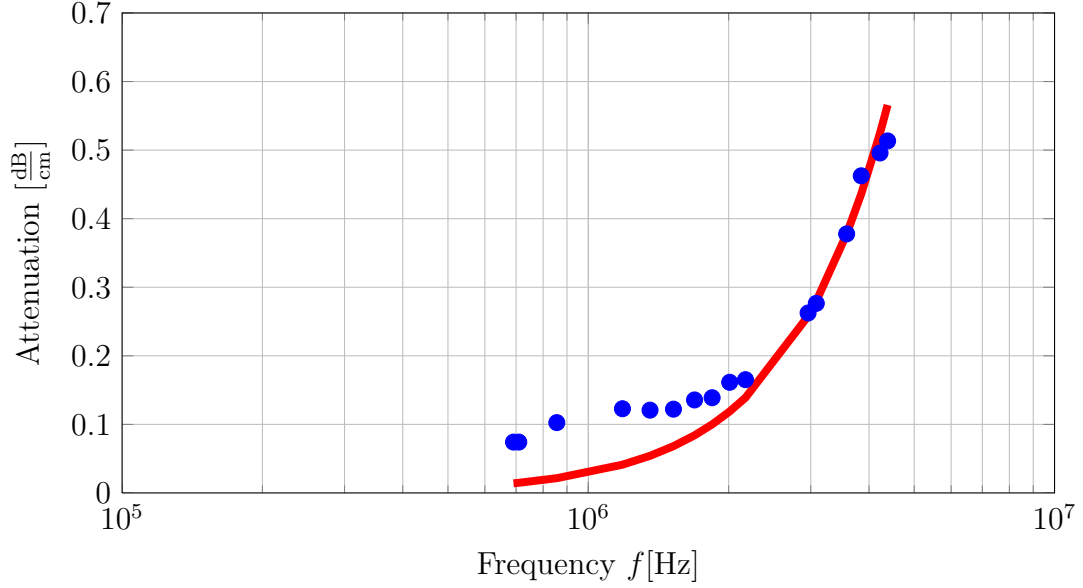


Figure 3.4: Comparison between experimental measurements of attenuation in bovine brain tissue and model (Eq. (3.82)) with curve-fitted parameters  $\mathcal{T}_d = 2.34 \times 10^{-7}$  msec. (●): Experimental measurements (Etoh *et al.*, 1994); (—): Model predictions (GOF=0.89).

course relies on the crude assumptions of the model, and needs to be subjected to further scrutiny.

### 3.6 Longitudinal Standing Waves in Linear Viscoelastic Rods

In this section, the longitudinal standing wave characteristics (mode shapes) of rods with finite length  $L$  are studied. Standing wave characteristics of rods with the following boundary conditions: fixed-fixed, fixed-free and linear Kelvin-Voigt viscoelastic supports are presented next.

Assuming a separable solution of the form  $v(\xi, \tau) = V(\xi)\eta(\tau)$  and replacing it into Eq. (3.12) yields

$$\frac{V''}{V} = \frac{\ddot{\eta}}{\eta + \alpha\dot{\eta}} = -\bar{k}^2, \quad (3.86)$$

where the prime denotes differentiation with respect to  $\xi$  and the dot differentiation with respect to  $\tau$ , and  $\bar{k}$  is the (real) wave number. As in the case of linear elastic rods, the general mode shape solution is given by

$$V(\xi) = A \sin(\bar{k}\xi) + B \cos(\bar{k}\xi). \quad (3.87)$$

In what follows, different boundary conditions are applied to determine the wave number  $\bar{k}$ .

### 3.6.1 Fixed–Fixed Boundary Conditions

In this case, the boundary conditions are given by

$$v(\xi = 0, \tau) = v(\xi = 1, \tau) = 0. \quad (3.88)$$

Applying the boundary conditions (3.88) to Eq. (3.87) yields  $B = 0$ , and in consequence, the mode shapes are given by

$$V(\xi) = \sqrt{2} \sin(\bar{k}\xi), \quad (3.89)$$

where the coefficient  $A = \sqrt{2}$  was chosen to make the mode shapes orthonormal, and the wave numbers are given by

$$\bar{k}_n = n\pi \quad n \in \mathbb{N}. \quad (3.90)$$

The largest wavelength, corresponding to the first vibratory mode is then given by

$$\lambda_{\max} = \frac{2\pi}{\bar{k}_1/L} = 2L. \quad (3.91)$$

### 3.6.2 Fixed–Free Boundary Conditions

In this case, the boundary conditions are given by

$$\begin{aligned} v(0, \tau) &= 0 \\ P^*(1, \tau) \mathcal{A}_0^* &= 0. \end{aligned} \tag{3.92}$$

Applying the boundary conditions (3.92) to Eq. (3.87) results in

$$\begin{aligned} v(0, \tau) = 0 &\Rightarrow B = 0, \\ P^*(1, \tau) \mathcal{A}_0^* = 0 &\Rightarrow V'(1) [\eta(\tau) + \alpha \dot{\eta}(\tau)] = 0 \Rightarrow \cos(\bar{k}) = 0. \end{aligned}$$

Therefore, the wave numbers are given by

$$\bar{k}_n = \frac{2n-1}{2} \pi \quad n \in \mathbb{N}. \tag{3.93}$$

Similar to the fixed-fixed case, the mode shapes for fixed-free boundary conditions are given by

$$V(\xi) = \sqrt{2} \sin(\bar{k}\xi). \tag{3.94}$$

The largest wavelength, corresponding to the first vibratory mode is then given by

$$\lambda_{\max} = \frac{2\pi}{\bar{k}_1/L} = 4L. \tag{3.95}$$

### 3.6.3 Linear Kelvin–Voigt Viscoelastic Supports at Both Ends

This particular case is shown in Fig. 3.5. In this case, the boundary conditions are given by

$$\begin{aligned} P^*(\xi = 0, \tau) \mu_0 \mathcal{A}_0 &= \left[ k_1 L v + d_1 c_0 \frac{\partial v}{\partial \tau} \right]_{\xi=0}, \\ P^*(\xi = 1, \tau) \mu_0 \mathcal{A}_0 &= - \left[ k_2 L v + d_2 c_0 \frac{\partial v}{\partial \tau} \right]_{\xi=1}, \end{aligned} \tag{3.96}$$

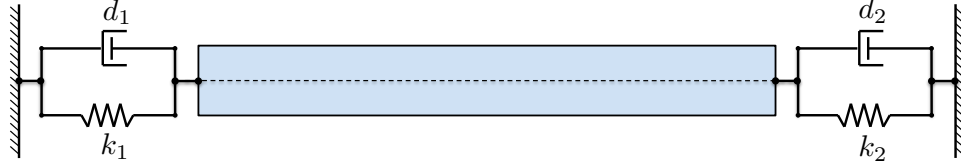


Figure 3.5: Rod with linear Kelvin–Voigt supports at both ends.

where  $k_1$  and  $d_1$ , and  $k_2$  and  $d_2$  are the (dimensional) stiffness and damping coefficient of the supports at the left and right ends, respectively. The stiffness values  $k_1$  and  $k_2$  should not be confused with the wave numbers indicated with the overbar notation.

The quantity  $K_C = \mathcal{A}_0\mu_0/L$  is identified as the equivalent stiffness of the rod, and  $D_C = \mathcal{A}_0\mu_0/c_0$  as a characteristic damping coefficient. Therefore, the following non-dimensional stiffness coefficients  $k_1^* := k_1/K_C$  and  $k_2^* := k_2/K_C$ , and damping coefficients  $d_1^* := d_1/D_C$  and  $d_2^* := d_2/D_C$  are defined.

Applying the boundary conditions (3.96) to Eq. (3.87), and assuming  $k_1^* \neq 0$  and  $k_2^* \neq 0$  yields

$$\begin{aligned}
 P^*(\xi = 0, \tau) &= k_1^* v(0, \tau) + d_1^* \frac{\partial v}{\partial \tau}(\xi = 0, \tau) \\
 V'(0) [\eta + \alpha \dot{\eta}] &= k_1^* V(0) \left[ \eta + \frac{d_1^*}{k_1^*} \dot{\eta} \right] \\
 \Rightarrow \bar{k} A [\eta + \dot{\eta}] &= k_1^* B \left[ \eta + \frac{d_1^*}{k_1^*} \dot{\eta} \right], \\
 P^*(\xi = 1, \tau) &= -k_2^* v(1, \tau) - d_2^* \frac{\partial v}{\partial \tau}(\xi = 1, \tau) \\
 \Rightarrow V'(1) [\eta + \alpha \dot{\eta}] &= -k_2^* V(1) \left[ \eta + \frac{d_2^*}{k_2^*} \dot{\eta} \right].
 \end{aligned}$$

It is observed that, in order for the previous system to have solution, it is necessary

to set

$$\frac{d_1^*}{k_1^*} = \alpha,$$

$$\frac{d_2^*}{k_2^*} = \alpha.$$

Under this condition, it follows that

$$\bar{k}A = k_1^*B,$$

$$\bar{k} [A \cos(\bar{k}) - B \sin(\bar{k})] = -k_2^* [A \sin(\bar{k}) + B \cos(\bar{k})].$$

A nontrivial solution for  $A$  and  $B$  is obtained provided the following transcendental equation is satisfied

$$\bar{k} (k_1^* + k_2^*) \cos(\bar{k}) + \sin(\bar{k}) (k_1^*k_2^* - \bar{k}^2) = 0, \quad (3.97)$$

or provided  $k_1^*k_2^* - \bar{k}^2 \neq 0$ ,

$$\tan(\bar{k}) = \frac{k_1^* + k_2^*}{\bar{k}^2 - k_1^*k_2^*} \bar{k}; \quad k_1^* \neq 0; \quad k_2^* \neq 0. \quad (3.98)$$

The following limit behavior of the wave number  $\bar{k}$  is observed,

$$\lim_{\bar{k} \rightarrow \infty} \tan(\bar{k}) = 0 \Rightarrow \bar{k} = n\pi \quad \text{as } \bar{k} \rightarrow \infty$$

$$\lim_{\substack{k_1^*, k_2^* \rightarrow \infty \\ \frac{k_2^*}{k_1^*} = \text{const.}}} \tan(\bar{k}) = 0 \Rightarrow \bar{k} = n\pi;$$

$$\lim_{\substack{k_1^* \text{ or } k_2^* \rightarrow \infty \\ k_2^*k_1^* = \text{const.}}} \tan(\bar{k}) = \infty \Rightarrow \bar{k} = \frac{2n-1}{2}\pi.$$

The values of the first solution  $\bar{k}$  (first vibration mode) of Eq. (3.97) for different values of  $k_1^*$  and  $k_2^*$  are presented in Fig. 3.6. From the figure and from Eq. (3.97), it is observed that for values of  $k_1^*$  such that

$$k_1^* \geq \frac{\pi^2}{4k_2^*}, \quad (3.99)$$

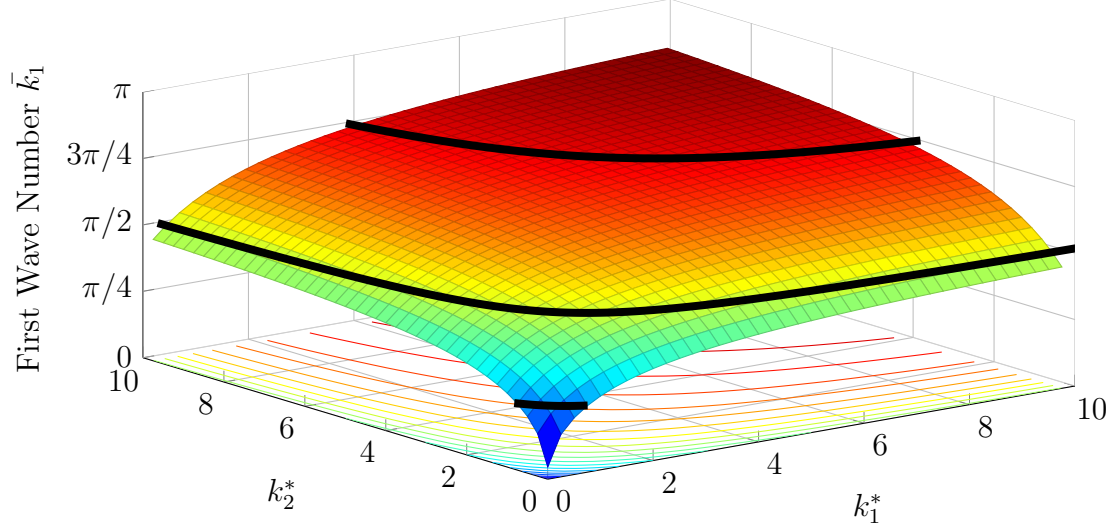


Figure 3.6: First wave number root  $\bar{k}_1$  of Eq. (3.97) as a function of the non-dimensional stiffnesses  $k_1^*$  and  $k_2^*$ . (—): Lines of constant wave numbers  $\bar{k}_1 = \pi/2, \pi/4, 3\pi/4$ .

the wave number corresponding to the first mode is  $\pi/2 \leq \bar{k} < \pi$ . The limits correspond to the values of  $\bar{k}$  for the first mode of the fixed-free and the fixed-fixed cases, respectively. For values of  $\bar{k} < \pi/2$ , the first mode shape has a rigid body component combined with a deformation component.

### 3.6.4 Free-Vibrations Characteristics

From Eq. (3.86), the modal amplitudes  $\eta_m$  satisfy the following ordinary differential equation (ODE):

$$\ddot{\eta}_m + \bar{k}_n^2 \eta_m + \alpha \bar{k}_n^2 \dot{\eta}_m = 0. \quad (3.100)$$

The characteristic equation is

$$s^2 + s\alpha \bar{k}_n^2 + \bar{k}_n^2 \eta = 0. \quad (3.101)$$

The roots of the characteristic equation are given by

$$r_{1n,2n} = -\alpha \frac{\bar{k}_n^2}{2} \pm \bar{k}_n \sqrt{\left(\frac{\alpha \bar{k}_n}{2}\right)^2 - 1}. \quad (3.102)$$

From Eq. (3.102), it is observed that a mode  $n$  will be oscillatory provided

$$\text{Im}[r_{1n,2n}] \neq 0 \Rightarrow \left(\frac{\alpha \bar{k}_n}{2}\right)^2 - 1 < 0. \quad (3.103)$$

The quantity  $\text{Im}[r_{1n,2n}]/\bar{k}_n$  is plotted against  $\alpha \bar{k}_n$  in Figure 3.7. It is observed that  $\text{Im}[r_{1n,2n}] = 0$  for all  $\bar{k}_n \geq 2/\alpha$ . This means that for a given value of  $\alpha \neq 0$ , all modes  $n$  such that  $\bar{k}_n \geq 2/\alpha$  are in general overdamped (or critically damped, if the equality is satisfied), and therefore, they are non-oscillatory modes. All the remaining lower modes are underdamped, and in consequence, oscillatory. Moreover, in the particular case that the first vibration mode is such that  $\bar{k}_1 \geq 2/\alpha$ , then all the modes are overdamped. The condition for all the modes to be overdamped can be expressed as a bound on the length of the rod as follows,

$$\alpha \geq \frac{2}{\bar{k}_1} \Rightarrow L \leq L_{\text{crit}} := \frac{c_0 \mathcal{T}_d}{2} \bar{k}_1. \quad (3.104)$$

This result may be applied to understand the way axons respond under impacts or rapid transient loads. If the length of the axon is smaller than the critical length  $L_{\text{crit}}$ , then the free-response of the axon will decay in time without oscillations. In addition, no resonance behavior will occur in these short axons. Using the results from §3.6.1 through §3.6.3, the critical length  $L_{\text{crit}}$  for different boundary conditions

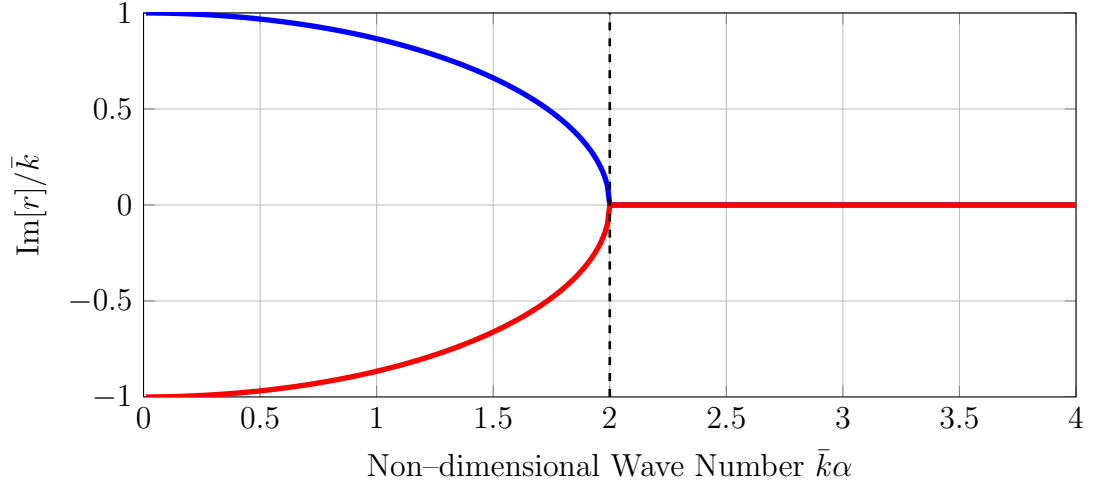


Figure 3.7:  $\text{Im}[r_{1n,2n}]/\bar{k}$  as a function of the non-dimensional wave number  $\bar{k}\alpha$ . ( — ):  $r_1$  root; ( — ):  $r_2$  root.

are:

Fixed – Fixed :

$$L_{\text{crit}} = \frac{c_0 \mathcal{T}_d}{2} \pi,$$

Fixed – Free :

$$L_{\text{crit}} = \frac{c_0 \mathcal{T}_d}{4} \pi,$$

Kelvin – Voigt Supports :

$$0 < L_{\text{crit}} \frac{c_0 \mathcal{T}_d}{2} \pi < \frac{c_0 \mathcal{T}_d}{2} \pi.$$

### 3.7 Nonlinear Viscoelastic Material Case

In the previous section, the mechanical wave propagation through a linear viscoelastic rod was studied. In this section, and in the remainder of this chapter, the attention is focused on the propagation of stress waves through a nonlinear viscoelastic material. The main objective is to further the understanding on how the material nonlinearities affect the characteristics of the mechanical waves that propagate through the material.

The governing equations for a uniform nonlinear viscoelastic rod, presented in §3.2 are restated here for clarity:

$$\left\{ \begin{array}{l} \frac{\partial P}{\partial X} = \rho_0 \frac{\partial^2 u}{\partial t^2} \\ \frac{\partial^2 u}{\partial X \partial t} = -\kappa g(\lambda)^{-2} [f(\lambda) - P] \\ \lambda = \frac{\partial u}{\partial X} + 1, \end{array} \right. \quad (3.105)$$

where

$$f(\lambda) := \frac{d\Psi}{d\lambda}, \quad (3.106)$$

$$g(\lambda) := \frac{d^2\Psi}{d\lambda^2} = \frac{df}{d\lambda}. \quad (3.107)$$

#### 3.7.1 Scaling of Variables

Similar to §3.3.1, a scaling of variables is carried out using the following characteristic variables  $L_C = L$ ,  $T_C = L/c_0$  and  $P_C = \mu_0 = d^2\Psi/d\lambda^2|_{\lambda=1}$ . Introducing the non-dimensional quantities  $\xi$ ,  $\tau$ ,  $v(\xi, \tau)$ ,  $P^*$ ,  $f^*$  and  $g^*$  defined in §3.3.1, the

scaled version of the governing equations are the following:

$$\frac{\partial P^*}{\partial \xi} = \frac{\partial^2 v}{\partial \tau^2}, \quad (3.108a)$$

$$P^* = f^*(\lambda) + \alpha [g^*(\lambda)]^2 \dot{\lambda}, \quad (3.108b)$$

$$\lambda = \frac{\partial v}{\partial \xi} + 1, \quad (3.108c)$$

where

$$g^*(\lambda) := \frac{1}{\mu_0} g(\lambda) \quad f^*(\lambda) := \frac{1}{\mu_0} f(\lambda). \quad (3.109)$$

### 3.8 Nonlinear Viscoelastic Rod: Asymptotic Analysis

In order to gain insights into the effects of the material nonlinearities on the propagation of longitudinal waves, an asymptotic solution of Eq. (3.108) is pursued. For small deformation, that is to say,  $0 < \lambda - 1 \ll 1$ , the Taylor series (3.5) and (3.6) apply. The non-dimensional versions of Eqs. (3.6) and (3.6) are the following

$$f^*(\lambda) := \frac{f(\lambda)}{\mu_0} = \sum_{n \geq 0}^{N-2} \frac{\mu_n^*}{(n+1)!} (\lambda - 1)^{n+1} + \mathcal{O}\left((\lambda - 1)^N\right), \quad (3.110)$$

$$g^*(\lambda) := \frac{g(\lambda)}{\mu_0} = \sum_{n \geq 0}^{N-1} \frac{\mu_n^*}{n!} (\lambda - 1)^n + \mathcal{O}\left((\lambda - 1)^N\right), \quad (3.111)$$

where

$$\mu_n^* := \frac{\mu_n}{\mu_0} = \frac{1}{\mu_0} \left. \frac{d^{n+2} \Psi}{d\lambda^{n+2}} \right|_{\lambda=1}.$$

Substituting Eqs. (3.110), (3.111) and (3.108c) into Eq. (3.108b) yields

$$\begin{aligned} P^* = & \sum_{n \geq 0}^{N-2} \frac{\mu_n^*}{(n+1)!} \left( \frac{\partial v}{\partial \xi} \right)^{n+1} + \alpha \frac{\partial^2 v}{\partial \xi \partial \tau} \sum_{n \geq 0}^{N-2} \sum_{m \geq 0}^{N-2-n} \frac{\mu_n^* \mu_m^*}{n! m!} \left( \frac{\partial v}{\partial \xi} \right)^{n+m} \\ & + \mathcal{O} \left( \left( \frac{\partial v}{\partial \xi} \right)^N ; \frac{\partial^2 v}{\partial \tau \partial \xi} \left( \frac{\partial v}{\partial \xi} \right)^{N-1} \right). \end{aligned} \quad (3.112)$$

Explicitly, for  $N = 3$  Eq. (3.112) becomes

$$P^* = \frac{\partial v}{\partial \xi} + \alpha \frac{\partial^2 v}{\partial \tau \partial \xi} + \frac{1}{2} \mu_1^* \frac{\partial v}{\partial \xi} \left( \frac{\partial v}{\partial \xi} + 4\alpha \frac{\partial^2 v}{\partial \tau \partial \xi} \right) + \mathcal{O} \left( \left( \frac{\partial v}{\partial \xi} \right)^3 ; \frac{\partial^2 v}{\partial \tau \partial \xi} \left( \frac{\partial v}{\partial \xi} \right)^2 \right). \quad (3.113)$$

Introducing Eq. (3.113) into Eq. (3.108a), and neglecting cubic terms yields

$$\frac{\partial^2 v}{\partial \xi^2} + \alpha \frac{\partial^3 v}{\partial \tau \partial \xi^2} + \frac{1}{2} \mu_1^* \frac{\partial}{\partial \xi} \left( \frac{\partial v}{\partial \xi} \right)^2 + 2\mu_1^* \alpha \left( \frac{\partial v}{\partial \xi} \frac{\partial^3 v}{\partial \tau \partial \xi^2} + \frac{\partial^2 v}{\partial \xi^2} \frac{\partial^2 v}{\partial \tau \partial \xi} \right) = \frac{\partial^2 v}{\partial \tau^2}. \quad (3.114)$$

An asymptotic solution of the PDE (3.114), for a semi-infinite rod ( $0 < \xi < +\infty$ ) with zero initial conditions,

$$v(\xi, \tau = 0) = 0 \quad \frac{\partial v}{\partial \tau}(\xi, \tau = 0) = 0, \quad (3.115)$$

and with a displacement boundary condition at  $\xi = 0$ ,

$$v(\xi = 0, \tau) = \epsilon \mu(\tau), \quad (3.116)$$

is sought. Here,  $\epsilon \ll 1$  is a small parameter. Since the rod has infinite length, an additional regularity condition  $|v(\xi, \tau)| < \infty$  is required.

Similar to the analysis performed in §3.4, the damping parameter is rescaled in terms of  $\epsilon$  as  $\alpha = \epsilon \vartheta$ . An asymptotic solution is pursued through the method of multiple scales. To this end, the fast spatial and time scales  $X_0 := \xi$  and  $T_0 := \tau$ , respectively, are introduced along with the slow time scale  $T_1 := \epsilon \tau$ . The new variable  $T_1$  is considered independent of  $T_0$ . When deemed convenient, the following fast scales are introduced as a replacement of  $X_0$  and  $T_0$ ,

$$s_1 := \xi - \tau = X_0 - T_0 \quad s_2 := \xi + \tau = X_0 + T_0. \quad (3.117)$$

Also, the notation  $(\check{\cdot})$  is employed to indicate functions of the variables  $s_1$  and  $s_2$  according Eq. (3.18). In terms of the new independent variables introduced, the time and space derivatives are given by Eqs. (3.20) and (3.21). The following asymptotic expansion solution is proposed:

$$\check{v}(s_1, s_2) \sim \epsilon \check{v}_1(s_1, s_2, T_1) + \epsilon^2 \check{v}_2(s_1, s_2, T_1) + \dots \quad (3.118)$$

Replacing Eqs. (3.20), (3.21) and (3.118) into Eq. (3.114), and collecting terms of the same order in  $\epsilon$  yields the following equations:

$$\mathcal{O}(\epsilon^1) : \quad \frac{\partial^2 \check{v}_1}{\partial s_1 \partial s_2} = 0, \quad (3.119)$$

$$\begin{aligned} \mathcal{O}(\epsilon^2) : \quad 4 \frac{\partial^2 \check{v}_2}{\partial s_1 \partial s_2} = & 2 \frac{\partial}{\partial T_1} \left( -\frac{\partial}{\partial s_1} + \frac{\partial}{\partial s_2} \right) \check{v}_1 \\ & - \vartheta \left( -\frac{\partial}{\partial s_1} + \frac{\partial}{\partial s_2} \right) \left( \frac{\partial^2}{\partial s_1^2} + \frac{\partial^2}{\partial s_2^2} + 2 \frac{\partial^2}{\partial s_1 \partial s_2} \right) \check{v}_1 \\ & - \frac{1}{2} \mu_1^* \left( \frac{\partial}{\partial s_1} + \frac{\partial}{\partial s_2} \right) \left( \frac{\partial \check{v}_1}{\partial s_1} + \frac{\partial \check{v}_1}{\partial s_2} \right)^2. \end{aligned} \quad (3.120)$$

Similarly, the initial conditions are

$$\mathcal{O}(\epsilon^1) : \quad v_1(X_0, 0, 0) = 0 \quad \frac{\partial v_1}{\partial T_0}(X_0, 0, 0) = 0, \quad (3.121)$$

$$\mathcal{O}(\epsilon^2) : \quad v_2(X_0, 0, 0) = 0 \quad \frac{\partial v_1}{\partial T_1}(X_0, 0, 0) + \frac{\partial v_2}{\partial T_0}(X_0, 0, 0) = 0. \quad (3.122)$$

Introducing Eq. (3.118) into (3.116), and collecting terms of equal power in  $\epsilon$  yields the boundary conditions for  $v_1$  and  $v_2$  in the form

$$\mathcal{O}(\epsilon^1) : \quad v_1(X_0 = 0, T_0, T_1) = \mu(T_0), \quad (3.123)$$

$$\mathcal{O}(\epsilon^2) : \quad v_2(X_0 = 0, T_0, T_1) = 0. \quad (3.124)$$

As in the analysis in §3.4, the general solution  $\check{v}_1(s_1, s_2, T_1)$  is given by

$$\check{v}_1(s_1, s_2, T_1) = \check{F}_1(s_1, T_1) + \check{G}_1(s_2, T_1), \quad (3.125)$$

where  $\check{F}_1(s_1, T_1)$  and  $\check{G}_1(s_2, T_1)$  are functions to be obtained from the initial conditions and from the boundary conditions. Applying the boundary condition (3.123), using the results from Eqs. (3.43), (B.4), (B.5) and (B.8), and setting  $\phi = 0$  and  $\psi = 0$ , the following result is obtained

$$\check{F}_1(s_1, T_1 = 0) = u(-s_1)\mu(-s_1); \quad \check{G}_1(s_2, T_1 = 0) = 0. \quad (3.126)$$

Substituting Eq. (3.125) into Eq. (3.120), it can be shown that for  $\check{v}_2$  to be bounded for  $(s_1, s_2) \rightarrow \infty$ , the equations requiring vanishing secular terms are

$$\frac{\partial \check{F}_1}{\partial T_1} - \frac{1}{2}\vartheta \frac{\partial^2 \check{F}_1}{\partial s_1^2} + \frac{1}{4}\mu_1^* \left( \frac{\partial \check{F}_1}{\partial s_1} \right)^2 = 0 \quad \text{for } -\infty < s_1 < +\infty, \quad (3.127)$$

$$\frac{\partial \check{G}_1}{\partial T_1} - \frac{1}{2}\vartheta \frac{\partial^2 \check{G}_1}{\partial s_2^2} - \frac{1}{4}\mu_1^* \left( \frac{\partial \check{G}_1}{\partial s_2} \right)^2 = 0 \quad \text{for } 0 \leq s_2 < +\infty. \quad (3.128)$$

Therefore,  $\check{F}_1(s_1, T_1)$  solves an initial value problem in the unbounded domain  $s_1 \in \mathbb{R}$ . It can be shown that by using a Cole–Hopf transformation (Evans, 2010), the solution to Eq. (3.127) is given by

$$\check{F}_1(s_1, T_1) = -2\vartheta \frac{1}{\mu_1^*} \ln \left[ \int_{-\infty}^{+\infty} \Phi(s_1 - y, T_1) e^{-\mu_1^* \frac{1}{2\vartheta} \check{F}_1(y, T_1=0)} dy \right], \quad (3.129)$$

where, as in §3.4,  $\Phi(x, t)$  is the *heat kernel* in  $\mathbb{R}$  for diffusivity equal to  $\vartheta/2$

$$\Phi(x, t) = \frac{1}{\sqrt{2\pi\vartheta t}} e^{-\frac{x^2}{2\vartheta t}}.$$

Introducing the expression of  $\check{F}_1(y, T_1 = 0)$  from Eq. (3.126) into Eq. (3.129) results in

$$\check{F}_1(s_1, T_1) = -2\vartheta \frac{1}{\mu_1^*} \ln \left[ \int_{-\infty}^{+\infty} \Phi(s_1 - y, T_1) e^{-\mu_1^* \frac{1}{2\vartheta} \mu(-y)u(-y)} dy \right]. \quad (3.130)$$

On the other hand,  $\check{G}_1(s_1, T_1)$  solves an initial–boundary value problem in the bounded domain  $s_2 > 0$ , with zero initial condition  $\check{G}_1(s_2, T_1 = 0) = 0$ , and boundary condition equivalent to Eq. (3.48),  $\check{G}_1(s_2 = 0, T_1) = -\check{F}_1(s_1 = 0, T_1) = 0$ . In consequence, the solution of Eq. (3.128) is the trivial solution  $\check{G}_1(s_2, T_1) = 0$ .

### 3.8.1 Stress–Wave Solution for Nonlinear Viscoelastic Rod Initially at Rest

In this particular case, similar to Eq. (3.50), the zero–*th* order approximation of the stress is given by

$$\check{P}_1^*(s_1, T_1) = \frac{\partial \check{F}_1}{\partial s_1}. \quad (3.131)$$

Thus, from Eqs. (3.130), the stress is obtained as

$$\check{P}_1^*(s_1, s_2, T_1) = 2\vartheta \frac{1}{\mu_1^*} \frac{\int_{-\infty}^{+\infty} \frac{s_1-y}{\vartheta T_1} \Phi(s_1-y, T_1) e^{-\mu_1^* \frac{1}{2\vartheta} \mu(-y)u(-y)} dy}{\int_{-\infty}^{+\infty} \Phi(s_1-y, T_1) e^{-\mu_1^* \frac{1}{2\vartheta} \mu(-y)u(-y)} dy}. \quad (3.132)$$

Explicitly, the stress solution is given by

$$\check{P}_1^*(s_1, s_2, T_1) = 2\vartheta \frac{1}{\mu_1^*} \frac{\int_{-\infty}^{+\infty} \frac{s_1-y}{\vartheta T_1} e^{-\frac{(s_1-y)^2}{2\vartheta T_1} - \mu_1^* \frac{1}{2\vartheta} \mu(-y)u(-y)} dy}{\int_{-\infty}^{+\infty} e^{-\frac{(s_1-y)^2}{2\vartheta T_1} - \mu_1^* \frac{1}{2\vartheta} \mu(-y)u(-y)} dy}. \quad (3.133)$$

In the particular case of vanishing damping (viscosity  $\vartheta/2$ ), it can be shown (Evans, 2010, sec. 4.5.2), that

$$\lim_{\vartheta \rightarrow 0} \frac{\mu_1^*}{2} \check{P}_1^*(s_1, T_1) = \frac{s_1 - y_1(s_1, T_1)}{T_1}, \quad (3.134)$$

where  $y_1(s_1, T_1)$  minimizes  $K(s_1, y, T_1) := \frac{(s_1-y)^2}{2T_1} + \frac{1}{2}\mu_1^* \mu(-y)u(-y)$  with respect to  $y$  for fixed  $s_1$  and  $T_1$ . Equation (3.134) is the Lax–Oleinik formula for the unique entropy solution of the Burger’s equation for  $\check{P}_1^* \mu_1^*/2$ , which could develop discontinuities across shock waves.

The previous analysis shows that for the nonlinear viscoelastic rod, there are two competing effects. The material nonlinearity, on one hand tends to produce discontinuous (shock) wave fronts. On the other hand, the material damping, even a small amount, will always smooth any discontinuity as well as produce diffusion. In consequence, wave fronts will steepen, but they will never generate shock fronts. The same phenomenon of wave steepening is also observed through numerical simulations in §3.10.

### 3.8.2 Representative Results for a Particular Displacement Input

In order to illustrate the effects of the material nonlinearity and of the dissipation on the stress waves, a particular case in which the prescribed stress at  $\xi = 0$  given by

$$\mu(\tau) = \pm \left[ \left( 1 - \cos \left( 2\pi \tilde{f} \tau \right) \right) \left( u(\tau) - u \left( \tau - 0.5\tilde{T} \right) \right) + u \left( \tau - 0.5\tilde{T} \right) \right] \quad (3.135)$$

is studied. Here,  $\tilde{T} = 1/\tilde{f}$ , and the plus or minus sign determines whether the deformation is a contraction or an elongation deformation. This particular displacement pulse is shown in Fig. 3.8.

In this particular example, the following parameters are chosen

$$\alpha = 0.001 \quad \frac{\mu_0}{\mu_1} = -0.03 \quad \epsilon = 0.001 \quad \tilde{f} = 10.$$

The stress solution for the system with linearized viscoelastic model, given by (3.51), is compared to the nonlinear model prediction, given by (3.133), in Figs. (3.9) and (3.10), for compression and tension wave pulses, respectively.

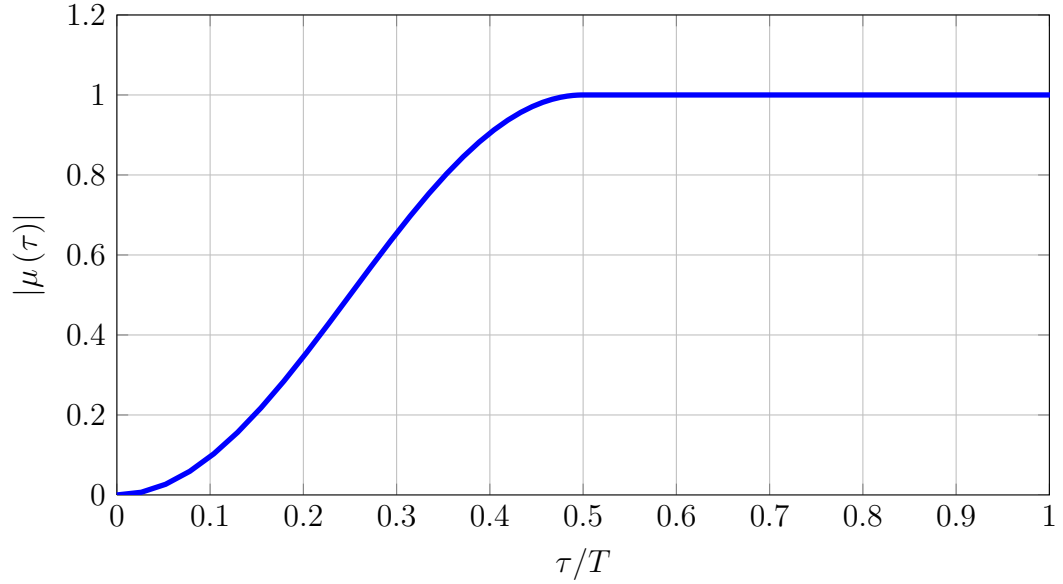


Figure 3.8: Shape of the displacement pulse (3.135) introduced at  $\xi = 0$ .

It can be clearly observed that the nonlinear compression pulse leads with respect to the corresponding linear compression pulse. On the other hand, the nonlinear tension pulse lags behind the corresponding linear pulse. Moreover, it is observed that the leading front of the compression wave and the trailing part of the tension wave pulses steepen as a consequence of the material nonlinearity. It is finally observed that for the same instant of time, the amplitude of the wave pulse in the nonlinear viscoelastic material is smaller than that in the linear viscoelastic material. This characteristic is related to the increased dissipation in the nonlinear viscoelastic material. These features depicted by the asymptotic solutions are also observed through numerical simulations in §3.10.

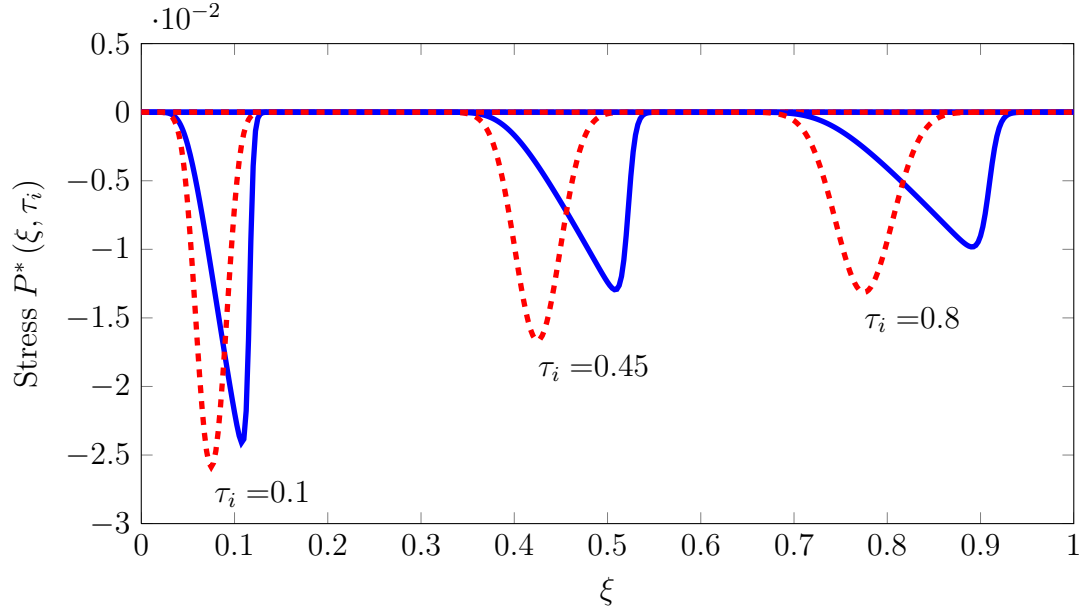


Figure 3.9: Comparison between asymptotic solutions for the compression stress wave corresponding to the linear and nonlinear viscoelastic rods. ( — ): Nonlinear model prediction (Eq. (3.133)); ( - - ): Linear model prediction (Eq. (3.51)).

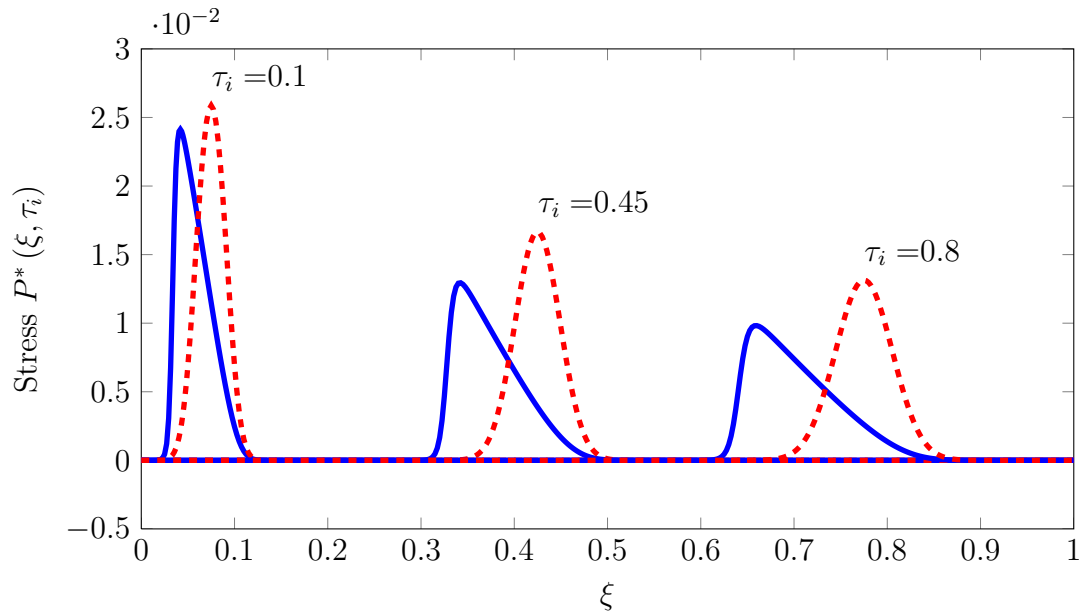


Figure 3.10: Comparison between asymptotic solutions for the tension stress wave corresponding to the linear and nonlinear viscoelastic rods. ( — ): Nonlinear model prediction (Eq. (3.133)); ( - - ): Linear model prediction (Eq. (3.51)).

### 3.9 Frequency Response of a Nonlinear Viscoelastic Rod

In this section, the frequency response for longitudinal vibrations of a nonlinear viscoelastic rod is studied. In order to do so, a (non-dimensional) body force  $b^*(\xi, \tau) = B^*(\xi) \cos(\omega\tau)$  is introduced in Eqs. (3.108) as follows,

$$\frac{\partial^2 v}{\partial \tau^2} = \frac{\partial P^*}{\partial \xi} + B^*(\xi) \cos(\omega\tau), \quad (3.136a)$$

$$P^* = f^*(\lambda) + \alpha [g^*(\lambda)]^2 \dot{\lambda}, \quad (3.136b)$$

$$\lambda = \frac{\partial v}{\partial \xi} + 1. \quad (3.136c)$$

Using expression (3.112) up to cubic terms ( $N = 4$ ), the stress can be written as,

$$\begin{aligned} P^* &= \frac{\partial v}{\partial \xi} + \frac{1}{2} \mu_1^* \left( \frac{\partial v}{\partial \xi} \right)^2 + \frac{1}{6} \mu_2^* \left( \frac{\partial v}{\partial \xi} \right)^3 \\ &+ \alpha \frac{\partial^2 v}{\partial \tau \partial \xi} \left( 1 + 2 \frac{\partial v}{\partial \xi} + (\mu_2^* + (\mu_1^*)^2) \left( \frac{\partial v}{\partial \xi} \right)^2 \right) \\ &+ \mathcal{O} \left( \left( \frac{\partial v}{\partial \xi} \right)^4; \frac{\partial^2 v}{\partial \tau \partial \xi} \left( \frac{\partial v}{\partial \xi} \right)^3 \right). \end{aligned} \quad (3.137)$$

In order to perform the asymptotic analysis, Eq. (3.136a) is transformed into a set of ODEs by the Galerkin projection method. To this purpose, a displacement solution is assumed in the form

$$v(\xi, \tau) = \sum_{n=0}^M \eta_n(\tau) \sin(\bar{k}_n \xi), \quad (3.138)$$

where  $\bar{k}_n$ , for  $n = 1, 2, \dots, M$  are the wave numbers of the linear viscoelastic elastic rod with fixed-free boundary conditions (Eq. (3.93)).

$$\bar{k}_n = \frac{2n-1}{2} \pi \quad \text{for } n = 1, 2, \dots, M.$$

Then, it follows that

$$\frac{\partial v}{\partial \xi} = \sum_{n=0}^M \eta_n(\tau) \bar{k}_n \cos(\bar{k}_n \xi), \quad (3.139)$$

$$\frac{\partial v}{\partial \tau \partial \xi} = \sum_{n=0}^M \dot{\eta}_n(\tau) \bar{k}_n \cos(\bar{k}_n \xi). \quad (3.140)$$

The details and mathematical steps of the Galerkin projection method are presented in Appendix C. As a result of the Galerkin projection, a set of ordinary differential equations for the modal coordinates  $\eta_k$  are obtained. The resulting ODEs for  $k = 1, 2, \dots, M$  are given by

$$\begin{aligned} \ddot{\eta}_k + \bar{k}_k^2 \eta_k = & -\alpha \bar{k}_k^2 \dot{\eta}_k + 2B_k \cos(\omega\tau) \\ & + \mu_1^* \sum_{j=1}^M \sum_{n=1}^M \bar{k}_n \bar{k}_j \eta_n (\eta_j + 4\alpha \dot{\eta}_j) F_{kjn} + \\ & + 2 \sum_{j=1}^M \sum_{n=1}^M \sum_{m=1}^M \bar{k}_n \bar{k}_j \bar{k}_m \eta_j \eta_n \left( \frac{1}{6} \mu_2^* \eta_m + (\mu_2^* + (\mu_1^*)^2) \alpha \dot{\eta}_m \right) G_{k j n m}, \end{aligned} \quad (3.141)$$

where  $F_{k j n}$ ,  $G_{k j n m}$  and  $B_k$  are defined in Eqs. (C.5). Different models (governing equations) can be obtained depending on how the external forcing term, the nonlinear terms and the linear damping term are balanced. In the following subsections, two different cases are explored.

### 3.9.1 Case 1: $B_k = \mathcal{O}(\eta_k^2) = \mathcal{O}(\alpha\dot{\eta}_k) = \mathcal{O}(\epsilon^2)$

For this particular case, the variables  $\eta_k$ , the damping  $\alpha$  and the forcing amplitude  $B_k$  are rescaled in the following form,

$$\eta_k = \epsilon\gamma_i \quad \text{with } \gamma_k = \mathcal{O}(1) \quad k = 1, 2, \dots, M,$$

$$\alpha = \epsilon\vartheta \quad \text{with } \vartheta = \mathcal{O}(1),$$

$$B_k = \epsilon^2 Q_k \quad \text{with } Q_k = \mathcal{O}(1) \quad k = 1, 2, \dots, M,$$

where  $\epsilon \ll 1$  is a small parameter. Upon inserting the rescaled quantities into

Eq. 3.141, the following ODEs for  $k = 1, 2, \dots, M$  are obtained

$$\begin{aligned} \ddot{\gamma}_k + \bar{k}_k^2 \gamma_k &= \left[ \mu_1^* \sum_{j=1}^M \sum_{n=1}^M F_{kjn} \bar{k}_n \bar{k}_j \gamma_n \gamma_j - \bar{k}_k^2 \dot{\gamma}_k \vartheta + 2Q_k \cos(\omega\tau) \right] \epsilon \\ &+ \left[ \frac{1}{3} \mu_2^* \sum_{j=1}^M \sum_{n=1}^M \sum_{m=1}^M G_{kijnm} \bar{k}_n \bar{k}_j \bar{k}_m \gamma_j \gamma_n \gamma_m \right] \epsilon^2 \\ &+ \left[ 4\mu_1^* \sum_{j=1}^M \sum_{n=1}^M F_{kjn} \bar{k}_n \bar{k}_j \vartheta \gamma_n \dot{\gamma}_j \right] \epsilon^2 \\ &+ \left[ 2 \sum_{j=1}^M \sum_{n=1}^M \sum_{m=1}^M G_{kijnm} \bar{k}_n \bar{k}_j \bar{k}_m \gamma_j \gamma_n \vartheta (\mu_2^* + (\mu_1^*)^2) \dot{\gamma}_m \right] \epsilon^3 + O(\epsilon^4). \end{aligned} \quad (3.142)$$

It is observed that this rescaling places the external forcing term at the same order in  $\epsilon$  as the linear damping term and the quadratic term in  $\gamma$ .

Now, the method of multiple scales is employed to obtain the frequency response of the system. Similar to previous analyses, the fast time scale  $T_0 := \tau$ , and the slow time scale  $T_1 := \epsilon\tau$  are introduced. Using this two scales as independent time variables, the time derivative operators become

$$\frac{d}{d\tau} = \frac{\partial}{\partial T_0} + \epsilon \frac{\partial}{\partial T_1} = D_0 + \epsilon D_1, \quad (3.143a)$$

$$\frac{d^2}{d\tau^2} = D_0^2 + \epsilon 2D_0 D_1 + \epsilon^2 D_1^2, \quad (3.143b)$$

where  $D_i^k := \partial^k / \partial T_i^k$ . The following asymptotic expansion solution for the modal variable  $\gamma_k$  is assumed:

$$\gamma_k(\tau) \sim \gamma_{k0}(T_0, T_1) + \epsilon \gamma_{k1}(T_0, T_1) + \dots \quad (3.144)$$

Substituting Eqs. (3.143) and (3.144) into Eq. (3.142), and collecting terms of the same order in  $\epsilon$  yields the following equations:

$$\mathcal{O}(\epsilon^0) : \quad D_0^2 \gamma_{k0} + \bar{k}_k^2 \gamma_{k0} = 0, \quad (3.145)$$

$$\begin{aligned} \mathcal{O}(\epsilon^1) : \quad D_0^2 \gamma_{k1} + \bar{k}_k^2 \gamma_{k1} = & -2D_0 D_1 \gamma_{k0} - \vartheta \bar{k}_k^2 D_0 \gamma_{k0} + 2Q_k \cos(\omega\tau) \\ & + \mu_1^* \sum_{j=1}^N \sum_{n=1}^N F_{kjn} \bar{k}_n \bar{k}_j \gamma_{n0} \gamma_{j0}. \end{aligned} \quad (3.146)$$

The general solution of Eq. (3.145) can be written as

$$\gamma_{k0} = A_k(T_1) e^{i\bar{k}_k T_0} + \bar{A}_k(T_1) e^{-i\bar{k}_k T_0} = A_k(T_1) e^{i\bar{k}_k T_0} + C.C., \quad (3.147)$$

where  $i = \sqrt{-1}$ ,  $\bar{A}_k$  is the complex conjugate of  $A_k$ , and  $C.C.$  stands for complex conjugate terms.

In order for the asymptotic solution (3.144) to be uniform for times up to  $\tau = \epsilon^{-1}$ , the secular terms appearing in the  $\mathcal{O}(\epsilon)$  solution must vanish. Therefore, it is necessary to determine whether the terms appearing in the RHS of Eq. (3.146) contain frequencies equal to the frequency  $\bar{k}_k$ . The first and second terms on the RHS of Eq. (3.146) involve the following factors, respectively

$$D_0 D_1 \gamma_{k0} = i\bar{k}_k D_1 A_k e^{i\bar{k}_k T_0} + C.C., \quad (3.148)$$

$$D_0 \gamma_{k0} = i\bar{k}_k A_k e^{i\bar{k}_k T_0} + C.C. \quad (3.149)$$

Since these two terms have frequency equal to the frequency  $\bar{k}_k$  they produce secular (resonant) terms in the asymptotic expansion. The external force term  $Q_k \cos(\omega\tau)$  can be conveniently expressed as

$$2Q_k \cos(\omega\tau) = Q_k (e^{i\omega\tau} + e^{-i\omega\tau}).$$

If only the primary resonance of mode  $k$  is of interest, then the components of the external force on all the other modes can be set to zero,  $Q_j = 0$  for  $j \neq k$ . Next, a detuning parameter  $\sigma$  is introduced to write the following:

$$\omega = \bar{k}_k + \epsilon\sigma. \quad (3.150)$$

Therefore, the external forcing term can be re-written as

$$2Q_k \cos(\omega\tau) = Q_k e^{i\sigma\epsilon\tau} e^{i\bar{k}_k\tau} + C.C. = Q_k e^{i\sigma T_1} e^{i\bar{k}_k T_0} + C.C. \quad (3.151)$$

Thus, it is observed that the external force also produces a secular term. The last term on the RHS of Eq. (3.146) involves the following product,

$$\gamma_{n0}\gamma_{j0} = A_n A_j e^{i(\bar{k}_n + \bar{k}_j)T_0} + A_n \bar{A}_j e^{i(\bar{k}_n - \bar{k}_j)T_0} + C.C. \quad (3.152)$$

It can be shown that  $\bar{k}_n + \bar{k}_j \neq \bar{k}_k$  and  $\bar{k}_n - \bar{k}_j \neq \bar{k}_k \forall n, j \in \mathbb{N}$ . Therefore, these terms do not produce secular terms. Collecting the results from Eqs. (3.148) through (3.152), the equation requiring vanishing secular terms for mode  $k$  is given by

$$-2i\bar{k}_k D_1 A_k - i\vartheta\bar{k}_k^3 A_k + Q_k e^{i\sigma T_1} = 0, \quad (3.153)$$

and for modes  $j \neq k$

$$2\bar{k}_j D_1 A_j + \vartheta\bar{k}_j^3 A_j = 0. \quad (3.154)$$

The solution of Eq. (3.154) is given by  $A_j(T_1) = C_j e^{-0.5\vartheta \bar{k}_j^2 T_1}$ . Therefore  $A_j \rightarrow 0$  as  $T_1 \rightarrow +\infty$ . In consequence all modes  $j \neq k$  are not excited at the steady-state.

To study Eq. (3.153), the polar notation  $A_k = a_k(T_1) e^{i\theta_k(T_1)}$  is introduced for convenience. Replacing into Eq. (3.153), and separating imaginary and real parts results in

$$\begin{aligned} -2\bar{k}_k a'_k - \vartheta \bar{k}_k^3 a_k + Q_k \sin \nu &= 0, \\ 2\bar{k}_k \theta'_k a_k + Q_k \cos \nu &= 0, \end{aligned}$$

where  $\nu(T_1) := \sigma T_1 - \theta_k(T_1)$  and the prime ( $'$ ) denotes differentiation with respect to  $T_1$ . The steady-state solution for the amplitude  $a_k$ , if it exists, is characterized by  $a'_k \rightarrow 0$  and  $\nu' = \sigma - \theta'_k \rightarrow 0$ . In consequence, the equations governing the steady-state amplitude  $a_k$  are given by

$$\begin{aligned} \vartheta \bar{k}_k^3 a_k &= Q_k \sin \nu, \\ 2\bar{k}_k \sigma a_k &= -Q_k \cos \nu. \end{aligned}$$

It can be shown that the amplitude  $a_k$  and phase  $\nu$  are given by

$$a_k = \frac{|Q_k|}{\bar{k}_k} \frac{1}{\sqrt{(2\sigma)^2 + (\vartheta \bar{k}_k^2)^2}}, \quad \tan \nu = -\frac{\vartheta \bar{k}_k^2}{2\sigma}, \quad (3.155)$$

which can be rewritten in terms of the original variables as

$$\epsilon a_k = \frac{B_k}{\bar{k}_k^2} \frac{1}{\sqrt{4 \left(1 - \frac{\omega}{\bar{k}_k}\right)^2 + (\alpha \bar{k}_k)^2}}, \quad \tan \nu = -\frac{\alpha \bar{k}_k}{2 \left(\frac{\omega}{\bar{k}_k} - 1\right)}, \quad (3.156)$$

where  $\epsilon a_k$  is nothing but the amplitude of  $\eta_k$  (original modal coordinate). It is observed that the obtained frequency response (3.156), although different, shares

certain characteristics with that of a linear  $m$ - $c$ - $k$  oscillator. An important feature to note in Eq. (3.156) is that the amplitude of the response is linearly proportional to the amplitude of the external loading. This feature can be explained if it is recalled that the quadratic terms did not produce resonant terms in the asymptotic expansion (Eq. (3.152)); therefore, they did not contribute to the steady-state response amplitude. In other words, the external forcing was balanced only by the linear terms. This result suggests that for this particular system the material nonlinearity becomes important from cubic terms on. Therefore, in order to make the effect of material nonlinearity appear, the amplitude of the external force needs to be such that it interacts with at least the cubic nonlinearity (and by induction, with odd nonlinearities) in the system. This is the reasoning that motivates the new following balancing of terms.

### 3.9.2 Case 2: $B_k = \mathcal{O}(\eta_k^3) = \mathcal{O}(\alpha\dot{\eta}_k) = \mathcal{O}(\epsilon^3)$

Based on the conclusions of last section, the variables  $\eta_k$ , the damping  $\alpha$  and the forcing amplitude  $B_k$  are rescaled so that the higher nonlinear term (cubic) in Eq. (3.141), the forcing and the linear damping term appear at the same order in  $\epsilon$ :

$$\begin{aligned} \eta_i &= \epsilon\gamma_i && \text{with } \gamma_i = \mathcal{O}(1) \quad i = 1, 2, \dots, M, \\ \alpha &= \epsilon^2\vartheta; && \text{with } \vartheta = \mathcal{O}(1), \\ B_k &= \epsilon^3Q_k && \text{with } Q_k = \mathcal{O}(1) \quad k = 1, 2, \dots, M. \end{aligned}$$

where  $\epsilon \ll 1$  is a small parameter. The rescaled ODEs now read as follows

$$\begin{aligned}
\ddot{\gamma}_k + \bar{k}_k^2 \gamma_k &= \left[ \mu_1^* \sum_{j=1}^M \sum_{n=1}^M F_{kjn} \bar{k}_n \bar{k}_j \gamma_n \gamma_j \right] \epsilon \\
&+ \left[ \frac{1}{3} \mu_2^* \sum_{j=1}^M \sum_{n=1}^M \sum_{m=1}^M G_{kijnm} \bar{k}_n \bar{k}_j \bar{k}_m \gamma_j \gamma_n \gamma_m - \bar{k}_k^2 \dot{\gamma}_k \vartheta + 2Q_k \cos(\omega\tau) \right] \epsilon^2 \\
&+ \left[ 4\mu_1^* \sum_{j=1}^M \sum_{n=1}^M F_{kjn} \bar{k}_n \bar{k}_j \vartheta \gamma_n \dot{\gamma}_j \right] \epsilon^3 \\
&+ \left[ 2 \sum_{j=1}^M \sum_{n=1}^M \sum_{m=1}^M G_{kijnm} \bar{k}_n \bar{k}_j \bar{k}_m \gamma_j \gamma_n \vartheta (\mu_2^* + (\mu_1^*)^2) \dot{\gamma}_m \right] \epsilon^4 + O(\epsilon^5).
\end{aligned} \tag{3.157}$$

Similar to the analysis in §3.9.1, the method of multiple scales is employed to obtain the frequency response of the system. In addition to the scales  $T_0 := \tau$  and  $T_1 := \epsilon\tau$  introduced in §3.9.1, an additional slow scale  $T_2 := \epsilon^2\tau$  needs to be introduced. Using these scales as independent time variables, the time derivative operators become,

$$\begin{aligned}
\frac{d}{d\tau} &= \frac{\partial}{\partial T_0} + \epsilon \frac{\partial}{\partial T_1} + \epsilon^2 \frac{\partial}{\partial T_2} = D_0 + \epsilon D_1 + \epsilon^2 D_2, \\
\frac{d^2}{d\tau^2} &= D_0^2 + 2\epsilon D_0 D_1 + \epsilon^2 [D_1^2 + 2D_0 D_2] + 2\epsilon^3 D_1 D_2 + \epsilon^4 D_2^2,
\end{aligned} \tag{3.158}$$

where, as before,  $D_i^k := \partial^k / \partial T_i^k$ . Again, an asymptotic solution of the form (3.144) is assumed. Substituting Eqs. (3.158) and (3.144) into Eq. (3.157), and collecting

terms of the same order in  $\epsilon$  yields

$$\mathcal{O}(\epsilon^0) : \quad D_0^2 \gamma_{k0} + \bar{k}_k^2 \gamma_{k0} = 0, \quad (3.159)$$

$$\begin{aligned} \mathcal{O}(\epsilon^1) : \quad D_0^2 \gamma_{k1} + \bar{k}_k^2 \gamma_{k1} = & -2D_0 D_1 \gamma_{k0} \\ & + \mu_1^* \sum_{j=0}^N \sum_{n=1}^N F_{k j n} \bar{k}_n \bar{k}_j \gamma_{n0} \gamma_{j0}, \end{aligned} \quad (3.160)$$

$$\begin{aligned} \mathcal{O}(\epsilon^2) : \quad D_0^2 \gamma_{k2} + \bar{k}_k^2 \gamma_{k2} = & -2D_0 D_2 \gamma_{k0} - 2D_0 D_1 \gamma_{k1} - D_1^2 \gamma_{k0} \\ & + \frac{1}{3} \mu_2^* \sum_{j=1}^N \sum_{n=1}^N \sum_{m=1}^N G_{k j n m} \bar{k}_n \bar{k}_j \bar{k}_m \gamma_{j0} \gamma_{n0} \gamma_{m0}, \\ & + 2\mu_1^* \sum_{j=1}^N \sum_{m=1}^N F_{k j m} \bar{k}_m \bar{k}_j \gamma_{m1} \gamma_{j0} - \bar{k}_k^2 D_0 \gamma_{k0} \vartheta \\ & + 2Q_k \cos(\omega\tau). \end{aligned} \quad (3.161)$$

The general solution of Eq. (3.159) is given by Eq. (3.147), which is repeated here for completeness.

$$\gamma_{k0} = A_k(T_1, T_2) e^{i\bar{k}_k T_0} + C.C.$$

In order for the asymptotic solution (3.144) to be uniform for times up to  $\tau = \epsilon^{-1}$ , the secular terms appearing in the  $\mathcal{O}(\epsilon)$  equation must vanish. Both terms on the RHS of Eq. (3.160) were previously analyzed in Eqs. (3.148) and (3.152). Therefore, the equation of the vanishing secular terms at  $\mathcal{O}(\epsilon)$  is given by

$$D_0 D_1 \gamma_{k0} = 0 \Rightarrow D_1 A_k = 0 \Rightarrow A_k = A_k(T_2) \quad \forall k. \quad (3.162)$$

Ignoring the homogenous solution according to Nayfeh and Mook (2008), the  $O(\epsilon)$

(steady-state) solution of Eq. (3.160) is given by

$$\gamma_{k1}(T_0, T_2) = \mu_1^* \sum_{j=1}^M \sum_{n=1}^M F_{kjn} \bar{k}_n \bar{k}_j \left[ \frac{A_n A_j}{\bar{k}_k^2 - (\bar{k}_j + \bar{k}_n)^2} e^{i(\bar{k}_j + \bar{k}_n)T_0} + \frac{\bar{A}_n A_j}{\bar{k}_k^2 - (\bar{k}_j - \bar{k}_n)^2} e^{i(\bar{k}_j - \bar{k}_n)T_0} + C.C. \right]. \quad (3.163)$$

In order for the asymptotic solution (3.144) to be uniform for times up to  $\tau = \epsilon^{-2}$ , again, the secular terms appearing in the  $\mathcal{O}(\epsilon^2)$  equation must vanish.

Let us analyze the terms in the RHS of Eqs. (3.161) to search for secular terms.

First, the products  $\gamma_{j0}\gamma_{n0}\gamma_{m0}$  are analyzed.

$$\begin{aligned} \gamma_{j0}\gamma_{n0}\gamma_{m0} = & A_j A_n A_m e^{i(\bar{k}_j + \bar{k}_n + \bar{k}_m)T_0} + A_j \bar{A}_n A_m e^{i(\bar{k}_j - \bar{k}_n + \bar{k}_m)T_0} \\ & + A_j A_n \bar{A}_m e^{i(\bar{k}_j + \bar{k}_n - \bar{k}_m)T_0} + A_j \bar{A}_n \bar{A}_m e^{i(\bar{k}_j - \bar{k}_n - \bar{k}_m)T_0} + C.C. \end{aligned} \quad (3.164)$$

From the previous expression, the following four frequencies are identified:

$$\begin{aligned} \bar{k}_j + \bar{k}_n + \bar{k}_m &= \bar{k}_k \frac{2(j+n+m) - 3}{2k-1}, \\ |\bar{k}_j - \bar{k}_n + \bar{k}_m| &= \bar{k}_k \left| \frac{2(j-n+m) - 1}{2k-1} \right|, \\ |\bar{k}_j + \bar{k}_n - \bar{k}_m| &= \bar{k}_k \left| \frac{2(j+n-m) - 1}{2k-1} \right|, \\ |\bar{k}_j - \bar{k}_n - \bar{k}_m| &= \bar{k}_k \left| \frac{2(j-n-m) + 1}{2k-1} \right|. \end{aligned}$$

Therefore, given  $k, j, n \in \mathbb{N}$ , secular (resonant) terms occur if  $\mathbb{N} \ni m = p_{mi} \leq M$  such that

$$\begin{aligned} \mathbb{N} \ni p_{m1} &:= k - j - n + 1 \leq M, \\ \mathbb{N} \ni p_{m2, m3} &:= \frac{1}{2} \pm \frac{2k-1}{2} - j + n \leq M, \\ \mathbb{N} \ni p_{m4, m5} &:= -\frac{1}{2} \mp \frac{2k-1}{2} + j + n \leq M, \\ \mathbb{N} \ni p_{m6, m7} &:= \frac{1}{2} \mp \frac{2k-1}{2} + j - n \leq M. \end{aligned} \quad (3.165)$$

It is noted that for certain combinations of  $k, j, n$  not all  $p_{mi}$  ( $i = 1, 2, \dots, 7$ ) may exist.

Secondly, the products  $\gamma_{j0}\gamma_{m1}$  are analyzed. It can be shown that

$$\begin{aligned} \gamma_{j0}\gamma_{m1} = \mu_1^* \sum_{n=0}^N \sum_{l=0}^N F_{mnl} \bar{k}_n \bar{k}_l \left[ \frac{A_n A_l A_j}{\bar{k}_m^2 - (\bar{k}_n + \bar{k}_l)^2} e^{i(\bar{k}_n + \bar{k}_l + \bar{k}_j)T_0} + \right. \\ \frac{A_n \bar{A}_l \bar{A}_j}{\bar{k}_m^2 - (\bar{k}_n - \bar{k}_l)^2} e^{i(\bar{k}_n - \bar{k}_l - \bar{k}_j)T_0} \\ \frac{A_n \bar{A}_l A_j}{\bar{k}_m^2 - (\bar{k}_n - \bar{k}_l)^2} e^{i(\bar{k}_n - \bar{k}_l + \bar{k}_j)T_0} + \\ \left. \frac{A_n A_l \bar{A}_j}{\bar{k}_m^2 - (\bar{k}_n + \bar{k}_l)^2} e^{i(\bar{k}_n + \bar{k}_l - \bar{k}_j)T_0} + C.C \right]. \end{aligned} \quad (3.166)$$

From where the following four frequencies are observed

$$\begin{aligned} \bar{k}_n + \bar{k}_l + \bar{k}_j &= \bar{k}_k \frac{2(n+l+j) - 3}{2k-1}, \\ |\bar{k}_n - \bar{k}_l - \bar{k}_j| &= \left| \bar{k}_k \frac{2(n-l-j) + 1}{2k-1} \right|, \\ |\bar{k}_n - \bar{k}_l + \bar{k}_j| &= \left| \bar{k}_k \frac{2(n-l+j) - 1}{2k-1} \right|, \\ |\bar{k}_n + \bar{k}_l - \bar{k}_j| &= \left| \bar{k}_k \frac{2(n+l-j) - 1}{2k-1} \right|. \end{aligned}$$

Similar to the analysis before, it is concluded that given  $k, j, n \in \mathbb{N}$ , secular terms occur for  $\mathbb{N} \ni l = p_{li} \leq M$ , where the  $p_{li}$  ( $i = 1, 2, \dots, 7$ ) are defined in Eqs. (3.165).

As it is observed from the previous analysis, the terms involving  $\gamma_{j0}\gamma_{n0}\gamma_{m0}$  and  $\gamma_{j0}\gamma_{m1}$  ( $j, m, n = 1, 2, \dots, M$ ) will produce many secular terms. The number of secular terms produced by those products increases with the number of modes  $M$  used in the Galerkin projection.

After using Eqs. (3.162) and (3.163) it can be easily shown that  $D_1^2 \gamma_{k0} = 0$  and  $D_0 D_1 \gamma_{k1} = 0$ . In addition, it observed that the terms  $D_0 D_2 \gamma_{k0}$  and  $D_0 \gamma_{k0}$  do

produce secular terms. The forcing term is again treated as in Eq. (3.151) to study the primary resonance of mode  $k$ . In this case, however, the detuning parameter  $\sigma$  is defined such that

$$\omega = \bar{k}_k + \sigma\epsilon^2 \quad (3.167)$$

For studying the primary resonance of mode  $k$ , the external force components on all other modes are set to zero,  $Q_j = 0$  for  $j \neq k$ .

Collecting the results, the equation requiring vanishing secular terms for mode  $k$  is

$$-i\bar{k}_k^3\phi A_k - i2\bar{k}_k D_2 A_k + Q_k e^{i\sigma T_2} + S_{1k} + S_{2k} = 0, \quad (3.168)$$

and for modes  $j = 1, 2, \dots, M$  with  $j \neq k$

$$-i\bar{k}_j^3\phi A_j - i2\bar{k}_j D_2 A_j + S_{1j} + S_{2j} = 0, \quad (3.169)$$

where

$$\begin{aligned} S_{1i} := & \frac{1}{3}\mu_2^* \sum_{j,n,m=1}^N G_{ijnm} \bar{k}_n \bar{k}_j \bar{k}_m [A_j A_n A_m \delta_{mpm_1} + A_j \bar{A}_n A_m \delta_{mpm_2} \\ & + A_j A_n \bar{A}_m \delta_{mpm_4} + A_j \bar{A}_n \bar{A}_m \delta_{mpm_6} + \bar{A}_j A_n \bar{A}_m \delta_{mpm_3} \\ & + \bar{A}_j \bar{A}_n A_m \delta_{mpm_5} + \bar{A}_j A_n A_m \delta_{mpm_7}], \end{aligned} \quad (3.170)$$

and

$$\begin{aligned} S_{2i} := & 2(\mu_1^*)^2 \sum_{j,m,n=1}^N \sum_{l=1}^N F_{ijm} F_{mnl} \bar{k}_n \bar{k}_j \bar{k}_m \bar{k}_l \\ & \left[ \frac{1}{\bar{k}_m^2 - (\bar{k}_n + \bar{k}_l)^2} (A_n A_l A_j \delta_{lp_{11}} + A_n A_l \bar{A}_j \delta_{lp_{17}} + \bar{A}_n \bar{A}_l A_j \delta_{lp_{16}}) \right. \\ & \left. + \frac{1}{\bar{k}_m^2 - (\bar{k}_n - \bar{k}_l)^2} (A_n \bar{A}_l A_j \delta_{lp_{14}} + \bar{A}_n A_l \bar{A}_j \delta_{lp_{15}} + A_n \bar{A}_l \bar{A}_j \delta_{lp_{13}} + \bar{A}_n A_l A_j \delta_{lp_{12}}) \right], \end{aligned} \quad (3.171)$$

with  $\delta_{ij}$  the Kronecker delta function. The system of equations given by Eqn. (3.168) and Eqs. (3.169) constitutes a system of  $M$  equations for the  $M$  amplitude unknowns  $A_m$ .

### 3.9.2.1 Primary Resonance of the First Mode

As it was noted in the previous section the number of secular terms at  $\mathcal{O}(\epsilon^2)$  increases with the number of modes  $M$  considered in the Galerkin projection (Eq. (3.138)). In this section, in order to illustrate the solutions that can be obtained, only two modes ( $M = 2$ ) are included in the Galerkin projection. In addition, the primary resonance of the first mode ( $k = 1$ ) is analyzed.

Upon introducing the polar notation  $A_m = a_m(T_2) e^{i\theta_m(T_2)}$  ( $m = 1, 2$ ) and considering imaginary and real parts, it can be shown (refer to App. C) that Eqs. (3.168) and (3.169) lead to the following ODEs for the amplitudes  $a_1$  and  $a_2$ , and phases  $\theta_1$  and  $\theta_2$ ,

$$\begin{aligned} 2\bar{k}_1 a_1' &= -\bar{k}_1^3 \vartheta a_1 + Q_1 \sin \nu - C_3 a_2 a_1^2 \sin \nu_{12}, \\ 2\bar{k}_2 a_2' &= -\bar{k}_2^3 \vartheta a_2 + \frac{1}{3} C_3 a_1^3 \sin \nu_{12}, \\ 2\bar{k}_1 a_1 \nu' &= 2\bar{k}_1 a_1 \sigma + Q_1 \cos \nu + C_1 a_1^3 + C_2 a_1 a_2^2 + C_3 a_2 a_1^2 \cos \nu_{12}, \\ 6\bar{k}_2 a_2 \nu' + 2\bar{k}_2 a_2 \nu_{12}' &= 6\sigma \bar{k}_2 a_2 + C_4 a_2^3 + C_2 a_2 a_1^2 + \frac{1}{3} C_3 a_1^3 \cos \nu_{12}, \end{aligned} \tag{3.172}$$

where  $\nu := \sigma T_2 - \theta_1$ ,  $\nu_{12} := 3\theta_1 - \theta_2$ , primes ( $'$ ) denotes differentiation with respect to  $T_2$ , and the coefficients  $C_i$  ( $i = 1, \dots, 5$ ) are defined in Eqs. (C.21).

In general, it is not possible to obtain a steady-state solution ( $a_1' = a_2' = \nu_{12}' = 0$ ) of Eq. (3.172). The sources of the difficulty are the internal resonance

terms involving  $\nu_{12}$ .

As shown by Eq. (C.21), the coefficient  $C_3$  could be conveniently set to zero by an appropriate choice of the material parameters  $\mu_1^*$  and  $\mu_2^*$ . In this case, a simple analytic solution can be found, and it is given by  $a_2 = 0$ , and

$$\sigma = \frac{\pm \sqrt{Q_1^2 - \vartheta^2 \bar{k}_1^6 a_1^2 - C_1 a_1^3}}{2 \bar{k}_1 a_1}, \quad \sin \nu = \frac{\bar{k}_1^3 \vartheta a_1}{Q_1}. \quad (3.173)$$

From Eqs. (C.21), the coefficient  $C_1$  is restated here to avoid confusion

$$C_1 = \frac{1364}{3375} (\mu_1^*)^2 \pi^2 - \frac{3}{128} \pi^4 \mu_2^*$$

The first of Eqs. (3.173) is an implicit function of the amplitude  $a_1$  in terms of the detuning parameter  $\sigma$ . In Figures 3.11, 3.12 and 3.13, the influences on the frequency response of the nonlinear material properties through the value of  $C_1$ , of the amplitude of the external excitation  $Q_1$  and of the dissipation in the system  $\vartheta$  are shown for this particular case. It is observed that the system depicts frequency hardening behavior for  $C_1 < 0$  and frequency softening for  $C_1 > 0$ . The effect of the damping  $\vartheta$  is to decrease the peak amplitude and to eliminate the unstable branch; and the amplitude of the external loading  $Q_1$  affects the width of the resonant peak, making it wider as  $Q_1$  increases.

### 3.10 Numerical Simulations of Longitudinal Wave Propagation

#### through Nonlinear Viscoelastic Rod with Uniform Cross-Section

As shown in §3.8, when the material mechanical behavior is nonlinear, the speed of propagation of waves depends on the level of stress (or deformation) and

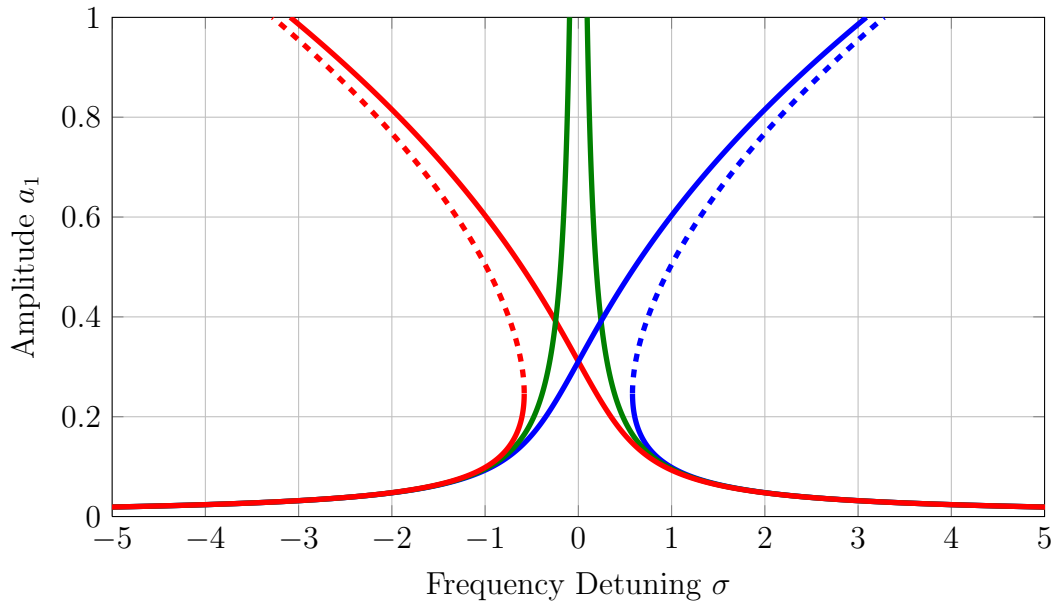


Figure 3.11: Effect of nonlinear material properties  $C_1$  on the frequency response for  $\vartheta = 0.01$  and  $Q_1 = 0.3$ . ( — ):  $C_1 = -10$ ; ( — ):  $C_1 = 0$ ; ( — ):  $C_1 = 10$ . Dashed lines indicate unstable branches.

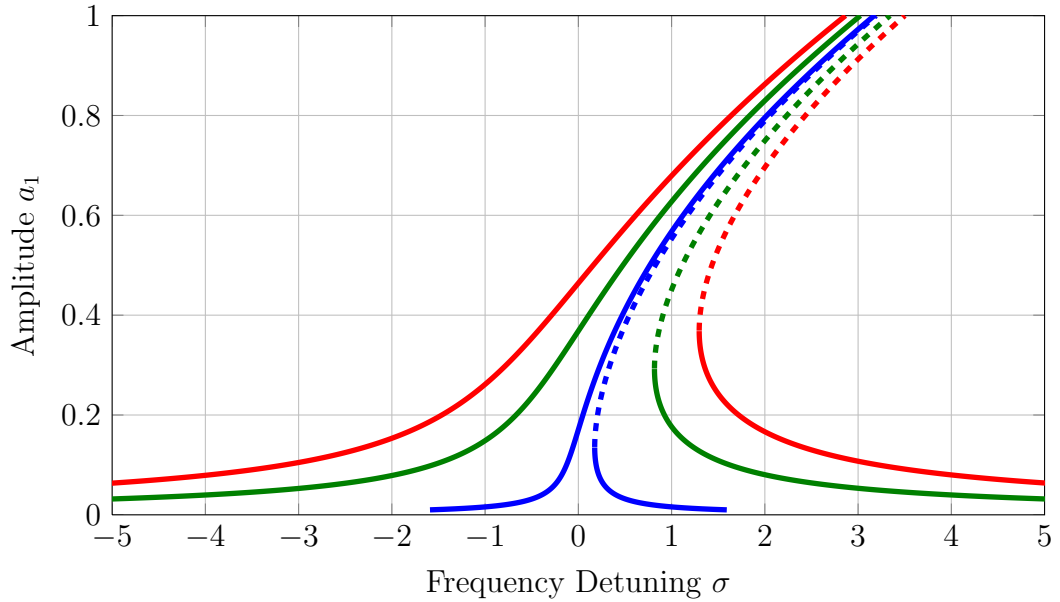


Figure 3.12: Effect of the amplitude of excitation  $Q_1$  on the frequency response for  $\vartheta = 0.01$  and  $C_1 = -10$ . ( — ):  $Q_1 = 0.05$ ; ( — ):  $Q_1 = 0.5$ ; ( — ):  $Q_1 = 1$ . Dashed lines indicate unstable branches.

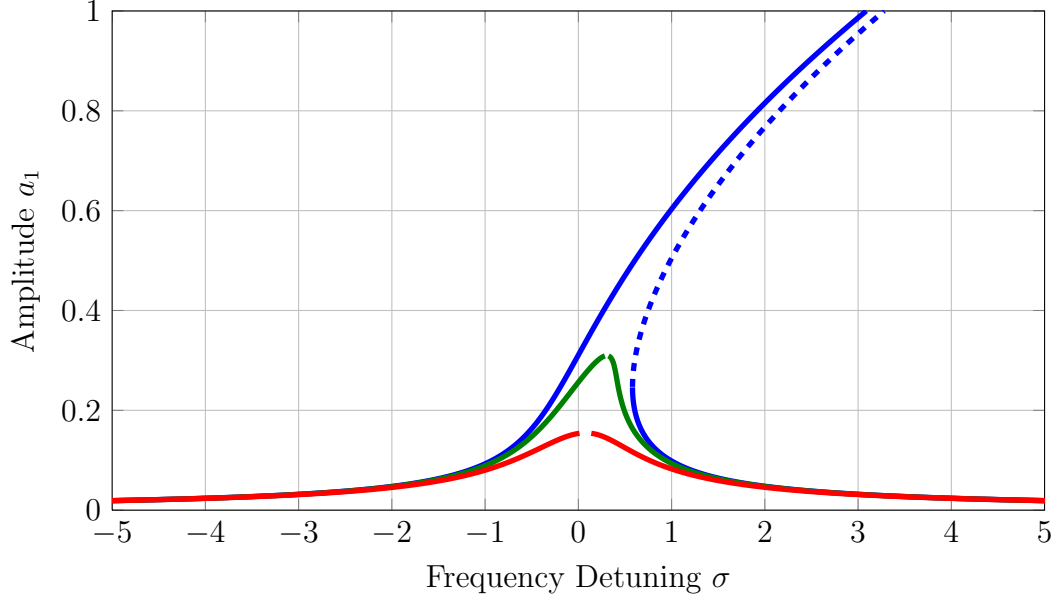


Figure 3.13: Effect of damping  $\vartheta$  on the frequency response for for  $C_1 = -10$  and  $Q_1 = 0.3$ . ( — ):  $\vartheta = 0$ ; ( — ):  $\vartheta = 0.25$ ; ( — ):  $\vartheta = 0.5$ . Dashed lines indicate unstable branches.

on whether the stress is of compressive or of tensile nature. In this section, the effect of the material nonlinearity on the speed of propagation and on the amplitude of stress waves is explored. To this end, the problem of a rod fixed at the left end and forced at the right end is considered. The contents presented in this and the following sections have been extracted and partly adapted from Valdez and Balachandran (2013) for the purposes of this dissertation.

Here, the non-dimensional version of the governing equations (Eqs. (3.108) and (3.109)) are employed. The following initial conditions are considered

$$v(\xi, \tau = 0) = 0, \quad P^*(\xi, \tau = 0) = 0, \quad \dot{v}(\xi, \tau = 0) = \dot{\lambda}(\xi, \tau = 0) = 0, \quad (3.174)$$

together with the following boundary conditions

$$v(\xi = 0, \tau) = 0, \quad P^*(\xi = 1, \tau) = P_B^*(\tau) = P_0^* e^{-\left(\frac{\tau - T_S}{\tau}\right)^2}, \quad (3.175)$$

where  $\mathcal{T}_S$  and  $\mathcal{T}$  are (non-dimensional) parameters that control the center and the width of the stress pulse, respectively. This Gaussian-type of forcing is chosen for the following reasons: i) a finite amount of energy is introduced into the system, and ii) the force approaches a shifted Dirac-delta function in the limit  $\mathcal{T} \rightarrow 0$ , which would represent an ideal impact at time  $\tau = \mathcal{T}_S$ . The value of  $\mathcal{T}_S$  is selected so that for all the simulations, the stress  $P^*$  at  $\tau = 0$  is approximately equal to zero, therefore, compatible with the initial conditions (3.174). For all the cases presented here, a value  $\mathcal{T}_S = 0.5$  is found to be sufficient for that purpose.

The remaining (non-dimensional) parameters of the forcing function  $P_0^*$  and  $\mathcal{T}$  are varied so that a measure of the energy content of the pulse is maintained constant throughout the simulations. The selected measure of energy content (Balachandran and Magrab, 2009) is given by

$$E_P(\tau) := \int_0^\tau P_B^{*2}(s) ds = \sqrt{\frac{\pi}{2}} \frac{P_0^{*2} \mathcal{T}}{2} h(\tau), \quad (3.176)$$

with

$$h(\tau) := \text{Erf}\left(\sqrt{2} \frac{\mathcal{T}_S}{\mathcal{T}}\right) + \text{Erf}\left(\sqrt{2} \frac{\tau - \mathcal{T}_S}{\mathcal{T}}\right) \quad (3.177)$$

where  $\text{Erf}(\cdot)$  is the error function. For the simulations carried out here, a final time of  $\tau_f = 1.5$  is used. This simulation time roughly allows the whole pulse to travel along the length of the rod.

In the cases presented next, the total energy of the pulse is chosen to be  $E_P = 0.01$ . In Fig. 3.14, different pulses with  $E_P = 0.01$  are shown, and their corresponding values of  $\mathcal{T}$  and  $|P_0^*|$  are shown in Table 3.1. It is observed that as

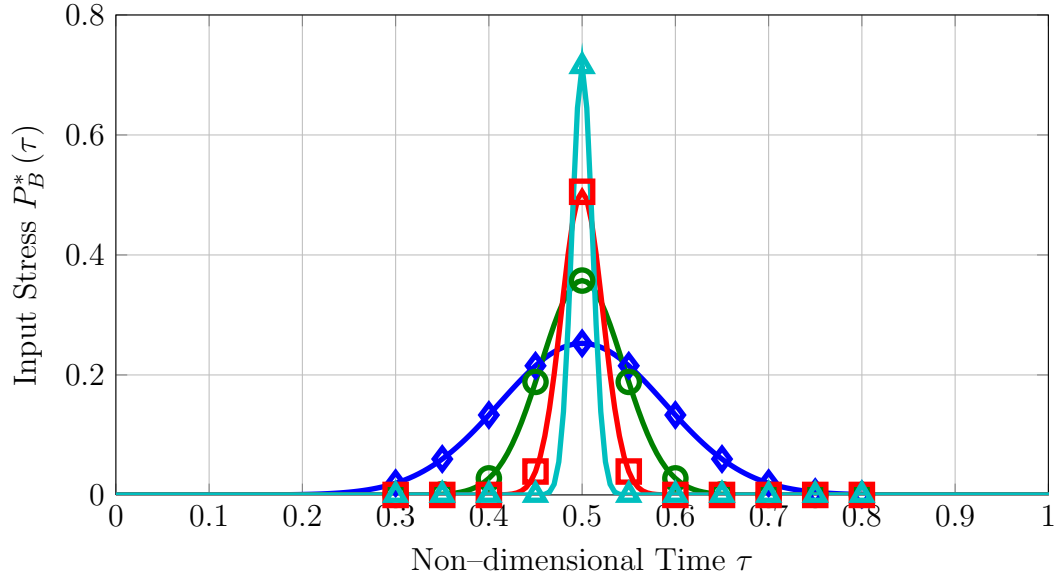


Figure 3.14: Input stresses with energy  $E_P = 0.01$  as a function of time for different values of  $\mathcal{T}$ . ( $\blacklozenge$ ):  $\mathcal{T}=0.125000$ ; ( $\ominus$ ):  $\mathcal{T}=0.062500$ ; ( $\boxplus$ ):  $\mathcal{T}=0.03125$ ; ( $\blacktriangle$ ):  $\mathcal{T}=0.015625$ .

the width of the pulse decreases ( $\mathcal{T} \downarrow$ ), its amplitude increases ( $P_0^* \uparrow$ ) so that  $E_P$  is kept constant. The line styles and/or colors used in Fig. 3.14, and indicated as well in Table 3.1 are used throughout the results section to refer to information corresponding to those particular inputs.

### 3.10.1 Nonlinear Viscoelastic Material Models

The numerical simulation results are compared across different viscoelastic material models, which are obtained through the construction presented in §2.4 by selecting different incompressible, hyperelastic strain energy functions  $\Psi(\lambda)$ . In particular, variations of the Mooney–Rivlin model are considered. For a uniaxial

Table 3.1: Values of  $\mathcal{T}$  and  $P_0^*$  for constant energy value  $E_P = 0.01$ .

Line Style	$\mathcal{T}$	$ P_0^*  = \sqrt{E_P} \left(\frac{8}{\pi \mathcal{T}^2}\right)^{1/4} (h(\tau_f))^{-1/2}$
1 	0.125000	0.25263
2 	0.062500	0.35730
3 	0.031250	0.50530
4 	0.015625	0.71460

stress state, the Mooney–Rivlin strain energy function (refer to A) is given by

$$\Psi(\lambda) = c_1 (\lambda^2 + 2\lambda^{-1} - 3) + c_2 (\lambda^{-2} + 2\lambda - 3), \quad (3.178)$$

where  $\lambda$  is the longitudinal stretch, and  $c_1 > 0$  and  $c_2 \geq 0$  are material constants. If  $c_2 = 0$ , the incompressible, uniaxial Neo–Hookean model is obtained. Introducing Eq. (3.178) into Eq. (3.2) yields

$$f(\lambda) := \frac{d\Psi}{d\lambda} = 2 \left( c_1 + \frac{c_2}{\lambda} \right) \left( \lambda - \frac{1}{\lambda^2} \right), \quad (3.179a)$$

and

$$g(\lambda) := \frac{d^2\Psi}{d\lambda^2} = 2c_1 \left( 1 + \frac{2}{\lambda^3} \right) + 6\frac{c_2}{\lambda^4}. \quad (3.179b)$$

In this particular case, using the definition of the constants  $\mu_n$  from Eq. (3.7), it can be shown that  $\mu_0 = 6(c_1 + c_2)$  and  $\mu_1 = -6(c_1 + 2c_2) = -(\mu_0 + 6c_2)$ . It is observed that there is an infinite number of possible combinations of the material constants  $c_1$  and  $c_2$  that will yield the same value  $\mu_0$ , therefore, the same linearized material model. The following three material models are considered in this study:

- i*) Viscoelastic Mooney–Rivlin model with  $c_1 = c_2 = \mu_0/12$
- ii*) Viscoelastic Neo–Hookean model with  $c_1 = \mu_0/6$ ,  $c_2 = 0$
- iii*) Linearized Viscoelastic model with  $\mu_0 = 6(c_1 + c_2)$

In the simulations carried out in the next section, a value of  $\alpha = 0.001$  is chosen. The non–dimensional Eqs. (3.108) are solved numerically through a self–implemented finite difference scheme (refer to Appendix D). In general terms, the finite difference scheme consists of central difference discretization for the spatial derivatives, incremental approach (iterative) for dealing with the nonlinear terms and trapezoidal (implicit) time marching scheme.

The results obtained with the two nonlinear material models are compared with the results obtained with the linearized model. The comparison is made in terms of the wave profiles, wave amplitude and wave speed for both compression and tension wave pulses.

### 3.10.2 Compression Waves

In Fig. 3.15, the compression wave profiles obtained with the different material models, and for the different inputs from Table 3.1 are compared. Two main features of the waves propagating in the nonlinear viscoelastic media are observed: *i*) change of shape of the wave profile as it travels through the structure; in particular, due to the steepening of the leading wave front, and *ii*) higher amplitude decay for loading inputs with small values of  $\mathcal{T}$  (or higher values of  $|P_0^*|$ ). By contrast, in the linear viscoelastic material case, the wave pulse retains its symmetry about the crest, while

decreasing its amplitude and widening.

The space evolutions of the compressive stress peak ( $P_{\text{peak}}^*/P_0^*$ ) are compared in Fig. 3.16 across material models, and for the different inputs from Table 3.1. As pointed out before, it is observed that the stress peak amplitude decays more drastically with the distance traveled for those waves corresponding to the faster input loads (smaller  $\mathcal{T}$  and larger  $|P_0^*|$ ). It is also noted that the predictions of the nonlinear models largely differ with respect to those of the linearized model. These differences are more pronounced for the cases where the input load has smaller characteristic times  $\mathcal{T}$  (or large amplitudes  $P_0^*$ ). In general, the linearized model predicts lower amplitude decay at any particular location of the stress peak  $\xi_{\text{peak}}$ . These results imply that the amount of energy that the tissue absorbs from the incoming wave pulse is under-predicted by the linearized model. In addition, it is observed that the Mooney–Rivlin viscoelastic model predicts higher amplitude decay when compared to that of the Neo–Hookean viscoelastic model for almost all the values of  $\xi_{\text{peak}}$ .

### 3.10.3 Tension Waves

In Fig. 3.17 the tension wave profiles obtained for the different material models, and for the different inputs from Table 3.1 are compared. The same conclusions regarding compression waves apply for tension waves. In this case, however, the steepening occurs on the trailing end of the wave pulse. In Fig. 3.18, the evolution of the amplitude of the tension peak in space for the different material models and

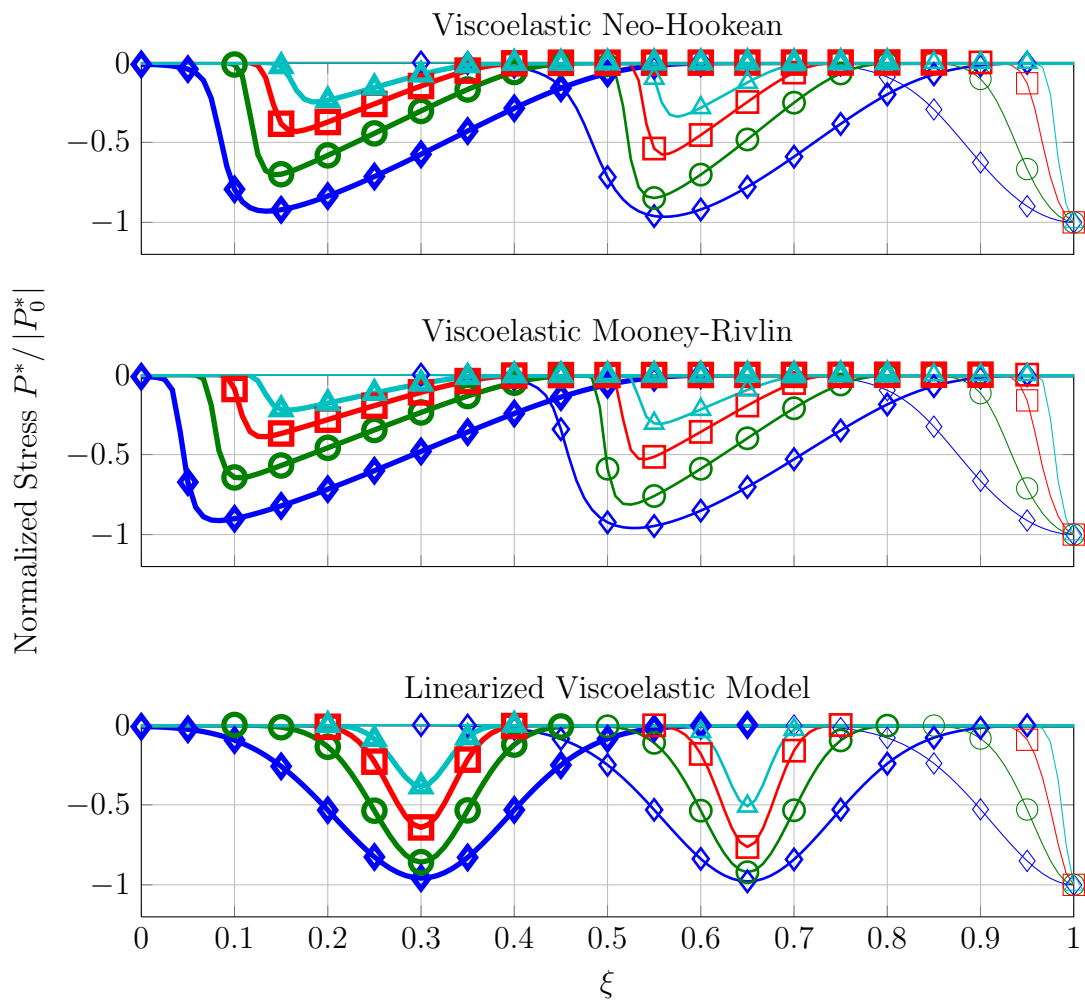


Figure 3.15: Snapshots of compression wave profiles obtained with the two nonlinear viscoelastic models and the linear viscoelastic model. Lines and symbols correspond to the inputs from Table 3.1. Line thickness corresponds to the time of the snapshot; from thinner to thicker, time instants are:  $\tau = 0.5, 0.85, 1.2$ .

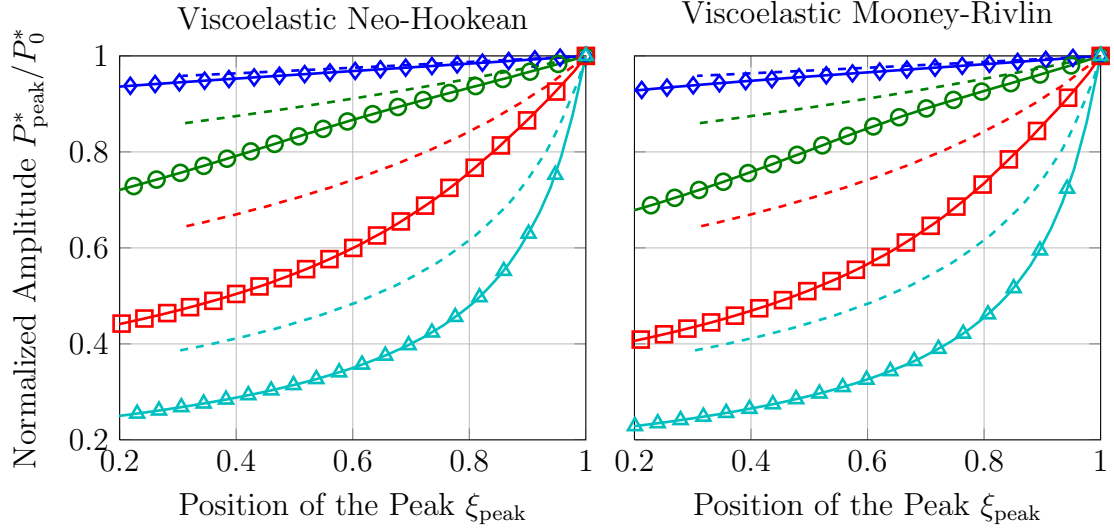


Figure 3.16: Normalized compression peak amplitude  $P_{\text{peak}}^*/P_0^*$  as a function of its location  $\xi_{\text{peak}}$  along the rod. Solid lines with markers: non-linear viscoelastic model; dashed lines: linear viscoelastic model. Line colors correspond to the inputs from Table 3.1.

for the different inputs are compared. Similar to the compression case, it is observed that the linearized model under-predicts the amplitude decay and that the Mooney-Rivlin viscoelastic model predicts higher amplitude decay than the Neo-Hookean viscoelastic model for almost all the values of  $\xi_{\text{peak}}$ .

### 3.10.4 Wave Speed

In this section, the wave speed of the wave pulses presented in §3.10.2 and 3.10.3 is analyzed; and the results are compared across material models and across the various input loads. In this analysis, the wave speed of a wave pulse is considered to be that of the wave crest. In Fig. 3.19, the results obtained with the two nonlinear material models, as well as those obtained with the linearized model are summarized. It is observed that the wave speed predicted with both nonlinear viscoelastic models

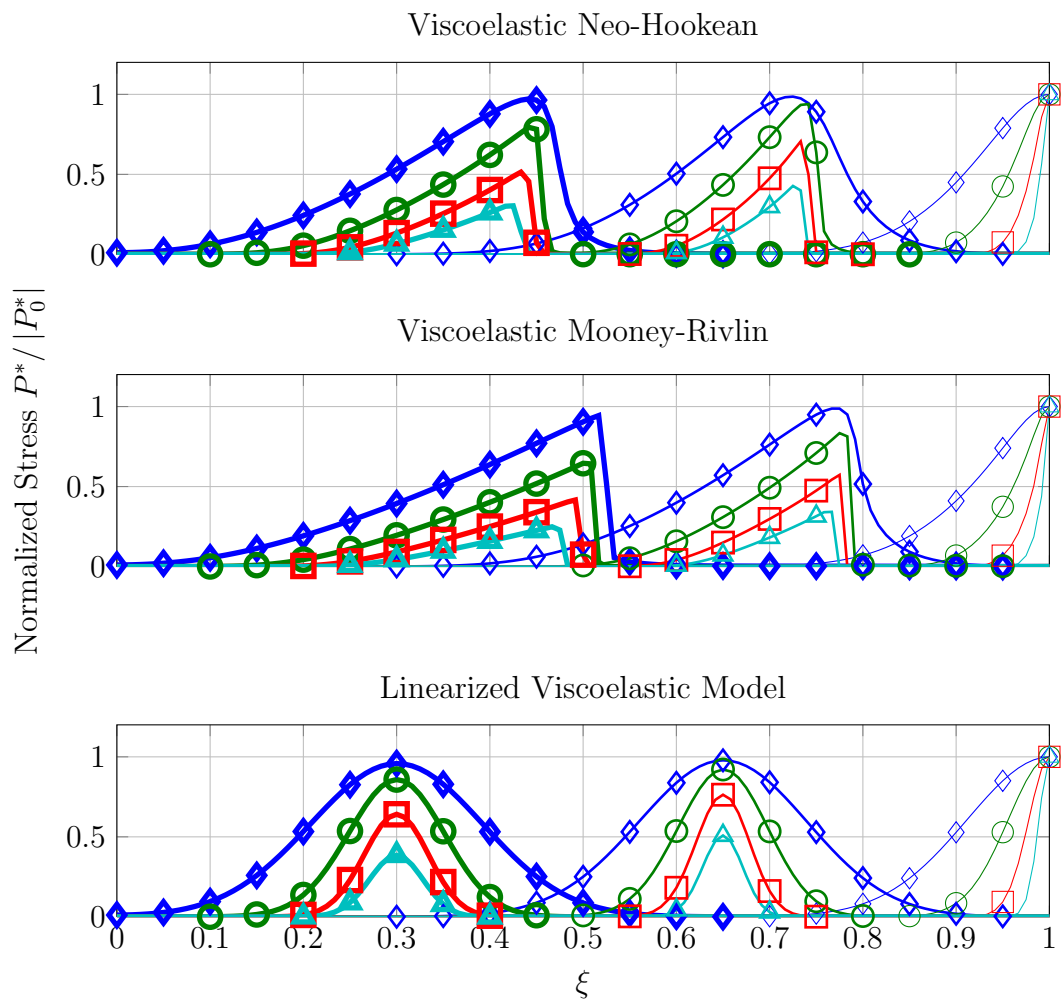


Figure 3.17: Snapshots of tension wave profiles obtained with the two nonlinear viscoelastic models and the linear viscoelastic model. Lines and symbols correspond to the inputs from Table 3.1. Line thickness corresponds to the time of the snapshot; from thinner to thicker, time instants are:  $\tau = 0.5, 0.85, 1.2$ .

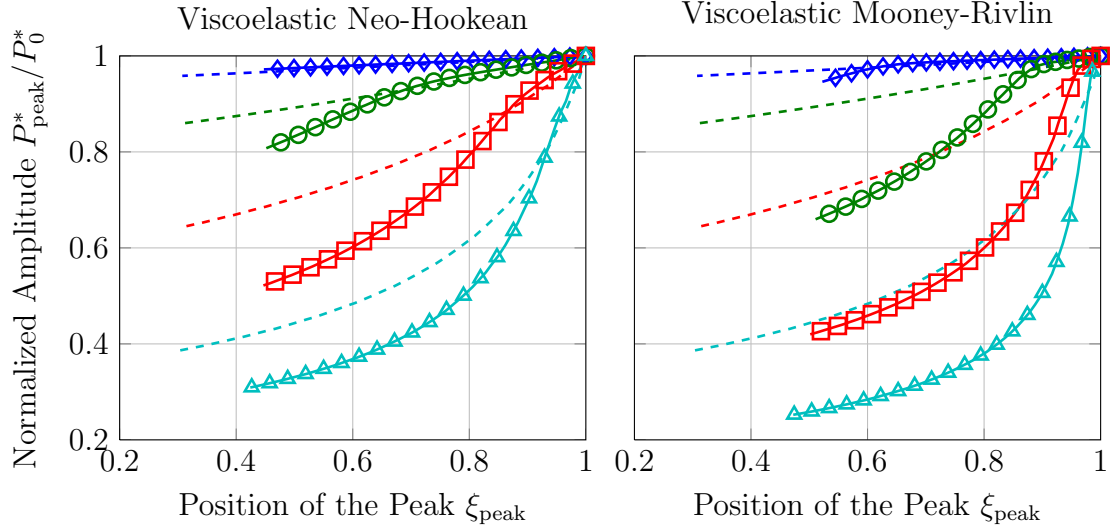


Figure 3.18: Normalized tension peak amplitude  $P_{\text{peak}}^*/P_0^*$  as a function of its location  $\xi_{\text{peak}}$  along the rod. Solid lines with markers: nonlinear viscoelastic model; dashed lines: linear viscoelastic model. Line colors correspond to the inputs from Table 3.1.

varies with the distance  $|\xi_{\text{peak}} - 1|$  traveled by the wave pulse. On the other hand, the wave speed in the linear viscoelastic material is independent of the nature of the stress (compression or tension) and remains the same as a wave pulse travels.

Tension waves propagate slower in the nonlinear viscoelastic material than in the linear viscoelastic material. In contrast, compression waves travel faster in the nonlinear viscoelastic material than in the linear viscoelastic material. This feature was previously observed through the asymptotic analysis of §3.8. This phenomenon is a consequence of the dependence of the wave speed on the local deformation  $\lambda(X, t)$  through the value of  $g(\lambda)$ . The higher the value of  $g(\lambda)$ , the higher the wave speed. For the materials studied here,  $g(\lambda)$  decreases monotonically as the stretch increases. Therefore, waves travel faster as the contraction increases, and slower as the elongation increases.

The implication of this behavior is that some parts of a wave pulse will speed up, while others will slow down. When the fast part of the wave pulse catches up with a slow part of the wave pulse, a steep variation in the stress wave profile is produced. The intensity of this steep variation depends on the dissipation in the material. A high value of dissipation (high value of  $\alpha$ ) will quickly smear out this steep variation. As observed from the results, a compression wave pulse will develop a steep front followed by a rather long lagging tail. On the other hand, a tensile wave pulse will develop a leading sloped front followed by a steep depression at the back.

Finally, it is observed for a compression wave that the higher the amplitude  $|P_0|$  of the input force, the slower the pulse travels. This result may appear contradictory with the statements presented before. However, since the values of  $|P_0|$  and  $\mathcal{T}$  of the input are linked through the fixed energy value  $E_p$ , a higher value of  $|P_0|$  implies a small value of  $\mathcal{T}$ , which in turn implies higher strain rates (as they scale with  $1/\mathcal{T}$ ), and therefore higher dissipation. In consequence, these pulses are attenuated faster, as confirmed by the results in Figs. 3.16. Once the amplitude is quickly decreased, the speed of the pulse decreases as well. The same reasoning can be applied to tension waves.

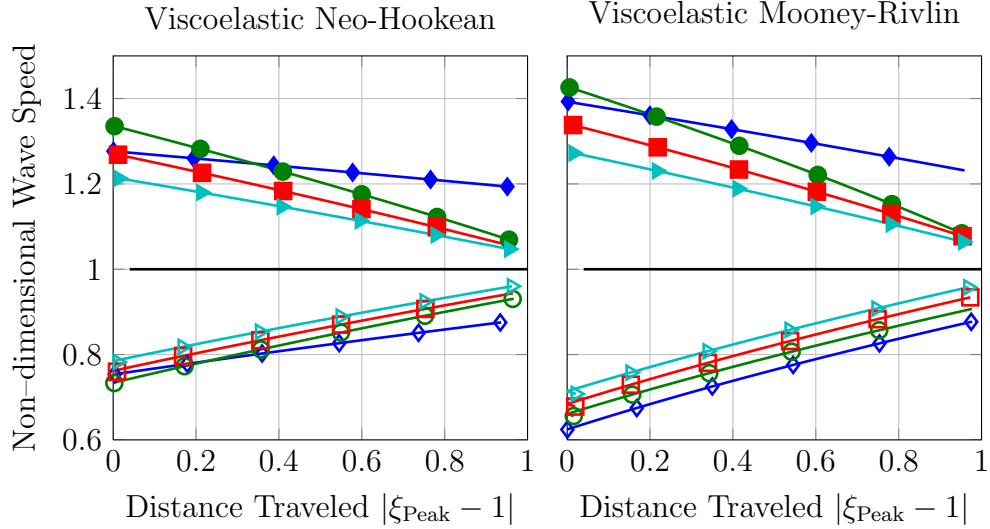


Figure 3.19: Compression and tension wave speeds as a function of distance traveled. Line colors correspond to the inputs from Table 3.1. Filled markers: compression; empty markers: tension. ( — ): linearized viscoelastic model prediction.

### 3.10.5 Concluding Remarks on Material Nonlinearity Effects on Longitudinal Wave Propagation

The occurrence of steep wave fronts may appear solely as an interesting non-linear phenomenon, as it is not clear how these steep wave fronts may contribute to tissue damage. In order to further explore the implications of steep wave fronts, the way in which energy is absorbed by the linear and nonlinear viscoelastic material is analyzed. As shown in Figs. 3.16 and 3.18, as the external loading applied to the nonlinear viscoelastic structure becomes faster ( $\mathcal{T} \searrow$ ) and more intense ( $|P_0^*| \nearrow$ ), for a fixed value of the total energy, the amplitude of the generated stress wave decays in a shorter distance. This observation applies to the linearized viscoelastic model as well. It was noted however, that in the nonlinear system the amplitude decay is

always higher than that in the linear system. A question that arises naturally is how the energy absorption process differs in both systems. The total (non-dimensional) energy absorbed by the material at time  $\tau$  can be shown to be given by

$$W_d = \int_0^\tau \left( \int_0^1 w(s, \tau) ds \right) d\tau, \quad (3.180)$$

where

$$w(\xi, \tau) = \alpha \left[ g(\lambda(\xi, \tau)) \frac{\partial \lambda}{\partial \tau}(\xi, \tau) \right]^2 \quad (3.181)$$

is the energy absorption density. Let us now look at the structure of  $w(\xi, \tau)$ , and how it correlates with the wave pulse shape. In Fig. 3.20 a snapshot of  $w(\xi, \tau)$  at time  $\tau = 0.61625$  corresponding to the input load with  $\mathcal{T} = 0.03125$  is plotted for both, the nonlinear Mooney–Rivlin viscoelastic and the linear viscoelastic model. The difference between the energy absorption patterns for these two materials is evident from the figure. Firstly, it is observed that for the nonlinear viscoelastic material model,  $w(\xi, \tau)$  has a very pronounced peak which is centered at the location of the steep wave front. For the linear viscoelastic material, in contrast, the density  $w(\xi, \tau)$  has two peaks distributed around the crest of the wave profile. Secondly, the maximum value of  $w(\xi, \tau)$  for the nonlinear material, at the particular instant of time, is almost 10 fold that of the linear material. These observations have two implications: the dissipation in the nonlinear viscoelastic material is higher than in the linear viscoelastic material, as was already pointed out; and that the wave pulse instantaneously deposits a highly concentrated amount of energy at the location of the moving step wave front. This highly localized deposition of energy may indeed be an undesirable situation that could lead to tissue damage.

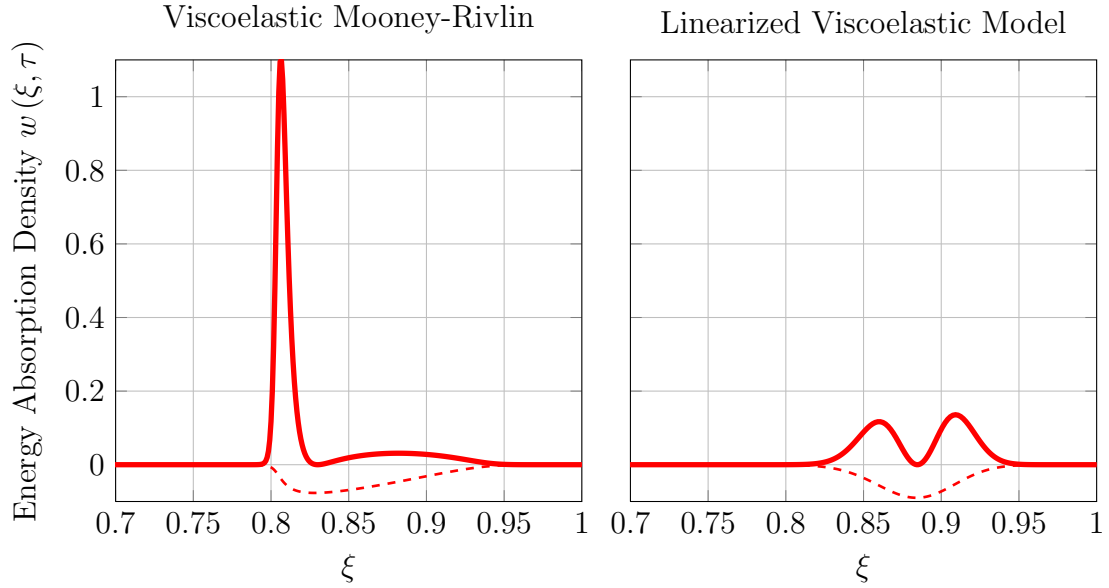


Figure 3.20: Snapshot of the energy absorption density  $w(\xi, \tau = \tau_i)$  at  $\tau_i = 0.61625$  for a compressive wave pulse propagating through nonlinear and linear viscoelastic materials. Solid lines:  $w(\xi, \tau = \tau_i)$ ; dashed lines: wave pulse at  $\tau = \tau_i$ .

In Fig. 3.21, snapshots of  $w(\xi, \tau)$  at different instants of time are presented for the linear viscoelastic and for the Mooney-Rivlin viscoelastic material models. The particular case depicted corresponds to a compressive input force with  $\mathcal{T} = 0.03125$ . An interesting observation is that for the linear viscoelastic material, the maximum value of  $w(\xi, \tau)$  monotonically decreases as the pulse propagates. On the other hand, for the nonlinear viscoelastic material, the maximum value of  $w(\xi, \tau)$  initially grows as the pulse propagates to reach an extreme value, and then it monotonically decreases. This can be appreciated through the shape of the envelope curve.

Finally, it is observed that as the intensity  $|P_0^*|$  of the applied load increases (or  $\mathcal{T}$  decreases), the steep compressive wave front is generated closer to the end where the load is applied. This implies that depending on the external load, damage

### Viscoelastic Mooney-Rivlin

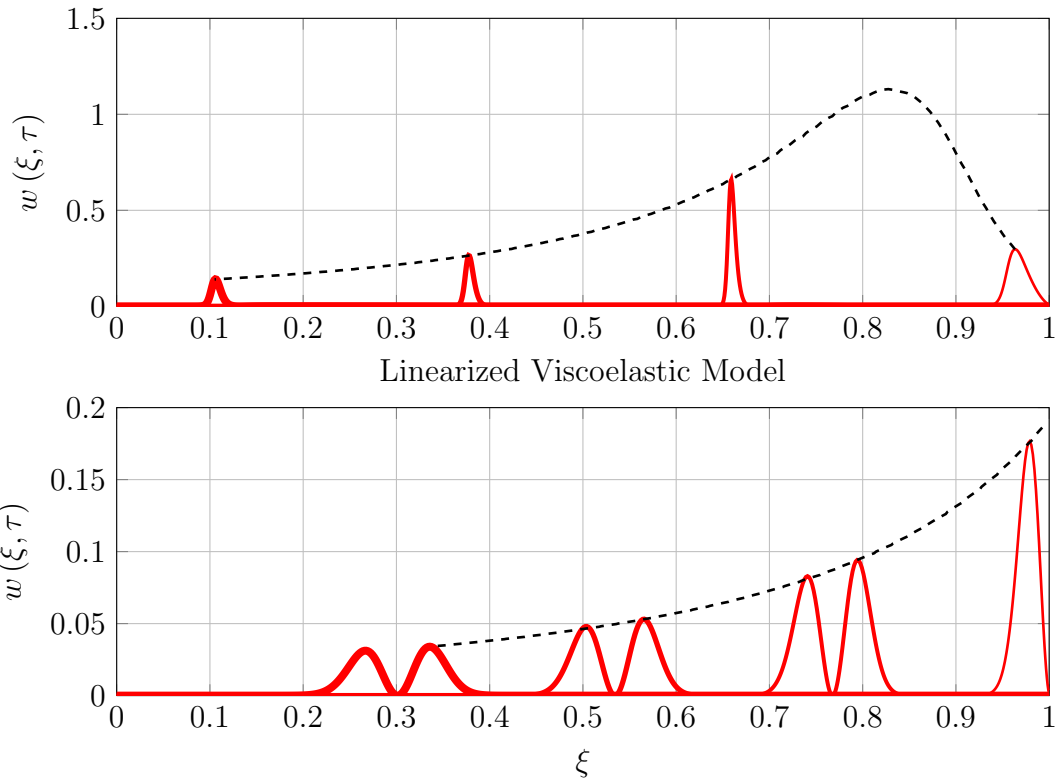


Figure 3.21: Snapshots of the energy absorption density  $w(\xi, \tau_i)$  at different instants of time  $\tau_i$ , corresponding to the compressive input load with  $\mathcal{T} = 0.03125$  and the indicated material models. ( — ): snapshots of  $w(\xi, \tau_i)$ ; ( - - ): envelope of  $w(\xi, \tau_i)$

to the tissue can be imparted at different depths. A load with high amplitude and short duration will mostly produce superficial damage in the area where the load was applied, whereas a load with lower amplitude and longer duration will produce damage in interior regions of the brain.

Another perspective regarding the implications of steep wave fronts can be given if the microscopic structure of the brain tissue is considered. It could be argued that axons in the brain can be damaged by a steep compressive wave front whose width is of the order of the axon diameter ( $\sim 1\mu\text{m}$ ). The damage will be a consequence of a rapid stress differential transversally imparted to the axon by the wave front. Since the wave amplitude is attenuated and the steep front is smoothed out with the distance traveled, it is more likely that axons closer to the cortical regions of the brain will suffer damage due to this mechanism. In addition, the same mechanisms could also be potentially dangerous along material interfaces, such as that between brain gray and white matter.

## Chapter 4

### Longitudinal Wave Propagation through Non–Uniform Structures

In this chapter, the effect of a non–uniform cross section on the longitudinal wave propagation characteristics is analyzed. This study can be applied to understand the effect of geometrical inhomogeneities in axons in the brain white matter.

#### 4.1 Introduction

The development of realistic models for wave propagation through axons, is hindered by the lack of physiological and anatomical data on axons (Segev and Schneidman, 1999). Related studies on the transport of action potential suggest that axons indeed have a cross–section that varies along their length. A branching point, for example, where an axon branches into several extensions can be modeled as a change in the effective cross–sectional area of the axon. In addition, local inhomogeneities such as presynaptic boutons (varicosities) also introduce localized changes of cross section distributed along the length of the axon. These changes in the cross–section have been shown to introduce delays in the transmission of action potentials through the axons, based on the impedance of the inhomogeneities, as compared with that of a uniform axon.

Segev and Schneidman (1999) present a summary of fundamental insights that were obtained through simplified models of action potential transmission through

axons. Schierwagen and Ohme (2008) investigated nerve impulse propagation in non-uniform axons in order to evaluate the impact of geometric non-uniformity on the properties of propagating action potentials. These researchers explored several axonal geometries analytically and concluded that the increase in diameter in axons produces an increase in the speed of propagation of the action potential front and a decrease in the amplitude of the spike. Schierwagen (2009) presented a review of mathematical and computational modeling of neuronal nerve impulse transmission. Although not concerned with mechanical wave propagation, these studies help identify the non-uniform geometry of axons in the white matter.

## 4.2 Non-Uniform Rod Model

The governing equations for longitudinal waves in a rod with non-uniform cross-section  $\mathcal{A}(X)$  are given by Eqs. (3.1) and (3.2) which are repeated here:

$$\left\{ \begin{array}{l} \frac{\partial}{\partial X} (P\mathcal{A}) = \rho_0 \mathcal{A} \frac{\partial^2 u}{\partial t^2} \\ \frac{\partial^2 u}{\partial X \partial t} = -\kappa g(\lambda)^{-2} [f(\lambda) - P] \\ \lambda = \frac{\partial u}{\partial X} + 1, \end{array} \right. \quad (4.1)$$

where

$$\begin{aligned} f(\lambda) &:= \frac{d\Psi}{d\lambda}, \\ g(\lambda) &:= \frac{d^2\Psi}{d\lambda^2} = \frac{df(\lambda)}{d\lambda}. \end{aligned} \quad (4.2)$$

### 4.2.1 Scaling of Variables

Similar to §3.7.1, Eqs. (4.1) and (4.2) are rescaled by using the following characteristic length, time, stress and area variables, respectively:  $L_C = L$ ,  $T_C =$

$L/c_0$ ,  $P_C = \mu_0$  and  $\mathcal{A}_C$ . Again, the following non-dimensional variables are defined:  $v := u/L_C$ ,  $\xi := X/L_C$ ,  $\tau := t/T_C$ ,  $P^* := P/P_C$ ,  $f^* := f/P_C$ ,  $g^* := g/P_C$  and  $\mathcal{A}^* := \mathcal{A}/\mathcal{A}_C$ . The scaled (non-dimensional) equations are then given by

$$\left\{ \begin{array}{l} \frac{\partial}{\partial \xi} (P^* \mathcal{A}^*) = \mathcal{A}^* \frac{\partial^2 v}{\partial \tau^2} \\ P^* = f^*(\lambda) + \alpha [g^*(\lambda)]^2 \frac{\partial \lambda}{\partial \tau} \\ \lambda = \frac{\partial v}{\partial \xi} + 1. \end{array} \right. \quad (4.3)$$

where  $\alpha$  is defined in Eq. (3.13)

$$\alpha := \frac{\mathcal{T}_d c_0}{L} = \frac{\mu_0 / \kappa}{L/c_0}.$$

### 4.3 Linear Viscoelastic Material Case

Similar to the analysis presented in §3.3, in order to obtain insights into the characteristics of the propagation of waves in systems described by Eqs. (4.3), the system with linearized viscoelastic material model is analyzed first. As discussed in §3.3, the linearized viscoelastic material model is obtained by using a quadratic strain energy function  $\Psi$ . Setting  $\Psi = \frac{1}{2} \mu_0 (\lambda - 1)^2$  in the expressions of  $f^*$  and  $g^*$ , and combining the resulting equations yields the following governing PDE,

$$\alpha \frac{\partial^3 v}{\partial \xi^2 \partial \tau} + \frac{\partial^2 v}{\partial \xi^2} - \frac{\partial^2 v}{\partial \tau^2} = -\frac{\partial \ln(\mathcal{A}^*)}{\partial \xi} \left[ \frac{\partial v}{\partial \xi} + \alpha \frac{\partial^2 v}{\partial \xi \partial \tau} \right]. \quad (4.4)$$

### 4.3.1 Dispersion Relation for a Semi-Infinite, Non-Uniform Linear Viscoelastic Rod

Similar to the analysis carried out in §3.5 for rods with uniform cross-section, here, the wave characteristics of semi-infinite rods with non-uniform cross-section, subjected to a harmonic stress boundary condition  $P^*(\xi = 0, \tau) = P_0 e^{-i\tilde{\omega}\tau}$  are studied.

In order to move forward with the analysis of Eq. (4.4), it is necessary to specify a shape of the cross-section. The particular choice of a cross-section that varies exponentially with  $\xi$  allows us to simplify the problem, and in turn, to observe the effects of increasing or decreasing (in the direction of propagation) cross-section. In particular, the cross-sectional area is considered to vary according to  $\mathcal{A}(\xi) = \mathcal{A}_0^* e^{2\tilde{\gamma}\xi}$ . In this particular case, Eq. (4.4) reduces to

$$\alpha \frac{\partial^3 v}{\partial \xi^2 \partial \tau} + \frac{\partial^2 v}{\partial \xi^2} - \frac{\partial^2 v}{\partial \tau^2} = -2\tilde{\gamma} \left[ \frac{\partial v}{\partial \xi} + \alpha \frac{\partial^2 v}{\partial \xi \partial \tau} \right]. \quad (4.5)$$

Now, a solution in the form

$$v(\xi, \tau) = V(\xi) e^{-i\tilde{\omega}\tau} \quad (4.6)$$

is assumed. Replacing Eq. (4.6) into Eq. (4.5), yields the following ODE

$$V'' + 2\tilde{\gamma}V' + \frac{\tilde{\omega}^2}{1 - i\alpha\tilde{\omega}}V = 0, \quad (4.7)$$

where the primes denote differentiation with respect to  $\xi$ . The general solution of Eq. (4.7) is given by  $V(\xi) = V_0 e^{i\tilde{k}\xi}$  where  $\tilde{k} \in \mathbb{C}$  is the (complex) wave number whose dependence on the frequency  $\tilde{\omega}$  is given by the following dispersion relation

$$D(\tilde{k}, \tilde{\omega}) = -\tilde{k}^2 + 2\tilde{\gamma}\tilde{k}i + \frac{\tilde{\omega}^2}{1 - i\alpha\tilde{\omega}} = 0. \quad (4.8)$$

Explicitly, the two solutions for the wave number are given by

$$\tilde{k}_{1,2} = i\tilde{\gamma} \pm \sqrt{-\tilde{\gamma}^2 + \frac{\tilde{\omega}^2}{1 - i\alpha\tilde{\omega}}} = i\tilde{\gamma} \pm \sqrt{A^2(\tilde{\omega}) e^{i\phi(\tilde{\omega})} - \tilde{\gamma}^2}. \quad (4.9)$$

where  $A(\tilde{\omega})$  and  $\phi(\tilde{\omega})$  were previously defined in Eq. (3.75) and are repeated here for clarity,

$$A(\tilde{\omega}) := \frac{\tilde{\omega}}{(1 + \alpha^2\tilde{\omega}^2)^{\frac{1}{4}}}, \quad \tan \phi(\tilde{\omega}) := \alpha\tilde{\omega}.$$

It can be shown that the wave numbers  $\tilde{k}_1$  and  $\tilde{k}_2$  can be expressed in the following form

$$\begin{aligned} \tilde{k}_1 &= C^{\frac{1}{2}} \cos \theta + i \left( \tilde{\gamma} + C^{\frac{1}{2}} \sin \theta \right), \\ \tilde{k}_2 &= -C^{\frac{1}{2}} \cos \theta + i \left( \tilde{\gamma} - C^{\frac{1}{2}} \sin \theta \right), \end{aligned} \quad (4.10)$$

where

$$C = \sqrt{(A^2 \cos \phi - \tilde{\gamma}^2)^2 + A^4 \sin^2 \phi}, \quad \tan 2\theta = \frac{A^2 \sin \phi}{A^2 \cos \phi - \tilde{\gamma}^2}. \quad (4.11)$$

Since  $-\pi < 2\theta \leq \pi$ , then  $-\pi/2 < \theta \leq \pi/2$ . Therefore,  $\cos \theta \geq 0$ . Then, it is observed that the solution  $\tilde{k}_2$  corresponds to a left traveling wave (with phase  $\xi C^{\frac{1}{2}} \cos \theta + \tilde{\omega}\tau$ ); and therefore, it is disregarded in view of the radiation condition previously discussed in the text after Eq. (3.71). In consequence, the wave number for right traveling waves is given by

$$\tilde{k} = C^{\frac{1}{2}} \cos \theta + i \left( C^{\frac{1}{2}} \sin \theta + \tilde{\gamma} \right) = \tilde{k}_{\text{Re}} + i\tilde{k}_{\text{Im}}. \quad (4.12)$$

Applying the boundary condition at  $\xi = 0$  yields the following result

$$P^*(\xi = 0, \tau) = \frac{\partial v}{\partial \xi} + \alpha \frac{\partial^2 v}{\partial \xi \partial \tau} \Big|_{\xi=0} = P_0 e^{-i\tilde{\omega}\tau} \Rightarrow V_0 = \frac{P_0}{i\tilde{k} (1 - i\alpha\tilde{\omega}\tilde{k})}. \quad (4.13)$$

Now, from Eqs. (3.14) and (4.13), the stress solution is given by

$$P^*(\xi, \tau) = P_0 e^{i(\tilde{k}\xi - \tilde{\omega}\tau)} \quad (4.14)$$

Performing algebraic manipulations and using trigonometric identities, it can be shown that

$$C = \frac{1}{1 + \alpha^2 \tilde{\omega}^2} \sqrt{(\tilde{\omega}^2 - \tilde{\gamma}^2 (1 + \alpha^2 \tilde{\omega}^2))^2 + \alpha^2 \tilde{\omega}^6}, \quad (4.15)$$

$$\cos \theta = \frac{1}{\sqrt{2}} \left[ 1 + \frac{\tilde{\omega}^2 - (1 + \alpha^2 \tilde{\omega}^2) \tilde{\gamma}^2}{\sqrt{(\tilde{\omega}^2 - (1 + \alpha^2 \tilde{\omega}^2) \tilde{\gamma}^2)^2 + \alpha^2 \tilde{\omega}^6}} \right]^{1/2}, \quad (4.16)$$

and

$$\sin \theta = \frac{1}{\sqrt{2}} \left[ 1 - \frac{\tilde{\omega}^2 - (1 + \alpha^2 \tilde{\omega}^2) \tilde{\gamma}^2}{\sqrt{(\tilde{\omega}^2 - (1 + \alpha^2 \tilde{\omega}^2) \tilde{\gamma}^2)^2 + \alpha^2 \tilde{\omega}^6}} \right]^{1/2}. \quad (4.17)$$

Finally, the stress solution for a right traveling wave can be written in the following form:

$$P^*(\xi, \tau) = P_0 e^{-\tilde{k}_{Im}\xi} e^{i(\tilde{k}_{Re}\xi - \tilde{\omega}\tau)} = P_0 e^{-\tilde{\beta}\xi} e^{i\tilde{k}_{Re}(\xi - \tilde{c}\tau)}, \quad (4.18)$$

where the phase speed  $\tilde{c}$  and the attenuation  $\tilde{\beta}$  are introduced. These quantities are defined as

$$\tilde{c} := \frac{\tilde{\omega}}{\tilde{k}_{Re}} = \frac{\tilde{\omega}}{C^{1/2} \cos \theta}, \quad (4.19)$$

and

$$\tilde{\beta} := \tilde{k}_{Im} = C^{1/2} \sin \theta + \tilde{\gamma}. \quad (4.20)$$

Introducing Eqs. (4.15) through (4.17) into Eqs. (4.19) and (4.20), and performing algebraic manipulations, the final expressions are obtained:

$$\tilde{c} = \left[ \frac{2\tilde{\omega}^2 (1 + \tilde{\omega}^2)}{\sqrt{(\tilde{\omega}^2 - (1 + \tilde{\omega}^2) \tilde{\gamma}^2)^2 + \tilde{\omega}^6} + \tilde{\omega}^2 - (1 + \tilde{\omega}^2) \tilde{\gamma}^2} \right]^{1/2} \quad (4.21)$$

and

$$\alpha\tilde{\beta} = \check{\gamma} + \left[ \frac{\sqrt{(\check{\omega}^2 - (1 + \check{\omega}^2)\check{\gamma}^2)^2 + \check{\omega}^6 - \check{\omega}^2 + (1 + \check{\omega}^2)\check{\gamma}^2}}{2(1 + \check{\omega}^2)} \right]^{1/2}. \quad (4.22)$$

where  $\check{\omega} := \alpha\tilde{\omega}$  and  $\check{\gamma} := \alpha\tilde{\gamma}$ . The phase speed and attenuation as a function of the frequency, for exponential variation of the cross-section, and for different values of  $\check{\gamma}$  are shown in Fig. 4.1. It is observed that the wave speed in this case is larger than that corresponding to a rod with uniform cross-section at all frequencies, regardless of the sign of  $\check{\gamma}$ . On the other hand, for positive values of  $\check{\gamma}$  (increasing cross-section) the attenuation is higher than that of a uniform rod. The contrary is true for negative values of  $\check{\gamma}$  (contracting or decreasing cross-section). It is also interesting to note that for  $\check{\gamma} \neq 0$ , the attenuation curves (and also the phase speed curves) present a minimum value at a particular value of the frequency  $\check{\omega}$ . If the non-uniform rod had no dissipation  $\alpha = 0$ , then a cutoff frequency (frequency for which  $\tilde{k}_{\text{Re}} = 0$ ) would have been observed. As a consequence of the dissipation, a non-uniform rod does not have a cutoff frequency, but instead, a frequency for minimum wave speed and attenuation.

#### 4.4 Semi-Infinite Linear Viscoelastic Rod with Weakly (Slowly) Varying Cross-Section

Here, the propagation of longitudinal waves along a linear, semi-infinite and non-uniform rod with small dissipation  $\alpha \ll 1$  and slowly varying cross-section is studied. An asymptotic solution of Eq. (4.4) is sought by the method of multiple scales. A small parameter  $\epsilon \ll 1$  is introduced and, similarly to previous analyses,

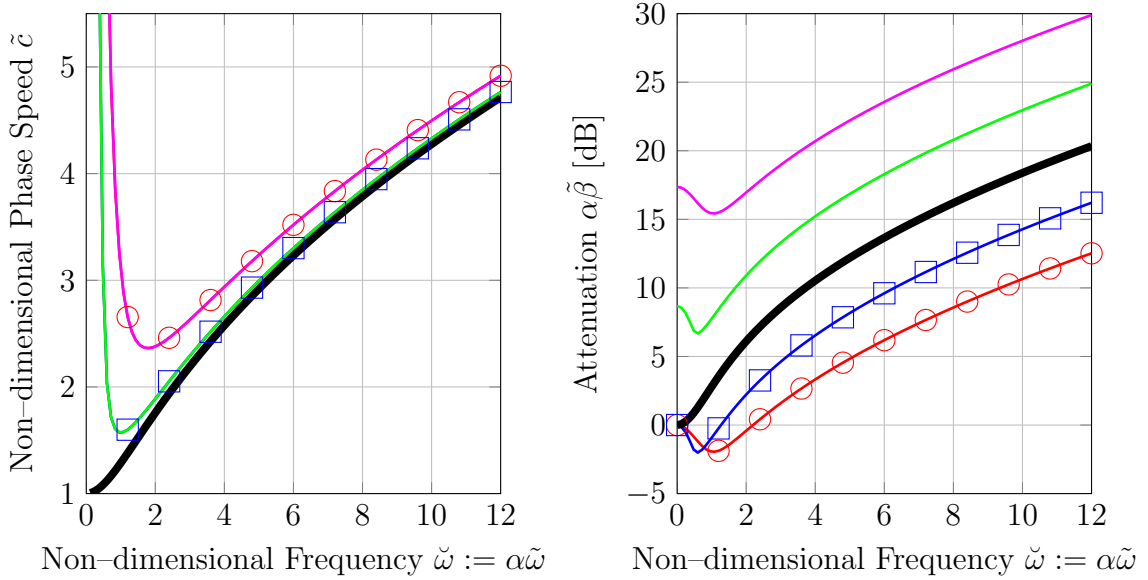


Figure 4.1: Phase speed and attenuation of harmonic waves for a rod with exponential cross-sectional area  $\mathcal{A}^* = e^{2\tilde{\gamma}\xi}$ . ( $\ominus$ ):  $\alpha\tilde{\gamma} = -1$ ; ( $\boxplus$ ):  $\alpha\tilde{\gamma} = -0.5$ ; ( $\text{—}$ ):  $\alpha\tilde{\gamma} = 0$ ; ( $\text{—}$ ):  $\alpha\tilde{\gamma} = 0.5$ ; ( $\text{—}$ ):  $\alpha\tilde{\gamma} = 1$ .

the dissipation term is rescaled as  $\alpha = \vartheta\epsilon$ .

In order to capture the effect of the slow variation in the cross-section, a short spatial scale  $X_1 := \epsilon\xi$  is introduced, in addition to a long spatial scale  $X_0 := \xi$  and a fast time scale  $T_0 := \tau$ . Moreover, the cross-section is considered to depend exclusively on the variable  $X_1$ , that is to say,  $\mathcal{A}^* = \mathcal{A}^*(X_1)$ . Similar to the analysis presented in §3.4, when deemed convenient the following fast scales are introduced in replacement of  $X_0$  and  $T_0$ ,

$$s_1 := \xi - \tau = X_0 - T_0 \qquad s_2 := \xi + \tau = X_0 + T_0. \qquad (4.23)$$

Also, the notation  $(\tilde{\cdot})$  is employed to indicate functions of the variables  $s_1$  and  $s_2$  according Eq. (3.18).

An asymptotic expansion solution is sought in the form

$$v(\xi, \tau; \epsilon) = \check{v}_0(s_1, s_2, X_1) + \epsilon \check{v}_1(s_1, s_2, X_1) + \mathcal{O}(\epsilon^2) \Big|_{\substack{s_1 = \xi + \tau \\ s_2 = \xi - \tau \\ X_1 = \epsilon \xi}}. \quad (4.24)$$

In order to simplify the analysis, homogenous initial conditions are considered:

$$v(\xi, \tau = 0) = 0 \quad \frac{\partial v}{\partial \tau}(\xi, \tau) \Big|_{\tau=0} = 0. \quad (4.25)$$

Considering  $s_1$ ,  $s_2$  and  $X_1$  as independent variables, the derivatives appearing in Eq. (4.4) are expressed as:

$$\frac{\partial}{\partial \tau} = -\frac{\partial}{\partial s_1} + \frac{\partial}{\partial s_2} \quad (4.26a)$$

$$\frac{\partial^2}{\partial \tau^2} = \frac{\partial^2}{\partial s_1^2} - 2\frac{\partial^2}{\partial s_1 \partial s_2} + \frac{\partial^2}{\partial s_2^2} \quad (4.26b)$$

$$\frac{\partial}{\partial \xi} = \frac{\partial}{\partial s_1} + \frac{\partial}{\partial s_2} + \epsilon \frac{\partial}{\partial X_1} \quad (4.26c)$$

$$\frac{\partial^2}{\partial \xi^2} = \frac{\partial^2}{\partial s_1^2} + \frac{\partial^2}{\partial s_2^2} + 2\frac{\partial^2}{\partial s_1 \partial s_2} + 2\epsilon \frac{\partial}{\partial X_1} \left( \frac{\partial}{\partial s_1} + \frac{\partial}{\partial s_2} \right) + \epsilon^2 \frac{\partial^2}{\partial X_1^2}. \quad (4.26d)$$

Replacing Eqs. (4.26) and (4.24) into Eq. (4.4), and equating coefficients of equal powers in  $\epsilon$  result in the following equations:

$$\mathcal{O}(\epsilon^0) : \quad \frac{\partial^2 \check{v}_0}{\partial s_1 \partial s_2} = 0, \quad (4.27)$$

$$\begin{aligned} \mathcal{O}(\epsilon^1) : \quad 4\frac{\partial^2 \check{v}_1}{\partial s_1 \partial s_2} = & -2\frac{\partial}{\partial X_1} \left( \frac{\partial}{\partial s_1} + \frac{\partial}{\partial s_2} \right) \check{v}_0 \\ & - \frac{\partial}{\partial X_1} (\ln \mathcal{A}^*) \left( \frac{\partial}{\partial s_1} + \frac{\partial}{\partial s_2} \right) \check{v}_0 \\ & - \vartheta \left( -\frac{\partial}{\partial s_1} + \frac{\partial}{\partial s_2} \right) \left( \frac{\partial^2}{\partial s_1^2} + \frac{\partial^2}{\partial s_2^2} + 2\frac{\partial^2}{\partial s_1 \partial s_2} \right) \check{v}_0. \end{aligned} \quad (4.28)$$

Similar to the analysis in §3.4, the general solution of Eq. (4.27) is given by

$$\check{v}_0(s_1, s_2, X_1) = \check{F}_0(s_1, X_1) + \check{G}_0(s_2, X_1). \quad (4.29)$$

However,  $G_0(s_2, X_1) = 0$  by invoking the radiation condition discussed in §3.5, or by the same arguments presented in §3.8. Substituting Eq. (4.29) into Eq. (4.28) the following equation is obtained

$$4 \frac{\partial^2 \check{v}_1}{\partial s_1 \partial s_2} = -2 \frac{\partial}{\partial X_1} \frac{\partial \check{F}_0}{\partial s_1} + \vartheta \frac{\partial^3 \check{F}_0}{\partial s_1^3} - \frac{\partial}{\partial X_1} (\ln \mathcal{A}^*) \frac{\partial \check{F}_0}{\partial s_1}. \quad (4.30)$$

Integrating with respect to  $s_1$  and  $s_2$ , the general solution for  $\check{v}_1$  is given by

$$2\check{v}_1 = \left( \frac{1}{2} \vartheta \frac{\partial^2 \check{F}_0}{\partial s_1^2} - \frac{\partial \check{F}_0}{\partial X_1} - \frac{1}{2} \check{F}_0 \frac{\partial}{\partial X_1} (\ln \mathcal{A}^*) \right) s_2 + \check{F}_1(s_1, X_1) + \check{G}_1(s_2, X_1). \quad (4.31)$$

If  $\check{F}_0$  and its derivatives are bounded, then for a uniformly valid expansion, the secular terms on the RHS of Eq. (4.31) (unbounded in  $s_1$  and  $s_2$ ) are to vanish.

This requirement is equivalent to

$$\frac{1}{2} \vartheta \frac{\partial^2 \check{F}_0}{\partial s_1^2} - \frac{\partial \check{F}_0}{\partial X_1} - \frac{1}{2} \check{F}_0 \frac{\partial}{\partial X_1} (\ln \mathcal{A}^*) = 0. \quad (4.32)$$

The solution for  $\check{F}_0$  can be obtained by performing the Fourier Transform  $\mathcal{F}$  to Eq. (4.32) with respect to  $s_1$  to obtain,

$$\omega^2 \frac{1}{2} \vartheta \hat{F}_0 + \frac{\partial \hat{F}_0}{\partial X_1} + \frac{1}{2} \hat{F}_0 \frac{\partial}{\partial X_1} (\ln \mathcal{A}^*) = 0, \quad (4.33)$$

where  $\hat{F}_0 := \mathcal{F}[\check{F}_0]$ . The solution of Eq. (4.33) can be shown to be given by

$$\hat{F}_0(\omega, X_1) = \hat{F}_0(\omega, 0) \left( \frac{\mathcal{A}^*(0)}{\mathcal{A}^*(X_1)} \right)^{1/2} e^{-\frac{1}{2} \vartheta \omega^2 X_1}. \quad (4.34)$$

Performing the inverse Fourier Transform  $\mathcal{F}^{-1}$ , it can be shown (Evans, 2010, sec. 4.3.1) that

$$\check{F}_0(s_1, X_1) = \left( \frac{\mathcal{A}^*(0)}{\mathcal{A}^*(X_1)} \right)^{1/2} \frac{1}{\sqrt{2\vartheta\pi X_1}} \int_{-\infty}^{+\infty} e^{-\frac{(s_1-y)^2}{2\vartheta X_1}} \check{F}_0(y, X_1 = 0) dy. \quad (4.35)$$

The zero-th order approximation of the stress, given by  $P_0 = \partial\check{v}/\partial X_0 = \partial\check{F}_0/\partial s_1$  is

$$\check{P}_0(s_1, X_1) = - \left( \frac{\mathcal{A}^*(0)}{\mathcal{A}^*(X_1)} \right)^{1/2} \frac{1}{\sqrt{2\vartheta\pi X_1}} \int_{-\infty}^{+\infty} \frac{s_1 - y}{\vartheta X_1} e^{\frac{(s_1 - y)^2}{2\vartheta X_1}} \check{F}_0(y, X_1 = 0) dy. \quad (4.36)$$

From Eq. (4.36), the effect of the varying cross-sectional area on the amplitude of the stress waves is directly appreciated. An increase in the cross-sectional area ( $\mathcal{A}^*(X_1) > \mathcal{A}^*(0)$ ) produces a decrease in the amplitude of the waves, whereas the opposite is true for a decreasing cross-sectional area ( $\mathcal{A}^*(X_1) < \mathcal{A}^*(0)$ ). On the other hand, dissipation in the system always makes the amplitude the waves decrease. Similar to the analysis in §3.4,  $\check{F}_0(s_1, X_1 = 0)$  is obtained from the boundary/initial conditions.

#### 4.4.1 Semi-Infinite Linear Viscoelastic Rod with Varying Cross-Section and with Prescribed Stress

As in §3.4.2 the following boundary condition at  $\xi = 0$

$$P(\xi = 0, \tau) = \frac{\partial v}{\partial \xi} + \alpha \frac{\partial^2 v}{\partial \tau \partial \xi} \Big|_{\xi=0} = \varrho(\tau) \quad (4.37)$$

is considered, where  $\varrho(\tau)$  is a given function, with  $\varrho(0) = 0$  and  $\varrho'(0) = 0$ . Using the result from Eq. (B.16), it can be shown that

$$F_0(s_1, X_1 = 0) = -u(-s_1) \int_0^{-s_1} \varrho(s) ds \quad (4.38)$$

Substituting Eq. (4.38) into (4.36), and operating on the integral results in

$$\check{P}(s_1, X_1) \sim \left( \frac{\mathcal{A}^*(0)}{\mathcal{A}^*(X_1)} \right)^{1/2} \frac{1}{\sqrt{2\vartheta\pi X_1}} \int_0^{+\infty} \frac{s_1 + y}{\vartheta X_1} e^{\frac{(s_1 + y)^2}{2\vartheta X_1}} \left( \int_0^y \mu(s) ds \right) dy \quad (4.39)$$

The treatment of a displacement boundary condition is entirely similar, and therefore, it is not pursued.

#### 4.5 Numerical Simulations for Longitudinal Wave Propagation through Nonlinear Viscoelastic Rod with Non-Uniform Cross-Section

Based on the experience gained through the asymptotic analyses performed in §3.8 for the nonlinear uniform rod, and in §4.4 for the linear, non-uniform rod, it is anticipated that the asymptotic analysis for a nonlinear, non-uniform rod may lead to equations for secular terms that cannot be analytically solved, therefore defeating the purpose of the asymptotic analysis. This is the reason why asymptotic solutions of Eqs. (4.1) and (4.2) are not pursued. Rather, numerical simulations, similar to the ones performed in §3.10, are carried out in the rest of this chapter.

The set up of the numerical simulations is similar to that described on §3.10 for uniform rods. The following boundary conditions are employed:

$$v(\xi = 0, \tau) = 0, \quad P^*(\xi = 1, \tau) = P_B^*(\tau) = P_0^* e^{-\left(\frac{\tau - \mathcal{I}_S}{\tau}\right)^2}. \quad (4.40)$$

Again, input loads from Table 3.1 are employed. The nonlinear governing equations are solved numerically through a self-implemented finite difference scheme (see App. D). This finite difference scheme is based on the scheme used in §3.10, which was modified to incorporate the variation in the cross-sectional area.

Two different types of geometries are explored. First, an exponentially de-

creasing/increasing cross-section is considered. Finally, a geometry in which the variation of the cross-section is localized at the center of the rod forming a bulb or bulge is analyzed.

For the numerical simulations, the nonlinear viscoelastic model (*i*): Viscoelastic Mooney–Rivlin with  $c_1 = c_2 = \mu_0/12$ , previously employed in §3.10.1 is considered. Also, the predictions of the linearized model are presented.

In order to quantify the effect of the non-uniform cross-section on the characteristics of the stress waves, the present results are compared with those previously presented in §3.10, corresponding to a rod with uniform cross-section. In particular, the influence of the geometry of the rod on the wave front steepening is of interest since, according to the discussion in §3.10.5, this steepening can be potentially linked to the tissue damage. For the purpose of this study, the steepness of a wave front at time  $\tau$  is measured through the magnitude of the slope  $s(\tau)$  of the stress profile at the location of the steep wave front  $\xi_s(\tau)$ . In mathematical terms, this means

$$s(\tau) := \left| \frac{\partial P^*}{\partial \xi}(\xi, \tau) \right|_{\xi=\xi_s(\tau)} = \max_{\xi} \left| \frac{\partial P^*}{\partial \xi}(\xi, \tau) \right|, \quad (4.41)$$

where  $\xi_s(\tau)$  is the location along the rod of the steep wave front. A reference slope is also defined as

$$s_0 := \max_{\tau>0} \left| \frac{\partial P_B^*}{\partial \tau}(\tau) \right| = \left( \frac{\sqrt{2}}{\mathcal{T}} \right) |P_0^*| e^{-\frac{1}{2}}. \quad (4.42)$$

This reference slope is the maximum slope that the wave pulse would have had, had the rod been non-dispersive and non-dissipative (the wave pulse travels unaltered).

This value  $s_0$  also corresponds approximately to the slope of the wave pulse just after

it has entered at the right end of the rod. For the purpose of the following studies, a wave front with initial slope  $s_0$  is said to steepen if  $s(\tau)/s_0 > 1$ . Therefore, the quantity  $s(\tau)/s_0$  is employed to compare the results corresponding to different input stresses and geometries.

#### 4.5.1 Exponential Cross-Section Variation

In this case, the following expression of the cross-sectional area is considered:

$$\mathcal{A}^* = \mathcal{A}_0^* e^{2\gamma(\xi-\beta)}, \quad (4.43)$$

where

$$\gamma = \pm \frac{1}{2} \ln \left( \frac{\mathcal{A}_0^*}{\mathcal{A}_{\min}^*} \right) \quad (4.44)$$

and  $\beta = u(\gamma)$  with  $u$  the unit step function.  $\mathcal{A}_{\min}^*$  and  $\mathcal{A}_0^*$  are the smaller and larger cross-sectional area, respectively. Since the input load is applied at the right end, the generated waves will travel to the left. In the present study, the cross-section is said to increase, if it increases in the direction of wave propagation, that is to say, from right to left. The converse interpretation applies to a decreasing cross-section.

For all the simulations carried out here, the following parameters are chosen

$$\mathcal{A}_0^* = 1, \quad \frac{\mathcal{A}_0^*}{\mathcal{A}_{\min}^*} = 2. \quad (4.45)$$

Here, it is noted that the value of  $\mathcal{A}_0^*$  is irrelevant since it cancels out on both sides of the first of Eqs. (4.1). If a circular cross-section is assumed, then the radius of the cross-section is given by

$$r(\xi) = \sqrt{\frac{\mathcal{A}^*(\xi)}{\pi}} = \sqrt{\frac{\mathcal{A}_0^*}{\pi}} e^{\gamma(\xi-\beta)}. \quad (4.46)$$

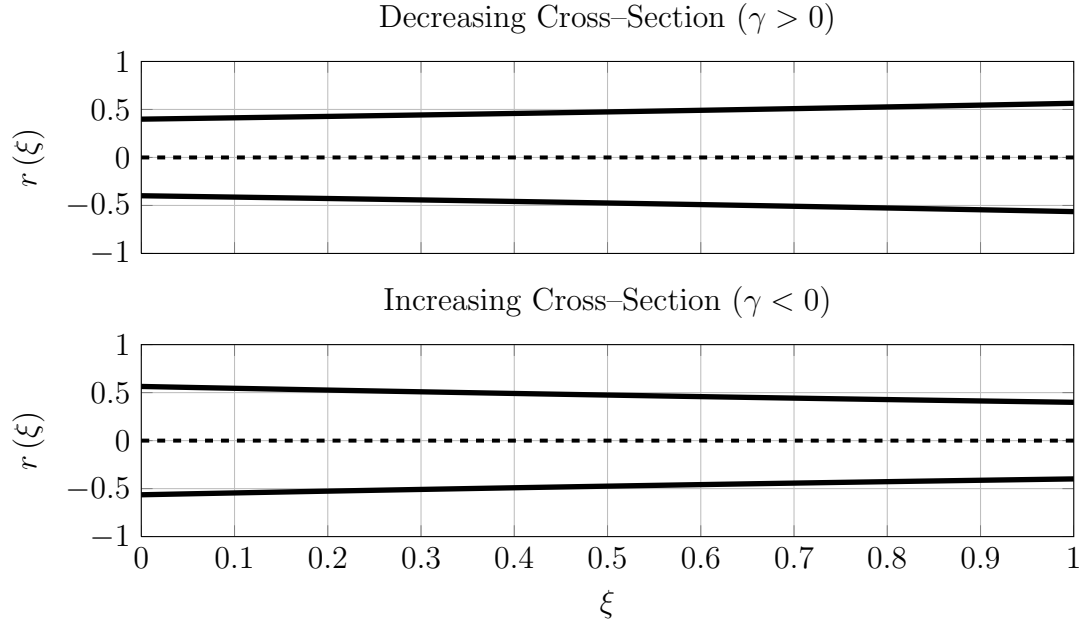


Figure 4.2: Two geometries of a rod with exponentially varying cross-section.

The geometries of the rod with exponentially decreasing and increasing cross-section are shown in Fig. 4.2.

#### 4.5.1.1 Results for a Rod with Exponentially Decreasing Cross-Section

Wave profiles at different instants of time, generated by different tension ( $P_0^* > 0$ ) and compression ( $P_0^* < 0$ ) inputs imparted at the right end of the non-linear viscoelastic rod are presented in Fig. 4.3. The corresponding predictions obtained with the linearized viscoelastic model are presented in Fig. 4.4. As was already discussed in §3.10, one of the main effects of the material nonlinearity on the propagating stress waves is to steepen the wave fronts.

In Fig. 4.5 the evolution of the stress peak in space for the uniform and non-uniform cross-sectional area cases are compared. In this particular case, the effect

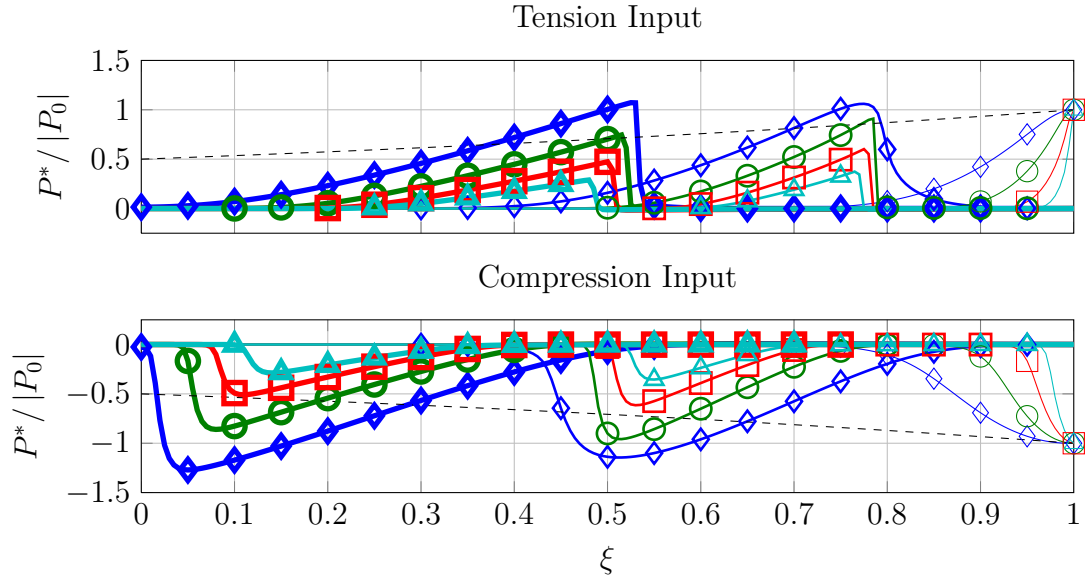


Figure 4.3: Snapshots of the tension and compression wave profiles propagating through the nonlinear viscoelastic rod with exponentially decreasing cross-section. Lines and symbols correspond to the inputs from Table 3.1. Line thickness indicate the time of the snapshot; from thinner to thicker, time instants are:  $\tau = 0.5, 0.85, 1.2$ . ( - - ): schematic representation of the geometry of the rod.

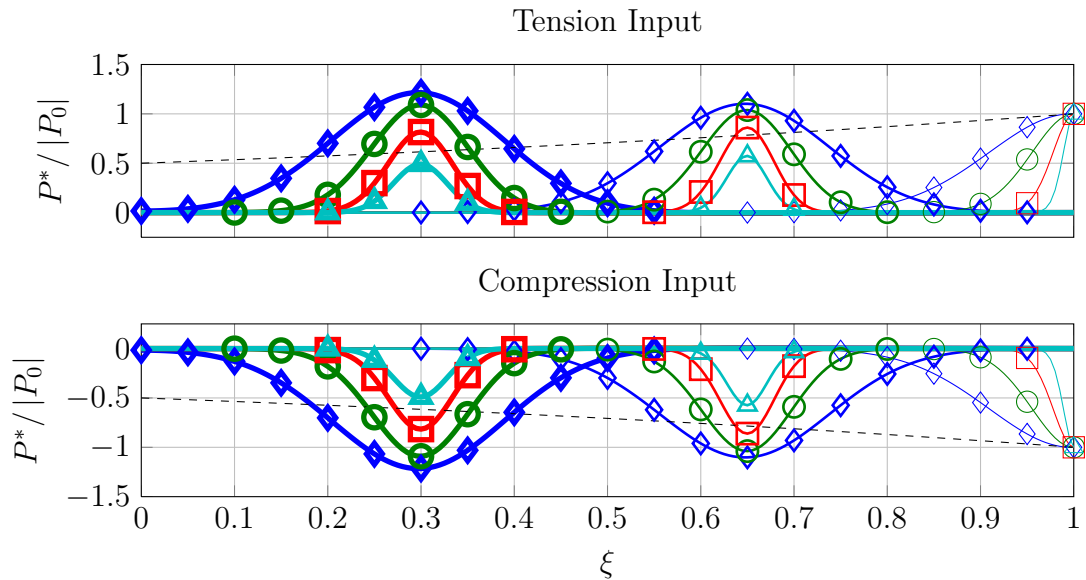


Figure 4.4: Snapshots of the tension and compression wave profiles propagating through the linear viscoelastic rod with exponentially decreasing cross-section. Refer to Fig. 4.3 for line references.

of the decreasing cross-section and of the material damping compete against each other. That is to say, material dissipation decreases the amplitude of the stress waves, whereas the shrinking cross-section tends to increase the amplitude of the stress waves. It is observed from Figs. 4.3 and 4.5 that for the input characterized by  $\mathcal{T} = 0.125$  (blue line) the effect of the decreasing cross-section dominates that of the dissipation. In consequence, the amplitude of this pulse increases as it travels along the rod. For the other pulses, the effect of the variable cross-section is evident near the right end of the rod, but the dissipation effects quickly overcome it to make the amplitude of the stress pulses finally decrease.

For an engineering problem involving viscoelastic materials, these results may suggest that if the variable cross-sectional area is chosen judiciously, then a potential situation may be achieved in which dissipation and geometric (cross-section) effects are balanced. In this situation, the amplitude of the stress pulses will remain unaltered as they travel along the rod.

In Fig. 4.6, the measure of the wave front slope  $s(\tau)/s_0$  is plotted as a function of the position of the steep wave front for tension and compression wave pulses. The results obtained with the uniform rod are also included in dashed lines in order to aid identifying the effect of the geometry on the wave steepening.

For both, tension and compression stress waves, it is observed that the decrease of the cross-sectional area produces steeper wave fronts, when compared to the cases with uniform cross-section. It is also observed that for both types of stress waves (tension and compression),  $s(\tau)/s_0$  reaches a maximum value and then gradually decreases as the wave front propagates. The position along the rod at which this

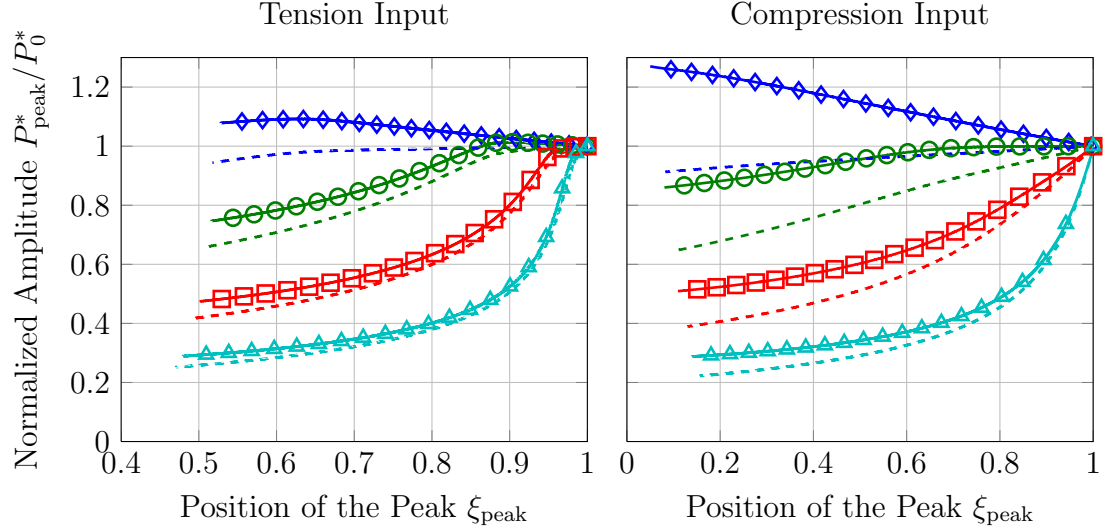


Figure 4.5: Stress peak stress peak  $P_{\text{peak}}^*/P_0^*$  as a function of its location  $\xi_{\text{peak}}$  along the rod corresponding to an exponentially decreasing cross-section. Solid lines with markers: non-uniform rod; dashed lines: uniform rod. Line colors correspond to the inputs from Table 3.1.

maximum occurs moves closer to the right end of the rod as the characteristic time of the input stress  $\mathcal{T}$  decreases. Furthermore, the maximum slope value increases as  $\mathcal{T}$  increases. In other words, fast and intense input forces (small  $\mathcal{T}$  and large  $|P_0^*|$ ) produce wave fronts that become steep close to the location of the input force is applied. On the other hand, less intense and slower inputs generate steep wave fronts deeper into the structure.

#### 4.5.1.2 Results for a Rod with Exponentially Increasing Cross-Section

Wave profiles at different instants of time, generated by different tension ( $P_0^* > 0$ ) and compression ( $P_0^* < 0$ ) inputs imparted at the right end of the nonlinear viscoelastic rod are presented in Fig. 4.7. The corresponding predictions obtained with the linearized viscoelastic model are presented in Fig. 4.8. As concluded in

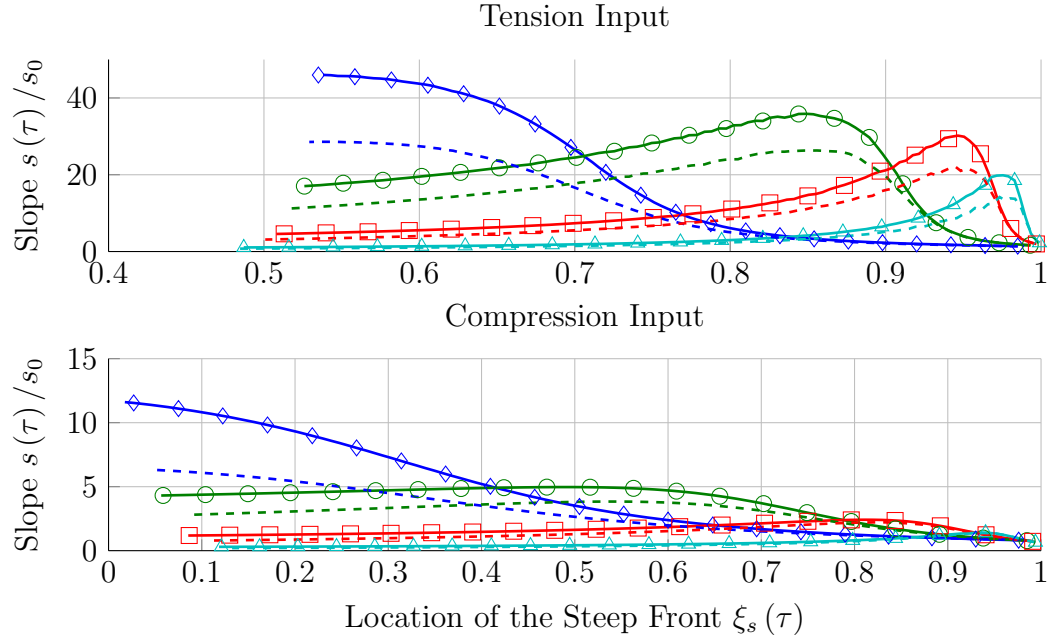


Figure 4.6: Effect of the exponentially decreasing cross-section on the steepening of tension and compression wave fronts. Refer to Fig. 4.5 for line references.

the analysis presented in §4.4, the effect of the increasing cross-section and of the material damping is to decrease the amplitude of the propagating stress waves. Therefore, for this particular geometry, it is difficult to discriminate between these two effects.

In Fig. 4.9 the evolution of the stress peak in space for the uniform and non-uniform cases are compared. It is observed that the effect of the variable cross-section is more pronounced for the case corresponding the input stress with  $\mathcal{T} = 0.125$  and for the compression inputs, in general.

In Fig. 4.10, the measure of the wave front slope  $s(\tau)/s_0$  is plotted as a function of the position of the step wave front for tension and compression wave pulses. The results obtained with the uniform rod are also included in dashed lines.

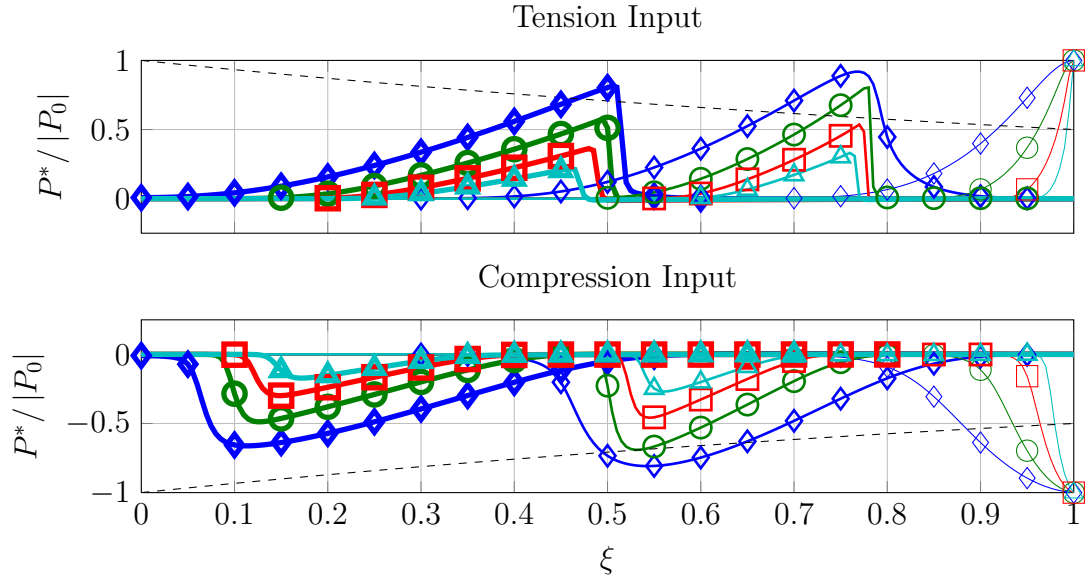


Figure 4.7: Snapshots of the tension and compression wave profiles propagating through the nonlinear viscoelastic rod with exponentially increasing cross-section. Lines and symbols correspond to the inputs from Table 3.1. Line thickness indicate the time of the snapshot; from thinner to thicker, time instants are:  $\tau = 0.5, 0.85, 1.2$ . ( - - ): schematic representation of the geometry of the rod.

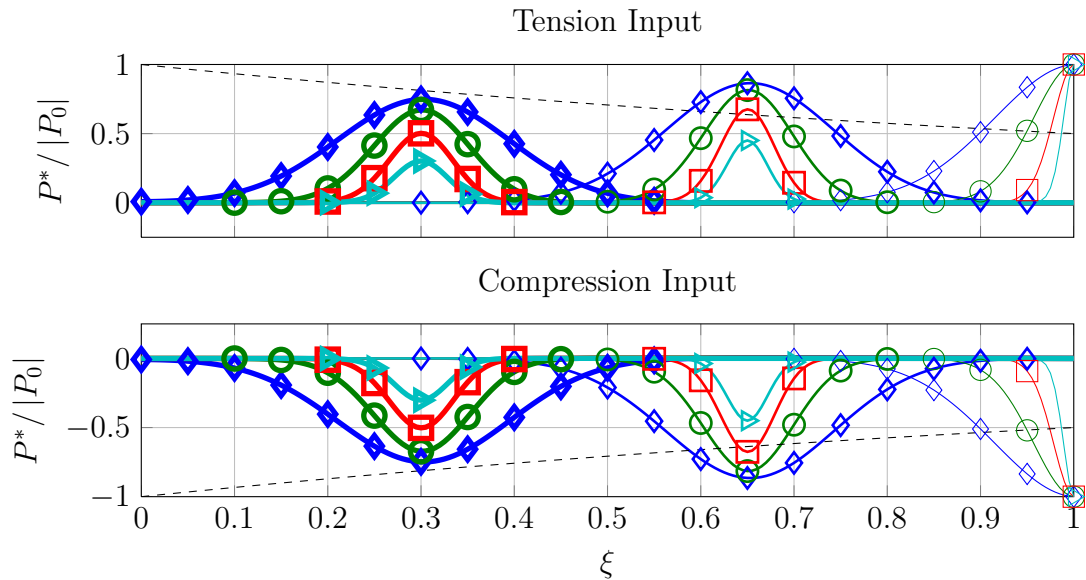


Figure 4.8: Snapshots of the tension and compression wave profiles propagating through the linear viscoelastic rod with exponentially increasing cross-section. Refer to Fig. 4.7 for line references.

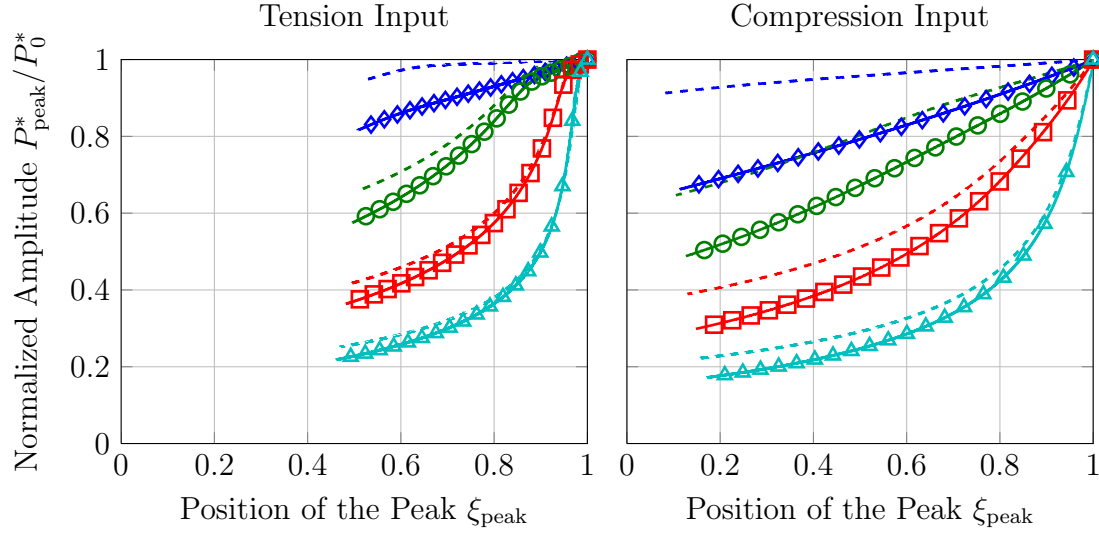


Figure 4.9: Stress peak  $P_{\text{peak}}^*/P_0^*$  as a function of its location  $\xi_{\text{peak}}$  along the rod corresponding to an exponentially increasing cross-section. Solid lines with markers: non-uniform rod; dashed lines: uniform rod. Line colors correspond to the inputs from Table 3.1.

For both, tension and compression stress waves, it is observed that the increase of the cross-section produces less steep wave fronts, when compared to the cases with uniform cross-section. It is also observed that for both types of stress waves (tension and compression),  $s(\tau)/s_0$  reaches a maximum value, and then gradually decreases as the wave front propagates. Similar to the case with decreasing cross-section, the position along the rod at which this maximum occurs moves closer to the right end of the rod as the characteristic time of the input stress  $\mathcal{T}$  decreases. Although it is not appreciable from the figure, it is noted that for the input stresses with smaller  $\mathcal{T}$ , the value  $s(\tau)/s_0$  becomes less than 1, indicating a combined smoothing effect of the geometry and of the material dissipation.

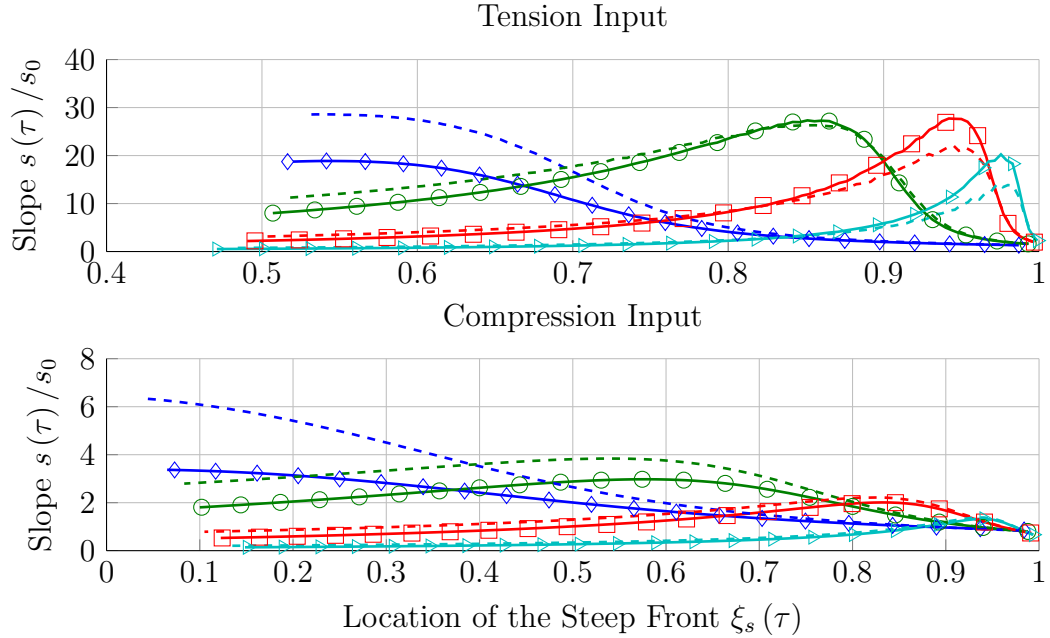


Figure 4.10: Effect of the exponentially increasing cross-sectional area on the steepening of tension and compression wave fronts. Refer to Fig. 4.9 for line references.

#### 4.5.2 Localized Cross-Section Variation: Bulge-Shaped Geometry

In the previous sections, the effects of several cross-section geometries on the propagation of longitudinal stress wave were studied. In this section, the focus is placed on the effect of localized area changes in the form of bulges.

It has been experimentally shown (Smith and Meaney, 2000, e.g.) that during axonal injury, a swelling in the form of a bulge is progressively developed in a portion of the axon. This swelling grows in time, and eventually leads to the disintegration of the axon. The studies presented in this section could provide clues regarding how the presence of this bulges affect the propagation of waves through axons.

In order to simplify the study, only one input load from Table 3.1, corresponding to  $\mathcal{T} = 0.06250$ , is considered here. In addition, bulges of different sizes are

explored. The cross-section geometry is parametrized in the following form:

$$\mathcal{A}^*(\xi) = \mathcal{A}_0^* \left[ \left( 1 - \frac{\mathcal{A}_{\min}^*}{\mathcal{A}_0^*} \right) e^{-\left(\frac{\xi-\xi_B}{\mathcal{X}_B}\right)^2} + \frac{\mathcal{A}_{\min}^*}{\mathcal{A}_0^*} \right], \quad (4.47)$$

where  $\xi_B = 0.5$  is chosen to position the bulge at the center of the rod.  $\mathcal{A}_0^*$  and  $\mathcal{A}_{\min}^*$  are the maximum and minimum cross-sectional area, respectively. The parameter  $\mathcal{X}_B$  determines the width of the bulge. It is noted that the variation of the cross-section resembles the shape of the time varying stress input imparted at the right end of the rod. This was purposely chosen in order to explore if the relative sizes of the bulge and the stress pulse produce any particularly interesting wave behavior.

In order to compare the results corresponding to bulges of different sizes, the parameter  $\mathcal{A}_{\min}^*/\mathcal{A}_0^*$  is set such that the ratio  $R$  of the mass of the bulge to the total mass of the rod, is kept constant for all the bulges. For the purpose of this study this ratio is chosen  $R = 0.25$ . The (non-dimensional) mass of material added by the bulge with  $\xi_B = 0.5$  is given by

$$m_b^* = \int_0^1 \rho_0^* \mathcal{A}_0^* \left( 1 - \frac{\mathcal{A}_{\min}^*}{\mathcal{A}_0^*} \right) e^{-\left(\frac{\xi-\xi_B}{\mathcal{X}_B}\right)^2} d\xi = \rho_0^* \mathcal{A}_0^* \left( 1 - \frac{\mathcal{A}_{\min}^*}{\mathcal{A}_0^*} \right) \mathcal{X}_B \sqrt{\pi} \text{Erf} \left( \frac{1}{2\mathcal{X}_B} \right). \quad (4.48)$$

Then  $R$  is given by

$$R := \frac{m_b^*}{m_b^* + 1\rho_0^* \mathcal{A}_{\min}^*}. \quad (4.49)$$

Fixing the value of  $R$  in Eq. (4.49) the value of  $\mathcal{A}_{\min}^*/\mathcal{A}_0^*$  can be obtained for different choices of  $\mathcal{X}_B$ . The values of  $\mathcal{X}_B$ , as well as the corresponding values of  $\mathcal{A}_{\min}^*/\mathcal{A}_0^*$  that will be used in the following studies are listed in Table 4.1. The different bulge geometries are showed in Fig. 4.11.

Table 4.1: Values of  $\mathcal{X}_B$  and  $\mathcal{A}_{\min}^*/\mathcal{A}_0^*$  defining bulges with mass ratio  $R = 0.25$ .

	$\mathcal{T}$	$\mathcal{A}_{\min}^*/\mathcal{A}_0^*$
1	0.125000	0.3992
2	0.062500	0.2494
3	0.031250	0.1425
4	0.015625	0.0767

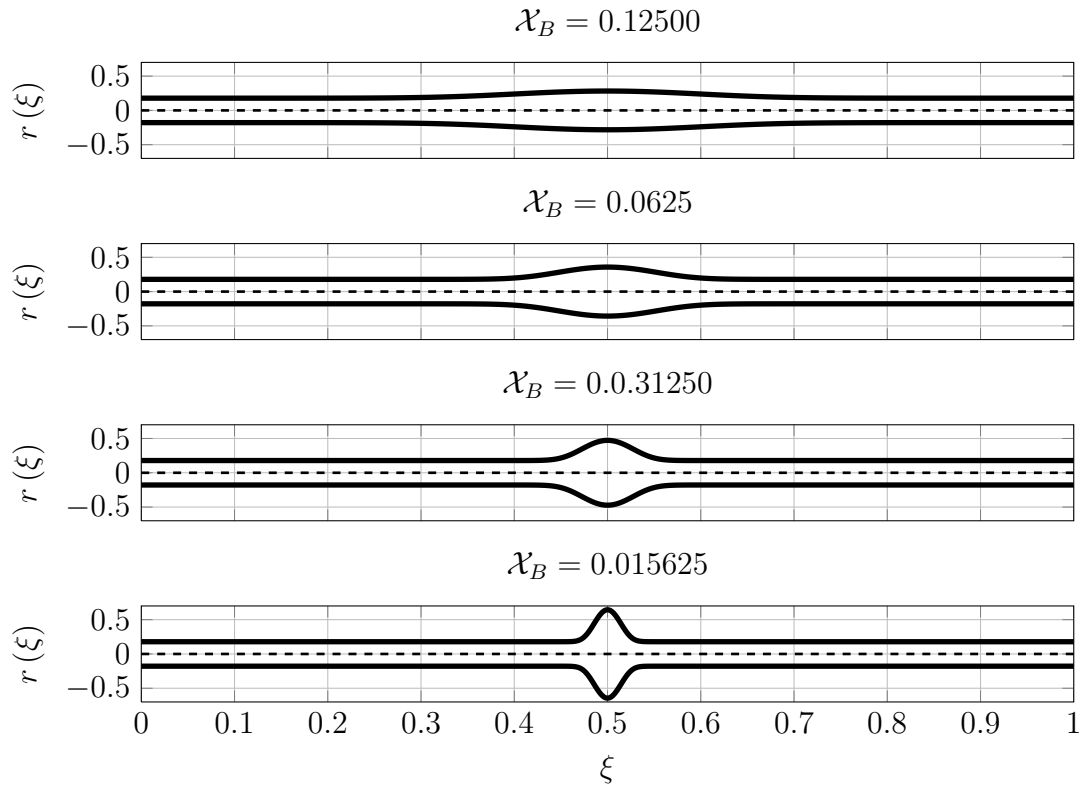


Figure 4.11: Different bulge geometries for constant mass ration  $R = 0.25$ .

### 4.5.2.1 Numerical Simulation Results

In Figs. 4.12 through 4.15 the stress wave profiles are plotted for compression and tension pulses propagating through the nonlinear viscoelastic rod with bulges of different sizes located at the center of the rod.

A general observation is that upon reaching the bulge, part of the incoming stress wave is transmitted through the bulge whereas another portion is reflected back. The ratio of transmitted-to-reflected wave at the bulge seems to depend inversely on the size of the bulge. The more concentrated the bulge ( $\mathcal{X}_B \searrow$ ) the higher the amount of reflected wave.

In addition, for the highly concentrated bulges, the amplitude of the compressive wave pulse increases considerably when it reaches the bulge, whereas that behavior is not observed for tension wave pulses. It is finally observed that both the reflected and transmitted wave pulses develop steep fronts. This behavior is more clearly appreciated for the compression pulses.

## 4.6 Final Remarks on Geometry Effects on Longitudinal Wave Propagation

In this chapter, the effect of several simplified geometries on the propagation of longitudinal stress waves was studied. Being a one-dimensional model, the geometry changes, characterized by a variation in the cross-sectional area, needs to be mild enough so that the effect of transverse (shear) waves can still be neglected.

It is recognized that conclusions based solely upon numerical simulations may

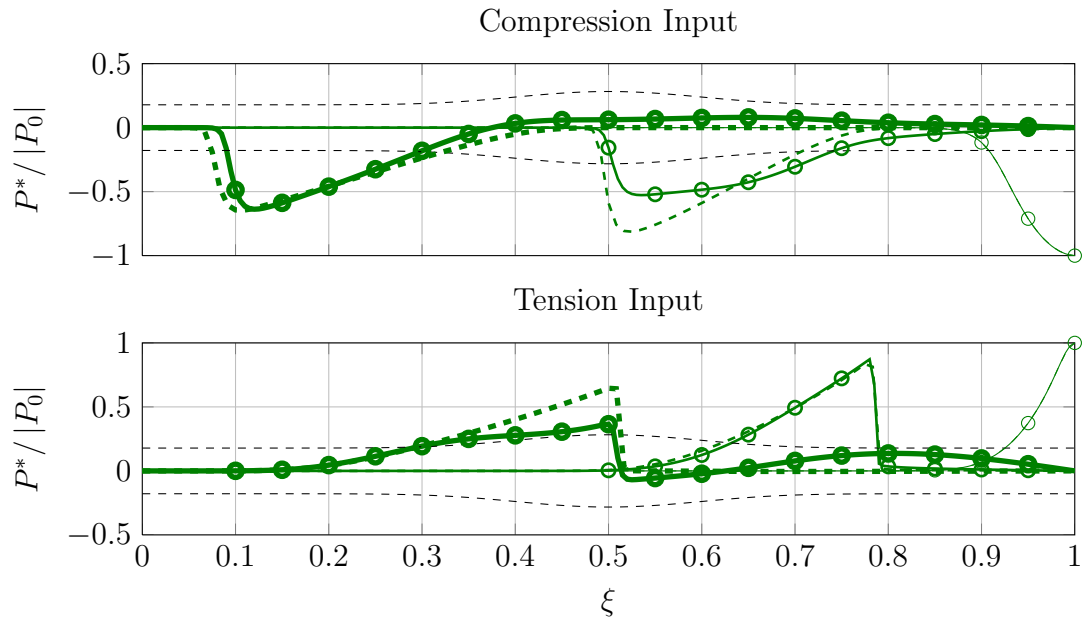


Figure 4.12: Snapshots of the compression and tension wave profiles propagating through the nonlinear viscoelastic rod with a bulge characterized by  $\mathcal{X}_B = 0.125000$  at the center. Line thickness indicate the time of the snapshot; from thinner to thicker, time instants are:  $\tau = 0.5, 0.85, 1.2$ . Solid lines with marker: non-uniform rod results; dashed green lines: uniform rod results; black dashed lines: geometry of the rod.

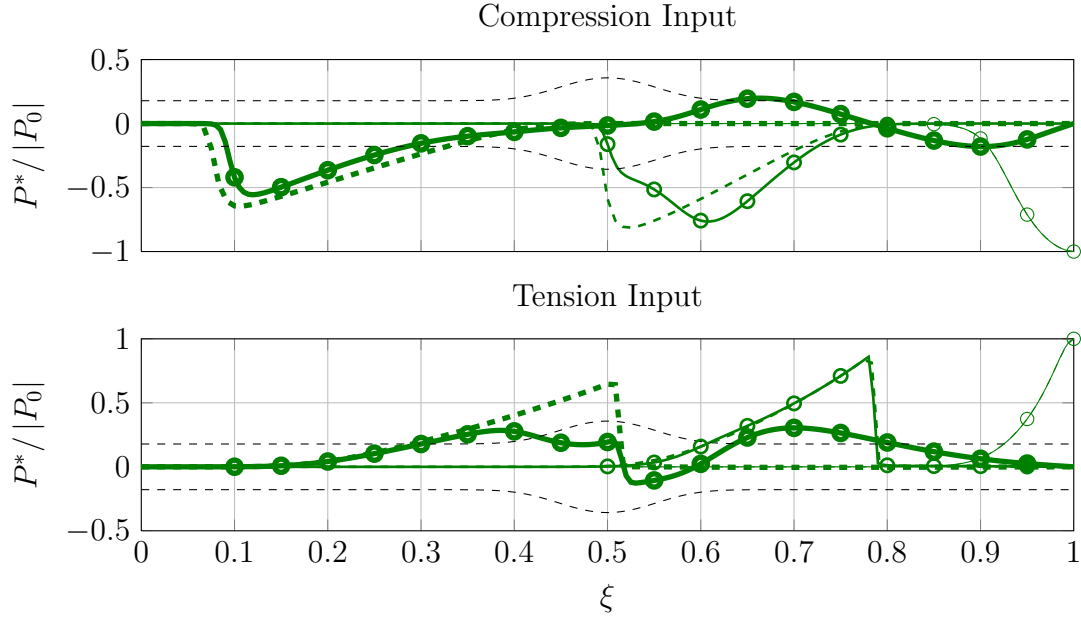


Figure 4.13: Snapshots of the compression (top) and tension (bottom) wave profiles propagating through the nonlinear viscoelastic rod with a bulge characterized by  $\mathcal{X}_B = 0.062500$  at the center. Refer to Fig. 4.12 for line references.

be misleading as they only present a limited picture of the phenomenon studied. However, some general trends were noted, which agree with the results from the analytic study on the linearized viscoelastic model. It was observed that if a stress wave encounters a decrease in the cross-sectional area of the rod, then its amplitude increases, competing against the effect of the material dissipation. Nonetheless, what the linear theory cannot predict is the effect of the variable cross-sectional area on the steepening effect of the material nonlinearity. As shown in the present studies, a narrowing rod will not only increase the stress wave amplitude, but also, it will produce steeper wave fronts. Following the discussion in §3.10.5, steeper wave fronts are associated with higher strain rates, and therefore, with higher energy absorption by the material.

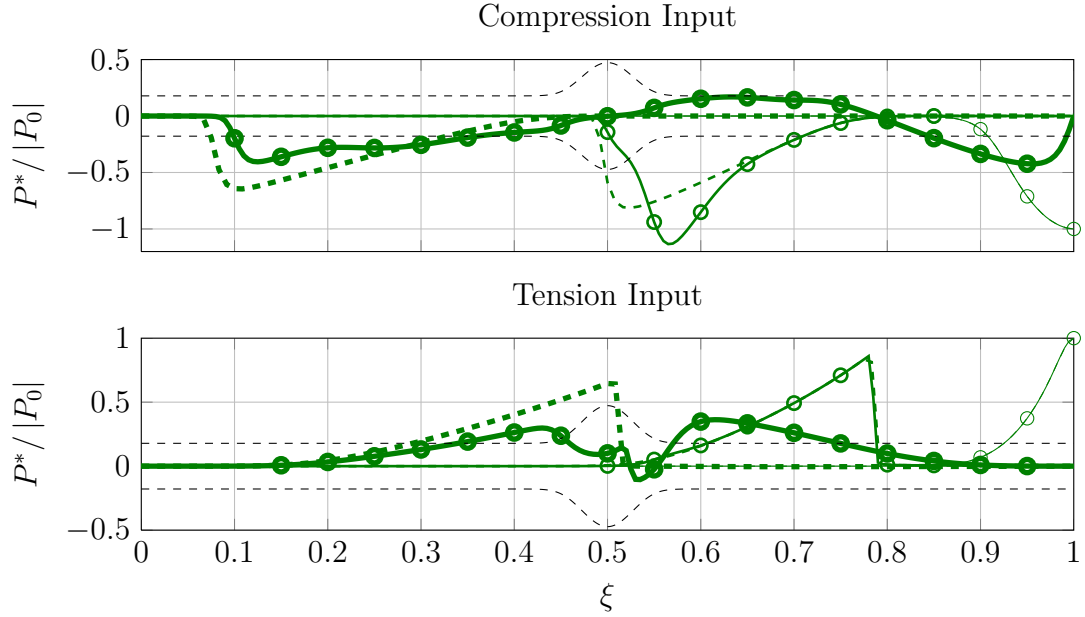


Figure 4.14: Snapshots of the compression (top) and tension (bottom) wave profiles propagating through the nonlinear viscoelastic rod with a bulge characterized by  $\mathcal{X}_B = 0.031250$  at the center. Refer to Fig. 4.12 for line references.

In the last section of this study, the effect of a bulge-shaped variation of the cross-sectional area was studied. It was observed that the introduction of this localized change generates both transmitted and reflected waves. The ratio of transmitted-to-reflected wave appears to be related to the shape of the bulge.

The studies presented here can be applied to study how some observed geometric features of axons affect the propagation of longitudinal stress waves. The diameter of an axon gradually increases at its ends: at the axon hillock (in its junction with the neuron cell body) and at the growth cone, where the axons forms a large number of terminals. As a consequence, these studies have shown that certain impulsive stresses introduced at either end of the axon will be magnified at the center section of the axon. Moreover, this particular geometry favors the generation of

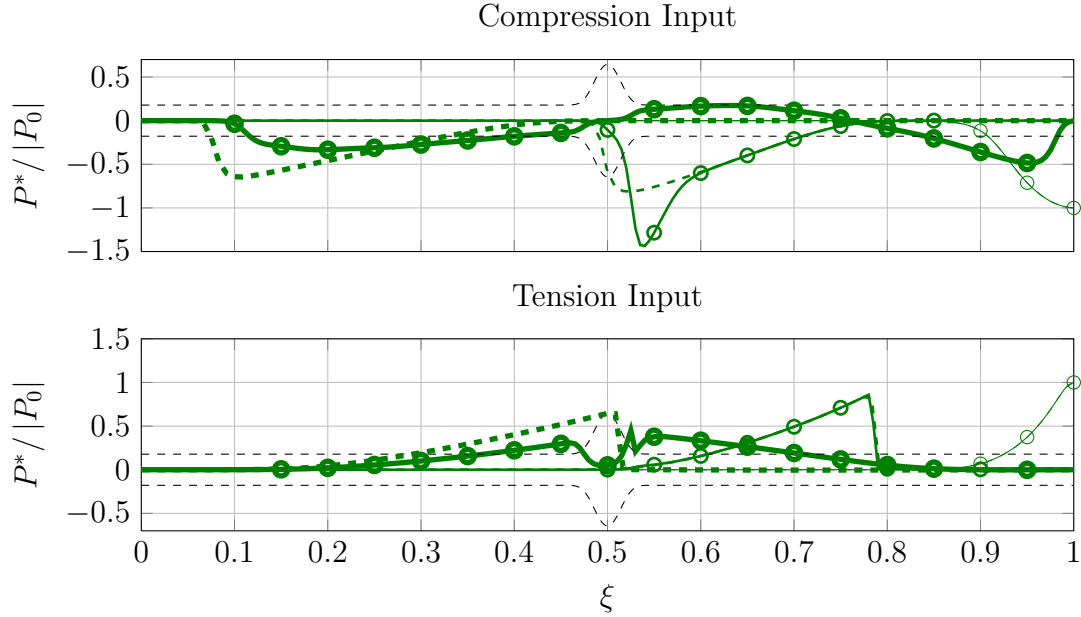


Figure 4.15: Snapshots of the compression (top) and tension (bottom) wave profiles propagating through the nonlinear viscoelastic rod with a bulge characterized by  $\mathcal{X}_B = 0.0156125$  at the center. Refer to Fig. 4.12 for line references.

steeper stress wave fronts within the axon. Localized inhomogeneities also may be present along axons. Swellings known as axonal varicosities/boutons serve as synaptic connections either at the ends or along the axons. These concentrated bulges may behave as the bulges presented in §4.5.2 with regards to longitudinal stress waves transmission. Moreover, due to wave reflections, standing waves of shorter wavelength could potentially be generated inbetween two consecutive boutons.

Finally, as examined by Smith and Meaney (2000), an axon may develop swelling as a result of accumulation of neurofilament protein after dynamic stretching. The geometry of this swelling resemble that of the bulges studied in §4.5.2. Therefore, the studies presented here could shed light into the wave behavior in injured axons.

## Chapter 5

### Summary and Concluding Remarks

The various studies carried out in this dissertation attempted to answer questions regarding the propagation of stress waves through soft tissue. In the context of this dissertation, the idea of soft tissue is closely related to the concept of soft viscoelastic materials. However, the theories and analysis laid down here only consider the mechanical aspects of the material response to external loads. It is clear that there exist fundamental aspects that distinguish biological soft tissues from engineering soft materials. These aspects go beyond the scope of this dissertation and need to be addressed in order to pursue further understanding of soft biological tissue mechanics and damage. It is important to consider, for example, that soft tissue microstructure not only responds and evolves due to mechanical excitations, but also, to chemical and electrical forces as well. The interconnection between these aspects is still not understood, and limited studies have been carried out to date.

Brain tissue, a soft tissue of particular interest in the present effort, is generally agreed to behave mechanically as a nonlinear material, not only with respect to strain, but also with respect to strain rate. However, experimental data available is far from being conclusive and comprehensive. This is mostly due to the large number of variables that need to be controlled in an experiment with biological

tissues and to the lack of standardized experimental protocols that allow consistent repeatability of results.

In addition, there has been a great deal of effort to consolidate a generally agreed upon constitutive model for brain tissue mechanical response. Numerous fundamentally different (nonlinear) constitutive models have been proposed by numerous researchers (see §1.3). To some extent, these models were often times able to reproduce a particular set of experimental data. Therefore, the obvious question comes to light: which constitutive model is right? Unfortunately, due to the nonlinear nature of the problem, answering this question may not be an easy task. A model needs to be able to predict other experimental data with different loading/kinematic conditions. What one can judge, however, is the validity of the assumptions that yielded the constitutive models. Unfortunately, most of the studies fail to explain the physical interpretation of their model construction (if there is any) and of their empirical coefficients, as many of those models are usually built upon other models known to work well for other types of materials. To date there is no record of a constitutive theory for brain tissue built upon fundamental principles, and until such theory is developed, no consolidated constitutive model can be envisioned.

## 5.1 Summary of Contributions

In this dissertation, a rather thorough study of longitudinal wave propagation along a geometrically simple nonlinear viscoelastic structure was presented. The objective motivating these studies was to determine how material nonlinear-

ties associated to large strains and strain rates affect the wave propagation. The intellectual contributions of this dissertation are listed below.

- A simplified phenomenological nonlinear viscoelastic material model for uniaxial deformation was developed to study brain tissue mechanical behavior. With the appropriate number of material constants, the model reproduces brain tissue mechanical behavior for constant strain rate, unconfined compression. This model was coupled to a point mass and an acoustic medium in order to study the interaction of blast waves and flexible structures.
- A model for longitudinal wave propagation along a rod whose mechanical behavior is described by a maximum dissipation material model (Haslach (2011)) was introduced. The linearized version of this model was employed to obtain frequency bounds for longitudinal wave propagation along brain white matter axons. In addition, an estimation of brain tissue dissipative characteristics was obtained through curve-fitting the theoretical attenuation expression to experimental data on brain tissue.
- Asymptotic analyses for wave propagation through linear and nonlinear viscoelastic rods with small dissipation were carried out. The asymptotic solutions obtained illustrate the combined wave-like and heat-like behavior of the mechanical waves. For the nonlinear material viscoelastic rod, these asymptotic solutions predict the wave front steepening behavior, observed as well through numerical simulations. Asymptotic analysis was also carried out to obtain the frequency response for longitudinal vibrations of a nonlinear vis-

coelastic rod. The effect of the material elasticity and damping constants, as well as the influence of the amplitude of the external load were assessed. Depending on the amplitude of the external load, characteristic frequency softening or hardening behavior was observed.

- A finite difference scheme was developed to carry out numerical simulations on longitudinal wave propagation through a nonlinear viscoelastic rod. The effects of external loading and material nonlinearity on the propagation of longitudinal stress waves were studied through numerical simulations. The effect of deformation-dependent wave speed on the nonlinear steepening of wave fronts was observed. It was observed that when steep wave fronts are developed, the energy absorption process on the material is focused on the propagating steep wave fronts. The location along the rod at which the maximum energy deposition occurs is related to the amplitude of the external load. This relation could serve as a basis to predict the spatial location of tissue damage.
- Simple geometry effects on the wave propagation characteristics were assessed. The effect of cross-sectional area changes were studied through asymptotic analysis of the linearized material case. This analysis showed that a narrowing cross-section produces an increase in the amplitude of the stress waves. The opposite is true for an widening cross-section. The effect of a variable cross-sectional area on the nonlinear steepening of wave fronts was also studied. A decrease in the cross-section in the direction of wave propagation produces much steeper wave fronts when compared to the uniform rod case. Finally,

the effect of localized changes in the cross-sectional area (bulges) were studied. The degree of localization of the cross-sectional area was observed to dictate the ratio between transmitted and reflected waves at the bulge.

## 5.2 Recommendations for Future Work

In this dissertation, the geometric simplicity of a longitudinal rod was chosen in order to ease the identification of nonlinear and geometric effects. However, it is recognized that in a real scenario, not only longitudinal waves may propagate, but also transverse (bending and shear) waves occur. Therefore, a model that incorporates bending and shear degrees of freedom will provide a more complete picture of the wave propagation characteristics of soft tissues. In the particular case of axons in the white matter, a geometrically exact theory (e.g. Antman, 2005) for rods may be a good approach to pursue that goal.

Another future direction that could build on the work in this dissertation relates to the question on how axons in the white matter are interconnected with their surroundings. In other words, how are the external loads transmitted to the structure? For example, in the case of a blast reaching the human head, how is the pressure wave transmitted from the skull to the brain surface?, and how the stress waves generated within the tissue are transmitted to the individual axons? A simple model that could help understand the interaction of an axon with the surrounding tissue is that of a rod embedded on an (visco)elastic matrix carrying pressure as well as shear forces.

## Appendix A

### Maximum Dissipation Nonlinear Viscoelastic Material Model

In this appendix, a brief description of the thermodynamically consistent, maximum dissipation mathematical construction employed to generate the material constitutive equation introduced in §2.4 is presented.

#### A.1 Mathematical Construction of the Constitutive Equation

The family of maximum dissipation nonlinear viscoelastic material models are obtained by using a thermodynamically consistent construction proposed by Haslach (2011). The main idea of this construction is that a non-equilibrium thermo-mechanical process evolves towards stable equilibria and away from unstable equilibria in the same way a dynamical system does. The fashion in which this evolution occurs is the main underpinning of the construction. The evolution of the system towards the equilibrium is dictated by a gradient dynamical system in terms of special variables called affinities. This characteristic, in turn guarantees that the system evolves so that the dissipation along a relaxation path is maximized.

The variables describing the system are collected in pairs according to their work conjugacy. In the context of isothermal material constitutive modeling, work conjugate pairs are composed of appropriate measures of stress and strain. One of the variables of the conjugate pair is called control variable  $y$  if it is manipulated,

or controlled externally, and the other one, the state variable  $x$ , responds to the control. If a system has  $n$  conjugate pairs  $(x_i, y_i)$ , the control and states variables are collected in  $n$ -tuples  $\mathbf{y} = (y_1, y_2, \dots, y_n)$  and  $\mathbf{x} = (x_1, x_2, \dots, x_n)$ , respectively.

A generalized thermodynamic energy function  $\varphi^*(\mathbf{x}; \mathbf{y})$  is defined by Haslach (2011) as

$$\varphi^*(\mathbf{x}; \mathbf{y}) := \Psi(\mathbf{x}) + \mathbf{x} \cdot \mathbf{y}, \quad (\text{A.1})$$

where  $\Psi(\mathbf{x})$  is a hyperelastic strain energy function, such that  $\mathbf{y} = -\partial\Psi/\partial\mathbf{x}$  at equilibrium. The affinities  $\mathcal{X}_i$  are defined as

$$\mathcal{X}_i(\mathbf{x}; \mathbf{y}) := \frac{\partial\varphi^*}{\partial x_i} = \frac{\partial\Psi}{\partial x_i}(\mathbf{x}) + y_i \quad i = 1, 2, \dots, n. \quad (\text{A.2})$$

Similarly, we collect the affinities in the  $n$ -tuple  $\mathbf{z} = (\mathcal{X}_1, \mathcal{X}_2, \dots, \mathcal{X}_n)$ . By the definition of  $\Psi(\mathbf{x})$ , the affinities are zero at equilibrium. If the Hessian matrix of  $\Psi$  is non-singular, then it is possible to express  $\varphi^*$  as a function of the affinities  $\mathbf{z}$  and the control variables  $\mathbf{y}$  in the following form

$$\varphi(\mathbf{z}; \mathbf{y}) = \varphi^*(\tilde{\mathbf{x}}(\mathbf{z}; \mathbf{y}); \mathbf{y}), \quad (\text{A.3})$$

where  $\tilde{\mathbf{x}} : \mathbf{z}, \mathbf{y} \mapsto \mathbf{x}$ . For fixed control variables, a gradient relaxation process is assumed to drive the system to equilibrium. From Haslach (2011), this reads as

$$\frac{D\mathbf{z}}{Dt} = -\boldsymbol{\kappa} \frac{\partial\varphi}{\partial\mathbf{z}} \quad (\text{A.4})$$

where  $\boldsymbol{\kappa}$  is a positive definite matrix, which is usually diagonal, and whose components  $\boldsymbol{\kappa}_i = \kappa_i$  determine the speed of the thermodynamic process and are called relaxation modulus coefficients. For the purpose of this work, it is assumed that

all the variables are defined in the reference configuration; therefore, the objectivity of time rates is automatically satisfied. In general, obtaining  $\varphi(\mathbf{z}; \mathbf{y})$  may be not possible; hence, it is useful to write the evolution equation in terms of the primitive state and control variables. From Haslach (2011) the evolution equation is rewritten as

$$\frac{\partial \mathbf{z}}{\partial \mathbf{x}} \cdot \frac{d\tilde{\mathbf{x}}}{dt} = -\boldsymbol{\kappa} \frac{\partial \varphi^*}{\partial \mathbf{x}} \cdot \frac{\partial \tilde{\mathbf{x}}}{\partial \mathbf{z}} = -\boldsymbol{\kappa} \mathbf{z} \cdot \frac{\partial \tilde{\mathbf{x}}}{\partial \mathbf{z}}, \quad (\text{A.5})$$

where

$$\begin{aligned} \frac{\partial \mathbf{z}}{\partial \mathbf{x}} &= \frac{\partial^2 \Psi}{\partial \mathbf{x} \partial \mathbf{x}} \\ \mathbf{I} &= \frac{\partial^2 \Psi}{\partial \mathbf{x} \partial \mathbf{x}} \cdot \frac{\partial \tilde{\mathbf{x}}}{\partial \mathbf{z}}, \end{aligned}$$

with  $\mathbf{I}$  an  $n$  by  $n$  identity matrix. Equation (A.5) can be conveniently expressed in the following compact form

$$\frac{\partial^2 \Psi}{\partial \mathbf{x} \partial \mathbf{x}} \cdot \dot{\mathbf{x}} + \boldsymbol{\kappa} \cdot \left( \frac{\partial^2 \Psi}{\partial \mathbf{x} \partial \mathbf{x}} \right)^{-1} \cdot \left( \frac{\partial \Psi}{\partial \mathbf{x}} + \mathbf{y} \right) = \mathbf{0}. \quad (\text{A.6})$$

More explicitly, the governing equation in matrix form is

$$\begin{aligned} & \begin{bmatrix} \frac{\partial^2 \Psi}{\partial x_1^2} & \cdots & \frac{\partial^2 \Psi}{\partial x_1 x_n} \\ \vdots & \ddots & \vdots \\ \frac{\partial^2 \Psi}{\partial x_n x_1} & \cdots & \frac{\partial^2 \Psi}{\partial x_n^2} \end{bmatrix} \begin{Bmatrix} \dot{x}_1 \\ \vdots \\ \dot{x}_n \end{Bmatrix} \\ & + \begin{bmatrix} \frac{\partial^2 \Psi}{\partial x_1^2} & \cdots & \frac{\partial^2 \Psi}{\partial x_1 x_n} \\ \vdots & \ddots & \vdots \\ \frac{\partial^2 \Psi}{\partial x_n x_1} & \cdots & \frac{\partial^2 \Psi}{\partial x_n^2} \end{bmatrix}^{-1} \begin{bmatrix} \kappa_1 & \cdots & 0 \\ \vdots & \ddots & \vdots \\ 0 & \cdots & \kappa_n \end{bmatrix} \begin{Bmatrix} \frac{\partial \Psi}{\partial x_1} + y_1 \\ \vdots \\ \frac{\partial \Psi}{\partial x_n} + y_n \end{Bmatrix} = \begin{Bmatrix} 0 \\ 0 \\ 0 \end{Bmatrix}. \quad (\text{A.7}) \end{aligned}$$

Equations (A.6), or (A.7) are used to derive constitutive equations by choosing the appropriate control and state variables and the hyperelastic strain energy function  $\Psi$  that relates them at equilibrium.

## A.2 Simple tension of incompressible, isotropic hyperelastic material

For incompressible, isotropic hyperelastic materials, the strain energy function  $\Psi_{\text{inc}}$  can be expressed in terms of the principal stretches  $\lambda_i$ ,  $i = 1, 2, 3$  as follows (Holzapfel, 2000),

$$\Psi_{\text{inc}}(\lambda_1, \lambda_2, \lambda_3) = \bar{\Psi}(\lambda_1, \lambda_2, \lambda_3) - p(J - 1), \quad (\text{A.8})$$

where the strain energy  $\bar{\Psi}$  is defined for  $J = \lambda_1\lambda_2\lambda_3 = 1$ ,  $J$  is the volume ratio of the deformed configuration to the reference configuration and equals the determinant of the deformation gradient  $\mathbf{F}$ . The scalar  $p$  is an indeterminate Lagrange multiplier, usually identified with the hydrostatic pressure.

The principal components of the first-Piola Kirchhoff stress tensor are given by,

$$P_i = \frac{\partial \Psi_{\text{inc}}}{\partial \lambda_i} = \frac{\partial \bar{\Psi}}{\partial \lambda_i} - p \frac{\partial J}{\partial \lambda_i}. \quad (\text{A.9})$$

Now, for a simple tension state with  $P_2 = P_3 = 0$  and  $P_1 = P \neq 0$ . Taking  $\lambda_1 = \lambda$ , from the incompressibility constraint and symmetry, it is needed that  $\lambda_2 = \lambda_3 = \lambda^{-1/2}$ . Under these assumptions, the hydrostatic pressure can be obtained from either the equation for  $P_2$  or  $P_3$  as follows

$$p = \left( \frac{\partial J}{\partial \lambda_3} \right)^{-1} \frac{\partial \bar{\Psi}}{\partial \lambda_3} = \lambda^{-1/2} \frac{\partial \bar{\Psi}}{\partial \lambda_3}. \quad (\text{A.10})$$

Thus, the only nonzero principal stress is given by

$$\begin{aligned} P &= \frac{\partial \bar{\Psi}}{\partial \lambda_1} - \lambda^{-1/2} \frac{\partial \bar{\Psi}}{\partial \lambda_3} \frac{\partial J}{\partial \lambda_1} = \frac{\partial \bar{\Psi}}{\partial \lambda_1} - \lambda^{-1/2} \lambda_2 \lambda_3 \frac{\partial \bar{\Psi}}{\partial \lambda_3}, \\ P &= \frac{\partial \bar{\Psi}}{\partial \lambda} - \lambda^{-3/2} \frac{\partial \bar{\Psi}}{\partial \lambda_3}. \end{aligned} \quad (\text{A.11})$$

It can be easily shown that Eq. (A.11) can be written as,

$$P = \frac{d\Psi}{d\lambda}, \quad (\text{A.12})$$

where

$$\Psi(\lambda) = \bar{\Psi}(\lambda, \lambda_2 = \lambda^{-1/2}, \lambda_3 = \lambda^{-1/2}). \quad (\text{A.13})$$

Equation (A.12) represents the relationship needed in Eq. (A.2) to express the conjugacy between  $-P$  and  $\lambda$ .

## Appendix B

### Particular Solutions for the Wave Equation in Semi-Infinite Domain

In this appendix, solutions to several initial–boundary value problems (IBVPs) for the linear wave equation are presented. These solutions are employed in the analyses presented in §3.4, §3.8 and §4.4.

#### B.1 Homogeneous Dirichlet (Displacement) Boundary Condition

In this section, the solution to the following problem is laid out,

$$\begin{cases} \frac{\partial^2 w}{\partial x^2} = \frac{\partial^2 w}{\partial t^2} & x \geq 0, t \geq 0, \\ w(x, t = 0) = \phi(x), \quad \frac{\partial w}{\partial t}(x, t = 0) = \psi(x), \\ w(x = 0, t) = 0. \end{cases} \quad (\text{B.1})$$

It can be shown (Evans, 2010) that the solution to the previous problem is given by

$$w(x, t) = \frac{1}{2} \begin{cases} [\phi(x - t) + \phi(x + t)] + \int_{x-t}^{x+t} \psi(y) dy & \text{for } x - t \geq 0, \\ [\phi(x + t) - \phi(t - x)] + \int_{t-x}^{x+t} \psi(y) dy & \text{for } x - t < 0. \end{cases} \quad (\text{B.2})$$

Equation (B.2) can be written in terms of the variables  $s_1$  and  $s_2$  defined in Eq. (3.17)

as follows:

$$\tilde{w}(s_1, s_2) = \begin{cases} \frac{1}{2} [\phi(s_1) + \phi(s_2)] + \frac{1}{2} \int_{s_1}^{s_2} \psi(y) dy & \text{for } s_1 \geq 0, \\ \frac{1}{2} [\phi(s_2) - \phi(-s_1)] + \frac{1}{2} \int_{-s_1}^{s_2} \psi(y) dy & \text{for } s_1 < 0, \end{cases} \quad (\text{B.3})$$

where the ( $\check{\cdot}$ ) notation introduced in Eq. (3.18) is employed. Eq. (B.3) can be written in the following compact form

$$\check{w}(s_1, s_2) = \begin{cases} \check{W}_1(s_1) + \check{W}_2(s_2) & \text{for } s_1 \geq 0, \\ \check{W}_3(s_1) + \check{W}_2(s_2) & \text{for } s_1 < 0, \end{cases} \quad (\text{B.4})$$

where the following definitions are employed:

$$\begin{aligned} \check{W}_1(y) &:= \frac{1}{2}\phi(y) - \frac{1}{2}\int_0^y \psi(s) ds, \\ \check{W}_2(y) &:= \frac{1}{2}\phi(y) + \frac{1}{2}\int_0^y \psi(s) ds, \\ \check{W}_3(y) &:= -\frac{1}{2}\phi(-y) - \frac{1}{2}\int_0^{-y} \psi(s) ds. \end{aligned} \quad (\text{B.5})$$

## B.2 Homogeneous Initial Conditions and Dirichlet Boundary Condition

In this section, the solution to the following problem is obtained,

$$\begin{cases} \frac{\partial^2 w}{\partial x^2} = \frac{\partial^2 w}{\partial t^2} & x \geq 0, t \geq 0, \\ w(x, t=0) = 0 & \frac{\partial w}{\partial t}(x, t=0) = 0, \\ w(x=0, t) = \mu(t). \end{cases} \quad (\text{B.6})$$

Taking the Laplace Transform  $\mathcal{L}$  of the first equation, the following result is obtained

$$\frac{\partial^2 W}{\partial x^2}(x, s) = s^2 W(x, s) - \cancel{sw(x, t=0)} - \cancel{\frac{\partial w}{\partial t}(x, t=0)}.$$

where the notation  $W(x, s) = \mathcal{L}[w(x, t)]$  is used. The solution to the previous equation is given by  $W(x, s) = A(s)e^{-sx} + B(s)e^{sx}$ . Therefore, it is found that

$$w(x, t) = a(t-x)u(t-x) + b(t+x)u(t+x),$$

where  $u(\cdot)$  is the unit step function. Applying the displacement initial condition results in the following

$$w(x, t = 0) = a(-x)u(-x) + b(x)u(x).$$

Since  $x \geq 0$ ,

$$w(x, t = 0) = b(x) = 0.$$

Therefore,

$$w(x, t) = a(t - x)u(t - x).$$

Applying the boundary condition at  $x = 0$  yields

$$a(t, 0) = \mu(t).$$

Therefore, the solution  $w(x, t)$  is given by

$$w(x, t) = \mu(t - x)u(t - x). \quad (\text{B.7})$$

In terms of the variables  $s_1$  and  $s_2$ , Eq. (B.7) can be written as

$$\check{w}(s_1, s_2) = \mu(-s_1)u(-s_1), \quad (\text{B.8})$$

where the ( $\check{\cdot}$ ) notation (Eq. (3.18)) was employed.

### B.3 Homogeneous Neumann (Force) Boundary Condition

In this section, the solution to the following problem is laid out,

$$\left\{ \begin{array}{l} \frac{\partial^2 w}{\partial x^2} = \frac{\partial^2 w}{\partial t^2} \quad x \geq 0, t \geq 0, \\ w(x, t = 0) = \phi(x), \quad \frac{\partial w}{\partial t}(x, t = 0) = \psi(x), \\ \frac{\partial w}{\partial x}(x = 0, t) = 0. \end{array} \right. \quad (\text{B.9})$$

The solution is obtained by using the even–reflection method to transform the previous initial–boundary–value problem into a initial–value–problem (IVP) on the real line ( $x \in \mathbb{R}$ ). The following even extensions variables are defined:

$$\tilde{w}(x, t) = \begin{cases} w(x, t) & x \geq 0, t \geq 0 \\ \tilde{w}(-x, t) & x < 0, t \geq 0, \end{cases}$$

$$\tilde{\phi}(x) = \begin{cases} \phi(x) & x \geq 0, \\ \phi(-x) & x < 0, \end{cases}$$

$$\tilde{\psi}(x) = \begin{cases} \psi(x) & x \geq 0 \\ \psi(-x) & x < 0. \end{cases}$$

Using the previous definitions, Eq. (B.9) is transformed into

$$\begin{cases} \frac{\partial^2 \tilde{w}}{\partial x^2} = \frac{\partial^2 \tilde{w}}{\partial t^2} & -\infty \leq x \leq \infty, t \geq 0, \\ \tilde{w}(x, t=0) = \tilde{\phi}(x), \quad \frac{\partial \tilde{w}}{\partial t}(x, t=0) = \tilde{\psi}(x). \end{cases} \quad (\text{B.10})$$

The solution to the problem (B.10) is given by d'Alembert's formula

$$\tilde{w}(x, t) = \frac{1}{2} [\tilde{\phi}(x-t) + \tilde{\phi}(x+t)] + \frac{1}{2} \int_{x-t}^{x+t} \tilde{\psi}(y) dy. \quad (\text{B.11})$$

Restricting the attention to  $x \geq 0$  in Eq. (B.11), and using the definitions of  $\tilde{w}$ ,  $\tilde{\phi}$ , and  $\tilde{\psi}$ , the desired solution  $w$  is obtained as follows

$$w(x, t) = \frac{1}{2} \begin{cases} \phi(x-t) + \phi(x+t) + \int_{x-t}^{x+t} \psi(y) dy & \text{if } x-t \geq 0 \\ \phi(t-x) + \phi(x+t) + \int_0^{x+t} \psi(y) dy + \int_0^{t-x} \psi(y) dy & \text{if } x-t < 0. \end{cases} \quad (\text{B.12})$$

Equation (B.12) and be conveniently expressed in terms of the variables  $s_1$  and  $s_2$  defined in Eq. (3.17) as

$$\check{w}(s_1, s_2, 0) = \begin{cases} \check{W}_1(s_1) + \check{W}_2(s_2) & \text{for } s_1 \geq 0 \\ \check{W}_2(-s_1) + \check{W}_2(s_2) & \text{for } s_1 < 0, \end{cases} \quad (\text{B.13})$$

where  $\check{W}_1$  and  $\check{W}_2$  were previously defined in Eq. (B.5),

$$\begin{aligned} \check{W}_1(y) &:= \frac{1}{2}\phi(y) - \frac{1}{2}\int_0^y \psi(s) ds \\ \check{W}_2(y) &:= \frac{1}{2}\phi(y) + \frac{1}{2}\int_0^y \psi(s) ds \end{aligned}$$

and the  $(\check{\cdot})$  notation (Eq. (3.18)) was employed.

## B.4 Homogeneous Initial Conditions and Neumann Boundary Condition

In this section, the solution to the following problem is obtained,

$$\begin{cases} \frac{\partial^2 w}{\partial x^2} = \frac{\partial^2 w}{\partial t^2} & x \geq 0, t \geq 0, \\ w(x, t = 0) = 0 & \frac{\partial w}{\partial t}(x, t = 0) = 0, \\ \frac{\partial w}{\partial x}(x = 0, t) = \varrho(t). \end{cases} \quad (\text{B.14})$$

Upon taking the Laplace Transform  $\mathcal{L}$  of the first equation, the following result is obtained:

$$\frac{\partial^2 W}{\partial x^2}(x, s) = s^2 W(x, s) - \cancel{sw(x, t=0)} - \frac{\partial w}{\partial t}(x, t=0),$$

where  $W(x, s) = \mathcal{L}[w(x, t)]$ . The solution to the previous equation is given by

$W(x, s) = A(s)e^{-sx} + B(s)e^{sx}$ . Therefore, it is found that

$$w(x, t) = a(t-x)u(t-x) + b(t+x)u(t+x),$$

where  $u(\cdot)$  is the unit step function. Applying the displacement initial condition yields

$$w(x, t = 0) = a(-x)u(-x) + b(x)u(x).$$

Since  $x \geq 0$ ,

$$w(x, t = 0) = b(x) = 0.$$

Therefore,

$$w(x, t) = a(t - x)u(t - x).$$

In order to apply the boundary condition at  $x = 0$ , the solution in the Laplace space is employed as follows

$$\frac{\partial W}{\partial x}(x = 0, s) = -sA(s) = \mathcal{L}[\varrho].$$

Using a Laplace Transform table, the following result is obtained:

$$a(t) = -\int_0^t \varrho(\zeta)u(t - \zeta)d\zeta = -\int_0^t \varrho(\zeta)d\zeta.$$

Therefore, the solution  $w(x, t)$  is given by

$$w(x, t) = -u(t - x) \int_0^{t-x} \varrho(\zeta)d\zeta. \quad (\text{B.15})$$

In terms of the variables  $s_1$  and  $s_2$  defined in Eq. (3.17), Eq. (B.15) can be written as

$$\tilde{m}(s_1, s_2) = -u(-s_1) \int_0^{-s_1} \varrho(s)ds, \quad (\text{B.16})$$

where the  $(\sim)$  notation (Eq. (3.18)) was employed.

## Appendix C

### Galerkin Projection Procedure and Particular Resonance Case Study

In this appendix, details on the Galerkin projection method employed in §3.9, as well as additional mathematical derivations, are included. In addition, the values of the coefficients appearing in Eqns. (3.172) are computed for the particular case studied in §3.9.2.1, corresponding to the primary resonance of the first vibration mode.

#### C.1 Galerkin Projection

As stated in §3.9, a solution in the form of Eq. (3.138) is assumed for the displacement,

$$v(\xi, \tau) = \sum_{n=0}^N \eta_n(\tau) \sin(\bar{k}_n \xi), \quad (\text{C.1})$$

where  $\bar{k}_n$ , for  $n = 1, 2, \dots, \infty$  are the wave numbers of the linear viscoelastic elastic rod with fixed-free boundary conditions

$$\bar{k}_n = \frac{2n-1}{2}\pi.$$

Inserting Eqns. (3.139) and (3.140) into Eq. (3.137) yields

$$\begin{aligned}
P^*(\xi, \tau) &= \sum_{n=1}^N \bar{k}_n (\eta_n + \alpha \dot{\eta}_n) \cos(\bar{k}_n \xi) \\
&+ \frac{1}{2} \mu_1^* \sum_{j,n=1}^N \bar{k}_n \bar{k}_j \eta_n (\eta_j + 4\alpha \dot{\eta}_j) \cos(\bar{k}_n \xi) \cos(\bar{k}_j \xi) \\
&+ \frac{1}{6} \mu_2^* \sum_{j,n,m=1}^N \bar{k}_n \bar{k}_j \bar{k}_m \eta_j \eta_n \eta_m \cos(\bar{k}_n \xi) \cos(\bar{k}_j \xi) \cos(\bar{k}_m \xi) \\
&+ (\mu_2^* + (\mu_1^*)^2) \alpha \sum_{j,n,m=1}^N \bar{k}_n \bar{k}_j \bar{k}_m \eta_j \eta_n \dot{\eta}_m \cos(\bar{k}_n \xi) \cos(\bar{k}_j \xi) \cos(\bar{k}_m \xi).
\end{aligned} \tag{C.2}$$

Substituting Eqns. (C.1) through (C.2) into the first of Eqns. (3.136), multiplying both sides by  $\sin(\bar{k}_k \xi)$ , integrating with respect to  $\xi$  from 0 to 1, and using the orthogonality properties of the modes results in

$$\int_0^1 \sin(\bar{k}_k \xi) \frac{\partial P}{\partial \xi} d\xi + B_k \cos(\omega \tau) = \frac{1}{2} \ddot{\eta}_k, \tag{C.3}$$

where

$$\begin{aligned}
\int_0^1 \sin(\bar{k}_k \xi) \frac{\partial P}{\partial \xi} d\xi &= \sum_{n=1}^N \bar{k}_n (\eta_n + \alpha \dot{\eta}_n) H_{kn} \\
&+ \frac{1}{2} \mu_1^* \sum_{j,n=1}^N \bar{k}_n \bar{k}_j \eta_n (\eta_j + 4\alpha \dot{\eta}_j) F_{kjn} \\
&+ \sum_{j,n,m=1}^N \bar{k}_n \bar{k}_j \bar{k}_m \eta_j \eta_n \left( \frac{1}{6} \mu_2^* \eta_m + (\mu_2^* + (\mu_1^*)^2) \alpha \dot{\eta}_m \right) G_{kijnm},
\end{aligned} \tag{C.4}$$

and

$$\begin{aligned}
H_{kn} &:= \int_0^1 \sin(\bar{k}_k \xi) \frac{d}{d\xi} \cos(\bar{k}_n \xi) d\xi = -\frac{1}{2} \delta_{kn} \bar{k}_k \\
F_{kjn} &:= \int_0^1 \sin(\bar{k}_k \xi) \frac{d}{d\xi} [\cos(\bar{k}_n \xi) \cos(\bar{k}_j \xi)] d\xi \\
G_{kijnm} &:= \int_0^1 \sin(\bar{k}_k \xi) \frac{d}{d\xi} [\cos(\bar{k}_n \xi) \cos(\bar{k}_j \xi) \cos(\bar{k}_m \xi)] d\xi \\
B_k &:= \int_0^1 \sin(\bar{k}_k \xi) B(\xi) d\xi
\end{aligned} \tag{C.5}$$

The following symmetries are observed:

$$\begin{aligned}
F_{kjn} &= F_{knj}, \\
G_{kijn} &= G_{knmj} = G_{kmjn} = G_{kjmn} = G_{kmnj} = G_{knjm}.
\end{aligned}
\tag{C.6}$$

Using the previous results, the projected ODE corresponding to mode  $k$  is given by

$$\begin{aligned}
\ddot{\eta}_k + \bar{k}_k^2 \eta_k &= -\alpha \bar{k}_k^2 \dot{\eta}_k \\
&+ \mu_1^* \sum_{j,n=1}^N \bar{k}_n \bar{k}_j \eta_n (\eta_j + 4\alpha \dot{\eta}_j) F_{kjn} + \\
&+ 2 \sum_{j,n,m=1}^N \bar{k}_n \bar{k}_j \bar{k}_m \eta_j \eta_n \left( \frac{1}{6} \mu_2^* \eta_m + (\mu_2^* + (\mu_1^*)^2) \alpha \dot{\eta}_m \right) G_{kijn} \\
&+ 2B_k \cos(\omega\tau).
\end{aligned}
\tag{C.7}$$

## C.2 Primary Resonance of the First Mode

Here, the mathematical details that led to Eq. (3.172) are presented. In this particular case of interest, a Galerkin projection with two modes ( $M = 2$ ) was employed to study the primary resonance of the first mode ( $k = 1$ ).

In order to construct the equations of the secular terms at  $\mathcal{O}(\epsilon^2)$ , Eqns. (3.168) and (3.169), the values  $p_{mi}$  ( $i = 1, 2, \dots, 7$ ) defined by Eq. (3.165) are explicitly computed. The values  $p_{mi}$ , corresponding to modes  $m = 1$  and  $m = 2$  are presented in Table C.1. By definition,  $p_{mi} \in \mathbb{N}$ ; therefore, only  $1 \leq p_{mi} \leq M = 2$  are allowed. Non-allowed values of  $p_{mi}$  are crossed out in Table C.1.

Using the symmetries of  $G_{kijn}$  (Eq. (C.6)), and performing symbolic manipulations with Mathematica, it can be shown that

$$S_{11} = P_{11} A_1^2 \bar{A}_1 + P_{12} A_1 \bar{A}_2 A_2 + P_{13} A_2 \bar{A}_1^2,
\tag{C.8}$$

Table C.1: Values of  $p_{mi}$  ( $i = 1, 2, \dots, 7$ ;  $m=1,2$ ) from Eq. (3.165) corresponding to  $k = 1$  and  $M = 2$

$j$	$n$	Mode 1							Mode 2						
		$p_{11}$	$p_{12}$	$p_{13}$	$p_{14}$	$p_{15}$	$p_{16}$	$p_{17}$	$p_{21}$	$p_{22}$	$p_{23}$	$p_{24}$	$p_{25}$	$p_{26}$	$p_{27}$
1	1	$\emptyset$	1	$\emptyset$	1	2	$\emptyset$	1	1	2	$\cancel{\mathcal{A}}$	$\emptyset$	$\mathfrak{B}$	$\cancel{\mathcal{A}}$	2
1	2	$\cancel{\mathcal{A}}$	2	1	2	$\mathfrak{B}$	$\cancel{\mathcal{A}}$	$\emptyset$	$\emptyset$	$\mathfrak{B}$	$\emptyset$	1	$\cancel{\mathcal{A}}$	$\cancel{\mathcal{A}}$	1
2	1	$\cancel{\mathcal{A}}$	$\emptyset$	$\cancel{\mathcal{A}}$	2	$\mathfrak{B}$	1	2	$\emptyset$	1	$\cancel{\mathcal{A}}$	1	$\cancel{\mathcal{A}}$	$\emptyset$	$\mathfrak{B}$
2	2	$\cancel{\mathcal{A}}$	1	$\emptyset$	$\mathfrak{B}$	$\cancel{\mathcal{A}}$	$\emptyset$	1	$\cancel{\mathcal{A}}$	2	$\cancel{\mathcal{A}}$	2	$\mathfrak{B}$	$\cancel{\mathcal{A}}$	2

and

$$S_{12} = P_{21}A_2^2\bar{A}_2 + P_{22}A_1A_2\bar{A}_1 + P_{23}A_1^3, \quad (\text{C.9})$$

where

$$\begin{aligned}
P_{11} &= \mu_2^* G_{1111} \bar{k}_1^3 = -\frac{3}{128} \pi^4 \mu_2^*, \\
P_{12} &= 2\mu_2^* G_{1122} \bar{k}_1 \bar{k}_2^2 = -\frac{9}{32} \pi^4 \mu_2^*, \\
P_{13} &= \mu_2^* G_{1112} \bar{k}_1^2 \bar{k}_2 = -\frac{3}{128} \pi^4 \mu_2^*, \\
P_{21} &= \mu_2^* G_{2222} \bar{k}_2^3 = -\frac{243}{128} \pi^4 \mu_2^*, \\
P_{22} &= 2\mu_2^* G_{2112} \bar{k}_1^2 \bar{k}_2 = -\frac{9}{32} \pi^4 \mu_2^*, \\
P_{23} &= \frac{1}{3} \mu_2^* G_{2111} \bar{k}_1^3 = -\frac{1}{128} \pi^4 \mu_2^*.
\end{aligned} \quad (\text{C.10})$$

Similarly,

$$S_{21} = C_{11}A_1^2\bar{A}_1 + C_{12}A_1A_2\bar{A}_2 + C_{13}\bar{A}_1^2A_2, \quad (\text{C.11})$$

$$S_{22} = C_{21}A_2^2\bar{A}_2 + C_{22}A_1\bar{A}_1A_2 + C_{23}A_1^3, \quad (\text{C.12})$$

where the coefficients  $C_{ij}$  ( $i = 1, 2; j = 1, 2, 3$ ) are obtained with Mathematica:

$$C_{11} = 2(\mu_1^*)^2 \left[ \frac{5}{3} \bar{k}_1^2 F_{111}^2 + \frac{\bar{k}_1^3}{\bar{k}_2} \frac{3\bar{k}_2^2 - 8\bar{k}_1^2}{(\bar{k}_2^2 - 4\bar{k}_1^2)} F_{112} F_{211} \right],$$

$$C_{11} = \frac{1364}{3375} (\mu_1^*)^2 \pi^2, \quad (\text{C.13})$$

$$C_{12} = 4(\mu_1^*)^2 \left[ F_{112} F_{222} \bar{k}_1 \bar{k}_2 + F_{111} F_{122} \bar{k}_2^2 + 2F_{112}^2 \frac{\bar{k}_1^2 \bar{k}_2^2}{4\bar{k}_1^2 - \bar{k}_2^2} \right. \\ \left. + 2F_{122} F_{212} \frac{\bar{k}_1 \bar{k}_2^3}{4\bar{k}_2^2 - \bar{k}_1^2} \right],$$

$$C_{12} = \frac{511832}{128625} (\mu_1^*)^2 \pi^2. \quad (\text{C.14})$$

$$C_{13} = 2(\mu_1^*)^2 \left[ \frac{1}{3} F_{111} F_{112} \bar{k}_1 \frac{5\bar{k}_1^2 + (\bar{k}_1 - \bar{k}_2)^2}{2\bar{k}_1 - \bar{k}_2} + 2F_{112} F_{212} \frac{\bar{k}_1 \bar{k}_2^2}{2\bar{k}_2 - \bar{k}_1} \right. \\ \left. + F_{122} F_{211} \frac{\bar{k}_1^2 \bar{k}_2^2}{\bar{k}_2^2 - 4\bar{k}_1^2} \right],$$

$$C_{13} = (\mu_1^*)^2 \frac{1108}{2625} \pi^2, \quad (\text{C.15})$$

$$C_{21} = 2(\mu_1^*)^2 \left[ \frac{5}{3} F_{222}^2 \bar{k}_2^2 + 2F_{122} F_{212} \frac{\bar{k}_2^3}{\bar{k}_1} + F_{122} F_{212} \frac{\bar{k}_1 \bar{k}_2^3}{\bar{k}_1^2 - 4\bar{k}_2^2} \right]$$

$$C_{21} = (\mu_1^*)^2 \frac{3145004}{128625} \pi^2, \quad (\text{C.16})$$

$$C_{22} = 4(\mu_1^*)^2 \left[ F_{211} F_{222} \bar{k}_1^2 + F_{1,1,1} F_{2,1,2} \bar{k}_1 \bar{k}_2 + 2F_{112} F_{211} \frac{\bar{k}_1^3 \bar{k}_2}{4\bar{k}_1^2 - \bar{k}_2^2} \right. \\ \left. + 2F_{212}^2 \frac{\bar{k}_1^2 \bar{k}_2^2}{4\bar{k}_2^2 - \bar{k}_1^2} \right],$$

$$C_{22} = (\mu_1^*)^2 \frac{511832}{128625} \pi^2, \quad (\text{C.17})$$

$$C_{23} = 2(\mu_1^*)^2 \left[ F_{211} F_{212} \frac{k_1^3 k_2}{\bar{k}_2^2 - 4\bar{k}_1^2} - \frac{1}{3} F_{111} F_{211} k_1^2 \right],$$

$$C_{23} = (\mu_1^*)^2 \frac{1108}{7875} \pi^2, \quad (\text{C.18})$$

Substituting Eqns. (C.8) through (C.18) into Eqns. (3.168) and (3.169), yields the following:

$$-i\bar{k}_1^3\phi A_1 - 2i\bar{k}_1 D_2 A_1 + Q_1 e^{i\sigma T_2} + C_1 A_1^2 A_1^* + C_2 A_1 A_2 A_2^* + C_3 A_2 (A_1^*)^2 = 0, \quad (\text{C.19})$$

$$-i\bar{k}_2^3\phi A_2 - 2i\bar{k}_2 D_2 A_2 + C_4 A_2^2 A_2^* + C_5 A_2 A_1 A_1^* + C_6 A_1^3 = 0, \quad (\text{C.20})$$

where

$$\begin{aligned} C_1 &= C_{11} + P_{11} = \frac{1364}{3375} (\mu_1^*)^2 \pi^2 - \frac{3}{128} \pi^4 \mu_2^*, \\ C_2 &= C_{12} + P_{12} = \frac{511832}{128625} \pi^2 (\mu_1^*)^2 - \frac{9}{32} \pi^4 \mu_2^*, \\ C_3 &= C_{13} + P_{13} = \frac{1108}{2625} \pi^2 (\mu_1^*)^2 - \frac{3}{128} \pi^4 \mu_2^*, \\ C_4 &= C_{21} + P_{21} = \frac{3145004}{128625} \pi^2 (\mu_1^*)^2 - \frac{243}{128} \pi^4 \mu_2^*, \\ C_5 &= C_{22} + P_{22} = \frac{511832}{128625} \pi^2 (\mu_1^*)^2 - \frac{9}{32} \pi^4 \mu_2^* = C_2, \\ C_6 &= C_{23} + P_{23} = \frac{1108}{7875} \pi^2 (\mu_1^*)^2 - \frac{1}{128} \pi^4 \mu_2^* = \frac{1}{3} C_3. \end{aligned} \quad (\text{C.21})$$

Introduction the polar notation  $A_m = a_m(T_2) e^{i\theta_m(T_2)}$  into Eqns. (C.19) and (C.20), and separation into imaginary and real parts leads to the following ODEs for the amplitudes  $a_k$  and phases  $\theta_k$ :

$$-\bar{k}_1^3\phi a_1 - 2\bar{k}_1 a_1' + Q_1 \sin(\sigma T_2 - \theta_1) - C_3 a_2 a_1^2 \sin(3\theta_1 - \theta_2) = 0, \quad (\text{C.22})$$

$$-\bar{k}_2^3\phi a_2 - 2\bar{k}_2 a_2' + \frac{1}{3} C_3 a_1^3 \sin(3\theta_1 - \theta_2) = 0, \quad (\text{C.23})$$

$$2\bar{k}_1 a_1 \theta_1' + Q_1 \cos(\sigma T_2 - \theta_1) + C_1 a_1^3 + C_2 a_1 a_2^2 + C_3 a_2 a_1^2 \cos(3\theta_1 - \theta_2) = 0, \quad (\text{C.24})$$

$$2\bar{k}_2 a_2 \theta_2' + C_4 a_2^3 + C_2 a_2 a_1^2 + \frac{1}{3} C_3 a_1^3 \cos(3\theta_1 - \theta_2) = 0. \quad (\text{C.25})$$

Defining  $\nu := \sigma T_2 - \theta_1$ ,  $\nu_{12} := 3\theta_1 - \theta_2$ , Eq. (C.22) can be rewritten as

$$\begin{aligned}
2\bar{k}_1 a_1' + &= -\bar{k}_1^3 \phi a_1 + Q_1 \sin \nu - C_3 a_2 a_1^2 \sin \nu_{12} = 0, \\
2\bar{k}_2 a_2' &= -\bar{k}_2^3 \phi a_2 + \frac{1}{3} C_3 a_1^3 \sin \nu_{12} = 0, \\
2\bar{k}_1 a_1 \nu' &= 2\bar{k}_1 a_1 \sigma + Q_1 \cos \nu + C_1 a_1^3 + C_2 a_1 a_2^2 + C_3 a_2 a_1^2 \cos \nu_{12} = 0, \\
6\bar{k}_2 a_2 \nu' + 2\bar{k}_2 a_2 \nu'_{12} &= 6\sigma \bar{k}_2 a_2 + C_4 a_2^3 + C_2 a_2 a_1^2 + \frac{1}{3} C_3 a_1^3 \cos \nu_{12} = 0.
\end{aligned} \tag{C.26}$$

## Appendix D

### Numerical Scheme for the Study of Wave Propagation through Nonlinear Viscoelastic Material

In order to carry out numerical simulations with Eqns. (3.1), a custom developed finite difference scheme is introduced in this appendix. In general terms, the finite difference scheme combines spatial central difference scheme for the discretization of spatial derivatives, incremental approach for handling of the nonlinear terms and a trapezoidal time marching scheme. The solution at each time step is found iteratively.

#### D.1 Finite Difference Scheme

The rod is divided in  $M + 1$  segments of length  $\Delta X$ . The number of internal points in the rod is  $M$ . The total number of points where the solution is to be computed is  $N = M + 2$ , as the two boundary points are included. Each internal point in the rod is labeled  $X_j$  ( $1 \leq j \leq M$ ). Left and right boundary points are labeled  $X_A$  and  $X_B$ , respectively. As it is customary in finite difference literature, the following notation is employed

$$\chi_j^n = \chi(X, t)|_{\substack{X=X_j \\ t=t_n}} \quad P_j^n = P(X, t)|_{\substack{X=X_j \\ t=t_n}} \quad \lambda_j^n = \lambda(X, t)|_{\substack{X=X_j \\ t=t_n}}, \quad (\text{D.1})$$

and similar notation is used for the corresponding derivatives. The function  $\chi$  is related to the displacement  $u$  through  $u = \chi - X$ .

The point central difference operators used for internal points in the rod ( $1 \leq j \leq M$ ) are

$$\frac{\partial}{\partial X} (P_j^{n+1} \mathcal{A}_j) = \frac{(P_{j+1}^{n+1} \mathcal{A}_{j+1}) - (P_{j-1}^{n+1} \mathcal{A}_{j-1})}{2\Delta X}, \quad (\text{D.2})$$

$$\frac{\partial \chi_j^{n+1}}{\partial X} = \lambda_j^{n+1} = \frac{\chi_{j+1}^{n+1} - \chi_{j-1}^{n+1}}{2\Delta X}. \quad (\text{D.3})$$

For the left and right boundary points,  $X_A = 0$  and  $X_B = L$ , spatially downwinded and upwinded schemes are used, respectively

$$\frac{\partial}{\partial X} (P_A^{n+1} \mathcal{A}_A) = \frac{P_1^{n+1} \mathcal{A}_1 - P_A^{n+1} \mathcal{A}_A}{\Delta X}, \quad (\text{D.4})$$

$$\frac{\partial}{\partial X} (P_B^{n+1} \mathcal{A}_B) = \frac{P_B^{n+1} \mathcal{A}_B - P_M^{n+1} \mathcal{A}_M}{\Delta X}, \quad (\text{D.5})$$

$$\frac{\partial \chi_A^{n+1}}{\partial X} = \lambda_A^{n+1} = \frac{\chi_1^{n+1} - \chi_A^{n+1}}{\Delta X}, \quad (\text{D.6})$$

$$\frac{\partial \chi_B^{n+1}}{\partial X} = \lambda_B^{n+1} = \frac{\chi_B^{n+1} - \chi_M^{n+1}}{\Delta X}. \quad (\text{D.7})$$

The trapezoidal rule time marching is given by

$$\chi^{n+1} = \chi^n + \frac{1}{2} (\dot{\chi}^n + \dot{\chi}^{n+1}) \Delta t, \quad (\text{D.8})$$

$$\dot{\chi}^{n+1} = \dot{\chi}^n + \frac{1}{2} (\ddot{\chi}^n + \ddot{\chi}^{n+1}) \Delta t. \quad (\text{D.9})$$

from where

$$\ddot{\chi}^{n+1} = \left( \frac{2}{\Delta t} \right)^2 (\chi^{n+1} - \chi^n) - \frac{4}{\Delta t} \dot{\chi}^n - \ddot{\chi}^n. \quad (\text{D.10})$$

Similarly,

$$\lambda^{n+1} = \lambda^n + \frac{1}{2} (\dot{\lambda}^n + \dot{\lambda}^{n+1}) \Delta t, \quad (\text{D.11})$$

from where,

$$\dot{\lambda}^{n+1} = \frac{2}{\Delta t} (\lambda^{n+1} - \lambda^n) - \dot{\lambda}^n. \quad (\text{D.12})$$

The following incremental approach is proposed:

$$(\chi_j^{n+1})_{k+1} = (\chi_j^{n+1})_k + \Delta\chi_j^{n+1}, \quad (\text{D.13})$$

$$(\lambda_j^{n+1})_{k+1} = (\lambda_j^{n+1})_k + \Delta\lambda_j^{n+1}, \quad (\text{D.14})$$

$$(P_j^{n+1})_{k+1} = (P_j^{n+1})_k + \Delta P_j^{n+1}, \quad (\text{D.15})$$

where  $k$  indicates the iteration number. Combining Eqns. (D.10) and (D.12) with Eqns. (D.13) and (D.14) it can be shown that

$$\Delta\ddot{\chi}_j^{n+1} = \left(\frac{2}{\Delta t}\right)^2 \Delta\chi_j^{n+1}, \quad (\text{D.16})$$

$$\Delta\dot{\lambda}_j^{n+1} = \frac{2}{\Delta t} \Delta\lambda_j^{n+1}. \quad (\text{D.17})$$

The governing equations at a material point  $X_j$  and time  $n + 1$ , corresponding to iteration  $k + 1$  are given by

$$\frac{\left((P_{j+1}^{n+1})_{k+1} \mathcal{A}_{j+1}\right) - \left((P_{j-1}^{n+1})_{k+1} \mathcal{A}_{j-1}\right)}{2\Delta X} = \rho_0 \mathcal{A}_j (\ddot{\chi}_j^{n+1})_{k+1}, \quad (\text{D.18})$$

$$\left(\dot{\lambda}_j^{n+1}\right)_{k+1} = -\kappa \left[ g(\lambda)^{-2} f(\lambda) \right]_{\lambda=(\lambda_j^{n+1})_{k+1}} - \kappa h(\lambda, P) \Big|_{\substack{\lambda=(\lambda_j^{n+1})_{k+1} \\ P=(P_j^{n+1})_{k+1}}}, \quad (\text{D.19})$$

$$(\lambda_j^{n+1})_{k+1} = \frac{(\chi_{j+1}^{n+1})_{k+1} - (\chi_{j-1}^{n+1})_{k+1}}{2\Delta X}, \quad (\text{D.20})$$

where  $h(\lambda, P) := g(\lambda)^{-2} P$  was defined. The nonlinear terms on the RHS of Eq. (D.19) are linearized by Taylor expansion around  $\lambda = (\lambda_j^{n+1})_k$  and  $P = (P_j^{n+1})_k$ .

Explicitly,

$$\begin{aligned} g(\lambda)^{-2} f(\lambda) \Big|_{\lambda=(\lambda_j^{n+1})_{k+1}} &\approx g(\lambda)^{-2} f(\lambda) \Big|_{\lambda=(\lambda_j^{n+1})_k} \\ &\quad - \left[ 2f(\lambda) g(\lambda)^{-3} \frac{dg}{d\lambda}(\lambda) \right]_{\lambda=(\lambda_j^{n+1})_k} \Delta\lambda_j^{n+1} \\ &\quad + \left[ g(\lambda)^{-2} \frac{df}{d\lambda}(\lambda) \right]_{\lambda=(\lambda_j^{n+1})_k} \Delta\lambda_j^{n+1} \end{aligned} \quad (\text{D.21})$$

and

$$\begin{aligned}
h(\lambda, P) \Big|_{\substack{\lambda=(\lambda_j^{n+1})_{k+1} \\ P=(P_j^{n+1})_{k+1}}} &\approx h(\lambda, P) \Big|_{\substack{\lambda=(\lambda_j^{n+1})_{k+1} \\ P=(P_j^{n+1})_{k+1}}} \\
&+ \left[ \frac{\partial h}{\partial \lambda}(\lambda, P) \Delta \lambda_j^{n+1} + \frac{\partial h}{\partial P}(\lambda, P) \Delta P_j^{n+1} \right]_{\substack{\lambda=(\lambda_j^{n+1})_{k+1} \\ P=(P_j^{n+1})_{k+1}}}, \tag{D.22}
\end{aligned}$$

where

$$\frac{\partial h}{\partial \lambda} = -2g(\lambda)^{-3} \frac{dg}{d\lambda}, \tag{D.23}$$

$$\frac{\partial h}{\partial P} = g(\lambda)^{-2}. \tag{D.24}$$

Substituting Eqns. (D.13)–(D.15) and (D.21)–(D.22) into Eqns. (D.18)–(D.20), it can be shown that the equations at an internal point  $X_j$  and time  $n + 1$ , corresponding to iteration  $k + 1$  are

$$\mathcal{A}_j \Delta \chi_j^{n+1} - \left( \frac{\Delta t}{2} \right)^2 \frac{1}{2\rho_0 \Delta X} (\Delta P_{j+1}^{n+1} \mathcal{A}_{j+1} - \Delta P_{j-1}^{n+1} \mathcal{A}_{j-1}) = RHS_{1j} \tag{D.25}$$

$$\left[ F(\lambda, P) \Delta \lambda_j^{n+1} + G(\lambda, P) \Delta P_j^{n+1} \right]_{\substack{\lambda=(\lambda_j^{n+1})_k \\ P=(P_j^{n+1})_k}} = RHS_{2j} \tag{D.26}$$

$$-\frac{\Delta \chi_{j+1}^{n+1} - \Delta \chi_{j-1}^{n+1}}{2\Delta X} + \Delta \lambda_j^{n+1} = RHS_{3j}, \tag{D.27}$$

where

$$F(\lambda, P) = -1 - \kappa \frac{\Delta t}{2} \left( -2g(\lambda)^{-3} \frac{dg}{d\lambda} f(\lambda) + g(\lambda)^{-1} \right) + \kappa \frac{\Delta t}{2} \frac{\partial h}{\partial \lambda}(\lambda, P), \tag{D.28}$$

$$G(\lambda, P) = \kappa \frac{\Delta t}{2} \frac{\partial h}{\partial P}(\lambda, P) \tag{D.29}$$

and

$$\begin{aligned}
RHS_{1j} = & - \left( \frac{\Delta t}{2} \right)^2 \mathcal{A}_j (\ddot{\chi}_j^{n+1})_k \\
& + \left( \frac{\Delta t}{2} \right)^2 \frac{1}{2\rho_0 \Delta X} \left[ (P_{j+1}^{n+1})_k \mathcal{A}_{j+1} - (P_{j-1}^{n+1})_k \mathcal{A}_{j-1} \right], \tag{D.30}
\end{aligned}$$

$$RHS_{2j} = \frac{\Delta t}{2} (\dot{\lambda}_j^{n+1})_k + \kappa \left[ \frac{\Delta t}{2} g(\lambda)^{-2} f(\lambda) - \frac{\Delta t}{2} h(\lambda) \right]_{\substack{\lambda=(\lambda_j^{n+1})_k \\ P=(P_j^{n+1})_k}}, \tag{D.31}$$

$$RHS_{3j} = - (\lambda_j^{n+1})_k + \frac{(\chi_{j+1}^{n+1})_k - (\chi_{j-1}^{n+1})_k}{2\Delta X}. \tag{D.32}$$

For the end point  $X_A = 0$  the finite difference equations are given by

$$\mathcal{A}_A \Delta \chi_A^{n+1} - \left( \frac{\Delta t}{2} \right)^2 \frac{1}{\rho_0 \Delta X} (\Delta P_1^{n+1} \mathcal{A}_1 - \Delta P_A^{n+1} \mathcal{A}_A) = RHS_{1A} \tag{D.33}$$

$$[F(\lambda, P) \Delta \lambda_A^{n+1} + G(\lambda, P) \Delta P_A^{n+1}]_{\substack{\lambda=(\lambda_A^{n+1})_k \\ P=(P_A^{n+1})_k}} = RHS_{2A} \tag{D.34}$$

$$-\frac{\Delta \chi_1^{n+1} - \Delta \chi_A^{n+1}}{\Delta X} + \Delta \lambda_A^{n+1} = RHS_{3A}, \tag{D.35}$$

with

$$\begin{aligned}
RHS_{1A} = & - \left( \frac{\Delta t}{2} \right)^2 \mathcal{A}_A (\ddot{\chi}_A^{n+1})_k \\
& + \left( \frac{\Delta t}{2} \right)^2 \frac{1}{\rho_0 \Delta X} \left[ (P_1^{n+1})_k \mathcal{A}_1 - (P_A^{n+1})_k \mathcal{A}_A \right], \tag{D.36}
\end{aligned}$$

$$RHS_{2A} = \frac{\Delta t}{2} (\dot{\lambda}_A^{n+1})_k + \kappa \left[ \frac{\Delta t}{2} g(\lambda)^{-2} f(\lambda) - \frac{\Delta t}{2} h(\lambda) \right]_{\substack{\lambda=(\lambda_A^{n+1})_k \\ P=(P_A^{n+1})_k}}, \tag{D.37}$$

$$RHS_{3A} = - (\lambda_A^{n+1})_k + \frac{(\chi_1^{n+1})_k - (\chi_A^{n+1})_k}{\Delta X}. \tag{D.38}$$

For the end point  $X_B = L$ , the finite difference equations are given by

$$\mathcal{A}_B \Delta \chi_B^{n+1} - \left( \frac{\Delta t}{2} \right)^2 \frac{1}{\rho_0 \Delta X} (\Delta P_B^{n+1} \mathcal{A}_B - \Delta P_M^{n+1} \mathcal{A}_M) = RHS_{1B} \quad (D.39)$$

$$\left[ F(\lambda, P) \Delta \lambda_B^{n+1} + G(\lambda, P) \Delta P_B^{n+1} \right]_{\substack{\lambda = (\lambda_B^{n+1})_k \\ P = (P_B^{n+1})_k}} = RHS_{2B}(\lambda, P) \Big|_{\substack{\lambda = (\lambda_B^{n+1})_k \\ P = (P_B^{n+1})_k}} \quad (D.40)$$

$$-\frac{\Delta \chi_B^{n+1} - \Delta \chi_M^{n+1}}{\Delta X} + \Delta \lambda_B^{n+1} = RHS_{3j}, \quad (D.41)$$

with

$$\begin{aligned} RHS_{1B} = & - \left( \frac{\Delta t}{2} \right)^2 \mathcal{A}_B (\ddot{\chi}_B^{n+1})_k \\ & + \left( \frac{\Delta t}{2} \right)^2 \frac{1}{\rho_0 \Delta X} [(P_B^{n+1})_k \mathcal{A}_B - (P_M^{n+1})_k \mathcal{A}_M] \end{aligned} \quad (D.42)$$

$$RHS_{2B} = \frac{\Delta t}{2} (\dot{\lambda}_B^{n+1})_k + \kappa \left[ \frac{\Delta t}{2} g(\lambda)^{-2} f(\lambda) - \frac{\Delta t}{2} h(\lambda) \right]_{\substack{\lambda = (\lambda_B^{n+1})_k \\ P = (P_B^{n+1})_k}} \quad (D.43)$$

$$RHS_{3B} = - (\lambda_B^{n+1})_k + \frac{(\chi_B^{n+1})_k - (\chi_M^{n+1})_k}{\Delta X}. \quad (D.44)$$

Expressing the finite difference equations for all the points in the rod results in the following algebraic system of equations for the  $\Delta \chi_j^{n+1}$ ,  $\Delta \lambda_j^{n+1}$  and  $\Delta P_j^{n+1}$  at iteration  $k + 1$

$$\left[ \begin{array}{c|c|c} [\mathcal{A}_j] & [A_{12}] & [0] \\ \hline [0] & [A_{22}] & [A_{23}] \\ \hline [A_{31}] & [0] & [I] \end{array} \right] \left\{ \begin{array}{c} \{\Delta \chi^{n+1}\} \\ \{\Delta P^{n+1}\} \\ \{\Delta \lambda^{n+1}\} \end{array} \right\} = \left\{ \begin{array}{c} \{rhs_1\} \\ \{rhs_2\} \\ \{rhs_3\} \end{array} \right\}, \quad (D.45)$$

where  $[0] \in \mathbb{R}^{N \times N}$  is a matrix of zeros,  $[I] \in \mathbb{R}^{N \times N}$  is the identity matrix and  $[\mathcal{A}_j] \in \mathbb{R}^{N \times N}$  is a diagonal matrix whose elements are the cross-sectional area  $\mathcal{A}_j$  of

the rod at  $X_j$ :

$$[\mathcal{A}_j] = \begin{bmatrix} \mathcal{A}_A & 0 & \cdots & 0 \\ 0 & \mathcal{A}_1 & \ddots & \vdots \\ \vdots & \ddots & \ddots & \vdots \\ 0 & 0 & \cdots & \mathcal{A}_B \end{bmatrix}. \quad (\text{D.46})$$

The matrices  $[A_{12}]$ ,  $[A_{22}]$ ,  $[A_{23}]$ ,  $[A_{31}] \in \mathbb{R}^{N \times N}$  are given by

$$[A_{12}] = \frac{1}{2\Delta X \rho_0} \left( \frac{\Delta t}{2} \right)^2 \begin{bmatrix} 2\mathcal{A}_A & -2\mathcal{A}_1 & 0 & \cdots & \cdots & \cdots & 0 \\ \mathcal{A}_A & 0 & -\mathcal{A}_2 & \ddots & \cdots & \cdots & \vdots \\ 0 & \ddots & \ddots & \ddots & \ddots & \cdots & \vdots \\ \vdots & \ddots & \ddots & \ddots & \ddots & \ddots & \vdots \\ \vdots & \cdots & \ddots & \ddots & \ddots & \ddots & 0 \\ \vdots & \cdots & \cdots & \ddots & \mathcal{A}_{M-1} & 0 & -\mathcal{A}_B \\ 0 & \cdots & \cdots & \cdots & 0 & 2\mathcal{A}_B & -2\mathcal{A}_B \end{bmatrix}, \quad (\text{D.47})$$

$$[A_{22}] = \begin{bmatrix} G((\lambda_A^{n+1})_k, (P_A^{n+1})_k) & 0 & \cdots & 0 \\ 0 & G((\lambda_1^{n+1})_k, (P_1^{n+1})_k) & \ddots & \ddots \\ \vdots & \ddots & \ddots & \ddots \\ 0 & \cdots & 0 & G((\lambda_B^{n+1})_k, (P_B^{n+1})_k) \end{bmatrix}, \quad (\text{D.48})$$

$$[A_{23}] = \begin{bmatrix} F((\lambda_A^{n+1})_k, (P_A^{n+1})_k) & 0 & \cdots & 0 \\ 0 & F((\lambda_1^{n+1})_k, (P_1^{n+1})_k) & \ddots & \ddots \\ \vdots & \ddots & \ddots & \ddots \\ 0 & \cdots & 0 & F((\lambda_B^{n+1})_k, (P_B^{n+1})_k) \end{bmatrix} \quad (\text{D.49})$$

and

$$[A_{31}] = \frac{1}{2\Delta X} \begin{bmatrix} 2 & -2 & 0 & \dots & \dots & \dots & 0 \\ 1 & 0 & -1 & \ddots & \dots & \dots & \vdots \\ 0 & \ddots & \ddots & \ddots & \ddots & \dots & \vdots \\ \vdots & \ddots & \ddots & \ddots & \ddots & \ddots & \vdots \\ \vdots & \dots & \ddots & \ddots & \ddots & \ddots & 0 \\ \vdots & \dots & \dots & \ddots & 1 & 0 & -1 \\ 0 & \dots & \dots & \dots & 0 & 2 & -2 \end{bmatrix}. \quad (\text{D.50})$$

The unknowns  $\{\Delta\chi^{n+1}\}, \{\Delta P^{n+1}\}, \{\Delta\lambda^{n+1}\} \in \mathbb{R}^N$  are given by

$$\{\Delta\chi\} = \begin{pmatrix} \Delta\chi_A^{n+1} \\ \Delta\chi_1^{n+1} \\ \vdots \\ \Delta\chi_B^{n+1} \end{pmatrix}; \quad \{\Delta P^{n+1}\} = \begin{pmatrix} \Delta P_A^{n+1} \\ \Delta P_1^{n+1} \\ \vdots \\ \Delta P_B^{n+1} \end{pmatrix}; \quad \{\Delta\lambda^{n+1}\} = \begin{pmatrix} \Delta\lambda_A^{n+1} \\ \Delta\lambda_1^{n+1} \\ \vdots \\ \Delta\lambda_B^{n+1} \end{pmatrix}. \quad (\text{D.51})$$

The terms in the RHS  $\{rhs_1\}, \{rhs_2\}, \{rhs_3\} \in \mathbb{R}^N$  are given by

$$\{rhs_1\} = \begin{pmatrix} RHS_{1A} \\ RHS_{11} \\ \vdots \\ RHS_{1B} \end{pmatrix}; \quad \{rhs_2\} = \begin{pmatrix} RHS_{2A} \\ RHS_{21} \\ \vdots \\ RHS_{2B} \end{pmatrix}; \quad \{rhs_3\} = \begin{pmatrix} RHS_{3A} \\ RHS_{31} \\ \vdots \\ RHS_{3B} \end{pmatrix}. \quad (\text{D.52})$$

In order to initialize the iteration  $k = 0$  at each time step  $n + 1$ , the following quantities are needed.

$$(P_j^{n+1})_0; \quad (\chi_j^{n+1})_0; \quad (\ddot{\chi}_j^{n+1})_0; \quad (\lambda_j^{n+1})_0; \quad (\dot{\lambda}_j^{n+1})_0 \quad \text{for all } j. \quad (\text{D.53})$$

In consequence, the following is set

$$(\ddot{\chi}_j^{n+1})_0 = 0; \quad (\dot{\lambda}_j^{n+1})_0 = 0; \quad (P_j^{n+1})_0 = 0 \quad \text{for all } j. \quad (\text{D.54})$$

Using formulas (D.8)-(D.9) yields

$$(\chi^{n+1})_0 = \chi^n + \dot{\chi}^n \Delta t + \left(\frac{\Delta t}{2}\right)^2 \ddot{\chi}^n. \quad (\text{D.55})$$

From Eq. (D.11) it results

$$(\lambda^{n+1})_0 = \lambda^n + \frac{\Delta t}{2} \dot{\lambda}^n. \quad (\text{D.56})$$

## Bibliography

- Akkas, N. Dynamic analysis of a fluid-filled spherical sandwich shell—a model of the human head. *Journal of Biomechanics*, 8(5):275–284, 1975.
- Alley, M.D., Schimizze, B.R., and Son, S.F. Experimental modeling of explosive blast-related traumatic brain injuries. *NeuroImage*, 54(1):S45–S54, 2011.
- Antman, S.S. *Nonlinear problems of elasticity*, volume 107. Springer, 2005.
- Arbogast, K. and Margulies, S. Material characterization of the brainstem from oscillatory shear tests. *Journal of Biomechanics*, 31(9):801–807, 1998.
- Balachandran, B. and Magrab, E. *Vibrations*. Cengage Learning, 2009.
- Bernal, R., Pullarkat, P., and Melo, F. Mechanical properties of axons. *Physical Review Letters*, 99(1):18301, 2007.
- Bilston, L., Liu, Z., and Phan-Thien, N. Large strain behaviour of brain tissue in shear: some experimental data and differential constitutive model. *Biorheology*, 38(4):335–345, 2001.
- Brands, D. *Predicting brain mechanics during closed head impact: numerical and constitutive aspects*. Ph.D. thesis, Technische Universiteit Eindhoven, 2002.
- Brands, D., Peters, G., and Bovendeerd, P. Design and numerical implementation of a 3–D non-linear viscoelastic constitutive model for brain tissue during impact. *Journal of Biomechanics*, 37(1):127–134, 2004. ISSN 0021-9290.
- Chatelin, S., Constantinesco, A., and Willinger, R. Fifty years of brain tissue mechanical testing: from in vitro to in vivo investigations. *Biorheology*, 47(5):255–276, 2010.
- Chen, Y. and Ostoja-Starzewski, M. MRI-based finite element modeling of head trauma: spherically focusing shear waves. *Acta Mechanica*, 213(1):155–167, 2010.
- Chetta, J., Kye, C., and Shah, S. Cytoskeletal dynamics in response to tensile loading of mammalian axons. *Cytoskeleton*, 67:650–665, 2010.
- Claessens, M., Sauren, F., and Wismans, J. Modeling of the human head under impact conditions: a parametric study. In *SAE Conference Proceedings P*, pp. 315–328. Soc Automotive Engineers Inc, 1997.
- Cowin, S. and Doty, S. *Tissue Mechanics*. Springer Verlag, 2007.
- Culjat, M., Goldenberg, D., Tewari, P., and Singh, R. A review of tissue substitutes for ultrasound imaging. *Ultrasound in Medicine & Biology*, 36(6):861–873, 2010.
- Darvish, K. and Crandall, J. Nonlinear viscoelastic effects in oscillatory shear deformation of brain tissue. *Medical Engineering & Physics*, 23(9):633–645, 2001. ISSN 1350-4533.

- Dennerll, T., Joshi, H., Steel, V., Buxbaum, R., and Heidemann, S. Tension and compression in the cytoskeleton of pc-12 neurites II: Quantitative measurements. *The Journal of Cell Biology*, 107(2):665–674, 1988.
- Dennerll, T., Lamoureux, P., Buxbaum, R., and Heidemann, S. The cytomechanics of axonal elongation and retraction. *The Journal of Cell Biology*, 109(6):3073–3083, 1989.
- Ehlers, W. and Markert, B. A linear viscoelastic biphasic model for soft tissues based on the theory of porous media. *Journal of Biomechanical Engineering*, 123:418–224, 2001.
- El Sayed, T., Mota, A., Fraternali, F., and Ortiz, M. Biomechanics of traumatic brain injury. *Computer Methods in Applied Mechanics and Engineering*, 197(51-52):4692–4701, 2008a. ISSN 0045-7825.
- El Sayed, T., Mota, A., Fraternali, F., and Ortiz, M. A variational constitutive model for soft biological tissues. *Journal of Biomechanics*, 41(7):1458–1466, 2008b.
- Elkin, B., Azeloglu, E., Costa, K., and Morrison III, B. Mechanical heterogeneity of the rat hippocampus measured by atomic force microscope indentation. *Journal of Neurotrauma*, 24(5):812–822, 2007.
- Engin, A. and Liu, Y. Axisymmetric response of a fluid-filled spherical shell in free vibrations. *Journal of Biomechanics*, 3(1):11–22, 1970.
- Estes, M. and McElhaney, J. Response of brain tissue to compressive loading. *Proceedings of the Fourth ASME Biomechanics Conference*, (70-BHF-13), 1970.
- Etoh, A., Mitaku, S., Yamamoto, J., and Okano, K. Ultrasonic absorption anomaly of brain tissue. *Japanese Journal of Applied Physics*, 33(Part 1, 5B):2874–2879, 1994.
- Evans, L.C. *Partial differential equations*, volume 19 of *Graduate Studies in Mathematics*. American Mathematical Society, Providence, Rhode Island, 2010.
- Fallenstein, G., Hulce, V., and Melvin, J. Dynamic mechanical properties of human brain tissue. *Journal of Biomechanics*, 2(3):217–226, 1969.
- Feng, Y., Abney, T., Okamoto, R., Pless, R., Genin, G., and Bayly, P. Relative brain displacement and deformation during constrained mild frontal head impact. *Journal of The Royal Society Interface*, 7(53):1677–1688, 2010.
- Feng, Y., Clayton, E., Chang, Y., Okamoto, R., and Bayly, P. Viscoelastic properties of the ferret brain measured in vivo at multiple frequencies by magnetic resonance elastography. *Journal of Biomechanics*, 46(5):863–870, 2013.

- Franceschini, G., Bigoni, D., Regitnig, P., and Holzapfel, G. Brain tissue deforms similarly to filled elastomers and follows consolidation theory. *Journal of the Mechanics and Physics of Solids*, 54(12):2592–2620, 2006. ISSN 0022-5096.
- Gao, L., Parker, K., Lerner, R., and Levinson, S. Imaging of the elastic properties of tissue—a review. *Ultrasound in Medicine & Biology*, 22(8):959–977, 1996.
- Graff, K.F. *Wave Motion in Elastic Solids*. Courier Dover Publications, 1975.
- Gross, A. A new theory on the dynamics of brain concussion and brain injury. *Journal of Neurosurgery*, 15(5):548–561, 1958. ISSN 0022-3085.
- Grujicic, M., Bell, W., Pandurangan, B., and He, T. Blast–wave impact–mitigation capability of polyurea when used as helmet suspension-pad material. *Materials & Design*, 31(9):4050–4065, 2010.
- Haslach, H. Nonlinear viscoelastic, thermodynamically consistent, models for biological soft tissue. *Biomechanics and Modeling in Mechanobiology*, 3(3):172–189, 2005. ISSN 1617-7959.
- Haslach, H. *Maximum Dissipation Non-Equilibrium Thermodynamics and Its Geometric Structure*. Springer, 2011.
- Holbourn, A. The mechanics of brain injuries. *British Medical Bulletin*, 3(6):147, 1945. ISSN 0007-1420.
- Holzapfel, G. *Nonlinear Solid Mechanics: A Continuum Approach for Engineering*. John Wiley & Sons Ltd., 2000.
- Hrapko, M., van Dommelen, J., Peters, G., and Wismans, J. The mechanical behaviour of brain tissue: large strain response and constitutive modelling. *Biorheology*, 43(5):623–636, 2006. ISSN 0006-355X.
- Hrapko, M., van Dommelen, J., Peters, G., and Wismans, J. Characterisation of the mechanical behaviour of brain tissue in compression and shear. *Biorheology*, 45(6):663–676, 2008a.
- Hrapko, M., van Dommelen, J., Peters, G., and Wismans, J. The influence of test conditions on characterization of the mechanical properties of brain tissue. *Journal of Biomechanical Engineering*, 130:031003, 2008b.
- Huang, H., Lee, M., Lee, S., Chiu, W., Pan, L., and Chen, C. Finite element analysis of brain contusion: an indirect impact study. *Medical and Biological Engineering and Computing*, 38(3):253–259, 2000. ISSN 0140-0118.
- Humphrey, J. Review paper: Continuum biomechanics of soft biological tissues. *Proceedings of the Royal Society of London. Series A: Mathematical, Physical and Engineering Sciences*, 459(2029):3–46, 2003.

- Kambouchev, N. *Analysis of Blast Mitigation Strategies Exploiting Fluid–Structure Interaction*. Ph.D. thesis, 2007.
- Kremkau, F., Barnes, R., and McGraw, C. Ultrasonic attenuation and propagation speed in normal human brain. *The Journal of the Acoustical Society of America*, 70(1):29–38, 1981.
- Lamoureux, P., Buxbaum, R., and Heidemann, S. Direct evidence that growth cones pull. *Letters to Nature*, 340:159–162, 1989.
- Mendis, K., Stalnaker, R., and Advani, S. A constitutive relationship for large deformation finite element modeling of brain tissue. *Journal of Biomechanical Engineering*, 117:279–285, 1995.
- Miller, K. and Chinzei, K. Constitutive modelling of brain tissue: experiment and theory. *Journal of Biomechanics*, 30(11-12):1115–1121, 1997.
- Miller, K. and Chinzei, K. Mechanical properties of brain tissue in tension. *Journal of Biomechanics*, 35(4):483–490, 2002. ISSN 0021-9290.
- Moore, D., Jérusalem, A., Nyein, M., Noels, L., Jaffee, M., and Radovitzky, R. Computational biology–modeling of primary blast effects on the central nervous system. *Neuroimage*, 47:T10–T20, 2009. ISSN 1053-8119.
- Moss, W., King, M., and Blackman, E. Skull flexure from blast waves: a mechanism for brain injury with implications for helmet design. *Physical Review Letters*, 103(10):108702, 2009. ISSN 1079-7114.
- Nayfeh, A.H. and Mook, D.T. *Nonlinear Oscillations*. Wiley-VCH, 2008.
- Neves, A. On the strongly damped wave equation and the heat equation with mixed boundary conditions. In *Abstract and Applied Analysis*, volume 5, pp. 175–189. Hindawi Publishing Corporation, 410 Park Avenue, 15 th Floor, # 287 pmb, New York, NY, 10022, USA,, 2000. ISSN 1085-3375.
- Newland, D.E. Harmonic wavelet analysis. *Proceedings of the Royal Society of London. Series A: Mathematical and Physical Sciences*, 443(1917):203–225, 1993.
- Nolte, J. *The Human Brain: An Introduction to Its Functional Anatomy*. Mosby, 2002.
- Nyein, M., Jason, A., Yu, L., Pita, C., Joannopoulos, J., Moore, D., and Radovitzky, R. In silico investigation of intracranial blast mitigation with relevance to military traumatic brain injury. *Proceedings of the National Academy of Sciences*, 107(48):20703, 2010. ISSN 0027-8424.
- Pervin, F. and Chen, W. Dynamic mechanical response of bovine gray matter and white matter brain tissues under compression. *Journal of Biomechanics*, 42(6):731–735, 2009. ISSN 0021-9290.

- Pervin, F. and Chen, W. Effect of inter-species, gender, and breeding on the mechanical behavior of brain tissue. *NeuroImage*, 54:S98–S102, 2011.
- Pinnoji, P. and Mahajan, P. Finite element modelling of helmeted head impact under frontal loading. *Sadhana*, 32(4):445–458, 2007. ISSN 0256-2499.
- Prange, M. and Margulies, S. Regional, directional, and age-dependent properties of the brain undergoing large deformation. *Journal of Biomechanical Engineering*, 124:244, 2002.
- Rashid, B., Destrade, M., and Gilchrist, M.D. Inhomogeneous deformation of brain tissue during tension tests. *Computational Materials Science*, 64:295–300, 2012a.
- Rashid, B., Destrade, M., and Gilchrist, M.D. Mechanical characterization of brain tissue in compression at dynamic strain rates. *Journal of the Mechanical Behavior of Biomedical Materials*, 10:23–38, 2012b.
- Rashid, B., Destrade, M., and Gilchrist, M.D. Mechanical characterization of brain tissue in tension at dynamic strain rates. *Journal of the Mechanical Behavior of Biomedical Materials*, (0):–, 2012c. ISSN 1751-6161. doi:<http://dx.doi.org/10.1016/j.jmbbm.2012.07.015>.
- Rashid, B., Destrade, M., and Gilchrist, M.D. Mechanical characterization of brain tissue in simple shear at dynamic strain rates. *Journal of the Mechanical Behavior of Biomedical Materials*, 28(0):71–85, 2013.
- Ruan, J., Khalil, T., and King, A. Dynamic response of the human head to impact by three-dimensional finite element analysis. *Journal of Biomechanical Engineering*, 116:44–50, 1994.
- Schierwagen, A. Mathematical and computational modeling of neurons and neuronal ensembles. In *Computer Aided Systems Theory-EUROCAST 2009*, pp. 159–166. Springer, 2009.
- Schierwagen, A. and Ohme, M. A model for the propagation of action potentials in nonuniform axons. In *AIP Conference Proceedings*, volume 1028, p. 98. 2008.
- Segev, I. and Schneidman, E. Axons as computing devices: basic insights gained from models. *Journal of Physiology-Paris*, 93(4):263–270, 1999.
- Shafieian, M., Darvish, K., and Stone, J. Changes to the viscoelastic properties of brain tissue after traumatic axonal injury. *Journal of Biomechanics*, 42(13):2136–2142, 2009.
- Smith, D. and Meaney, D. Axonal damage in traumatic brain injury. *The Neuroscientist*, 6(6):483, 2000.
- Smith, D., Wolf, J., Lusardi, T., Lee, V., and Meaney, D. High tolerance and delayed elastic response of cultured axons to dynamic stretch injury. *The Journal of Neuroscience*, 19(11):4263, 1999.

- Snell, R. *Clinical Neuroanatomy*. Lippincott Williams & Wilkins, 2009.
- Stuhmiller, J. *Blast Injury: Translating Research into Operational Medicine*. US Army Medical Research and Materiel Command, 2008.
- Suh, C., Kim, S., and Oh, S. Analysis of traumatic brain injury using a finite element model. *Journal of Mechanical Science and Technology*, 19(7):1424–1431, 2005. ISSN 1738-494X.
- Takhounts, E., Ridella, S., Hasija, V., Tannous, R., Campbell, J., Malone, D., Danelson, K., Stitzel, J., Rowson, S., and Duma, S. Investigation of traumatic brain injuries using the next generation of simulated injury monitor (simon) finite element head model. *Stapp Car Crash Journal*, 52:1–31, 2008.
- Talhouni, O. and DiMaggio, F. Dynamic response of a fluid-filled spheroidal shellan improved model for studying head injury. *Journal of Biomechanics*, 8(3):219–228, 1975.
- Tang-Schomer, M., Patel, A., Baas, P., and Smith, D. Mechanical breaking of microtubules in axons during dynamic stretch injury underlies delayed elasticity, microtubule disassembly, and axon degeneration. *The FASEB Journal*, 24(5):1401, 2010.
- Taylor, P. and Ford, C. Simulation of blast-induced early-time intracranial wave physics leading to traumatic brain injury. *Journal of Biomechanical Engineering*, 131:061007, 2009.
- Valdez, M. and Balachandran, B. Wave transmission through soft tissue. *Simulation-based Innovation and Discovery*, pp. 129–154, 2011.
- Valdez, M. and Balachandran, B. Longitudinal nonlinear wave propagation through soft tissue. *Journal of the Mechanical Behavior of Biomedical Materials*, 20(0):192 – 208, 2013. ISSN 1751-6161. doi:10.1016/j.jmbbm.2013.01.002.
- van Dommelen, J., van der Sande, T., Hrapko, M., and Peters, G. Mechanical properties of brain tissue by indentation: Interregional variation. *Journal of the Mechanical Behavior of Biomedical Materials*, 3(2):158–166, 2010.
- Velardi, F., Fraternali, F., and Angelillo, M. Anisotropic constitutive equations and experimental tensile behavior of brain tissue. *Biomechanics and Modeling in Mechanobiology*, 5(1):53–61, 2006.
- Voo, L., Kumaresan, S., Pintar, F., Yoganandan, N., and Sances, A. Finite-element models of the human head. *Medical and Biological Engineering and Computing*, 34(5):375–381, 1996. ISSN 0140-0118.
- Wang, H.C. and Ma, Y.B. Experimental models of traumatic axonal injury. *Journal of Clinical Neuroscience*, 17(2):157–162, 2010.

- Willinger, R., Kang, H., and Diaw, B. Three-dimensional human head finite-element model validation against two experimental impacts. *Annals of Biomedical Engineering*, 27(3):403–410, 1999. ISSN 0090-6964.
- Wittek, A. and Omori, K. Parametric study of effects of brain-skull boundary conditions and brain material properties on responses of simplified finite element brain model under angular acceleration impulse in sagittal plane. *JSME International Journal Series C*, 46(4):1388–1399, 2003. ISSN 1344-7653.
- Young, P. An analytical model to predict the response of fluid-filled shells to impact—a model for blunt head impacts. *Journal of Sound and Vibration*, 267(5):1107–1126, 2003. ISSN 0022-460X.
- Zhang, Q., Teo, E., and Ng, H. Development and validation of a c0–c7 fe complex for biomechanical study. *Journal of Biomechanical Engineering*, 127:729–735, 2005.
- Zheng, J., Lamoureux, P., Santiago, V., Dennerll, T., Buxbaum, R., and Heide-  
mann, S. Tensile regulation of axonal elongation and initiation. *The Journal of Neuroscience*, 11(4):1117–1125, 1991.
- Zong, Z., Lee, H., and Lu, C. A three-dimensional human head finite element model and power flow in a human head subject to impact loading. *Journal of Biomechanics*, 39(2):284–292, 2006. ISSN 0021-9290.